Development of 2D Ultrasound Tracking Software and Hardware to Monitor Multiple Flexor Tendon Displacement for Applications Toward Hand Prostheses

by

Kelly Joanne Stegman
M.A.Sc., University of Victoria, 2009
B.Sc., University of Victoria, 2007

A Dissertation Submitted in Partial Fulfillment
of the Requirements for the Degree of

DOCTOR OF PHILOSOPHY

in the Department of Mechanical Engineering

Supervisory Committee

Development of 2D Ultrasound Tracking Software and Hardware
to Monitor Multiple Flexor Tendon Displacement
for Applications Toward Hand Prostheses

by

Kelly J. Stegman
M.A.Sc., University of Victoria, 2009
B.Sc., University of Victoria, 2007

Supervisory Committee

Dr. Nikolai Dechev, Department of Mechanical Engineering
Supervisor

Dr. Stephanie Willerth, Department of Mechanical Engineering
Departmental Member

Dr. Edward Park, Department of Mechanical Engineering
Departmental Member

Dr. Andrew Jirasek, Department of Physics and Astronomy
Outside Member

Abstract

Supervisory Committee
Dr. Nikolai Dechev, Department of Mechanical Engineering
Supervisor
Dr. Stephanie Willerth, Department of Mechanical Engineering
Departmental Member
Dr. Edward Park, Department of Mechanical Engineering
Departmental Member
Dr. Andrew Jirasek, Department of Physics and Astronomy
Outside Member

This thesis work provides a new way to detect and track the displacement of flexor tendons within the human arm, using a non-invasive, ultrasound-based, speckle tracking technique. By tracking the tendons in the arm, it provides a way to monitor a person's intention to move their hands and fingers. This has application to hand prosthetic control, as well as tendon injury assessment, which has significant contributions to the medical and rehabilitation community. The system works by capturing and processing a sequence of B-scan ultrasound images, to detect and track the flexor tendon motion (excursion) in the wrist, as the user flexes their muscles. Given the biomechanics of the hand, tendon displacement is correlated to the user's intention to move their finger. Several speckle tracking techniques using B-scan ultrasound image sequences are developed in this work, including: auto-location of the tendon, a stationary ROI (region of interest), and novel use of similarity measures such as FT (Fisher Tippett), and hybrid methods. As well, work is done to investigate various speckle tracking parameters, and their effects on tracking accuracy. The different speckle tracking techniques are developed using data obtained from cadaver hands, and human volunteers undergoing regular surgery. The tracking techniques are compared in terms of successfully detecting the tendon, accurately tracking tendon displacement, successfully tracking multiple tendons, successfully detecting and tracking the onset of low tendon displacement, and computational efficiency of the algorithms. Another major aspect of this work is the design of a novel quad-array transducer that can collect image sequences from up to four tendons simultaneously. This transducer is instrumental to the motivation for controlling an advanced prosthesis. As well, specialized hardware is designed for the cadaver-based studies. Overall, this thesis successfully demonstrated the proposed tracking algorithms and newly designed hardware, for tracking the displacement of single and multiple flexor tendons. It has provided several important contributions to the field.

Table of Contents

List of Tables

List of Figures

Acknowledgments

I would like to express my deepest appreciation to my supervisor and mentor, Dr. Nikolai Dechev, whom I hold in the highest regard. Of his many attributes, his intelligence, resourcefulness, hard work, advice, kindness and humor, were all instrumental aspects to the success of this thesis. I cannot express enough, the gratitude I will forever have for him. I would also like to thank Dr. Slobodan Djurickovic and Kurt McBurney, without which, the experimentation would not have been possible. They allowed this thesis to have many unique features, by facilitating experiments involving humans and cadaver material. As well, I would like to thank Dr. Claudia Krebs, Ciaran Connolly, and Erin Gloeden from Life Sciences at the University of British Columbia, for their help and use of the facilities for the cadaver experimentation. Also, I would like to express gratitude to the patients, staff, nurses and ethics committee at the Vancouver Island Health Authority and the University of Victoria, for their participation and help with the human-based studies. I am also very grateful to my committee members, Dr. Stephanie Willerth, Dr. Edward Park and Dr. Andrew Jirasek, for their advice and guidance. In addition, I would like to thank my early physics professors Dr. Russ Pierce and Bob Sedlock from Camosun College, who have been so inspiring and influenced my career path.

I would like to acknowledge those who have helped with technical aspects: Kris Dickie at Ultrasonix Analogic Ultrasound, Randy Cyron and Bill Aurand at Blatek, and Larry Busse and Will Eddins at LJB Developement. As well, I would like to thank members of the PEO Women's Scholars for financial assistance as well as the ladies at the local Chapter for all their support.

I am most grateful to my loving husband Jason Brooks and to my mother Joanne Stegman. Without their love and support, this endeavour could not be accomplished. Their constant encouragement, hugs and gourmet dinners have been instrumental to my success.

Dedication

This thesis is dedicated
to my loving husband, Jason Brooks, and
to my mother, Joanne Stegman.

CHAPTER 1:

INTRODUCTION

1.1 MOTIVATION

Hands are vital to our interaction with the environment and the interpretation of our surroundings. The simple daily tasks we undertake, such as holding an object with a particular force, is the result of optimized and choreographed connections between the motor cortex in the brain, and the nerves, muscles, tendons and bones. However, normal hand function can be disrupted by trauma or disease to the fingers or hand, which can result in a range of hand function impairment. Such impairments can include tendon injury [1] and carpal tunnel syndrome [2], for example. According to the United States Department of Labor, Bureau of Labor Statistics, injuries to the fingers and hands accounted for 17% of all reported work-related, non-fatal bodily injuries in 2009 [3]. This amounts to 161,720 reported hand injuries in the private sector, second only to back sprain. In the most severe cases of injury, limb deficiencies can occur at the finger, hand or wrist level. In 2005 for example, there were 500,000 persons living in the United States with hand or finger amputations [4].

In some of the instances where there is hand or digit loss, the body's biological signals remain intact to various degrees. These biological signals, or bio-signals, refer to measurable signals that result from a person's action, desire or intent for motion. Examples include detecting a person's nerve impulses, their contracting muscles, or their brain's activity, to name a few. Bio-signals are of particular interest to researchers developing new ways to control an advanced hand prosthesis. This is because the bio-signals directly represent the user's intent for motion, and thus can be used as an input for prosthetic control. Often, amputees are underserved by today's conventional electric hand prosthesis, which predominantly have one or occasionally two, motorized degrees-of-freedom (DOF) [5]. The DOF of a prosthetic device is a way to describe its mechanical mobility. In general, it would be desirable to have a 1:1 ratio between independent bio-signals measured from the body, and the corresponding DOF of the prosthetic to be controlled. Hence, a prosthesis with a low DOF is generally a consequence of the fact that there are limited independent bio-signals that can be measured from the body using current technology. As a result, next generation hand prostheses will require multiple bio-signals collected from the amputee, to independently control multiple mechanical fingers and wrist motions.

1.2 THESIS OBJECTIVES

The primary goal of the thesis is to develop a new sensing strategy to *non-invasively* detect the intention of a user to move his/her fingers. This novel sensing strategy uses B-scan ultrasound to detect and track the flexor tendon motion (excursion) in the wrist, as the user flexes their muscles. Given the biomechanics of the hand, tendon displacement is correlated to the user's intention to move their finger. Ultimately, the aim is to use the tendon displacement signal in order to control a prosthetic device for those with hand or finger loss. Several B-Scan image-based ultrasound tracking techniques (auto-location and speckle tracking) are developed in order to test the validity of the proposed method. The different speckle tracking techniques are developed using data obtained from hand cadavers and human volunteers. The tracking techniques are compared in terms of successfully detecting the tendon, accurately tracking cumulative tendon displacement, successfully tracking multiple tendons, successfully detecting and tracking the onset of low tendon displacement, and computational efficiency of the algorithms. The key deliverables of this thesis are separated into the following software, hardware, and experimental objectives:

A. The development of 2D B-Scan ultrasound software algorithms to:
  - **(1)** Automatically locate the tendon position within a sequence of image frames,
  - **(2)** Track the displacement of a single tendon within a sequence of image frames,
  - **(3)** Track the displacement of multiple tendons simultaneously, within a sequence of image frames, and
  - **(4)** Detect and track the onset of small tendon displacements, within a sequence of image frames.

B. The development of custom hardware, specifically to:
  - **(5)** Design a custom ultrasound transducer, capable of monitoring multiple tendons simultaneously, and
  - **(6)** Design custom test-bed hardware to verify the Objectives in (1-4).

C. Develop experiments in order to test the validity of the proposed tracking techniques:

- **(7)** A Cadaver-based study: a preliminary experiment to optimize the hardware and software configuration,
- **(8)** A Human study: an experiment using volunteers undergoing carpal surgery to validate the techniques for tracking a single tendon (Objective 2), and
- **(9)** A Cadaver-based study: an experiment using two cadaver hands to validate the techniques for detecting and tracking single and multiple tendons (Objectives 1-4).

In order to accomplish the proposed research, the defined Objectives (1-9) are separated into software, hardware and experimental deliverables. For Objective (1), an auto-location algorithm is developed in order to determine the optimal tracking location within a sequence of 2D B-Scan images of a moving tendon. The optimal location determined by this technique is used in Objectives (2-4). For Objectives (2-4), algorithms are developed in order to determine how accurate various ultrasonic tracking approaches are at quantifying tendon motion. This includes using different mathematical metrics to track single tendons, multiple tendons simultaneously, and the onset of tendon motion with low displacement. The algorithms are further described in Chapter 5. For Objective (5), a custom ultrasound transducer is designed in order to monitor several tendons simultaneously. This allows for multiple independent tendon displacement signals to be collected from a person. The custom transducer is further described in Chapter 5. For Objective (6), custom test-bed hardware is developed in order to verify Objectives (1-4), using cadaver material. Two different platforms are developed, with the first being a preliminary system to actuate a single tendon. The second platform has the ability to actuate multiple tendons simultaneously. Designing such test-bed platforms includes: coupling stepper motors motion to linearly displace the tendon(s), securing the tendons to the apparatus, developing a clamp-system for the cadaver hand, and a developing a holder to keep the transducer in a static position. The test-bed hardware is further described in Chapter 6. Objectives (7-9) describe the experiments performed in order to test the validity of the algorithms described by Objectives (1-4). These studies are important because it allows for a direct comparison of the proposed tracking technique to a standard reference. The use of a standard reference provides an independent measurement technique in order to verify the ultrasound-based displacement estimation method. Objective (7) describes a preliminary cadaver-based study, which is performed using a single tendon in order to further develop the software and hardware. Objective (8) describes a human-based study in which persons undergoing a scheduled carpal tunnel surgery are used to validate the tracking technique (Objective 2) on a single tendon. For this experiment, total and incremental displacement is compared to the reference displacement given by the exposed tendons. Objective (9) describes an additional cadaver-based study in which upgraded hardware and software are used to verify the tracking techniques (Objectives 1-4) on single and multiple tendons. For this experiment, total displacement, incremental displacement, and the onset of small displacements are compared to the standard displacement given by the motor.

1.3 THESIS CONTRIBUTION

This work provides a new way to detect user intention, with application to prosthetic device control, which has significant contributions to the medicine and rehabilitation community. Using tendon displacement as a bio-signal for prosthetic control is a completely new concept. The novelty of the proposed sensor system itself is comprised of two major developments, which are introduced below, and described in full detail in Chapter 9. The first development is creating a new signal processing routine to estimate tendon tissue motion from a sequence of ultrasound images. Since it is ultrasound-based, it allows for non-invasive monitoring of bio-signals. The second is hardware development, in the design of a new custom ultrasonic transducer, capable of imaging up to four tendons simultaneously. Developing such a sensor is instrumental to the success of controlling a multi-DOF prosthetic. Together, the two aforementioned developments can provide a user with up to four independent signals to control an advanced prosthetic system, thereby significantly improving the state of the art by allowing for a prosthetic device to have increased functionality. This could help those suffering with hand impairment from multiple finger amputations, by restoring some function. In addition, the tendon tracking algorithm that has been developed has applicability to clinicians dealing with other hand injuries. Clinicians can use the proposed ultrasonic technique to access tendon motion in order to determine tendon velocity and displacement. This technique may be useful for applications involving the treatment, diagnosis or assessment of post/pre-operative repair of tendon injuries.

These experiments provide a comprehensive study into estimating tendon incremental displacement, total displacement, tendon velocity, as well as the onset of small displacements. These experiments are unique in that they use human material (cadavers and human volunteers) instead of gel-based medical calibration phantoms. For the experiments involving hand cadavers, novel hardware is developed to attach the mechanical actuation system to the biological tendon tissue. This task is non-trivial, due to the delicate nature of experiments involving biological tissue, and the limited experimental time before biological tissue deteriorates. Experiments that employ biological tissue allow for a gold standard reference for comparison to the estimated values. Hence, one of the novelties of this thesis is that tracking techniques are verified by directly observing real tendon motion in live human subjects with exposed tendons, or by observing real tendon motion in cadaver hands which are actuated by motors. This way, the tendon tracking techniques are verified in the most realistic way.

1.4 THESIS ORGANIZATION

This thesis is divided into nine chapters as follows:

In Chapter 1, the motivation of this thesis is introduced by reporting the prevalence of hand injuries, and describing the concept of controlling hand prosthesis mechanisms by detecting user intention. The thesis objectives are also outlined in order to show the structure of this document. As well, the contributions of this thesis are described. In Chapter 2, background information is provided which describes the structural and functional anatomy of a healthy hand, as well as that of an amputated hand or hand with amputated digits. Given that the tendon system will lose function to various degrees as a result of a hand amputation, a surgical protocol is proposed, which will facilitate the use of the proposed application. In Chapter 3, a full literature review into the state of the art of prosthetic devices and controlling strategies are described. Chapter 4 describes the physics of ultrasound imaging and tracking theory. This chapter forms the basis to understand the background of the new bio-sensing method presented in this thesis. Chapter 5 describes the proposed technique and methodology. This chapter provides detail into the developed tracking algorithms. This chapter also includes the new multi-array transducer hardware design. Chapter 6 describes the experimental methodology used to validate the techniques outlined in Chapter 5. A description of the experimental objectives is included with a discussion on the importance of a standard reference. This is followed by an overview of all experiments, each with experimental set-up and protocol descriptions. Chapter 7 reports all the results from the previously described experiments. The results are disseminated in a quantitative and illustrative way. Chapter 8 provides a discussion of all the research presented in this thesis, as well as the feasibility of approach for the intended application. In Chapter 9, conclusions are drawn concerning the results, the future potential, and the thesis contribution. These Chapters are then followed by the references used in this thesis, and an appendix containing additional material.

CHAPTER 2:

HAND STRUCTURE AND FUNCTIONAL ANATOMY

2.1 PHYSICAL ANATOMY OF THE NORMAL HAND

2.1.1. *Bones and Joints*

Bones are hard connective tissue that performs a structural and mechanical role in the body. The bones in the hand are generally considered long bones and are comprised of an outer dense compact layer known as cortical bone, and an inner spongy layer called cancellous bone (Fig. 1) [6,7]. The main function of cortical bone is to carry structural loads, and to carry the nerves, blood and lymph vessels through inner canals. The cancellous bone is in contact with bone marrow, where most of the blood cell production takes place [6].

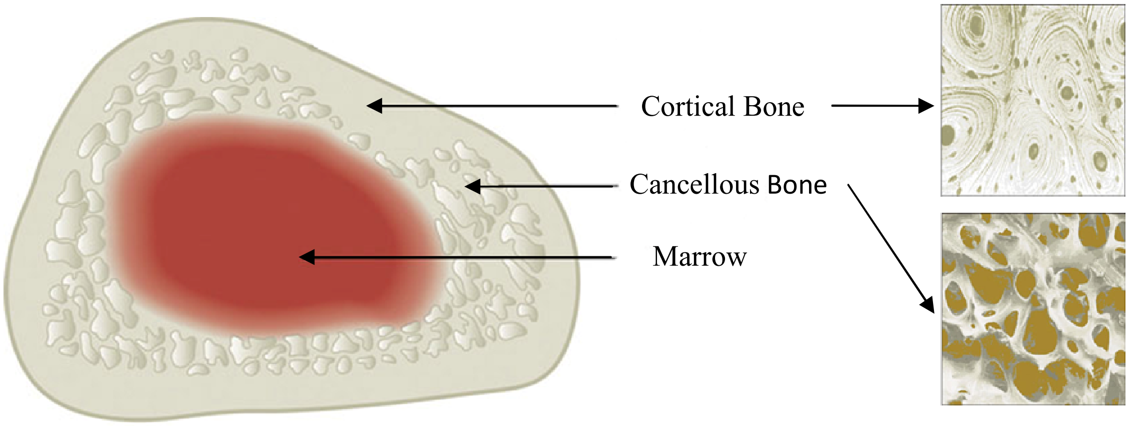

Figure 1: The cross-section of a human bone contains a harder outer layer known as cortical bone, and a spongy inner layer called cancellous bone. The marrow is the inner layer [7].

The normal human hand contains 27 bones, with 14 of them in the phalanges of the fingers [8]. There are 8 carpal bones in the wrist, 5 metacarpal bones in the main body of the hand, and 14 bones in the phalanges of the fingers and thumb (Fig. 2). The fingers have three phalanges (proximal, intermediate and distal phalanges), while the thumb has two (proximal and distal) phalanges. The typical average length of an adult male hand is 189 mm with a breadth of 84 mm, while the average length for the adult female hand is 172 mm with a breadth of 74 mm [9]. Other measurements are available in Table 1.

The joints in the fingers are named for the bones in which they interconnect. The base of each bone has an articular surface where it forms a joint with the adjacent bone. Each joint is stabilized by ligaments to prevent dislocation. There are four joints in each of the fingers (Fig. 2): carpometacarpal (CMC), metacarpophalangeal (MCP), proximal interphalangeal (PIP) and distal interphalangeal (DIP) joints. The thumb has CMC, MCP and the interphalangeal (IP) joints. The CMC joints lie between the carpals and metacarpal bones, the MCP joints lie between the metacarpals and the phalanges, and the IP joints (proximal, intermediate and distal) lie between the phalanges (respectively). The CMC joint in the thumb is considered a saddle joint with 2 degrees-of-freedom (DOF), and the MCP joints in the fingers and thumb are considered condyloid and ‘hinge-like” joints (respectively), each with 2 DOF. The IP joints of the fingers and thumb are hinge joints, each with 1 DOF [**10**]. Thus, the hand has 27 DOF, with 4 DOF in each finger for flexion/extension and adduction/abduction, 5 DOF in the thumb, and an additional 6 DOF for the wrist’s rotation (pronation/supination, flexion/extension, radial and ulnar deviation) [11].

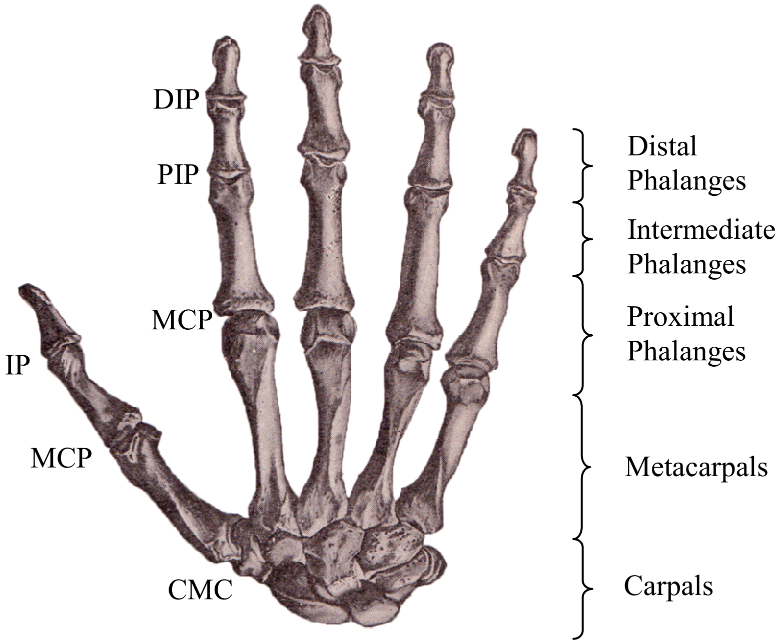

Figure 2: Bones and joints in a healthy hand [12].

TABLE 1: PHALANGE LENGTHS AS A PERCENT OF HAND LENGTH FOR MALES AND FEMALES [8]

Phalanx	Proximal (mm)	Medial (mm)	Distal (mm)
Thumb	17.1	-	12.1
Index	21.8	14.1	8.6
Middle	24.5	15.8	9.8
Ring	22.2	15.3	9.7
Little	17.7	10.8	8.6

2.1.2. Muscles and Tendon

Skeletal muscles are striated in nature, and are comprised of individual muscle cells called muscle fibers, which run the entire length of the muscle. Each muscle fiber contains a contractile sub-unit, called myofibrils (Fig. 3). Enclosed in each myofibril are strands of filaments (actin and myosin), which functionally contract the muscle upon their interaction [13].

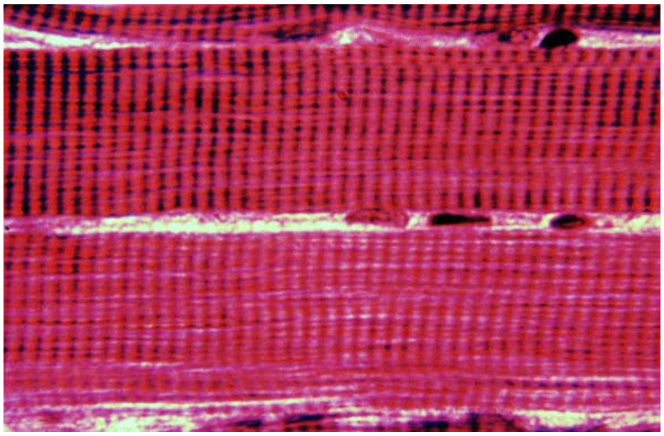

Figure 3: Microscopic view of muscle myofibril tissue, showing the striations characteristic of actin and myosin filaments [14].

The skeletal muscles that produce finger motion are divided into intrinsic and extrinsic groups depending on their origin. The smaller intrinsic muscles originate in the hand, and provide precise coordination for the fingers. The larger extrinsic muscles originate in the forearm and mainly provide strength and articulate the finger joints upon activation.

The distal ends of the extrinsic muscles transition into flexor tendons on the anterior (palm) side of the forearm and extensor tendons on the posterior side of the forearm. These tendons attach to either side of a joint, to allow for finger articulations. Tendon tissue, like ligaments and cartilage, is part of the connective tissue group, which transmits forces and provides structural integrity to the musculoskeletal system. Tendons are primarily composed of parallel bundles of collagen fibers, which are amassed into larger bundles called fascicles (Fig. 4) [15]. The fascicles are encompassed by loose connective tissue, or endotenon. The epitenon is a fibrous outer layer, containing the endotenon. The tendon is enclosed in a synovial sheath, which provides protection and facilitates proper nutrition and gliding to the tendons. The hand tendons have high stiffness characteristics in the longitudinal (lengthwise) direction, and under physiological loads on the tendon, the strain is under 2% [16]. This indicates that there is negligible tendon stretch before displacement when a physiological force is applied. Additionally, hand tendons have low stiffness in the transverse (cross-sectional) direction.

The flexor tendons of the fingers include the flexor digitorum superficialis (FDS) and the flexor digitorum profundus (FDP), which attach to the base of the intermediate and distal phalanx, respectively (Figs. 5-6). The FDP tendons are attached to a common muscle bundle in the forearm, thus the muscle works as a whole to perform a flexion from an individual finger. Unlike the FDP tendons, the FDS tendons usually have separate muscle bundles, allowing for independent tendon motion [17].

The flexor tendons of the thumb are the flexor pollicis brevis and longus which attach at the base of the proximal and distal phalanges, respectively. The extensor tendons of the fingers include the extensor digitorum tendon which attaches to the base of both the intermediate and distal phalanges of the fingers and the extensor indicis which attaches to the extensor digitorum of the index finger. The extensor digitorum tendons are also connected to each other by bands on the middle and ring fingers. The extensor pollicis brevis and longus attach to the thumb at the base of the proximal and distal phalanges, respectively.

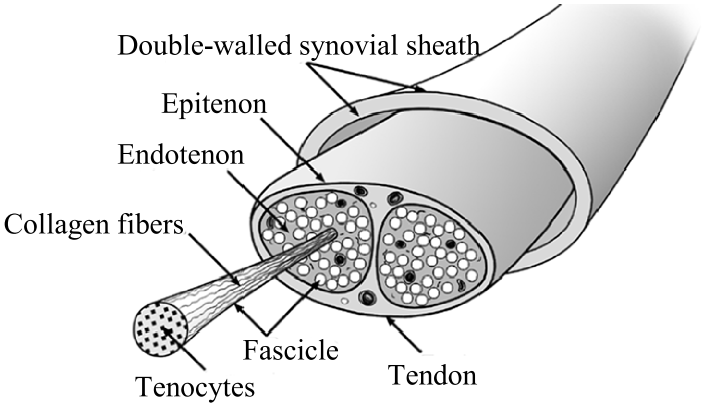

Figure 4: Tendon structure, showing the inner tendon cells (tenocytes), collagen fibers, fascicle, endotenon, epitenon and the outer sheath [15].

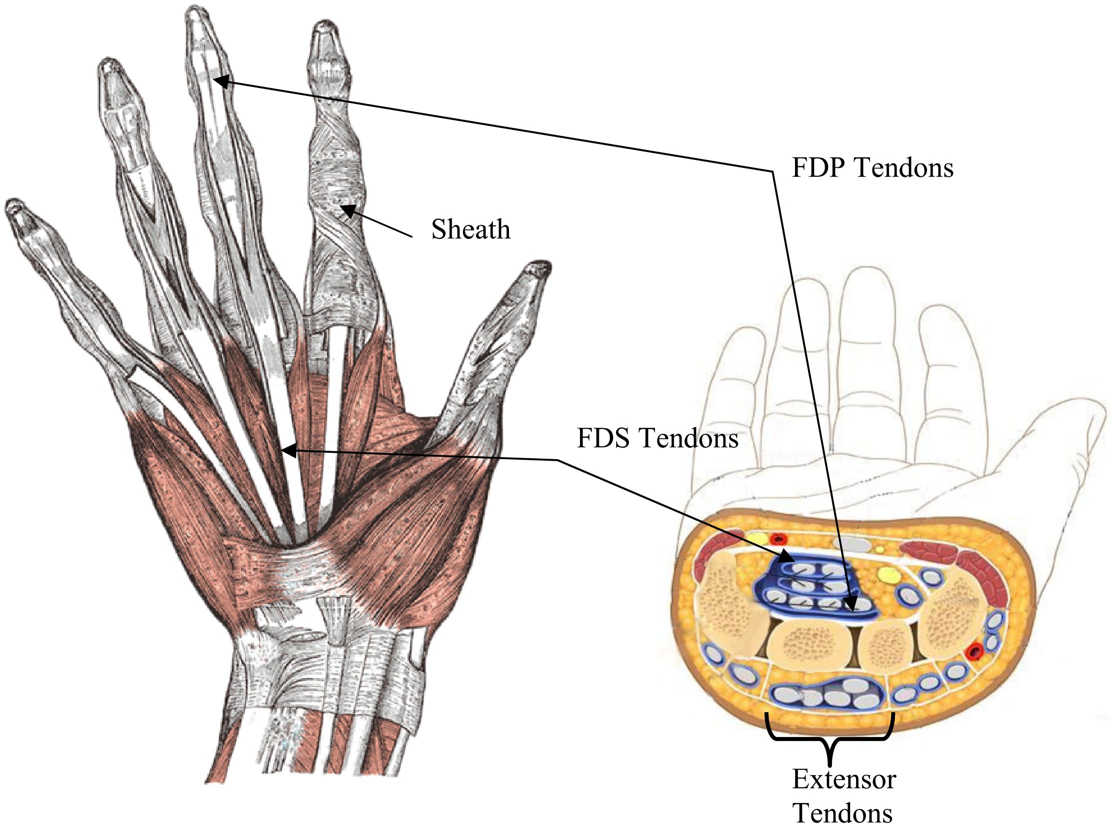

Figure 5: Palmar view of the hand, showing the FDP and FDS flexor tendons, and the sheath surrounding them [18].

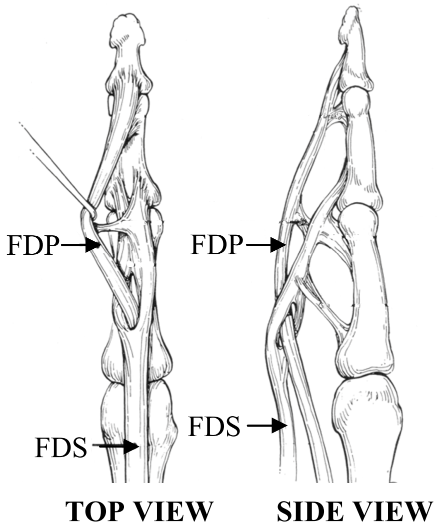

Figure 6: Top view and side view of a finger, showing the FDP and FDS flexor tendons. As shown, the FDS tendon inserts at the proximal phalange and also splits to let the FDP tendon pass through to insert at the distal phalange [19].

2.1.3. Nerves

The nerves of the arm and hand are part of the peripheral nervous system (PNS), which relay information to and from the central nervous system (CNS) in the brain. The nerves themselves constitute a vast communication network, which relay commands such as the desired motion as well as receiving sensory feedback information. In the CNS, the central nerves connect the brain to the spinal cord. The PNS consist of a network of nerves connecting the spinal cord to the limbs as well as the spinal cord to other organs, like the intestines, stomach, blood vessels and heart. Also included in the PNS, are the nerves that connect the eyes, ears, nose and mouth to the brain. Essentially, the CNS constitutes the brain and spinal column, and the PNS encompasses the peripheral nerve branches leaving the brain or spinal column.

As shown in Fig. 7, the structure of a nerve contains an outer layer (epineurium), and inner bundles (fascicles) which encompass the nerve's communication network (neurons) [20]. The inner communication network consists of interconnected neurons, which electrochemically transmit signals. A typical single motor neuron which can be found within this interconnected chain is illustrated in Fig. 8. On one end, there are dendrites, which are hair like structures conducting incoming signals. The dendrites surround a cell body, with an inner nucleus. The axon is the elongated fiber which conducts outgoing signals. The axon is surrounded by a myelin sheath, which is an insulating fatty substance (and along with the nodes of ranvier) allows for the electrochemical signal (action potential) to be accelerated along its fiber. The axon ends with terminals which can then send signals to the next neuron by neurotransmission at the synapse. A sensory neuron differs from a motor neuron by having dendrites on both ends. The PNS nerves which allow communication between the limbs and spinal column are considered mixed nerves. This is because they contain both sensory and motor neurons.

The major nerve branches in the spinal column's vertebrae send and receive nerve impulses to the arm and digits. The nerves of the arm and hand include the radial, median, and ulnar nerves. The radial nerve supplies muscles on the back of the arms and the skin of the forearms and hands. The median nerve passes down the full length of the arm into the hand and provides feedback from sensory receptors in the fingertips, and other palmar areas. The ulnar nerves supply impulses to and from the forearm muscles, hand muscles and the skin on the hand.

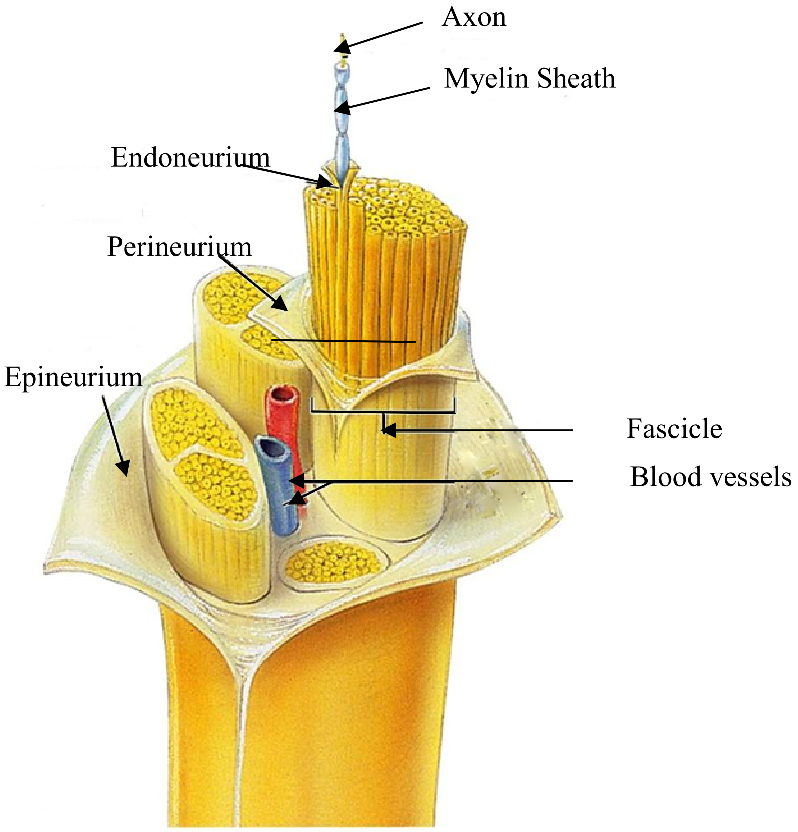

Figure 7: Structure of the neuron, showing the outer layer (epineurium) enclosing inner bundles (perineurium) containing neurons [21].

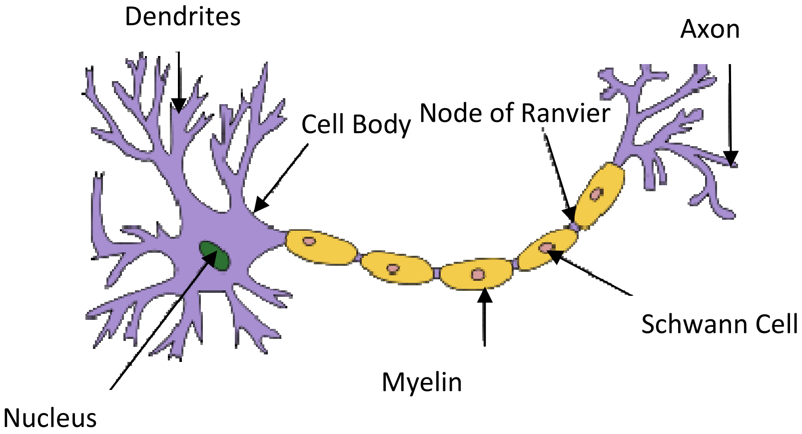

Figure 8: Structure of a motor neuron, showing the dendrites which collect the incoming signal, the axon nerve fiber with sheath and node of ranvier which accelerate the signal (action potential), and the axon terminals which neurotransmit the information to the adjacent neuron [22].

2.2 FUNCTIONAL ANATOMY OF THE NORMAL HAND

2.2.1 Pathway from the CNS, to the PNS and then to the muscle cells

The human hand is a biomechanical prehensile structure, with nearly a quarter of the primary motor cortex in the brain devoted to its control [23]. In order to carry out an intended motion, the motor cortex in the brain receives information from its neighbouring lobes that indicate properties like the body's position in space, strategies pertaining to the intended goal and memories from previous actions. Once the voluntary action is decided upon, the axons in the motor cortex relay the information through interconnected neurons, all the way to the spinal column [24]. From the spinal column, the signal (impulse or action potential) travels through the first motor neuron by means of an action potential traveling along the axon, with help from the nodes of ranvier. The action potential is a voltage potential across the axon membrane that is the result of an electrochemical process (sodium and potassium ion exchange). Given the physiology of cells, and the electrochemical nature causing the action potential, the action potential impulse will propagate from the dendrites to the axon terminal ends [25,26]. At the axon terminal ends, the impulse enters the synapses where it is transferred into neurotransmitters (such as epinephrine and dopamine), and then received by the adjacent neuron's dendrites. This process is repeated through several neurons until the impulse (or action potential) reaches the muscles in the forearm responsible for hand control. At the neuromuscular junctions, bundles of neuron ends meet the muscle cells at neurotransmitter synapses, causing electrochemical exchanges.

This results in the generation of post-synaptic action potentials that propagate through the muscle cell membrane, and eventually into the muscle fibers. Each muscle fiber contains a contractile sub-unit, called myofibrils (Fig. 3). Enclosed in each myofibril are strands of filaments (actin and myosin), which functionally contract the muscle upon their interaction [13]. The resulting contraction from the forearm muscle actuates the tendon, which in turn articulates the attached finger bone.

2.2.2 Tendon excursion and joint articulation

To accomplish a hand grasp, several muscles work together in order to perform the desired grip, mostly to optimize the body from becoming fatigued. There are typically two sets of muscles around a joint: one set as an active primary mover, and the other set passively opposing. A second set of muscles is required to return the limb to its original position, since the reverse action is not possible with soft tissues. Therefore, some muscles called agonists act as primary movers while others, usually on the other side of the joint, act as antagonists counteracting and opposing the motion. Therefore, typically one set of muscles is active while the opposite set is relaxed (passive) [8]. Thus, the active muscle set is contracting and shortening, hence moving the tendon more than the passive muscle.

When the muscle contracts by the previously described processes, the muscle shortens and displaces the tendon at the muscle's distal end. As the tendon displaces towards the contracting muscle, the attached bone articulates. The joints articulations in the hand (MCP, PIP and DIP joint in Fig. 2) form the basis for finger motion while the CMC, MCP and IP joints allow for motion of the thumb. Functional articulations of the hand are described by flexion, extension, abduction, adduction, circumduction and opposition. Flexion is defined as the movement of a joint that results in a decrease of the angle between two bones at the joint, while extension refers to the increase of the angle at the joint. Adduction is a movement of the joints which brings the fingers closer to the sagittal plane (midline of the arm and hand), and abduction is the opposite motion of moving away from the sagittal plane. Circumduction is defined as the movement pattern which moves the limb in a circular pattern using a combination of flexion/extension and abduction/adduction. Opposition motions refer to the combinations of flexion and abduction and axial rotation of the joints. One of the most remarkable motions of the human hand, opposition of the thumb sets humans apart from many animals by opposing (or turning back) against the other four fingers which allows for refined grip.

Even though the CMC joints in the fingers are stabilized by the interosseous ligament to form a relatively immobile joint, its main function is to allow the hand to conform to objects being handled [8]. The CMC joint in the thumb however, permits flexion/extension in the plane of the palm of the hand, abduction/adduction in a plane at right angles to the palm, circumduction, and opposition. The MCP joints in the fingers and thumb allows for flexion/extension, abduction/adduction (when not flexed) and circumduction motions. The interphalangeal joints only permit flexion and extension in the finger and thumb. The intrinsic muscles and tendons involved with flexion, extension, abduction, adduction of the fingers and thumb are summarized in Table 2.

Many researchers have categorized the functional position of the hand when it manipulates objects. These classifications are not universally standardized, but convenient names are often adopted: pinch, key grip, hook grip and power grip. One of the unique characteristics of human hands is their ability to conform around many different objects. Although several other variations of these grips exist, the index pinch, key grip, hook grip and power grips may adequately describe hand prehension patterns. Examples of the pinch grip can be seen when picking up a small object from a flat surface, such as a grape or sugar cube. The key grip involves the thumb pressing against the side of the index finger, as would be done when gripping a key for putting it into a lock. The hook grip involves the flexion of the PIP finger joints, and is often used with holding a briefcase, or rock climbers gripping climbing holds. The power grip involves the flexion of all finger and thumb joints in order to conform around objects, such as holding a ball, or making a fist. It is difficult to quantify how often these configurations are used throughout the day, although some researchers have reported various percentages for the average human [27].

TABLE 2: THE INTRINSIC MUSCLES AND TENDONS INVOLVED WITH FLEXION, EXTENSION, ABDUCTION, ADDUCTION OF THE FINGERS AND THUMB

Motion	Phalanx	Joint	Muscle
flexion	all fingers	MCP	Lumbricals/Flexors
			dorsal interossei
			palmer interossei
	little finger		digiti minimi brevis
	thumb		flexor pollicis brevis
	all fingers	PIP	flexor digitorum superficialis
	all fingers	DIP	flexor digitorum profundus
	thumb	IP	flexor pollicis longus
Extension	all fingers	all joints	extensor digitorum
			extensor carpi ulnaris
	index		extensor indicis
	little finger		extensor digiti minimi
	all fingers	DIP/PIP	lumbricals
			dorsal interossei
			palmer interossei
	thumb	MCP	extensor pollicis brevis
		IP	extensor pollicis longus
Adduction	fingers	MCP	palmer interossei
	thumb		adductor pollicis
Abduction	fingers		abductor digiti minimi
			dorsal interossei
	thumb	CMC/MCP	abductor pollicis longus
			abductor pollicis brevis

There are also studies that involve the amount of FDP or FDS excursion which results from different joint configurations and different tendon loads. One study used cadaver material and reported up to 12mm of active FDS tendon displacement with a tendon load of 5N during the hook grip and various DIP and PIP articulations [28]. Another study with humans reported a mean active FDS displacement of 24 mm with an immobilized wrist, and up to 49 mm with wrist motion [29]. In terms of joint articulation, it was also reported that only a small fraction of the available joint range of motion is used for daily activities, using only 61° at the MCP joint, 60° at the PIP joint, and 39° at the DIP joint [30].

2.3 FUNCTIONAL AND STRUCTURAL ANATOMY FOLLOWING AMPUTATION

2.3.1 Plasticity Following Amputation

Following a hand or digit amputation, the brain will undergo an organizational change, or neuro-plasticity, in response to the change in its environment [31-37]. From these studies, it was shown that the area of the brain associated with motor control underwent a massive functional change following an amputation. One study in particular investigated the cortical reorganization present with monkeys who have a long-standing amputated forelimb [38]. It was shown that when the residual stump was stimulated, the deprived area in the brain that would normally just show activated neurons, also showed additional emerging receptive fields. Another study investigated the timescale in which plasticity occurs after a man’s ring and middle finger were amputated [31]. This study shows that cortical reorganization for the remaining fingers on the affected hand underwent a neural source shift within 10 days. Although these shifts are millimeter-scale in magnitude, it was also discussed that large cortical reorganizational shifts can contribute to phantom pain. Phantom pain was first reported by the French army surgeon Ambroise Pare in the 1600’s, and is associated with sensations of the amputated limb still existing as well as pain at location sites no longer present [39]. It is a widely reported phenomenon, with a prevalence of 67% for phantom pain and 90% for phantom sensations, 6 months after amputation of an upper limb [40-42]**.** It is accepted that the CNS and PNS are determinants of phantom limb pain and sensations [39]. Evidence suggests that there are spinal mechanisms causing a hyper-state when there is a peripheral nerve injury [39]. Further, when the peripheral nerves are cut or injured at amputation site, a regenerative process occurs, causing the injured axon to “sprout” [39]. This in turn leads to a disorganization and causes an increased rate of spontaneous neuron activity. Although peripheral nerve activity in this sense is a negative outcome of an amputation, there can also be benefits in terms of prosthetic devices. For instance, the functioning peripheral nerves, even years following a trauma, can provide a solution to interface a prosthetic device with a human [43-45]. Nerve-controlled prosthetics are further described in Chapter 3. As well, recent findings into the effects of neuro-plasticity have shown to be modulated by the use of hand prostheses. This may be due to the restorative nature of a prosthetic control system which uses sensory inputs to execute motor commands [46]. Also, it is thought that the feedback given by such devices can help regulate peripheral nerve activity [46].

2.3.2 Amputation protocol

Surgical amputations have been archeologically documented throughout history, with an abundance of technology advancement during World War I and 2 [47]. Today's amputation procedures have evolved to include the post-biomechanics and the configuration of the injured limb, in order to have better outcomes for prosthetic functionality and usage [47-50]. This section provides insight into the usual protocol involving amputations of the fingers or the hand (at the wrist level), and then an additional procedure is proposed which will facilitate the use of the proposed ultrasonic tracking system for hand prosthetic applications. As well, the concept of the post-amputation small tendon displacement, referred to as the onset displacement, is further discussed.

Usual Surgical Protocol

With hand or digit loss, there will be a number of reduced anatomical elements; including bones, intrinsic muscles, tendon length, and other connective tissues. If a single finger is amputated at the metacarpal (MCP) or proximal interphalangeal (PIP) level (Fig. 2), part of the flexor muscle-tendon unit responsible for the missing finger's flexion cannot function normally. This is because the distal flexor tendon is no longer attached to the finger bone. Left alone, the tendon will retract into the hand and part of the attached flexor muscle can weaken and atrophy [51-53]. Atrophy refers to the loss of mass and strength of the muscles, which lessens one's ability to functionally contract. Although the flexor muscle is responsible for the entire finger's flexion, it is functionally subdivided (in the case of the FDS muscle-tendon unit) [54-56]. Hence, the flexor muscle will not completely atrophy since there are other functioning fingers. In more severe cases, where there are multiple fingers, partial hand, or total hand loss at the wrist level, the remaining muscle-tendon units will be severely functionally limited. Thus, early surgical management includes the initial preservation of the muscle, bones and tendon length for subsequent reconstructive procedures [50]. Since muscle loss or retention is the best predictor for residual limb (or prosthetic) function, surgical considerations make use of transferring and suturing techniques. Transferring techniques are comprised of a donor unit being attached elsewhere in order to improve function. These can be nerve-based [43-45,50], muscle-based [50,57-59], or tendon-based transfers [60].

The suturing techniques used for muscles and tendons, such as myodesis and myoplasty, can be a factor to improve the residual function following limb amputation [48-50]. Depending on the amputation specifics, the muscle is attached by suturing to remnant bone (myodesis) or to opposing muscle groups (myoplasty) for muscle-stump stabilization [49]. As well, myodesis and myoplasty techniques also retain function by allowing for muscle contractions, which is an ideal interface for prosthetic control [61]. Myodesis and myoplasty are important procedures; without which, the muscles can atrophy (lose strength) with disuse over time, as previously mentioned [51,52]. This will severely limit the residual function of the limb itself or the prosthetic device. Thus, the muscle must have resistance or a connection to an interface, such as remnant bones or other stable tissue. These muscle-stump stabilization techniques, along with a rehabilitative regime, can greatly improve residual muscle strength and function [62,63].

Proposed Surgical Protocol

This thesis describes a technique to track tendon displacement for the purposes of prosthesis control; however, such displacement implies a hand-tendon system that is able to function to various degrees. Given the previous description of the functionally limited tendon-system following an amputation, the proposed tracking system requires that the muscle must still have the ability to contract. This will provide the tendon with the ability to perform the small displacements needed for the proposed technique. As well, the tendon must return to its original position upon relaxation. Thus, the following additional surgical technique is proposed to complement the existing protocol, which may be suitable to facilitate the use of the proposed tracking system. Depending on the level of amputation, instead of suturing the muscle to bone as previously described, it is proposed that one can alternatively suture the remnant tendon to nearby structures like bones or ligaments. Thus, suturing the tendon to nearby structures can provide the needed resistance to the muscle-tendon unit, in order to keep the muscle from atrophic effects, as well as allowing for small tendon displacements. After consulting with a local hand surgeon, this is a reasonable conjecture [64]. As well, the user must undergo rehabilitation to exercise the muscles to retain strength. This is not an additional protocol, and is within the usual standard following an amputation. Thus, the proposed myodesis procedure can allow for muscle contractions, since the tendon will provide tension, which is ideal for interfacing with prosthetics.

One potential drawback to suturing flexor tendons to nearby bones or ligaments is that quadriga effects can be introduced [53,65]. The quadriga effect occurs because the four FDP tendons are attached to a common muscle bundle, and thus do not act independently. Suturing one of the tendons will affect the biomechanics of the FDP muscle, and hence limit/restrict the motion of the other intact FDP tendons. This in turn, will limit the grip strength of the healthy non-injured fingers during flexion [53,65]. Therefore, if the FDP tendons were cut and left to retract, the remaining FDP tendons in the healthy fingers will retain greater function. The proposed technique is to instead suture the remnant FDS tendon from the injured digit to nearby structures, while leaving the FDP tendon cut free. This may be a viable solution to retain a muscle-tendon connection to a remnant digit, especially in the case of severe multi-finger or total hand amputation. This way, atrophic effects can be lessened, and muscle contractions can be preserved to implement small tendon excursions.

The proposed myodesis technique for hand tendons is already used with transfemoral amputations (above the knee) or a foot amputation, where the muscle-tendon unit is sutured directly to bone [66-68]. As well, suturing a tendon by a similar myodesis procedure is most commonly seen with avulsion tendon injuries. Avulsion occurs when the tendon is torn completely free from its insertion (attachment) to the bone, leaving the tendon to retract. Avulsion also occurs when the tendon remains attached to a bone fragment, which has broken free and left to retract until getting caught in adjacent structures. First reported in 1933, it was found that muscle-tendon failure usually occurs at its bony attachment [69]. Most reported cases involve the FDP tendon, with a small number of reports involving the FDS tendon [69]. The usual repair techniques for the avulsed tendon are the “pull-through button technique” or the “anchor technique” [70,71]. The pull-through technique sutures the tendon with a thin cord using accepted methods, and then pulling the cord-tendon unit through the nail bed in order to secure the cord to a button. The other technique uses a metal anchor which is first adhered to the bone with screws, then a cord is attached to the anchor, and then the tendon is sutured to a cord using accepted methods (Fig. 9). Both of these techniques have analogous uses for adhering the remnant tendon to bone, in order to improve muscle strength for interfacing with a prosthetic. After the tendon is sutured directly to the bone, the area eventually heals as the sutures dissolve [64]. This technique has been proven to retain the strength of the tendon-bone bond [64]. Alternatively, one can use an implantable mechanical device, such as a spring between the tendon-anchor system, which may help with resistance and tendon tightness. Unfortunately, such mechanical devices can eventually fail, and implanting such a device is non-trivial [64].

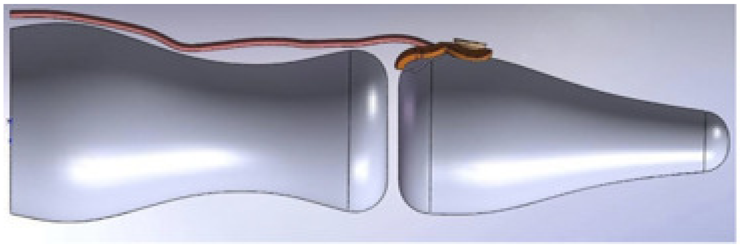

Figure 9: The anchor technique for tendon avulsion surgeries. The torn tendon is sutured and anchored to the bone [71].

Onset of Small Tendon Displacement Following an Amputation

Given that the proposed myodesis procedure will connect the remnant tendon to nearby structures, small tendon displacement is made possible upon muscle contraction. The biomechanics of a tendon which has undergone the proposed myodesis procedure has not been reported. There will undoubtedly be differences in the amount of muscle contraction and tendon displacement available, in comparison to a healthy hand. It is envisioned that the available tendon displacement following the described procedure will be small. This small displacement is referred to as the onset of displacement. The onset of displacement is investigated in Experiment 5 (Chapters 6 and 7), in order determine if the proposed tracking technique can detect this small displacement so it can be used for the intended application of prosthetic control.

CHAPTER 3:

PROSTHETIC CONTROL

3.1 PROSTHETIC DEVICES

Prosthetic mechanisms for the hand are wearable glove or gauntlet-like devices which supplement the appearance or function of a healthy hand. Historically, artificial prosthetic limbs were mainly used for cosmetic purposes, with only a few allowing for functional articulations. During the mid-sixteenth century, several prosthetic hand devices were developed in Germany and France (Fig. 10a-c). Perhaps the most celebrated medieval prosthesis were the iron devices made for the German Imperial Knight, Gotz von Berlichingen, when he lost his right arm from a cannon ball at the battle of Landshuf in 1504 (Fig. 10a) [72]. Similar to Gotz's prosthetic, later sixteenth century mechanisms pioneered by the French army surgeon Ambroise Pare, have manually controlled fingers which use a series of buttons, levers, springs and gears to articulate (Fig. 10c) [73].

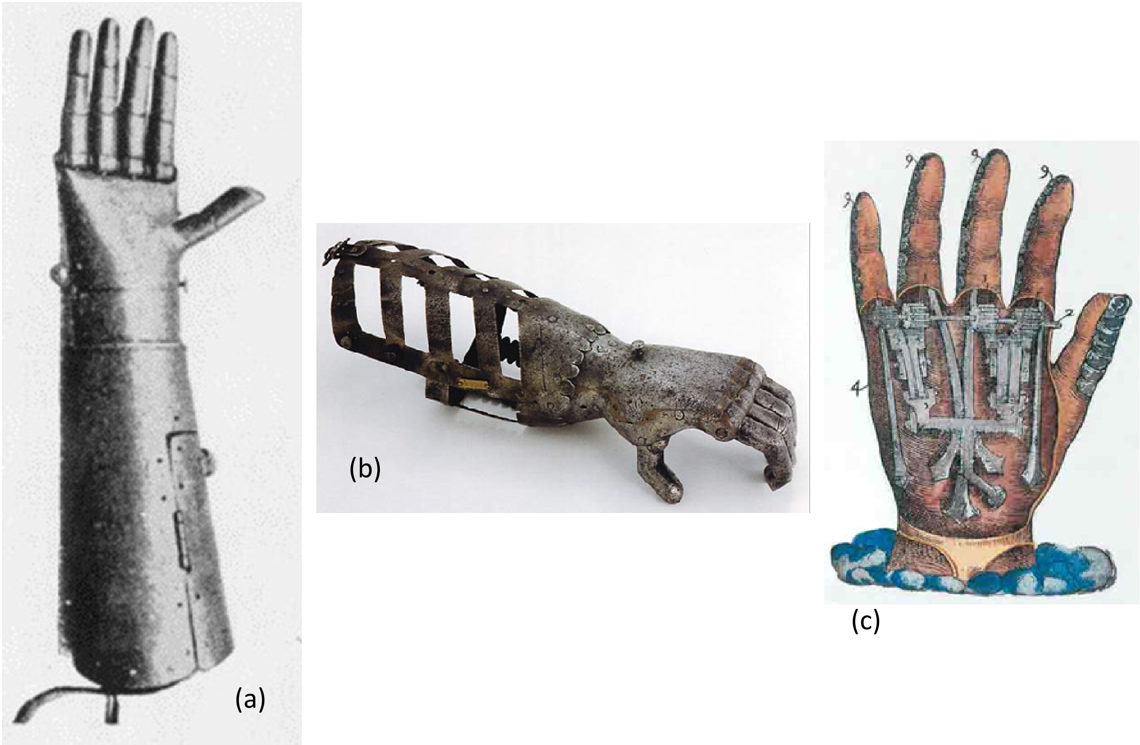

Figure 10: Examples of historical prosthetic limbs: (a) a German prosthetic designed for Gotz von Berlichingen in the mid 1500's [72], a rare 1580 German prosthetic [74], and a French prosthetic hand by Ambroise Pare in 1564 [73].

Users of current prosthesis often compromise between appearance and function of the terminal device. Selection of an appropriate device is usually dependent on the user's physical and cognitive capacity, recreational and vocational needs, psychosocial acceptance, and availability of health resources [75]. The most natural looking prosthetic hands are usually passive devices (Fig. 11). These prostheses are usually painted silicone, and even though they have no mechanical function, they emulate the hand's natural appearance [76].

Figure 11: Example of the passive prosthetic from Touch Bionics, called Living Skin. The hand is made from painted silicone [76].

Another example of a passive terminal device is the hook made famous by the 16th century sea voyager Christopher Newport (Fig. 12). Not only did he inspire the Captain Hook Disney character with his acts of piracy and hook prosthetic, he also is attributed to colonising Jamestown [77]. In contrast to passive devices, active prosthetics are advanced mechanical systems, allowing for functional articulations and improved grip strength. These include split-hook or mechanical hand end-effectors. Split-hook end-effectors are simplistic designs, with generally two hook shaped prongs which pivot to open and close, providing a single degree-of-freedom (DOF). Some designs also include passive wrist rotation, providing additional function [78]. The hook prongs are held together by spring force, and can be designed to remain in either in open position or closed position when not activated. Hook terminal devices are generally more durable, reliable, accessible and cost effective than others [79]. Some examples include those from Hosmer, RSL, and Ottobock (Fig. 13). The basic hand mechanism terminal device operates similarly to the split hooks. They are single DOF mechanisms, allowing for opening/closing actions of the hand. Examples include those from Becker, Hosmer, Otto Bock, and RSL (Fig. 14).

Figure 12: 16th century sea voyager Christopher Newport. He lost his hand during a battle in Cuba, and used a simple hook passive prosthetic [77].

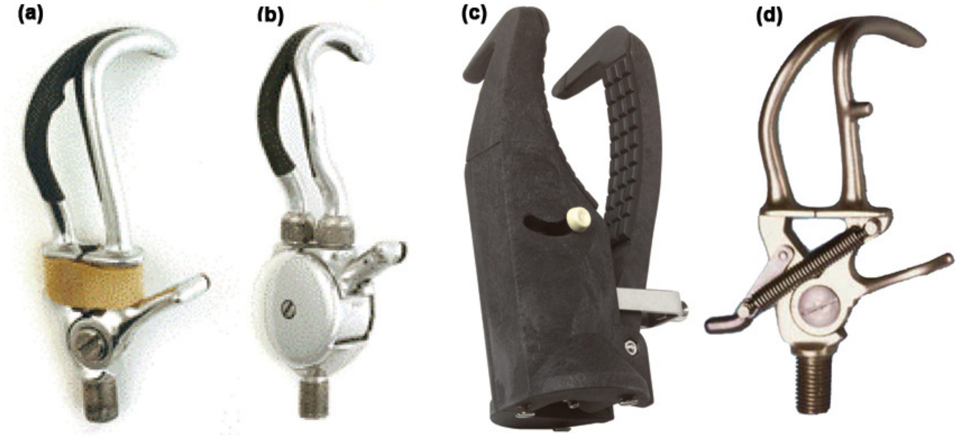

Figure 13: Examples of split hook prosthesis: (a) Hosmer model 5XA hook, (b) Hosmer Sierra 2, (c) RSL Steeper Carbon Gripper, and (d) Otto Bock model 10A60 hook [79].

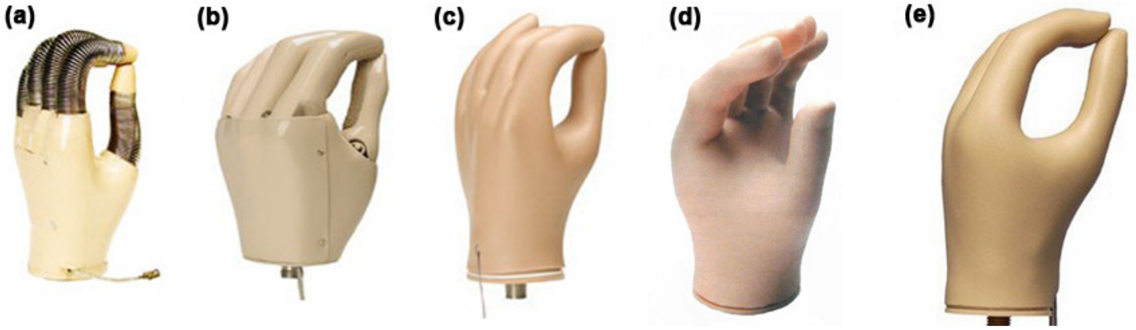

Figure 14: Examples of single DOF hands: (a) Becker Imperial hand, (b) Hosmer Sierra VO hand, (c) Hosmer Soft VO hand, (d) RSL Steeper VO hand and (e) Otto Bock VO hand [79].

The more advanced hand mechanism terminal devices are usually comprised of individual articulating finger joints, an opposable thumb and a rotational wrist, allowing for a multi-DOF device. Examples of commercially available devices include those from Touch Bionics [80] and Otto Bock [81], for example (Fig. 15a,b). Another device that was developed in the Biomedical Design and Systems Laboratory at the University of Victoria involves the design of a 4-DOF hand prosthetic mechanism. This design uses four microgeared DC motors, aluminum fingers and thumb digits, and a polycarbonate 3D printed palm and lower thumb piece (Fig. 15c). The design is based on an earlier prototype, with each finger comprised of six-linkages that has a completely defined path in space using one linear input [82]. The new additions from the earlier prototype include a motor for the index and thumb to flex/extend, a motor for the middle finger to flex/extend, a motor for the ring and little finger to flex/extend and a motor for the thumb to adduct/abduct.

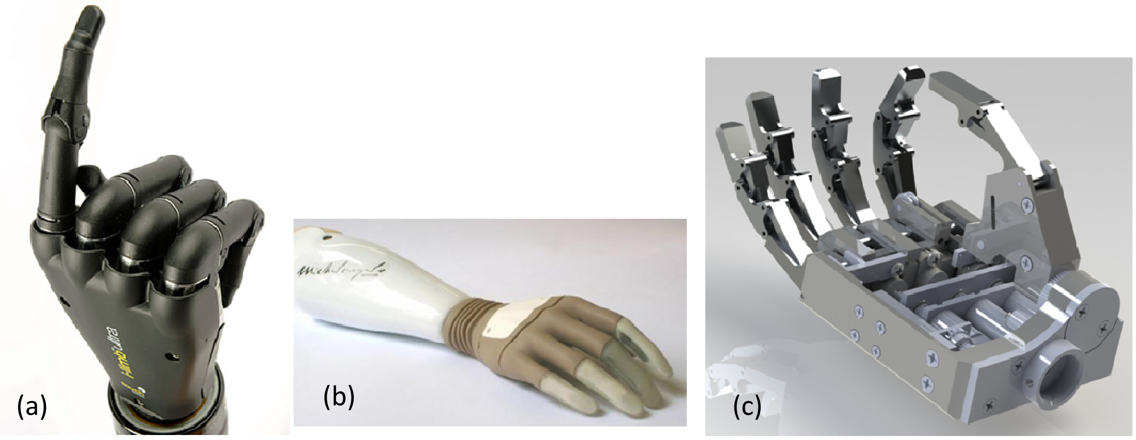

Figure 15: Examples of more advanced multi-DOF prosthetic hands: (a) i-Limb from Touch Bionics [80], (b) the Michelangelo hand by Otto Bock [81], (c) 4-DOF prosthetic hand based on the previous design by Dechev et. al. [82] from the BioMedical Design and Systems Laboratory.

3.2 PROSTHETIC CONTROL

Even though current multi-DOF prosthetic devices are functionally sophisticated, they can still be rejected by their users. In a 1996 study on upper-limb prosthesis use and desired features, the authors revealed that 33% of all children and 25% of all adults surveyed rejected their devices [83]. One of the major attributing factors of rejection is dissatisfaction with prosthetic control; thus demonstrating the need for advanced control regimes [75]. For a prosthetic to have multiple functions, there must be multiple independent bio-signals collected from the user. Given this limitation, there is considerable interest in developing control schemes for active prosthetic devices. Currently implemented control schemes for active devices can be separated into two categories, *human controlled* and *electric controlled*:

3.2.1 Human Controlled

Human control refers to body-powered or switch-activated devices. Body-powered control refers to the user moving parts of their body to change the state of the prosthetic, while switch-control refers to manual switch activation to change the state of the prosthetic. In terms of their demographic, a study in 1996 on upper-limb prosthesis use and desired features revealed that 65% of 1575 surveyed participants use human-controlled prostheses [84]. Split hooks and single DOF hands (Figs. 13-14) are controlled using the body-powered method. First patented in 1857, body-powered devices are controlled by using a harness that transfers the user's motion through a cable system to the single DOF terminal device (Figs. 16-17). The usual motion action required from the user can be shrugging the shoulders, or flexing the back. Body-powered terminal devices can be voluntary closing (VC) or voluntary opening (VO). The main difference between VC and VO control is that with VC, the device remains open until the cable is pulled with an appropriate force, while VO devices remain closed until activated with a force to open. In general, VO control allows the user to easily hold and move objects, but has limited grip strength. In contract, VC control allows for a strong grip force, but required effort to hold and move objects. A major drawback to body-powered devices is not only the single available DOF, but the large activation force required for motion [85]. This limitation is perceived as uncomfortable, and can cause irritation in the shoulder region of its users [86,87].

Historically, switch-activated control is used with the sixteenth century devices, where there are a series of buttons on the prosthetic mechanism which can be activated by the healthy hand (Fig. 10). Current devices use switches enclosed inside the prosthetic or harness system which can be activated by a remnant digit or bony prominence [88].

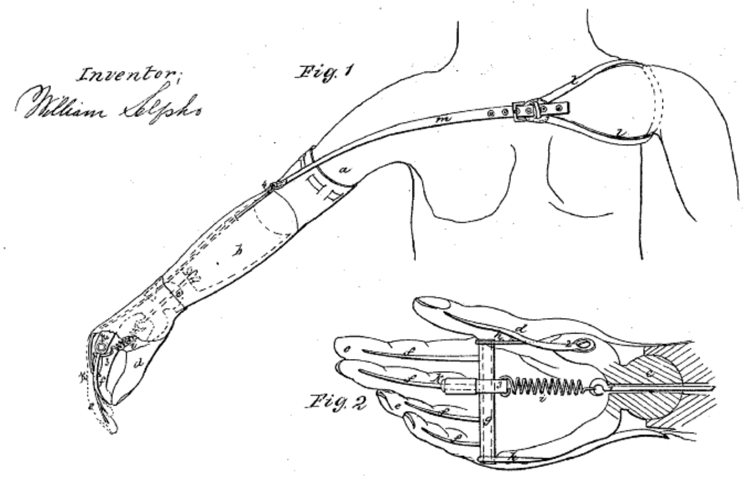

Figure 16: Example a body controlled prosthesis. This is an 1857 patent for the mechanism and control scheme [89].

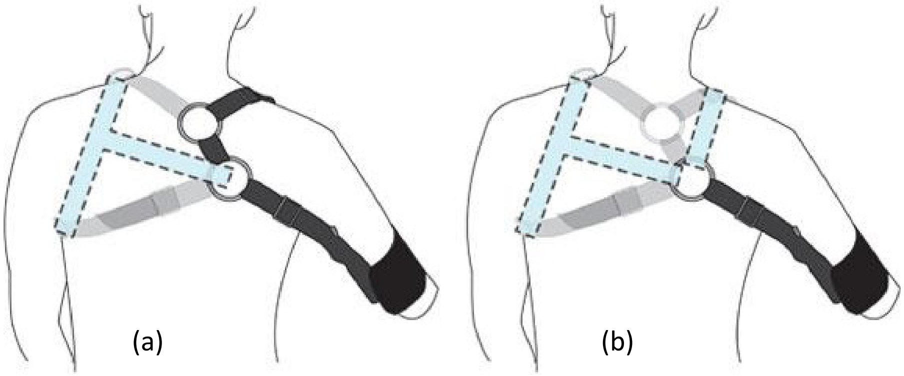

Figure 17: Example of a currently used body powered harness: (a) the strap pulls vertically over the shoulder, or (b) the strap pulls vertically over both shoulders [90].

3.2.2 Electric Control

Electric control refers to devices which contain sensors that can collect and process bio-signals in order to determine the user's intent for motion. By detecting multiple bio-signals, there exist independent channels of information, which can in turn be used to control a multi-DOF device. Even though these devices are more sophisticated than the body-powered hooks, they are heavier, more expensive, and require extensive therapy for its use [88]. In fact, in the previously mentioned 1996 study on upper-limb prosthesis use and desired features, only 28% of the 1575 surveyed participants use electric prosthesis [84]. The type of electric control chosen is based on the level of injury and the patient's cognitive/physical capacity. Current bio-sensing methods which detect user intention include using central nervous system (CNS)-based, peripheral nervous system (PNS)-based, and musculoskeletal (MSK)-based methods, as shown in Fig. 18.

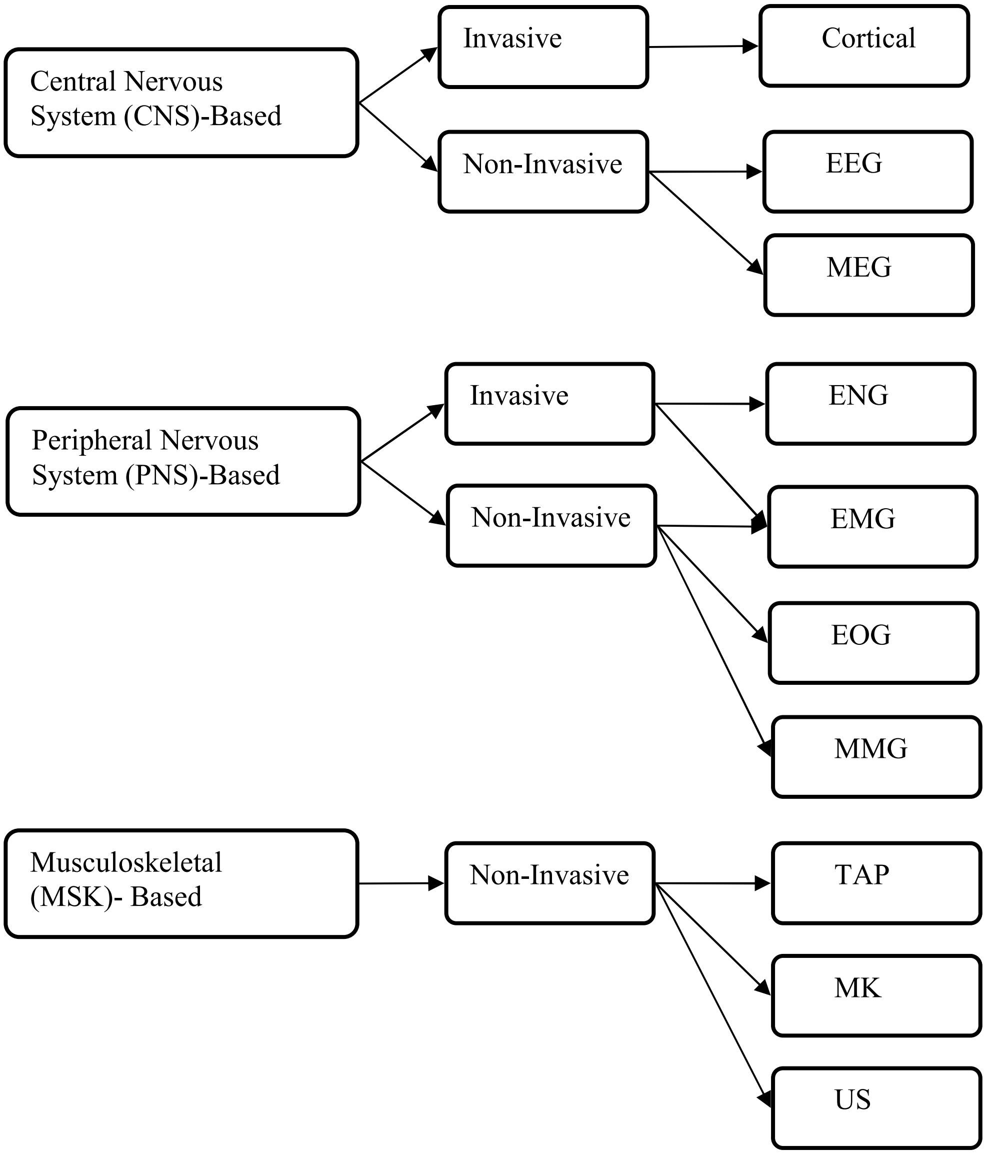

Figure 18: Flow chart illustrating the different types of prosthetic control: Cortical (brain implantables), Electroencephalography (EEG), Magnetoencephalography (MEG), Electroneurography (ENG), Electromyography (EMG), Electrooculography (EOG), Mechanomyography (MMG), Tendon Activated Pneumatic (TAP), Myokinemetric (MK), and Ultrasound (US) tissue tracking.

Cortical Sensing

Cortical sensing is an invasive central nervous interface method in which sensors are implanted into the primary motor cortex of the brain, in order to capture the action potentials of the motor neurons [91]. This can provide a direct brain-machine-interface (BMI) link between the intent of the user and the prosthetic terminal device. Such techniques are invasive procedures, and prosthesis devices using cortical implants are usually considered for severely injured persons [92,93].

These sensors are implantable arrays which are micro-electrical-mechanical-systems (MEMS)-based. Examples include the 96-electrode array from BrainGate [94], or the 100-electrode Utah Array [95]. These arrays can provide a direct BMI link between the intent of the user and the prosthetic terminal device. For instance, studies focusing on the interpretation of information extracted from neurons in the motor cortex have found that they can distinguish the user's intended arm reaching trajectories [96-98]. Thus, the processed neural information can be used to predict intended terminal device trajectories which are usable to the prosthetic hand control system. Studies involving animals [92] and humans [93] have produced promising results using this technique.

Conceivably even more inspiring is the bio-robot being developed at the University of Reading. It is solely controlled by biological brain matter made from a rat's cultured brain neurons [99]. These 50,000 to 100,000 active cultured rat neurons are placed onto a multi electrode array with 60 electrodes which pick up the generated signals from the cells. When the robot mechanism nears an object, these signals are directed by electrodes to stimulate the brain matter. The responded brain output is then used to drive the wheels of the robot mechanism, or to steer left and right to avoid hitting the object. The next step is to determine if the cultured brain can learn and remember.

Electroencephalography (EEG) and Magnetoencephalography (MEG)

Electroencephalography (EEG) is a non-invasive CNS-based technique to measure the electrical activity produced by the brain. The electrical activity measured by EEG sensors are micro-volt potentials generated by the neurons in the cortical levels in the brain [100]. In a typical surface EEG event, electrodes are placed onto the scalp with conductive gel and the consequential signal is digitized and filtered. Although this technique is not as sensitive as implantable cortical sensors, it is a commonly investigated BMI technique for prosthetic control [101, 102].

Magnetoencephalography (MEG) signals are often used in conjunction with EEG signals to complete a more accurate data set for brain-machine interface (BMI)-based control. MEG is a non-invasive imaging technique used by clinicians and researchers to measure the magnetic fields produced by electrical activity in the brain. The main difference in quality between EEG and MEG signals is that magnetic fields are less distorted by the resistive properties of the skull and cap [103]. One study compared simultaneous EEG and MEG recordings of hand motions, and decoded the signals with a 67% success rate [104]. Although these results are promising, the accuracy of the decoded signal is not coherent enough to fully control a prosthetic device. Some examples of prosthesis controlled by EEG/MEG based systems are for patients with severe trauma [101,105]. In addition, MEG or EEG systems are not discreet, are expensive and require long training periods for accurate system calibration and repeatable results.

Electroneurographic (ENG)

The premise behind using the neural PNS network as a control interface for prosthetic use is that neural pathways are still preserved following amputation [106,107]. Even years after amputation, the signals from the CNS are translated to the peripheral nerve connections, thus becoming candidates for prosthesis control. Bi-directional intraneural electrode implantable sensors, known as electroneurographic (ENG) sensors, are used to collect the projected CNS signal from the brain to the stump nerves [108]. The bi-directional interface allows the stimulation of nerve fibers and for recording nerve impulses. This allows for controlling the terminal prosthetic device [109], and allowing for tactile feedback [110]. ENG sensors are categorized as extraneural (cuff-based) or intrafascicular electrodes. Cuff electrodes are extraneural sheaths that contain contacts connected to lead wires which completely encompass the nerve [111,112]. These encircled cuffs cause less injury to the nerve, but there is reduced sensitivity [113-116]. In contrast, intrafascicular electrodes are placed inside a peripheral nerve and can increase the sensitivity and the signal-to-noise (SNR) of the recordings [117-118]. Longitudinally implanted intrafascicular electrodes (LIFEs) have been implanted for investigation into the feasibility of ENG for prosthesis control [119,120]. ENG sensing can have benefits over other sensing methods like electromyography (EMG), in that ENG can provide a clearer signal with high-level amputees [88]. Also ENG has been shown to be a more natural technique when providing feedback [119-121]. However, ENG is invasive in nature, and can be prone to noise from muscle activity, thermal, capacitive couplings sources [88].

Electromyography (EMG)

Electromyography (EMG) is a peripheral nervous system (PNS)-based technique in which the electrical potential of muscles generated by active muscle fibers can be detected. The electric potential of muscle tissue was first documented by Francesco Redi in the late 1600's using an electric ray fish [122], and has evolved to be used in many clinical and biomedical applications [123-126]. The electrical activity, or potential, is a result of efferent neurons transmitting information from the CNS, to the PNS and then to the muscle fibers, constituting the motor unit. A muscle contraction occurs when the nervous system increases the number of motor units activated, by increasing the frequency of action potentials to each motor unit [88]. The action potentials from the active motor units are measurable by non-invasive surface sensors or implantable EMG electrodes. These bio-signals can be used to determine the user's intent for motion, and thus for prosthetic control of a multi-DOF device [88,125,126]. In order to use this control method, the EMG signals must be acquired from suitable muscle sites, the signal needs to be pre-processed, dimensionally reduced and feature extracted. Finally, the pattern for motion intention must be recognized in order to implement the prosthetic [5]. The success and suitability in using the EMG signal for prosthetic hand control will depend on the level of amputation or disability, signal strength and the fatigue level of the muscle [5,127]. Current commercially available hand prosthetics use EMG signals to provide very few practical DOF, mainly from the contraction and relaxation of the upper arm muscles to open and close the prosthetic [5]. Examples of commercially available EMG controlled prosthetic hands include, the iLimb Hand [80], and the OttoBock Michelangelo Hand [81]. Although these hands mainly differ by weight, materials, speed, and touch sensors, they are still limited by low functional DOF which is based upon detecting the EMG signal from the user. Extensive signal processing efforts are currently researched to gain extra information from the EMG signal to improve the DOF using time-frequency domains, wavelet analysis, neural network and fuzzy classification [5]. EMG-based control can be unnatural and not intuitive, and thus difficult to use for control [88,98]. In order to overcome this issue, some studies use nerve reinnervation (transfer) to transplant nerves to new muscle sites [43-45].

Electrooculograpic (EOG)

Electrooculograpic (EOG) is a PNS-based technique in which an electrical signal (potential difference) is produced between the retina and cornea of the eye [128]. EOG technology has been used to control a prosthetic eye to mimic the movements of an existing healthy eye, and in prosthesis control for patients with serious spinal injuries [129,130]. Since devastating spinal injuries leaves few voluntary actions available, EOG signals from eye gaze direction were measured and used as a bio-signal to move a robot arm [130]. This non-verbal control method shows promise in severely injured or disabled people to control prosthetic limbs and equipment in order to participate in daily tasks.

Mechanomyography (MMG)

Mechanomyography (MMG) is a PNS-based technique in which the sound generated by the muscles during contraction is collected in order to determine the user's intent for motion. This signal represents muscle dimensional changes and is widely researched for kinesiology purposes in determining muscle fatigue and muscle responses [131-133]. MMG has issues when being considered for prosthetic control because it is very sensitive to external factors like muscle temperature, outside noise, skin fold thickness and sensor attachment [134-136]. Even with these problems, a MMG-based prosthesis was successfully controlled with 2 DOF, which demonstrates insight to other control methods not currently used in the commercial market [134].

Tendon Activated Pneumatic (TAP)

Tendon Activated Pneumatic (TAP) is a MSK-based pneumatic sensor that is placed in the socket of a prosthetic arm to detect residual tendon motion for multi-digit control [137]. The sliding motion of the residual tendon causes soft tissue displacement between the skin and the socket, and the measured resulting pressure differential was used to demonstrate binary or proportional prosthetic control. TAP sensors were noted to fail if the tissues were too fatty or damaged and are limited to residual tendon function. Over the last decade, few updates were available from using TAP sensors, and have yet to be implemented in a fully functional prosthetic device [138].

Myokinemetric (MK)

Myokinemetric (MK) is a MSK-based technique in which signals are derived from measurements in the dimensional changes in the muscle normal to the skin during contractions. The use of MK signals was first documented in 1999 as a solution to address the limitations of using EMG signals to solely control a wearable robot [139,140]. This signal is measured using a socket-located Hall Effect based transducer. In this study, amputee subjects were able to follow a series of trajectories, hence showing promise in potentially controlling a fully functional prosthetic. Recent contributions have started to compare EMG and MK signals for degree of control [140].

Ultrasound (US)-Imaging

Ultrasonography is a non-invasive imaging technique used in the medical industry in which high frequency sound is transmitted through the body and is then reflected off of MSK tissue boundaries. A typical ultrasound set up includes a computer connected to a transducer probe which emits high frequency (1-20 MHz) sound waves into the body. These sound waves travel until they hit a boundary between tissues, where some of the waves reflect back to the probe, while the rest continue on until another boundary is encountered. The reflected waves that are detected by the probe are relayed to the computer, where the probe boundary distance is calculated in order to display the image or perform other user specified applications. Since ultrasonography can image moving tissue in real time, it also has the potential to be used for controlling an upper limb prosthetic device. This concept is demonstrated in the literature by using an ultrasound system to detect the thickening of a forearm muscle when the wrist extends and flexes in normal subjects, and when the forearm muscle is flexed in amputees [141]. In this case, the forearm muscles motion was taken with a B-Scan ultrasound, and the data was later analyzed. A tracking and matching algorithm had to be employed offline in order to track the muscle changes from each B-Scan image frame. Although this technique was not in real time, it resulted in correlating the muscle tissue deformation as a function of the wrist angle. A simpler approach was later employed, using a hybrid system consisting of a 1-D A-Scan ultrasound sensor and an EMG device [142]. The hybrid system was supposed to be a more economical approach; however a B-Scan ultrasound system had to be initially employed in order to locate the proper forearm muscle before positioning the A-Scan transducer. Also, skeletal muscles work as a group to perform certain motions, and only one muscle was investigated in this study. Thus, it may be difficult to extend this sensing idea to control a multi-functional device. EMG and 1-D ultrasound sensor position are also reported to be difficult to place when the muscles investigated were small. Although several issues were noted, both experiments showed a correlation between muscle deformation and wrist contraction angle, which showed promise in sensing user intention for eventual prosthetic control.

Previous studies by the Biomedical Design and System Laboratory at the University of Victoria investigated whether Doppler Ultrasound was a feasible approach to detect the user's intent for motion [143-146]. This technique employed the Doppler Effect to detect the frequency shift of the reflected soundwave from the residual tendon displacement in the forearm. A frequency spectrogram was then generated, which was a 3-dimensional plot with axes of time, frequency and amplitude on the *x,y,z* axes, respectively. The spectrogram revealed velocity and displacement estimations of the moving tendon. Although promising, it was discovered that the Doppler technique could not adequately capture slow moving tendons. This is mainly due from the fact that the signal from slow moving tendons and the noise floor are both at low frequency with high amplitude. For faster tendons however, a high-pass Wall-filter can be applied, which removes the low frequency noise components. Such filtering cannot be used on slow moving tendons, thus foreseeably limiting this approach for disabled users. As well, there was significant error introduced by the fact that the tendon was displacing longitudinally, and at a nearly perpendicular angle to the incident soundwave. These factors reduce the effectiveness of using Dopper ultrasound for prosthetic control.

CHAPTER 4:

ULTRASOUND IMAGING

4.1 THE PHYSICS OF ULTRASOUND

4.1.1 Sound Principles

Sound is a form of mechanical energy that propagates as a pressure wave through a medium. Often encountered in medical ultrasound, a compression or longitudinal soundwave is produced by a vibrating source. During vibration, the forward movement of the sound source causes a pressure rise in the adjacent medium. Likewise, as the source moves backwards, there is a pressure drop in the medium such that the molecules move apart [147,148]. This constant push-pull action of the sound source results in alternating molecular compression and rarefaction in the propagating medium, with the molecules vibrating in parallel to the soundwave's propagation. A soundwave is described by various properties, such as its frequency, period, wavelength, propagation speed, amplitude and intensity [148]. An in-depth discussion regarding the physics of ultrasound can be found in an elementary text [147-149]; therefore, this section provides a brief introduction to relevant material used in this thesis. The frequency, f, is a measure of how many complete cyclic variations in pressure occur in one second of time. This property is measured in units of Hertz (Hz), and for medical diagnostic ultrasound imaging, the transmitted frequency is usually between 1 - 40 MHz. The period, P, is the time (usually in units of μs) is takes for one cycle to occur, and is calculated as the inverse of frequency. The wavelength, λ, (usually in units of mm) is the length of space in which one cycle occurs. The propagation speed, c, is the speed with which a wave moves through a given medium and depends on the density and stiffness of the medium. It is mathematically calculated as the soundwave's wavelength multiplied by its frequency. Amplitude is defined as the maximum amount of variation in pressure, and is usually measured in mega-Pascals (MPa). The average intensity in a sound beam is the total power in the beam divided by the cross sectional area of the beam, measured in units of mW/cm^2.

Diagnostic medical ultrasound uses pulsed soundwaves, where a single pulse contains a few cycles of oscillation (Fig. 19). Pulsing ultrasound allows for distinct echoes to be produced at the medium's interfaces, thus allowing for adequate depth (axial) resolution. The number of pulses occurring in one second is the pulse repetition frequency *PRF*, and each pulse is separated into time by the pulse-repetition period, *PRP*. Each pulse of ultrasound does not contain a single frequency, but includes a range centered on its nominal frequency, f_o. This is illustrated in Fig. 20, where the spectrum of the pulse in Fig. 19 indicates a range of frequencies. The width of the spectrum is referred to as its bandwidth, and is commonly measured in terms of the frequency locations, f_1 and f_2, at which the amplitude has dropped 3dB from the center value, f_o [148]. Every transducer is designed to have a specific bandwidth, but the ultrasound system electronics can transmit at specific frequencies within this bandwidth [149,150]. This is often referred to as 'broad-bandwidth', or 'multi-frequency' transducers, whereby the frequency is selected in the transmit mode [149].

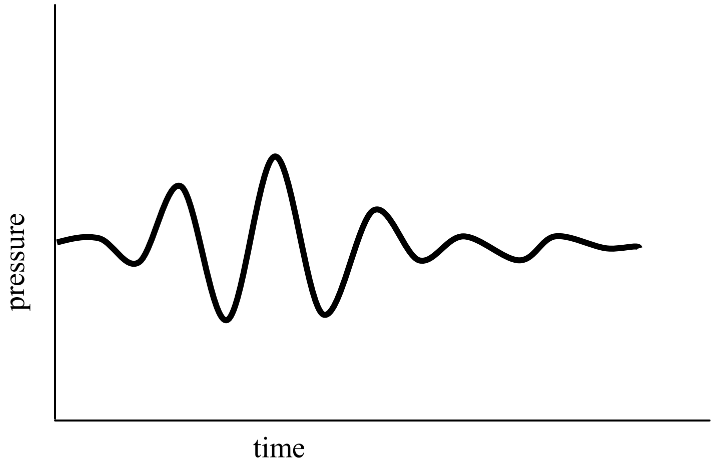

Figure 19: A typical single ultrasound pulse containing a few cycles of oscillations. Adapted from [148].

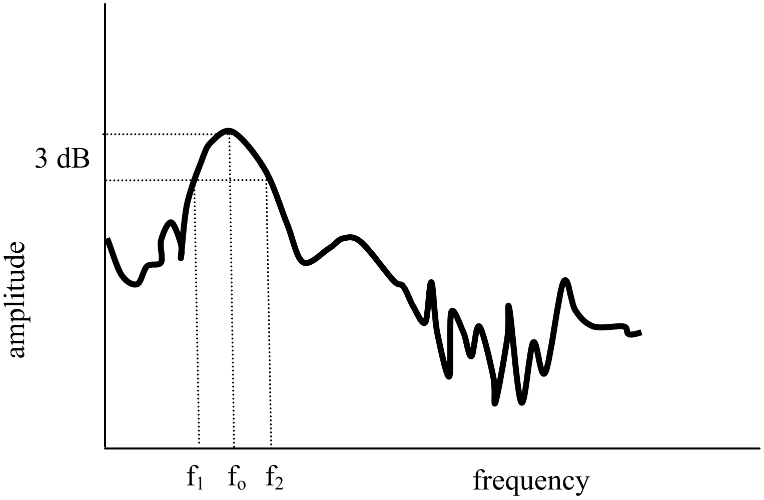

Figure 20: A spectrum of the pulse from Fig. 19, indicating the frequencies which are present. The center frequency, f_o, is shown, along with the bandwidth f_1 to f_2, where the amplitude has dropped 3 dB. Adapted from [148].

4.1.2 Sound Interaction With the Medium

As an ultrasound wave propagates through a medium, the wave's energy is gradually lost with distance of travel. This effect is known as attenuation, where the wave's intensity decreases exponentially with depth [147,148]. Furthermore, attenuation is linearly dependant on frequency and type of medium. Absorption is the main type of attenuation in which the ultrasound's energy is gradually converted into heat within the medium.

The acoustic impedance, z, is a material property which is calculated by the density and propagation speed within a given medium. When an ultrasound wave encounters interfaces of different acoustic impedances, part of its energy is reflected back to the transducer as an echo, while the remainder is transmitted through the medium. If the interface was large (in comparison to the wavelength of the wave), and was also flat and smooth, the angle of reflection is equal to the angle of incidence (Fig. 21). Further, as the wave enters the medium at an oblique incidence, the transmission angle can refract. This description of events is for specular reflections, where the interface is large (such as organ boundaries), and the boundary is flat and smooth [147,148]. If however, the reflector is small in size (comparable in size to the wavelength of the wave), or if the interface was not smooth, the soundwave will scatter. The amount of ultrasound energy scattered by a small reflector is dependent on the target reflector size, d_r, and the wavelength, λ, (and hence frequency, f) of the wave. When $d_r << \lambda$, the scattered power is proportional to f^4, which is commonly referred to as Rayleigh scattering [148]. This describes an ideal situation however, where the density in the medium is uniform.

When an ultrasound pulse encounters many scatters along its direction of travel, several echoes are simultaneously generated, and may arrive at the transducer by constructively or destructively interfering [147,151]. The resulting interference pattern produces a displayed image with a granular structure, which is often described as speckle texture [151]. The speckle texture does not directly represent the scatters, but rather the interference pattern of the scattering distribution. Speckle itself can be thought of as a form of acoustic noise in an image [152], but it also allows for tracking moving tissue, since the motion of tissue can be estimated by quantifying the motion of speckles. Tracking the motion of tissue by speckle tracking is described in Chapter 5.

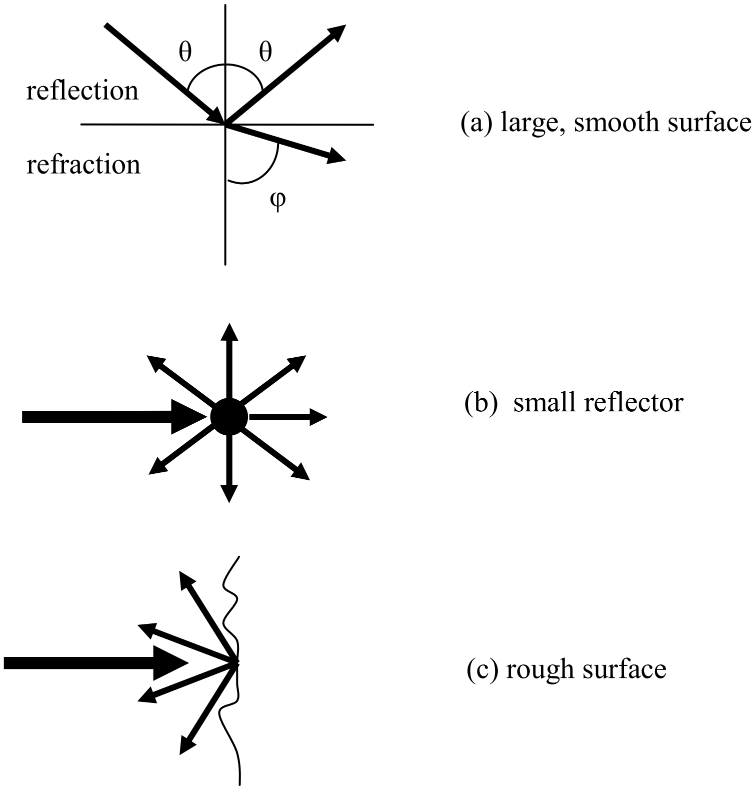

(a) large, smooth surface

(b) small reflector

(c) rough surface

Figure 21: Examples of (a) specular reflection and refraction, (b) scatter from a small reflector, and (c) scatter from a rough surface. Adapted from [148].

4.2 ULTRASOUND HARDWARE

Ultrasound hardware, used in medical environments, can vary based on the required application. Usual medical ultrasound hardware which displays a 2D B-Scan sequence of images includes the transducer, beamformer, signal processor, image processor and display, as shown in Fig. 22.

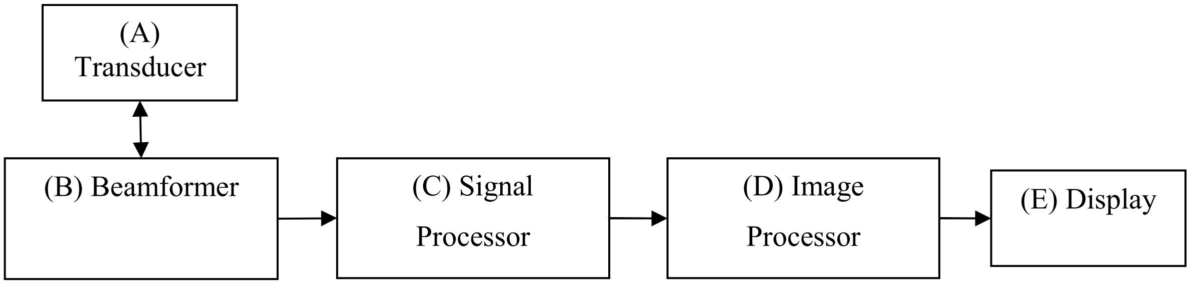

Figure 22: A block diagram of a pulse echo imaging system with (A) the transducer, (B) the beamformer, (C) the signal processor, (D) the image processor and (E) the display. Adapted from [147].

4.2.1. The Transducer

The ultrasound transducer is the device which converts the electrical transmission pulses into ultrasonic pulses that propagates through the medium. Conversely, the ultrasonic echo pulses which are reflected from the medium arrive back at the transducer and are converted into electrical echo pulses. A typical transducer is comprised of a piezoelectric (PZT) plate, backing layer, matching layer and sensor electrodes all encompassed by a plastic housing [147-149]. The PZT material expands and contracts when a positive or negative voltage is applied to it, respectively. Conversely, PZT materials can generate positive or negative voltages when an external force stretches or compresses them, respectively. This process exists due from the characteristic and well-defined molecular arrangement of dipoles within PZT materials, which contain positive and negative charges [149]. The reflected echo from the medium is a mechanical pressure wave, which is received at the PZT material. The pressure wave incident on the PZT causes an imbalance of the charge distribution of dipoles within the PZT. This produces a net positive charge on one side of the PZT, and a net negative charge on the side, creating a potential difference. The surface electrodes then measure the magnitude of this voltage, which is proportional to the amplitude of the echo [149]. As well, when the voltage is applied to the PZT through the surface electrodes for transmission, its surface mechanically expands and contracts at the desired frequency. Thus, the PZT can generate a soundwave to propagate through the medium, and can also receive the reflected echo soundwave from the medium. The PZT material has a high density and acoustic impedance, thus an emitted soundwave would be reflected at the skin boundary, and not enter the body [147]. To correct this, a matching layer is commonly used on the transducer face, which has an intermittent impedance value between that of the skin's surface and the PZT, thereby improving sound transmission. The backing layer is a damping material attached to the rear transducer face. The damping material reduces the number of cycles in each pulse, which has the effect of widening the bandwidth thus introducing additional frequencies. An example of a damped pulse and resulting bandwidth was illustrated in Figs. 19-20. Emitting short pulses and responding to the returning echoes over a wide bandwidth of frequencies is desirable in many medical ultrasound applications, and therefore many transducers are heavily damped [153]. Also, by reducing the number of cycles in each pulse, the axial resolution is increased. The resolution (axial and lateral) is further discussed in Section 4.3.2.

A transducer can be a single element or multi-element array. A typical linear array transducer can be comprised of 128 piezoelectric (PZT) elements, with each element having dimensions approximately 280 μm in width, and spaced 300 μm (center-to-center) to adjacent elements (known as the pitch). This transducer can image a 2D plane in the body. Alternatively, there are 3D, 4D (i.e. 3D *and* time), and 2D matrix transducers. A 3D transducer is essentially the same design as a 2D array except there are additional components which mechanically oscillate the array in order to sweep into the third dimension. This creates a 3D volume image. However, the sweep rate is slow and processing this amount of data requires additional time, thus the refresh rate (frame rate) of the resulting 4D volume data sets can usually only contain a few volumes per second. Therefore, 4D imaging is not practical for imaging fast moving objects unless the resolution or field of view is reduced. Alternatively, 2D matrix arrays contain several thousand elements arranged into a 2D matrix grid. By electrically steering the beam, the matrix array can create a 2D image in a single plane, and can then steer in elevation to create a volume.

4.2.2. The Beamformer

The beamformer is responsible for driving the PZT, generating electronic delays for individual transducer elements and achieving transmit/receive focusing. The beamformer consists of a pulser, pulse delays, transmit/receive switch, amplifiers, analogue to digital converters, echo delays and a summer (Fig. 23).

Pulser and Pulse Delays

The pulser (Fig. 23A) produces the electrical voltages which forms the ultrasonic beam. The frequency of the voltage pulse determines the center frequency of the resultant ultrasonic pulse that travels through the medium [147]. This frequency usually ranges from 1-40 MHz and the pulse repetition frequency (PRF) usually ranges from 4 to 30 kHz for medical purposes [147]. Phase delays (Fig. 23B) are necessary for the complicated sequencing and phasing operations which are involved to control beam steering, scanning and transmission focusing.

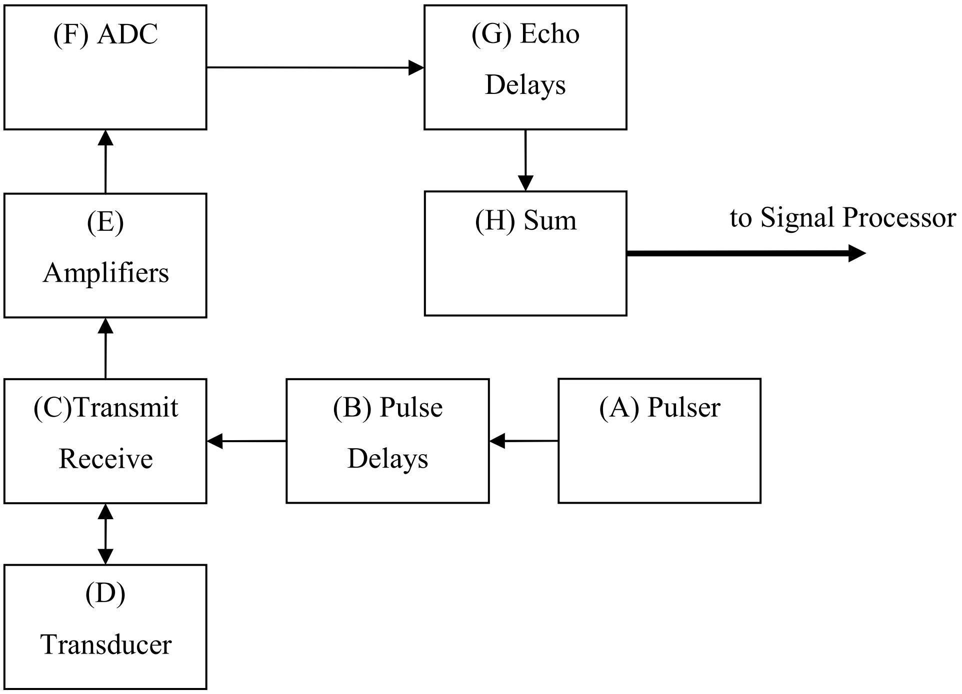

Figure 23: Beamformer schematic with (A) the pulser, (B) pulse delays, (C) transmit and receive switch, (D) the transducer, (E) amplifiers, (F) analog-to-digital converter, (G) echo delays, and (H) the summer. Adapted from [147].

Transmit/Receive (T/R) Switch and Amplifiers

The T/R switch (Fig. 23C) directs the pulser's voltage to the transducer (Fig.23D) during transmission. It also directs the returning voltage from the transducer to the amplifier (Fig. 23E) during reception. The amplifiers then increase the small voltage amplitude received from the transducer.

ADC, Echo Delays and the Summer

After amplification, the echo voltages pass through an analogue-to-digital converter (ADC) (Fig. 23F). The resulting echoes from all active signal element channels are delayed (Fig. 23G) to achieve proper receive focusing and steering [149]. They are then added together in the summer (Fig. 23H) to produce the final echo that represents the information gathered during a pulse repetition period along a single beam direction (scan line) [149]. This information is then relayed to the signal processor.

4.2.3. *The Signal Processor*

The signal processor receives the digital signals from the beamformer which represents the echo information as a function of depth along a single scan line. The signal is further processed by time gain compensation (TGC), rectification and demodulation, rejection filtering, and dynamic range compression, as illustrated in Fig. 24.

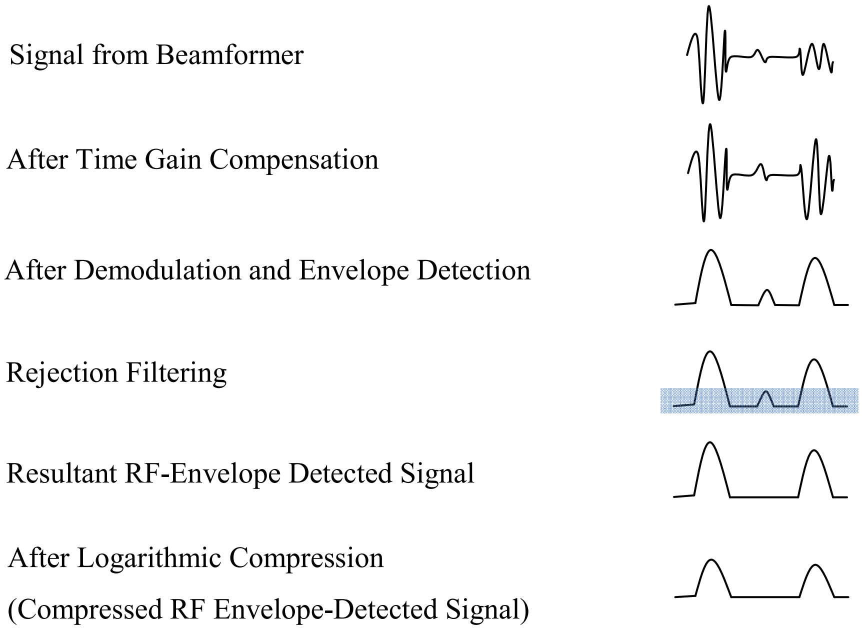

Figure 24: The signal processing steps which illustrates the effect on the signal from a single scan line as it undergoes time gain compensation, demodulation and envelope detection, rejection filtering and logarithmic compression. Adapted from [149].

Time Gain Compensation (TGC)

TGC is a user controlled feature on many ultrasound machines in which the beamformed echo can be amplified as a function of time along the scan line (i.e. depth), in order to compensate for beam attenuation. The ideal TGC curve will allow all equally reflective boundaries equal in amplitude, regardless of depth [149]. As illustrated in Fig. 24, the deeper echo has been amplified by TGC.

Rectification, Demodulation, Envelope-Detection and Rejection

The echoes are difficult to use in the current form for image processing, thus the signals are rectified and demodulated. The signal is first rectified by inverting half of the waveform and then smoothed by passing it through a low pass filter, as illustrated in Fig. 24. This removes the high frequency oscillations and retains the slowly varying envelope. This is a useful technique in ultrasound signal processing because only the amplitude of each echo is needed for the grayscale display. The signal is further passed through a rejection filter in order to reduce electronic noise. The resulting signal is referred to as the RF-envelope-detected signal.

Logarithmic Compression

The dynamic range defines the minimum and maximum signal level of an imaging system, and is limited by the effective range of the display [149]. Logarithmic compression increases the smallest echo amplitudes and decreases the largest amplitudes in order to properly render a 2D B-scan ultrasonic image. This is illustrated in Fig. 24, where the final signal has been logarithmically compressed.

4.2.4. The Image Processor and Display

The signal is now digitized, filtered, demodulated and compressed. The echo data requires further processing in order to be displayed on the screen as a 2D B-Scan image. These processing steps include a scan converter, preprocessor, image memory, postprocessor and digital-to-analogue-converter (DAC) [147]. The scan converter reformats the echo signal into an image form for further processing, storage and display. The image is preprocessed using edge enhancement, pixel interpolation and then stored in memory. Other post processing techniques determine how the echo data is displayed on screen. The data is then converted into a voltage using a DAC, and is then relayed to a monitor where the echo brightness is displayed, usually as a grayscale grid of pixels with intensity values between 0 and 255. The display can include a graphical user interface (GUI) where the 2D B-Scan sequence is shown alongside various user-defined controls.

4.3 IMAGE GENERATION

In order to render a suitable 2D B-Scan image by the previously described processes in Section 4.2, the transmitted and received ultrasonic beam must be properly focused using an aperture. This has a direct effect on the resulting image quality by means of axial and lateral resolution.

4.3.1 Beams, Aperture and Focusing

In medical ultrasound systems which use the pulse-echo technique for imaging, the transmit beam is a pulsed soundwave, as previously described in Section 4.1. An active group of adjacent elements on a linear array transducer, form an aperture which transmits this beam along a single scan line (Fig. 25). The aperture has a width equal to that of the active elements. Focusing the transmitted beam is usually controlled by the operator, who selects the required depth of focus thereby ensuring the beam is narrowed at this point. A focal zone close to the transducer face is produced by firing the outer active group elements before the inner ones in a symmetrical pattern in order to create the proper timing delays for the beam to converge at the desired focal depth [149]. Greater focal depths can be accomplished by reducing the delay time differences among the active elements which results in a more distal beam convergence. Therefore, the focal depth has many limiting factors, namely: the aperture size, operating frequency and the presence of acoustic lenses on the array.

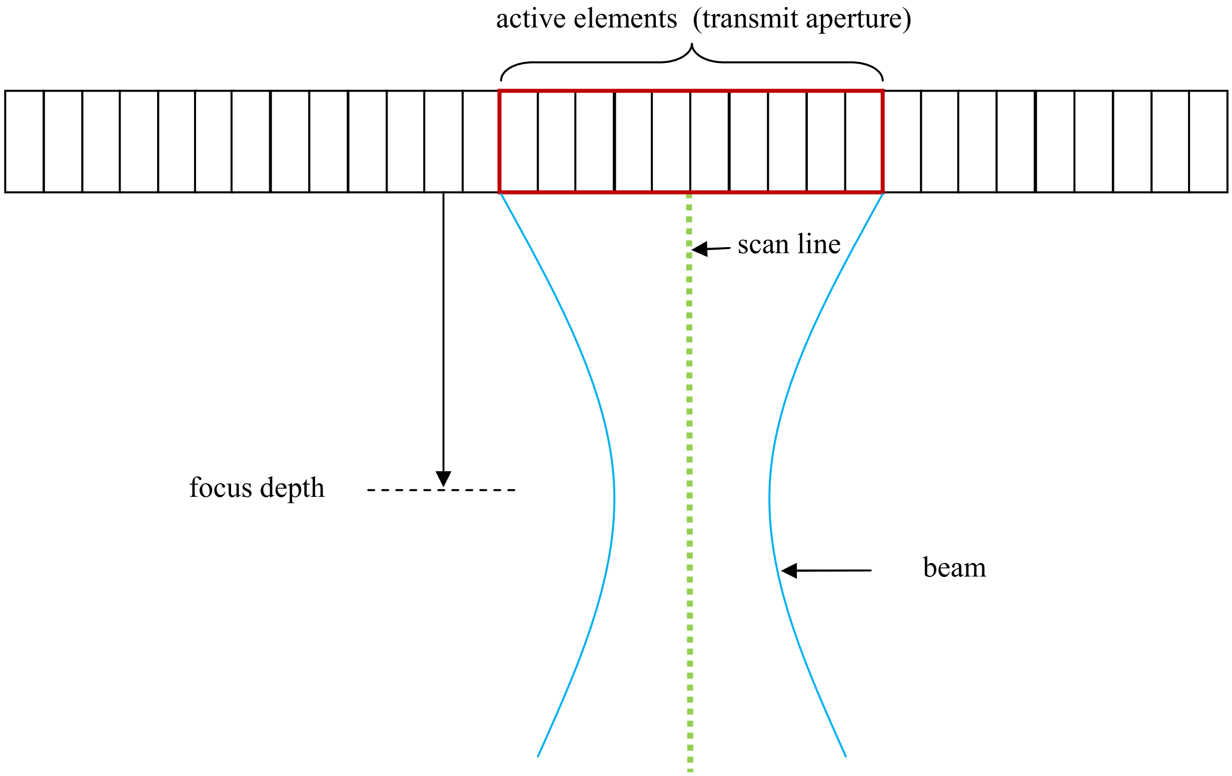

Figure 25: A linear array contains many elements, with a sub-set being active (outlined in red) forming a transmit aperture. This aperture forms a beam (in blue), with a focus depth, and with a scan line centered on the aperture.

As soon as the pulse has been transmitted, a subset of the group of previously active elements from the transmission listens for the echo of the reflected soundwave from the medium in reception [148]. This acts as a receiving aperture centered on the same scan line which defines the receive beam. The number of active receive elements (aperture) is initially less than the transmitted aperture in order to be sensitive for echoes originating at closer depths. The aperture is then varied in width until all echoes are received from different depths, thus continually advancing the focus [148]. This is known as dynamic focusing and aperture in reception.

As discussed in Section 4.2.2, the beamformer provides an electronic delay and summer in order to account for the firing delay and resulting receiving delay from the active elements. The information from this scan line is then processed by the remaining steps in Fig. 23, and the signal processing described in Section 4.2.3. This entire process is then repeated on the next set of active elements for the next scan line, by shifting the transmission group by a single increment, until the last set of active elements has fired and received the echoes. The resulting data set is sent to the image processor described in Section 4.2.4, in order to display the 2D B-Scan image from all the scan lines.

4.3.2 Axial, Lateral and Temporal Resolution

Axial resolution refers to the minimum separation of two reflectors in a medium in a direction along the direction of the beam (i.e. depth), allowing for two resolvable structures along the scan line [147-149,154]. As illustrated in Fig. 19, the transmitted soundwave is damped and pulsed, and has a defined pulse length. The pulse length of the transmitted soundwave determines the axial resolution, with a minimum separation distance between two reflectors being one-half the pulse length [149]. The pulse length is the number of cycles of oscillations in the pulse multiplied by the wavelength [149]. Thus, highly damped transducers can provide a shorter pulse length which improves axial resolution. This requires a powerful impulse however, which can be harmful for medical-based applications [154]. As well, a higher frequency (lower wavelength) transmission pulse can increase the axial resolution. However, a higher frequency transmitted pulse limits the imaging depth. Therefore, there is a trade-off with imaging parameters and axial resolution.

Lateral resolution is defined as the minimum separation of two reflectors in the medium which are aligned in a direction perpendicular to the ultrasonic beam, allowing for two resolvable structures [147-149,154]. The width of the ultrasound beam (ie. the aperture) is the main determinant of the lateral resolution [154]. Since the aperture can be electronically varied for transmit and receive focusing, the lateral resolution can be maintained with depth. This is because the beam width is inversely proportional to the aperture, so that the successive focal zones with the variable aperture allow the beam width to remain fairly constant, thus preserving lateral resolution at all depths. This is unlike a single element transducer, which has a fixed aperture for transmitting and receiving. Further, increasing the scan line density can improve lateral resolution because it allows for increased sampling. A typical 128 element linear array can have 100 or so scan lines, since the end elements are required to form an aperture [148]. Increasing the number of elements in the array will improve the lateral resolution by increasing the number of scan lines; however, this is often very expensive and computationally costly. An alternative approach involves beam steering by small angles or by using an even number of elements in the first sweep, and then an odd number in the next sweep [148].

Temporal resolution refers to the ability for the 2D B-Scan image frames to be refreshed, which is indicative of the system's frame rate. The time it takes to render a single image and then to render subsequent images to create a cine loop movie is described by the frame rate. In order to resolve moving structures, the frame rate must be high enough to avoid aliasing. Further, the previously described processing steps described for improving lateral resolution, will decrease the frame rate.

4.3.3 Image Ambiguity

As with many imaging systems, artefacts can occur causing image ambiguity. Typical artefacts found in ultrasound image frames are reverberations, acoustic shadowing or enhancement, and displaced structures [149]. Reverberation artefacts arise from multiple echoes which are generated between two interfaces in the media that reflect the soundwave in reception [149]. This is often seen with highly reflective metallic objects or air/partial liquid interfaces in the body. The resultant artefacts are interpreted as ghost images, which manifest itself as multiple, equally spaces boundaries with decreasing amplitude along the axial dimension. Acoustic shadowing occurs when a highly attenuating or reflective structure is casting a distal shadow, or decrease in intensity. Likewise, enhancement occurs distal to structures having a lower attenuation, allowing the appearance to the distal structure to have a high intensity [149]. Structures can also incorrectly appear at a particular location on the image. This is mainly due from the refraction of the soundwave as well as the fact that the velocity in medical ultrasound applications is assumed to be constant. Some interfaces, such as collagen and fat, have considerably different velocities, thus allowing for a significant error in the displayed location [154].

CHAPTER 5:

PROPOSED TECHNIQUE AND METHODOLOGY

5.1 USING TENDON DISPLACEMENT TO PROVIDE INPUT FOR PROSTHETIC CONTROL

As described in Chapter 3, the sophistication of current prosthetic devices is limited by the inability to fully control them [75]. The state-of-the-art in current prosthesis control systems use electromyography (EMG) based sensors, which detect the independent bio-signals (i.e. muscle contraction) from the user [88,125,126]. EMG sensors can sense independent signals from placement sites along the biceps and chest, which can augment functionality to a wider range of upper limb amputees. However, EMG sensing has many drawbacks that limit its use. This includes signal cross-talk and the fact that the chosen muscle sites for control input can be non-intuitive to the user, among other issues [5,88,98,127]. Other sensing methods, such as cortical, EEG/MEG and ENG (described in Chapter 3) can be invasive in nature, and are usually reserved for severely injured users.

This thesis work proposes that the bio-signals obtained from an amputee's residual tendon displacement in the wrist can be used to provide input in order to control a multi-DOF prosthetic. It represents a novel, less-invasive and more refined user-intention sensing method. Such an approach is suitable for upper limb amputees that are missing a single finger, multiple fingers or the hand at the wrist level. Tendon motion measurement is able to determine a person's intention/desire to move the fingers in their hand, since the tendons are attached to individual joints in the fingers, as shown in Fig. 5 in Chapter 2. As well, the ability to measure the displacement of multiple tendons also offers an interesting way to gather multiple independent motion signals (channels) from a user, at a localized location on the arm. For instance, there are up to four FDS tendons which are independently used by a person, providing four independent signals that can be sensed and used as input to a prosthetic controller. The tendons responsible for finger flexion are located in a confined physical region proximal to the wrist, which would allow a single sensor head to track them all. Using tendon displacement to control prostheses is a new concept, and offers a unique way to control multi-degree-of-freedom hand prostheses.

5.2 METHODS FOR ESTIMATING TENDON DISPLACEMENT FOR OTHER PURPOSES

The practice of measuring tendon displacement has been done for other applications. Measurement of tendon displacement is useful to clinicians wanting to quantify pre-operative hand/tendon injuries or post-operative repair. For example, clinical researchers have measured the tendon's residual displacements in the lower arm to assess the functional capabilities of the injured fingers and hands [10,155-159]. Presently, these methods for estimation of tendon displacement in the lower arm are done with an *indirect* method. This consists of measuring the joint rotation angles of the fingers while they are flexed and extended. They also measure various dimensional parameters of the finger joints, such as: tendon-to-joint distances, joint thickness and joint-center to joint-center distances. All of this measured data is then used with one of three hand biomechanical models developed by Landsmeer [160]. However, the accuracy of the Landsmeer models has been debated and there is a lack of consensus on which model best predicts tendon displacement [10,155-159]. The models developed by Landsmeer can only provide general estimations since the model is based on population averages, and may not correspond directly to the specific tendon displacement of a particular patient. Some researchers estimate patient hand parameters using calipers to measure around the skin surface of the intact finger joint, or used averaged data from other publications [156,158,161]. Since hand anatomical dimensions are highly individual, such indirect estimates will affect the accuracy of the biomechanical models.

Alternatively, clinicians could use ultrasound machines to provide a *direct* method to assess tendon function. Ultrasound imaging is a non-invasive and cost effective way to obtain internal images for medical applications and diagnosis of human health. In particular, researchers and clinicians have used commercial ultrasound scanners with Pulsed-Wave (PW) Doppler and Color Doppler Imaging (CDI) functions to quantify tendon displacement and velocity [162-169]. Unfortunately, there are two main issues with Doppler ultrasound-based measurements of tendon motion, which are: angle dependence of the transducer, and fast motion requirements for the tissue. The angle dependence refers to the angle between the incident sound wave and the tendon motion direction, which are not parallel. Since the flexor tendon mainly displaces longitudinally in the arm, and is nearly perpendicular to the incident soundwave, proper alignment can be difficult. In previous work, Doppler technique was employed with an angled standoff wedge in order to minimize the error introduced by the angle dependence [167-168]. Through this study, it was also discovered that tendon displacement estimations using Doppler are only effective when tendons have velocities over 25 mm/s, since the noise floor level is around 20 mm/s. This is due to the high-amplitude, low-frequency noise which overtakes the signal at lower velocities [167-168]. For tendons with excursion occurring at lower velocities, such as those in the wrist, Doppler ultrasound estimation is not an effective tool.

Since there are issues with using Doppler ultrasound for slow moving tissues, researchers developed a method to estimate tissue displacement by tracking the motion of the 'speckles' on the sequence of ultrasound images [170-179]. As described earlier, medical ultrasound images are rendered by the reflected soundwave from tissues, and are characterized by a granular appearance. This structure is often described as speckle texture, and is analogous to optical speckle phenomena present with lasers [180]. As described in Section 4.1.2, speckle arises from the constructive and destructive interference pattern from the underlying scattering medium and is inherent to ultrasound imaging. Even though the observed speckle pattern does not visually correspond to the underlying tissue, the intensity of the speckle pattern reveals the echogenicity of the local tissue. Thus, this speckle pattern can be tracked throughout the ultrasound B-Scan image sequences in order to estimate tendon displacement. Speckle tracking on medical ultrasound images has become a widely used method to design speckle reduction filters [181], estimate strain (elastography) [178], and displacement analysis [170-172,179]. While earlier studies focus on tracking blood flow with either phantoms [171] or volunteers [170] to demonstrate their algorithms, later speckle tracking studies successfully estimate the displacement of tendons [177-179].

5.3 PROPOSED SPECKLE TRACKING ALGORITHM TO ESTIMATE INTERFRAME TENDON DISPLACEMENT

The following sections in this chapter describe the proposed speckle tracking method which provides *direct* and non-invasive estimations of the instantaneous and total displacement of tendon excursion proximal to the wrist. This method makes use of a block matching technique combined with novel attributes in order to first auto-locate the tendon in a sequence of B-Scan ultrasound images, and then use this location to provide incremental and total displacement estimations of a displacing tendon. This proposed thesis forms the basis and proves the concept towards using the tendon displacement user-intended signal as an input to control a hand prosthesis.

5.3.1 Defining the Template, Region of Interest and Potential Matching Blocks

Estimating frame-to-frame (interframe) tissue displacement is made possible by tracking the motion of the speckles between a pair of consecutive B-Scan ultrasound image frames, a process often described as speckle tracking. To track the tissue displacement between consecutive frames *t* and *t+1*, a data block of size *I by J* is defined, where *I* is the number of pixels in x (width), and *J* is the number of pixels in *z* (depth), as shown in Fig. 26. This is regarded as the template and is located at x_1,z_1 on the tendon in frame *t,* and is to be matched to a block with the same dimensions in frame *t+1*. The image sub-sections to be investigated as a potential match in frame *t+1* are regarded as blocks, and lie within a region of interest (ROI) with dimensions *A by B*, centered on the location of the template. The template in frame *t* is compared to a block in *t+1* by use of a similarity measure in order to quantify which block is the best match to the template. A similarity measure is a mathematical metric that scores the level of similarity between the potential blocks and the template, and is described further in Section 5.3.2. The choice of similarity measure is often application specific, and depends on the hardware performance and data type, such as B-Scan or RF data. The block with the score of extrema value is chosen as the match and the interframe displacement vector, *d*, is calculated. The displacement vector *d*, is the difference in location between the template (at x_1,z_1), and the matching block (at x_2,z_2), where:

$$d = (x_1 - x_2,\ z_1 - z_2) \qquad \{1\}$$

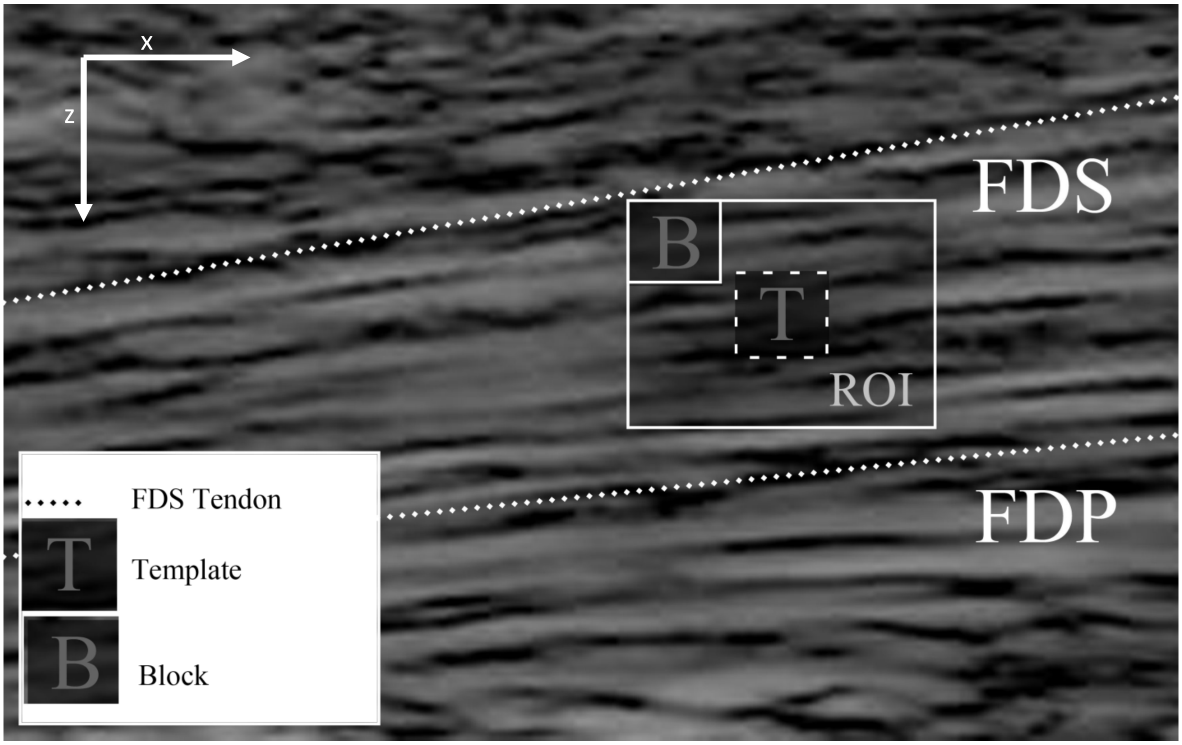

Figure 26: Interframe displacement estimation using speckle tracking. The region of interest (ROI), within the tendon of interest's (FDS) dotted boundary on frame *t+1*, is searched with blocks (an example is labeled 'B'). Once the match is found, the displacement vector is calculated as the difference in position between the template (labeled 'T') from the previous frame, *t*, and matching block.

5.3.2 Similarity Measures

A similarity measure is a mathematical metric which scores the level of similarity between the potential blocks and the template. Examples of similarity measures include the Laplacian (L1-norm) sum of absolute difference (SAD), the Gaussian (L2-norm) sum of squared difference (SSD), or normalized cross correlation (NCC). Alternatively, one can use techniques like Rayleigh (or Fisher-Tippett (FT)) as maximum likelihood operators, and other hybrid combinations of metrics, all offering variations to the block matching technique. The derivation of the similarity measures used in this thesis is as follows:

Sum of Absolute Difference (SAD) and Sum of Squared Difference (SSD)

The Sum of Absolute Difference (SAD) and Sum of Squared Difference (SSD) technique are used as similarity measures for calculating the maximum likelihood that the template in frame *t*, and a block in frame *t+1*, are matching [172,182-186]. The SAD similarity measure is the computationally easiest metric to implement, in comparison to all the other metrics derived in this thesis, as it has no square operations [184]. The SAD and SSD techniques assume that the speckle noise on the B-Scan image is independent and additive, such that $n = \tilde{a}_j - \tilde{b}_j$, where $\tilde{a} = [\tilde{a}_1, \tilde{a}_2 .. \tilde{a}_j]$ represents a vector of all intensities in a displayed B-Scan image in the template in frame *t*, and $\tilde{b} = [\tilde{b}_1, \tilde{b}_2 .. \tilde{b}_j]$ represents a vector of all intensities in a displayed B-Scan image in the investigated block in frame *t+1*. Also, *n* is a noise process with probability density *p(n)*. Using the maximum likelihood method for parameter estimation, the matching block to the template is found by maximizing the following conditional probability density function (pdf) [182,183]:

$$\max \sum_{\mathrm{j}=1}^{\mathrm{IJ}} \mathrm{p}_{\mathrm{j}}(\mathrm{n}) = \max \sum_{\mathrm{j}=1}^{\mathrm{IJ}} \mathrm{p}_{\mathrm{j}}\left(\tilde{a}_j - \tilde{b}_j\right) \qquad \textbf{\{2\}}$$

Assuming that *n* is a generalized Gaussian process, the maximization of Eqn. {2} can be written as a minimization of the following Laplacian SAD (c=1), or Gaussian (c=2) objective function [182,183]:

$$\min \sum_{\mathrm{j}=1}^{\mathrm{IJ}} |\tilde{a}_j - \tilde{b}_j|^{\mathrm{c}} \qquad \textbf{\{3\}}$$

The maximum likelihood given by Eqn. {3} chooses the template and block which are most alike, based on their minimum difference in pixel intensities. The summation in Eqn.{3} is applied to all pixels in the *I by J* template and block, giving a single SAD or SSD likelihood coefficient. The summation is then repeated for all blocks in the ROI, giving *A by B* SAD or SSD coefficients. The block with the SAD or SSD likelihood coefficient satisfying Eqn.{3} (i.e. the minimum coefficient) is deemed the matching block, and the displacement vector is computed using Eqn. {1}.

Normalized Cross Correlation (NCC)

NCC is a commonly used similarity metric for block matching [177-179,187]. For ultrasound imaging applications, the brightness of the template and the comparison image frame in a B-Scan image can fluctuate, leading to interframe displacement calculation errors. The NCC metric is a measure that accounts for the uneven illumination by first individually subtracting the mean from the template and investigated block, and then normalizing the function. Maximizing the NCC objective function determines the block that is most like the template. The NCC objective function is defined as:

$$\max \frac{\sum_{j=1}^{IJ}(\tilde{a}_j - \bar{\tilde{\boldsymbol{a}}})(\tilde{b}_j - \bar{\tilde{\boldsymbol{b}}})}{(\sum_{j=1}^{IJ}(\tilde{a}_j - \bar{\tilde{\boldsymbol{a}}})^2 \sum_{j=1}^{IJ}(\tilde{b}_j - \bar{\tilde{\boldsymbol{b}}})^2)^{\frac{1}{2}}} \quad \mathbf{\{4\}}$$

Where: $\tilde{\boldsymbol{a}} = [\tilde{a}_1, \tilde{a}_2 .. \tilde{a}_j]$ represents a vector of all intensities in the template in a B-Scan image in frame *t* with mean $\bar{\tilde{\boldsymbol{a}}}$, and $\tilde{\boldsymbol{b}} = [\tilde{b}_1, \tilde{b}_2 .. \tilde{b}_j]$ represents a vector of all intensities in the block in a B-Scan image in frame *t+1* with mean $\bar{\tilde{\boldsymbol{b}}}$.

The sum calculation is performed over all pixels in the *I by J* template and block, giving a single NCC likelihood coefficient. This is then repeated for all blocks in the *A by B* ROI. The block having the NCC coefficient with the maximum value is considered a match, and the interframe displacement vector is calculated, using Eqn.{1}.

Rayleigh and Fisher-Tippett (FT)

The Rayleigh (and FT) technique is used as a similarity measure for calculating the maximum likelihood that the template in frame *t*, and a block in frame *t+1* are matched to each other. When speckle in an RF envelope-detected image frame is fully developed, it has been shown to follow a Rayleigh distribution, as previously described in Section 4.1.2 [151,182,183]. The following statistical speckle model was first initialized by Strintzis et al. [182], and then was evolved further by Cohen and Dinstein [183] and then by Boukerroui et al. [175]. The full derivation is not shown in the literature; therefore, it is provided here for clarity to show how the similarity measure is derived. Assume that $\boldsymbol{a} = [a_1, a_2 .. a_j]$ is the vector of all intensities in the template in frame *t* and $\boldsymbol{b} = [b_1, b_2 .. b_j]$ is the vector of all intensities in a block in frame *t+1*, where *j* is the total number of pixels in the template and block. Given that ***a*** and ***b*** have respective Rayleigh distributed noise n_1 and n_2, the probability density function (pdf) $p_1(n_1)$, and $p_2(n_2)$ can be written as:

$$p_1(n_1) = \frac{n_1}{\sigma^2} \exp\left(\frac{-n_1^2}{2\sigma^2}\right) \quad \mathbf{\{5\}}$$

$$p_2(n_2) = \frac{n_2}{\lambda^2} \exp\left(\frac{-n_2^2}{2\lambda^2}\right) \quad \mathbf{\{6\}}$$

Where: σ^2, λ^2 are the mean square scattering amplitudes from ***a*** and ***b***, respectively [151]. Assuming that the speckle noise on the ultrasound images is multiplicative, the noise can be modeled as:

$$a_j = n_1 s_j \quad \mathbf{\{7\}}$$

$$b_j = n_2 s_j \tag*{\{8\}}$$

Where s_j is the true (noiseless) signal and j is a pixel within the block.

Combining Eqns.{7} and {8} gives:

$$\frac{a_j}{b_j} = \frac{n_1}{n_2} = N, \qquad or \qquad a_j = Nb_j \tag*{\{9\}}$$

Where: N $=n_1/n_2$, a division of two Rayleigh distributed variables.

Using the maximum likelihood method for parameter estimation, the matching block to the template is found by maximizing the following conditional probability density function (pdf) [182,183]**:**

$$max_d\, p(\boldsymbol{a}|\boldsymbol{b},\boldsymbol{d}) \tag*{\{1\}}$$

Where: $\boldsymbol{d}$ is the displacement vector, $p(\boldsymbol{a}|\boldsymbol{b},\boldsymbol{d})$ is the conditional probability, $\boldsymbol{a}$ is the vector containing all intensities in the template in frame t, and $\boldsymbol{b}$ is the vector containing all intensities in the block in frame $t+1$.

Eqn.{1} states that the conditional probability is maximized when $\boldsymbol{b}$ is most like $\boldsymbol{a}$, (i.e. a particular block matches a template). Since $\boldsymbol{a}$ and $\boldsymbol{b}$ are both vectors with j independent elements, the pdf in Eqn.{1} is equal to the multiplication of each single element's probability function. A probability function for a single element is calculated using the general Fundamental Theorem for any independent elements α and β [188]:

$$p_\beta(\beta) = \frac{p_\alpha(\alpha)}{|g'(\alpha)|} \tag*{\{2\}}$$

Where: $g(\alpha)$ is a real solution to the random variable α*'s* function $\beta=g(\alpha)$.

In the case of using RF envelope-detected data, and using Eqn. {9}:

$$g(N) = Nb_j, \qquad and \qquad |g'(N)| = b_j \tag*{\{3\}}$$

Using Eqn.{2} the conditional pdf for one template and one block in Eqn.{1} can be written as a product of single element pdf's:

$$p(\boldsymbol{a}|\boldsymbol{b},\boldsymbol{d}) = \prod_{j=1}^{IJ} \frac{1}{b_j} p_j(N) \tag*{\{4\}}$$

Where: $p_j(N)$ is the joint probability function of n_1 and n_2, i.e. $p_j\left(\frac{a_j}{b_j}\right) = p_j(\frac{n_1}{n_2})$, and IJ is the total number of pixels in the template or block.

An expression for $p_j(N)$ is evaluated by using Eqns. {5} and {6} and the following integral [188]:

$$p_j(N) = \int_0^\infty n_2 p_1(Nn_2) p_2(n_2) dn_2 \qquad \textbf{\{5\}}$$

$$= \int_0^\infty n_2 \left\{ \frac{Nn_2}{\sigma^2} \exp\left(\frac{-1}{2\sigma^2} (Nn_2)^2 \right) \right\} \left\{ \frac{n_2}{\lambda^2} \exp\left(\frac{-1}{2\lambda^2} (n_2)^2 \right) \right\} dn_2 \qquad \textbf{\{6\}}$$

$$= \frac{N}{\sigma^2 \lambda^2} \int_0^\infty {n_2}^3 \exp\left(\frac{-N^2\lambda^2 - \sigma^2}{2\sigma^2\lambda^2} (n_2)^2 \right) dn_2 \qquad \textbf{\{7\}}$$

$$p_j(N) = \frac{\sigma^2}{\lambda^2} \frac{2N}{(N^2 + \frac{\sigma^2}{\lambda^2})^2} \qquad \textbf{\{8\}}$$

The last step uses the integral 3.381.4 from [189], i.e. $\int_0^\infty t^{v-1} e^{-ut}\, dt = \frac{1}{u^v}(v-1)!$ Assuming that σ=λ, Eqn. {8} becomes:

$$p_j(N) = \frac{2N}{(N^2 + 1)^2} \qquad \textbf{\{9\}}$$

Therefore the conditional pdf for RF-envelope-detected (uncompressed B-Scan) data in Eqn. {13} becomes:

$$p(\boldsymbol{a}|\boldsymbol{b},\boldsymbol{d}) = \prod_{j=1}^{IJ} \frac{1}{b_j} p_j(N) = \prod \frac{1}{b_j} \frac{2N}{(N^2+1)^2} = \prod \frac{1}{b_j} \frac{2\frac{a_j}{b_j}}{(\frac{{a_j}^2}{{b_j}^2} + 1)^2} = \prod_{j=1}^{IJ} \frac{2a_j}{({a_j}^2 + {b_j}^2)^2} \qquad \textbf{\{10\}}$$

The maximization of Eqn. {10} is equivalent to the maximization of Eqn. {4}.

Since the envelope-detected-RF data is logarithmically compressed for displaying B-Scans, Eqn. {9} becomes

$$\ln(a_j) = \ln(N) + \ln(b_j) \qquad \textbf{\{11\}}$$

Similar to the previous process with uncompressed B-Scan data:

$$g(N) = \ln(N) + \ln(b_j) \qquad \textbf{\{12\}}$$

So that,

$$g'(N) = \frac{1}{N} = \frac{b_j}{a_j} \qquad \textbf{\{13\}}$$

Similar to the previous process for uncompressed B-Scan data, the conditional pdf of B-Scan data becomes:

$$p(\boldsymbol{a}|\boldsymbol{b},\boldsymbol{d}) = \prod_{j=1}^{IJ} \frac{a_j}{b_j} p_j(N) = \prod \frac{a_j}{b_j} \frac{2N}{(N^2+1)^2} = \prod_{j=1}^{IJ} \frac{a_j}{b_j} \frac{2\frac{a_j}{b_j}}{(\frac{{a_j}^2}{{b_j}^2}+1)^2} \qquad \textbf{\{14\}}$$

Let $\tilde{a}_j = \ln(a_j)$, and let $\tilde{b}_j = \ln(b_j)$, so that $\frac{a_j}{b_j} = \exp(\tilde{a}_j - \tilde{b}_j)$, where $\tilde{a}_j$ and $\tilde{b}_j$ are the vectors of B-Scan intensities in the template and a single block in frame *t* and *t+1*, respectively. Eqn.{14}becomes:

$$p(\tilde{\boldsymbol{a}}|\tilde{\boldsymbol{b}},\boldsymbol{d}) = \prod_{j=1}^{IJ} \frac{2\exp\ 2(\tilde{a}_j - \tilde{b}_j)}{(\exp(2\left(\tilde{a}_j - \tilde{\tilde{b}}_j\right)) + 1)^2} \qquad \textbf{\{15\}}$$

The maximization of Eqn.{15} is equivalent to the maximization of Eqn. {1}. Eqn.{15} is a double exponential, and is considered a Fisher-Tippet (FT) distribution.

It is often easier to compute the log-likelihood of Eqn.{15} instead of direct calculation. This is valid because logarithms are monotonically increasing, so that the logarithm of a function achieves the maximum at the same place as the function itself. Eqn.{15} then becomes the following objective function:

$$\ln L = \ln\left(p(\tilde{\boldsymbol{a}}|\tilde{\boldsymbol{b}},\boldsymbol{d})\right) = \sum_{j=1}^{IJ} \ln(2) + 2(\tilde{a}_j - \tilde{b}_j) - 2\ln(\exp(2(\tilde{a}_j - \tilde{b}_j)) + 1) \qquad \textbf{\{16\}}$$

The maximization of Eqn.{16} is equivalent to the maximization of Eqn.{15}. The sum calculation is performed over all pixels in the *I by J* template and block, giving a single FT likelihood coefficient. This is then repeated for all blocks in the *A by B* ROI. The block having the FT coefficient with the maximum value is considered a match, and the displacement vector is calculated. This process is then repeated for the next two frames, i.e. defining a template at x_1,z_1 in frame *t+1* and calculating FT coefficients for all block the ROI in frame *t+2*.

Hybrid Method Based on Signal-to-Noise Ratio (SNR) using FT and SAD

This hybrid similarity measure employs two different metrics, and combines them together to obtain a similarity score. It is based on the local speckle density in the ROI. For the local speckle density to be Rayleigh distributed, the signal-to-noise ratio of the ROI must be evaluated, in order to validate the use of Eqn.{16}. The instantaneous envelope-detected RF signal, in units of its standard deviation, is commonly referred to as the signal-to-noise ratio (SNR), and is defined as [151].

$$SNR = \frac{\overline{AB}}{AB_\sigma} \quad \{17\}$$

Where: $\overline{AB}$ is the mean and AB_σ is the standard deviation of all the pixel's intensities of the ROI in the comparison frame.

For a Rayleigh distribution, the SNR was theoretically derived as 1.91 [151]. The B-Scan intensities have been log-compressed, therefore the intensities in the B-Scan ROI were uncompressed prior to calculating the SNR. If the SNR is below 1.91, which represents areas of dense speckle, the FT metric given by Eqn. {16} is used as the similarity measure on the log-compressed B-Scan data. If the SNR is above 1.91, the SAD measure given by Eqn. {3} is used.

Hybrid Method Accounting for Noise, using SAD and NCC

When examining sequences of B-Scan images where no tissue motion is present, it was observed that the intensities at each location in the ROI vary as time progressed. This was mainly due to non-stationary system noise or other imaging artefacts. Therefore, when analyzing two frames of a moving tendon, the similarity measure used for computing a score may be plagued by noise, which may lead to an erroneous interframe displacement value. In an ideal case, the computed minimum similarity score represents the best match. However, with the presence of noise, the true minimum score can be obscured within a range of scores, where the lowest computed score may not represent the true location of the interframe displacement (Fig. 27). Therefore, this hybrid measure employs a tolerance that includes blocks around the original matching block. These blocks form a subset, in which all entries are considered as a possible match. The tolerance value is calculated by using an image frame subtraction technique with data taken prior to experimentation. In order to estimate the noise present in all images taken with the ultrasound machine at the same settings, the frame subtraction technique is used to create an intensity distribution histogram centered about its mean, and then this distribution is used to evaluate the expectation value. In the first step, this technique uses a set of frames containing stationary tissue, and then calculates the average frame difference, F_{avg}, for a single location (x_1,z_1) in the ROI using:

$$F_{avg}(x_1, z_1) = \frac{\sum_{k=1}^{F} f_1 - f_k}{F} \quad \{18\}$$

Where: F is the total number of sequential frames with stationary tissue, k is the frame number, and $f_1 - f_k$ represents a subtraction of a single location's intensities in the *A by B* ROI.

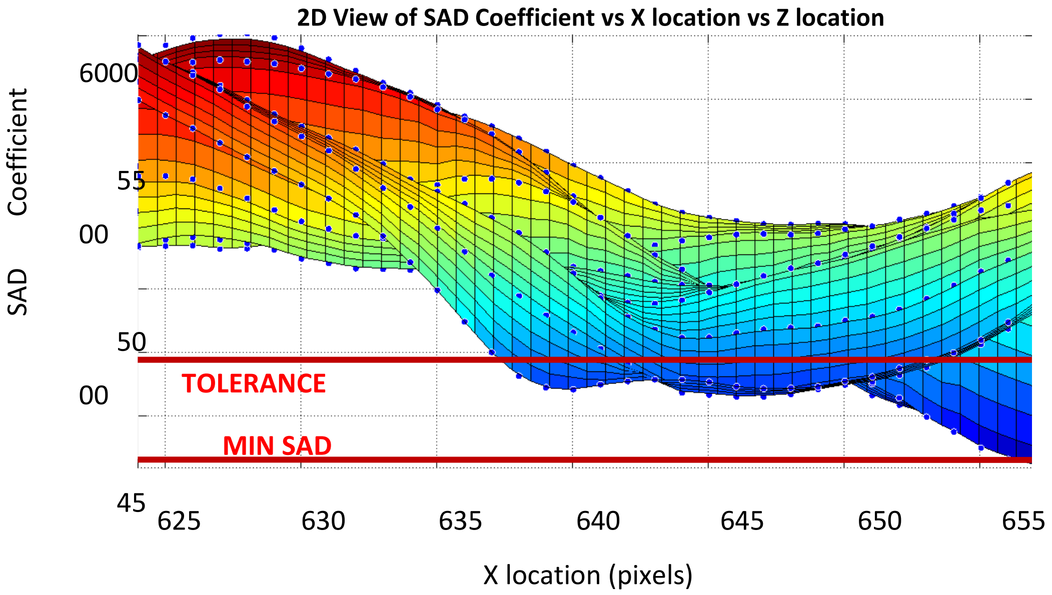

Figure 27: The second hybrid technique: this is a 2D view of a 3D surface plot from one interframe displacement calculation, with the SAD coefficient vs x vs z location on the image. Usually, the block with the extrema coefficient (minumum SAD in this case) is chosen as the match. Since there is noise in the images, a subset of potential matching block is selected. These potential matches are located with an x,z coordinate lying within the minimum SAD value and the tolerance value.

If there were no noise present at location (x_1,z_1) in the frames with stationary tissue, F_{avg} would be zero. Since there is non-stationary noise present, an estimate of the noise at location (x_1,z_1) for the k^{th} frame is obtained using:

$$D(x_1,z_1)_k = f_k - F_{avg} \qquad \{19\}$$

This process is repeated on each location in the (*A by B*) ROI, in order to create a histogram that is centered on its mean value. The histogram represents the probability density of the non-stationary noise. Looking at this histogram, 2σ is easily calculated, representing the most probable value of the noise intensity. The expectation value, *E*, is calculated using Eqn. {20} and the $D(x,z)$ values within 2σ on the histogram:

$$E = \sum_{i=m}^{2\sigma} D(x,z)_i p_i \qquad \{20\}$$

Where: p_i is the probability of $D(x,z)$ occurring, and the summation of i is applied to the $D(x,z)$ values which lie within the mean value and 2σ

In other words, the expectation value represents the most probable amplitude of the noise intensity, or the error on every pixel's intensity value in every frame. Using data obtained prior to experimentation, the expectation value was determined as *2.2*.

In order to utilize the expectation value as a tolerance for determining the subset of potential matches for an interframe displacement calculation, the expectation value is used as an upper error bound on the calculated minimum SAD coefficient, using:

$$tolerance = \min SAD + E(IJ) \qquad \mathbf{\{21\}}$$

Where $minSAD$ is the minimum SAD coefficient calculated by Eqn. {3}, *E* is the expectation value (with a value of *2.2*), and *IJ* is the number of elements in the block. (Recall, each absolute difference $|\tilde{a}_j - \tilde{b}_j|$ in Eqn. {3} will now have an upper bound error given by *E*, and is thus compounded *I by J* times in the summation giving a SAD coefficient).

The subset of potential matches now includes block which have SAD coefficients between the $minSAD$ value and the upper bound tolerance given by Eqn. {21}.

In order to determine which block represents the true interframe displacement within this smaller subset, NCC is used as a secondary measure (Eqn. {4}). The block with the largest NCC coefficient within this subset is considered a match, and then the interframe displacement is calculated.

5.3.3 Estimating Cumulative and Total Displacement

The methods in Sections 5.3.1 and 5.3.2 describe the process to estimate frame-to-frame or interframe displacement, between consecutive frames *t* and *t+1*. In order to determine the next interframe displacement, the previous process is repeated on the next set of consecutive frames *t+1* and *t+2*. The template block is now updated with the data from frame *t+1* at location x_1,z_1. This process can be visualized in Fig. 28 as a ‘stationary ROI technique’, whereby the displacement through a gate located at x_1,z_1 is estimated using a stationary ROI [179].

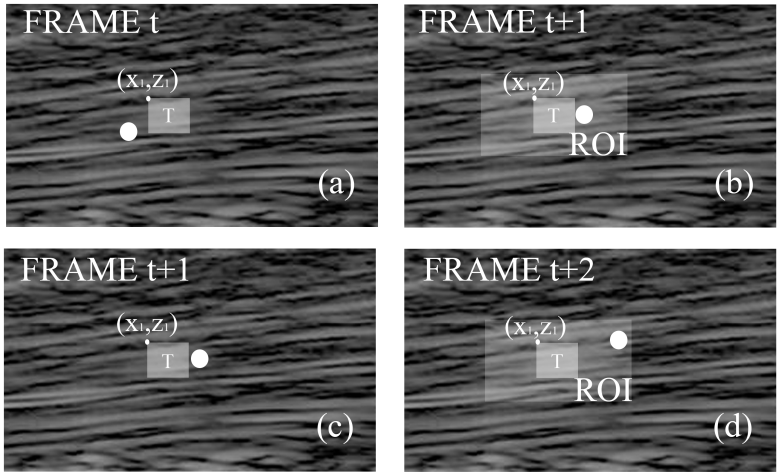

Figure 28: The stationary ROI technique is demonstrated: (a) in frame *t*, a template is located at x_1,z_1. (b) In the next image frame *t+1* a ROI is centered on the template, the matching block inside the ROI is found and the interframe displacement is calculated. This process is repeated: (c) the template is located at x_1,z_1 in frame *t+1*,(d) the matching block is found within the ROI in frame *t+2*, and the interframe displacement is calculated.

Traditional tracking techniques will track a specific location on the tendon itself (represented as a white circle in Fig. 28) as it displaces throughout the image sequences. However, in the method used in this thesis, the template is always updated when the frames are incremented, and is always located at x_1,z_1. This way, if the B-Scan had a small field-of-view, or if there was a tracking mis-match at some place in its displacement, the remaining displacement estimations would not suffer by compounding the error (temporal drift). This is in contrast to many speckle tracking algorithms in the literature which track the same location on the tendon, as the tendon displaces across consecutive frames.

In order to estimate the total displacement, the interframe displacements are added cumulatively to obtain the total displacement from the entire excursion. Likewise, the cumulative displacement can be plotted as a displacement versus time curve. As well, in order to estimate the velocity at a given point in time, the data can be linearly extrapolated from the displacement versus time curve. The velocity at a given point is the difference in displacement between two adjacent points divided by their difference in time.

5.4 PROPOSED AUTO-LOCATION ALGORITHM

The previous speckle tracking algorithms outlined in Section 5.3, all place a template at location x_1,z_1 in frame *t*. However, a suitable value (position) for x_1,z_1 must be determined in some way. For example, a trained ultrasound operator could determine these coordinates by viewing several datasets containing the moving tendon. In fact, several commercial software packages for ultrasonic elastography (tissue strain) rely on the trained operator to select the template location and size, as well as ROI location and size [190,191]. Although the algorithms presented in this thesis have clinical benefits for general tissue tracking, the motivation is to use such algorithms to detect tendon displacement for prosthesis control. Thus, this necessitates the development of an automatic technique to determine the ideal location x_1,z_1 within the image frame, for the template. The auto-location algorithm would be used as an initial calibration step in order to define the ideal tracking location for monitoring a tendon's displacement. Since the transducer is static relative to the arm, the auto-location algorithm can be used initially, and then at occasional intervals, to ensure the tendon location is known with respect to the transducer. At other times, only regular tracking as described in Section 5.3 takes place.

The auto-location technique used in this thesis, estimates the total displacement at many locations in a sequence of image frames. When many discrete locations are chosen to estimate the total displacement, a displacement field can be created. The resulting field represents the estimated displacement at a given location on the tendon, for the tendon's entire excursion. The field can be graphically illustrated as a 2D view of a 3D colormap: with x-z locations on the x-z plane, and the total displacement at each x-z point is shown as a colour-magnitude (Fig. 29). Thus, the location with the maximum total displacement is defined as the ideal template location.

In order to create the displacement fields, the speckle tracking techniques described in Section 5.3, with the similarity measures SAD, FT and NCC, are used. The speckle tracking algorithm for a given similarity measure is applied by first placing the template at a location in a large area within frame t. The interframe displacements are then estimated by the previous technique using a stationary ROI. When these interframe displacements are cumulatively added, the total displacement for that location can be estimated. This entire process is then repeated for another location within the large area on frame t, giving another total displacement estimation. This is repeated for many locations, thus creating a displacement field. The location with the maximum total displacement is defined as the ideal template location. Once the auto-location calibrating procedure is completed, this location can be used for all future excursions, assuming the transducer hasn't moved.

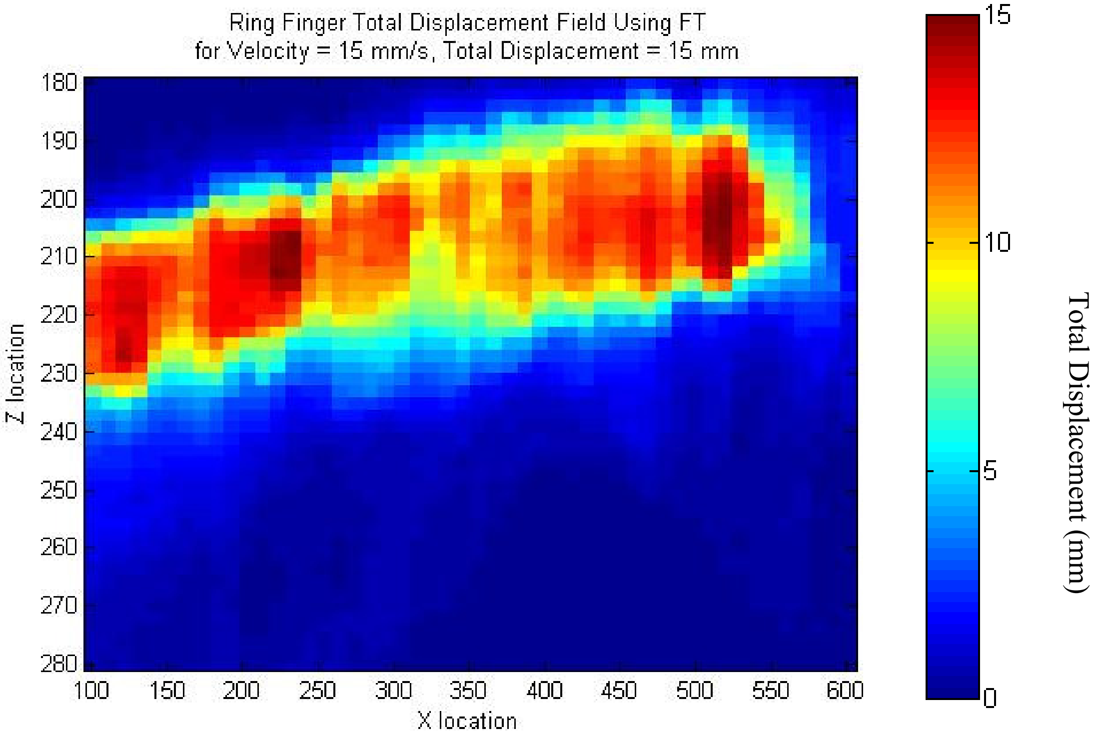

Figure 29: An example of a displacement field from the middle finger FDS tendon total excursion. This plot is a 2D view of a 3D colormap: with *x-z* locations on the *x-z* plane, and the total displacement at each *x-z* point is shown as a colour-magnitude.

5.5 DETERMINING THE OPTIMAL PARAMETER SETTINGS FOR THE PROPOSED SPECKLE TRACKING ALGORITHMS

The success of any speckle tracking algorithm itself depends on many parameters. Such parameters include the similarity measure chosen, searching strategy, computational efficiency, the size and location of the template and the ROI, the axial and lateral resolution, the frame rate (temporal resolution), the velocity of the moving tendon, the plane of the moving tendon and frame skipping. Most speckle tracking studies state their choices of algorithmic parameters, such as template sizes and optimal searching strategies, but they frequently do not explain the implications of such choices. For example, one study used the NCC similarity measure with RF data, and investigated the parameters of: noise, bandwidth, stationary echoes, template size, downsampling, interpolation and demodulation [176]. Another study, investigated the relative performance of NCC and SAD on simulated RF data [172]. In general, a study is needed that discusses the relevant parameters, or the effect of parameter choices using B-Scan image sequences of tissue displacement. Also, many ultrasound machines are closed systems, and do not allow for RF data access, thus necessitating further investigation into optimizing parameters using B-Scan. Thus, this thesis investigates the effect of relevant parameters on tracking success when using B-Scan images of human tendon data. Important algorithmic parameters are first introduced in Sections 5.5.1 to 5.5.5, and the effect of varying such parameters is shown using experimental data in Chapters 6 and 7.

5.5.1 Similarity Measure

The choice of similarity measure is often application specific, depending mostly on computational efficiency requirements, and the availability of open-architecture hardware to have RF-data access. For instance, as described in Section 5.3.2, the Rayleigh measure can be used for RF-envelope-detected data, and when the image is logarithmically compressed to become a B-Scan, the Fisher-Tippet measure can be used. There are many permutations of similarity measures and searching techniques seen in the literature. For instance, the SAD similarity measure assumes that the speckle distribution is Laplacian, and this measure can be used for its ease of implementation in hardware. This is because it has no square operations; however, it can be more susceptible to noise [184]. SSD assumes the distribution of speckles is Gaussian, and it has been shown in other studies to be more reliable than SAD [174,192]. This measure penalizes large differences between the template and investigated block more heavily, thus the block with the minimum SSD value is more easily found. NCC is a common similarity measure because it overcomes uneven illumination and other issues, because this measure removes local means [177-179]. When assuming the distribution is Rayleigh distributed (i.e. the SNR of the image is <1.91), and direct uncompressed B-Scan or RF data is not available, the Rayleigh similarity measure should account for the logarithmic compression by using the Fisher-Tippet metric [151,175,181-183]. Other novel hybrid metrics developed in this thesis use FT or SAD based on the SNR of the speckle data, or account for the non-stationary noise in the speckle data by first considering a subset of potential matches found with SAD, and then using NCC as a secondary measure to determine the ultimate matching block. The aforementioned similarity measures are used for the experiments described in Chapters 6 and 7.

5.5.2 Searching Strategy

The searching strategy describes a technique whereby the template is compared to potential blocks by a particular method, which may increase matching accuracy, or may reduce the computational time. For the work proposed in this thesis, the potential matching blocks within a stationary ROI in frame *t+1* are individually compared to the template in frame *t*, using an exhaustive search method. Although this can be computationally more intensive, it is generally more accurate than other adaptive sub-searching approaches [193]. There are other techniques which optimize the searching strategy by hierarchical or pyramid searching [175,178]. It makes use of a template and ROI that change size from coarse-to-fine. In the first iteration to determine interframe displacement, a larger template is used and the matching block is found in the next frame, as previously described. In the second iteration, the template size is reduced by half, and the new matching block to this smaller template is found within an ROI centered on the previous matching block. In the third iteration, the template is again reduced in size by half and the new matching block is found within an ROI centered the previous matching block. This process is illustrated in Fig. 30. The ROI is also decreased with each iteration. The hierarchical search method proposed bin this thesis differs from the literature in a sense that the second and third iteration is performed with a larger ROI that is centered on the previous match. This is in contrast to others, who use the previous match size as the new ROI size.

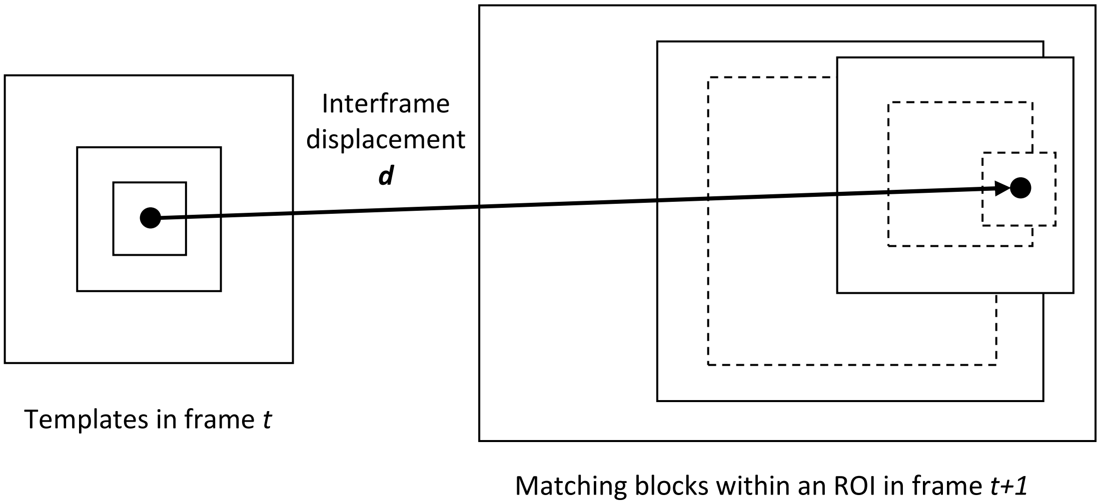

Figure 30: **Hierarchical searching technique. In the first iteration to determine interframe displacement, a larger template is used and the match is found in the next frame within a ROI. In the second iteration, the template size is reduced by half, and the new match to this smaller template is found within a ROI centered on the previous match. In the third iteration, the template is again reduced in size by half and the new match is found within the a ROI centered previous match. The interframe displacement vector, *d*, is calculated as the difference in position between the smallest template in frame *t* and *t+1*.**

Another technique used in this thesis employs the stationary ROI method, whereby the template is always located at x_1,z_1, and the ROI always encompasses this location. The use of a stationary ROI technique is useful to overcome issues like temporal drift, which is the drift of the cumulative displacement form its true value throughout time. If a stationary ROI is not used, temporal drift can occur with a singular interframe displacement mismatch. This is because the next interframe displacement calculation uses the previous match as the new template. If the previous match was incorrect, this mistake is carried through and tracking can be lost completely.

5.5.3 Template size, ROI size and template location

The size of the template and ROI can affect the success of tracking. For instance, if the template is too large, it may include regions of non-uniform motion. If the template is too small, it is susceptible to noise and can cause ambiguity and mismatch. Furthermore, a small template can contribute to an aperture problem. This issue can occur if a tendon has larger regions of uniform grayscale intensity. In this case, as the tendon displaces across the field of view, it moves through the ROI centered on the template, and thus the tendon can appear like it is not moving. The size of the template chosen in frame t is also the size of the blocks within the ROI in the subsequent frame, $t+1$.

In terms of choosing the optimal size of the ROI, a large ROI may cause ambiguous matches, as there is an increased chance of having several local extrema when calculating the similarity measure. Also, a larger ROI is more computationally intensive. However, if the ROI is too small, large tendon displacements between the frames may not be captured, causing mis-match leading to poor tracking.

The template location at different points along the tendon in the B-Scan image sequence can affect the success of tracking. Investigating the effect of changing the template location is important since it is often observed that there are regions on the B-Scan sequences that have enhancement or shadow artefacts. Placing the template near these regions may cause loss of tracking. As well, although the majority of the tendon's displacement is in the x-direction, the tendon may shift in the y-direction during the image sequence. A linear array transducer can only image displacement in a single plane (i.e. the x-z plane). Therefore, any motion in or out of this image plane (into the y-direction) can cause tracking errors, because the template may not remain on the tendon for the entire excursion when using the stationary ROI technique. This issue can be mitigated by the initial use of a displacement field, in order to determine the optimal location for estimating displacement for subsequent data sets (assuming the transducer is static). There are other studies that attempt to rectify tracking loss due to out-of-plane shifts, by implementing deformable mesh algorithms which quantify torsions in 3D from 2D ultrasound images [194,195].

5.5.4 Axial, Lateral and Temporal Resolution

As presented in Chapter 4, axial, lateral and temporal resolution are important imaging parameters. Axial resolution (*z*-direction) is directly affected by the pulse length, while the lateral resolution (*x*-direction) is affected by the beam width and scan line density, among other factors. Poor resolution in either *x*- or *z*-directions can affect the success of tracking, because the speckle pattern from the tendon may become indistinguishable from background tissue. Further, image sequence frame rate (number of frames per second) is an important consideration for speckle tracking in terms of temporal resolution. This is an important consideration when tracking tendon motion with a particular displacement and velocity per frame. In particular, the tendon velocity must not be too fast, and the frame rate of the B-Scan image capture must be high enough such that the inter-frame estimated displacement is not too high. If the interframe displacement was too high and was captured with a low frame rate, speckle decorrelation can occur, causing matching errors.

5.5.5 Frame Skipping

The previously described speckle tracking technique described in Section 5.3 explains how the template in frame t is compared to the blocks in the next frame in $t+1$, to estimate interframe displacement. Since every ultrasound imaging system is different, the resolution may not be sufficient to detect small interframe displacements. This is a function of the system's frame rate and lateral resolution, as well as the tendon's lateral displacement and velocity. For instance, if the system's frame rate is high, the lateral resolution is coarse, and the expected interframe displacement is small, the algorithm may not detect any tendon displacement. One way to mitigate such issues when estimating interframe displacement, is to skip frames when comparing the template to the potential blocks in the ROI, i.e. by comparing the template in frame t, to the blocks in frame $t+k$, where k is an integer. The assumption using frame skipping is that the speckle does not decorrelate to much between frames t and $t+k$, and that the velocity is constant (the displacement is linear) in the interval between frames t and $t+k$. Thus, this necessitates the development of a technique which can determine the optimal frame skipping number, k. This thesis proposes a novel technique in order to determine the optimal frame skipping number, k, in terms of the expected lateral displacement per frame, the system's frame rate and lateral resolution. The lateral resolution, R_L, is where the majority of the displacement is occurring, and is obtained by calibration studies in which an object of known dimensions is placed between gel pads under the transducer. This way, the mm/pixel ratio can be estimated, giving R_L. The expected lateral displacement per frame, ε, can be determined by the experimental set-up. The expected total lateral displacement, d_T, can be given by the encoders from the motors, or by using biomechanical models such as the previously described Landsmeer models from Section 5.2. The frame rate, *FR*, is usually given by the ultrasound machine's GUI, or within the file header. The *FR* and expected total lateral displacement together are used in order to obtain an estimate of the expected lateral displacement per frame, ε. This is achieved by using Eqn. {22}, and assuming the velocity (given by d_T and *T*, or by the encoders/biomechanical models) is constant.

$$\varepsilon = \frac{\mathrm{d_T}}{\mathrm{T}} \cdot \frac{1}{\mathrm{FR}} \tag*{\{22\}}$$

Where: d_T is the expected total displacement, *T* is the total time and *FR* is the system's frame rate. The expected lateral displacement per frame, ε, is in units of mm/frame.

If the lateral resolution is coarse, and ε is small, the speckle tracking algorithm may not be able to detect any interframe displacement. Thus, by comparing frames *t* and *t+k*, the expected displacement (in the *x*-direction) in *k* frames becomes $k \cdot \varepsilon$. This thesis proposes an empirical method using data from Chapter 7, and introduced a constant, γ, in which:

$$\frac{\mathrm{k} \cdot \varepsilon}{\mathrm{R_L}} \cong \gamma \tag*{\{23\}}$$

Where *k* is the frame skipping number, ε is the expected lateral displacement per frame, R_L is the lateral resolution and γ is the empirically derived constant.

Thus, rearranging Eqn.{23}, the ideal frame skipping number for subsequent data sets is estimated as:

$$\mathrm{k} \cong \frac{\gamma\, \mathrm{R_L}}{\varepsilon} \tag*{\{24\}}$$

5.6 PROPOSED SPARSE QUAD-ARRAY TRANSDUCER DESIGN

This thesis proposes a tracking system for monitoring multiple tendons simultaneously, to allow for multi-DOF prosthesis control. Therefore, an ultrasound transducer that can perform this task is needed. Commercially available linear array transducers can image a single 2D plane of tissue, and are suitable for imaging a single displacing tendon. Other commercially available transducers, such as 4D or matrix transducers which were described in Section 4.2.1, either have a low frame rate (and reduced resolution), require powerful processors, or can be very expensive. Other researchers use a sparse matrix array, which has an altered firing sequence and electronically deactivated elements in order to improve computational efficiency [196-198]. Sparse-matrix sparse arrays are still limited by their complexity, both by hardware and software requirements, since they require powerful processors. The motivation of the thesis is to use the tracking system with future hardware that has the potential to be miniaturized, thus commercial 4D/matrix systems cannot be used.

To facilitate the ability for multi-tendon tracking, an alternative hardware solution that can monitor several tendons simultaneously, has been developed in the form of a custom sparse quad-array transducer (US Patent filing # 14058022, Oct.18, 2013). The proposed sparse quad-array design has been developed to be compatible with the Ultrasonix Touch Research open architecture ultrasound machine (Ultrasonix, Richmond, BC, Canada) [199]. This is so that the 128-channel beamformer within the Ultrasonix Touch Research can still be used, along with the system's proprietary software development kit (SDK). The custom sparse quad-array transducer presented in this thesis is a completely new concept. The proposed quad-array transducer design is a 10 MHz frequency linear array transducer, and is custom fabricated to our requirements by Blatek (State College, PA, USA), and is compatible with the Ultrasonix machine (Fig. 31). The quad-array transducer has four 32-element sub-arrays in parallel, spaced 3 mm apart (Fig. 32).

As observed in (Fig. 32), elements 32 and 33 are not located adjacent to each other. In a conventional linear array, elements 32 and 33 are side by side, and so the moving aperture and firing sequences are not interrupted at this location. However, in the new quad-array, since these elements are no longer side-by-side, custom software was written to redesign the firing sequence and aperture size, using the SDK provided by Ultrasonix. The custom software was written by LJB Development, Inc. (Fort Mitchell, KY, USA), which provides custom ultrasound software development. This software is comprised of two parts. Firstly, as with the linear array, the elements for a given sub-array are programmed to activate in groups, forming an aperture. There are a limited number of elements per sub-array; hence a variable aperture is used so that the field of view would not be reduced further. Recall, an aperture of active elements in transmission produces a single scan line, as described in Section 4.3.1. Thus, if a 32-element sub-array implemented a fixed-size aperture for all active groups in transmission, the end elements would reduce the side portions of the image. Therefore, if the aperture is tapered at the end elements, the field of view will not be reduced, as there are scan lines producing the side portions of the image). As well, since the end elements (i.e. element 32 and 33) are no longer side by side as previously described, the aperture must be tapered at the ends of a given sub-array so that elements from the adjacent sub-array does not contribute to the formed soundwave beam.

A second feature of the custom software is the front end GUI, which was designed to suit this work by displaying the B-Scan image sequences from all sub-arrays simultaneously. The GUI allows for user controls in order to change the focus depth, scan line density, power and gain. Also, beamformed RF and B-Scan data can be saved and exported into Matlab 2012b (Mathworks, USA).

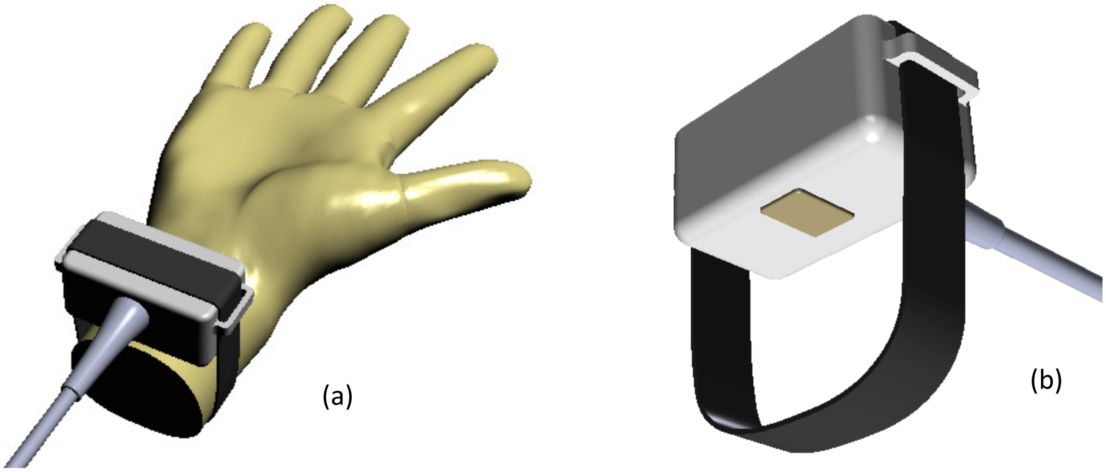

Figure 31: Novel sparse quad-array design. (a) The quad array is placed on the user's palmer-side wrist area, in order to collect tendon displacement signals from four separate *x*-*z* planes. (b) Underside view of quad-array.

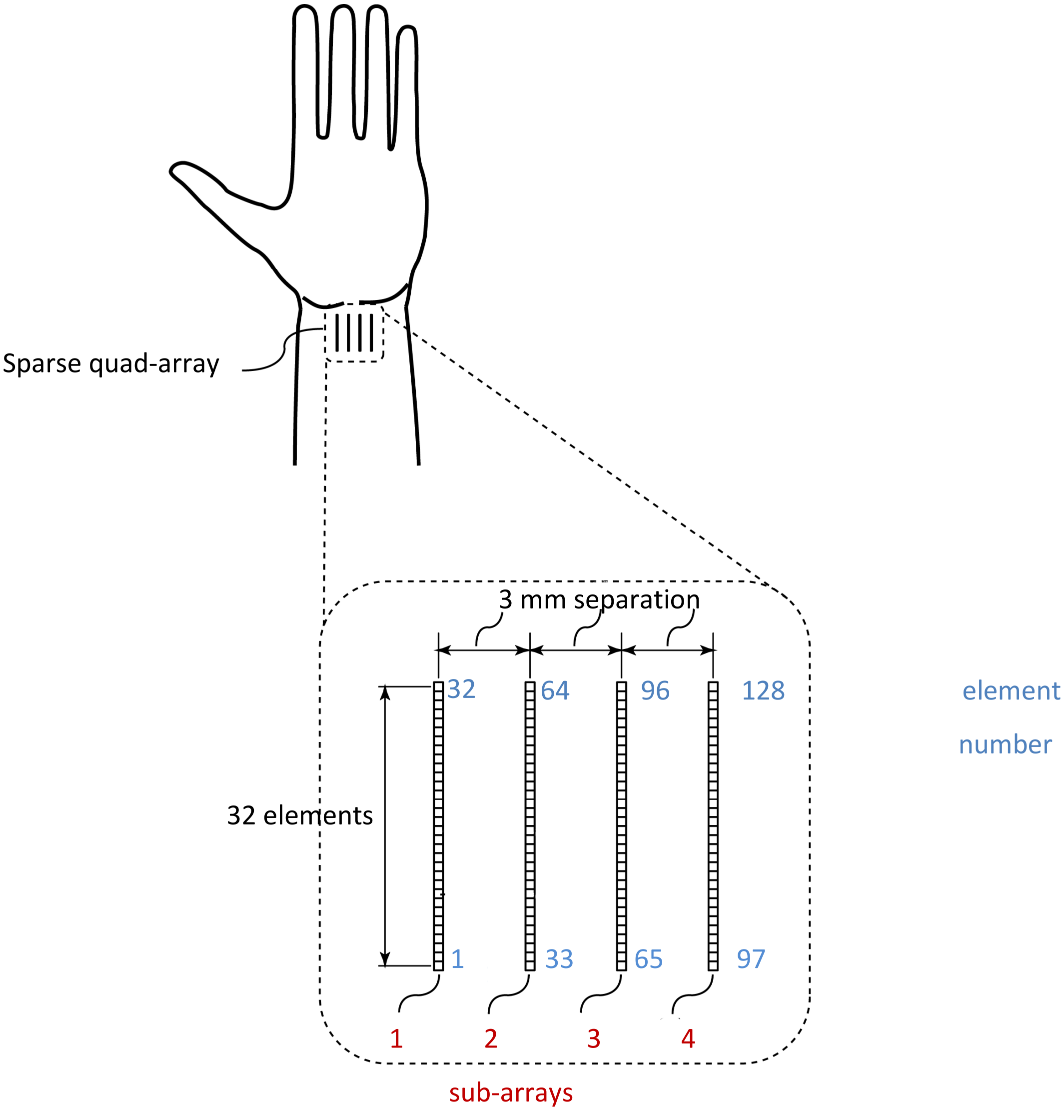

Figure 32: Novel sparse quad-array design. The quad array is placed on the user's palmer-side wrist area, in order to collect tendon displacement signals from four separate *x-z* planes. Each sub-array consists of 32 elements, spaced 3 mm apart.

CHAPTER 6:

EXPERIMENTAL OBJECTIVES AND METHODOLOGY

6.1. EXPERIMENTAL OVERVIEW AND METHODOLOGY

The experiments performed in this thesis are designed to verify the proposed techniques in Chapter 5, as well as to verify the deliverables outlined in Chapter 1. Thus, the verification experiments include a standard reference, whereby a known motion value can be used as a gold standard and be compared to the values estimated by the tracking algorithms, for validation. Validation can be achieved by comparing the estimated displacement given by the ultrasonic speckle tracking technique to the actual displacement taken place. This can be accomplished by using simulations, medical phantoms, cadaver materials or humans, in which the tendons are accessible in order to determine the standard reference displacement. Cadaver materials and human subjects present a more realistic test-bed in comparison to using simulations and medical phantoms. Thus, the experimentation in this thesis uses cadaver material and human subjects undergoing surgery with exposed tendons, in order to validate the proposed techniques.

In total, five major experiments were conducted in this thesis, as described in Sections 6.2 – 6.6. Experiment 1 is a preliminary study at the University of British Columbia's Life Science Laboratory, in which a single human cadaver tendon is coupled to a mechanical system in order to produce joint articulation and tendon excursion, using novel mechanical hardware. As well, the data collected is used as an image library in order to further develop the speckle tracking techniques. Experiment 2 uses the knowledge gained from Experiment 1, and further validates the speckle tracking techniques using humans undergoing carpal tunnel release surgery at the Royal Jubilee Hospital. This provides a unique and ideal data-set for single tendon tracking, in that humans represent the most realistic test-bed. Experiments 3 through 5 are performed over a four-day data collection period at the University of British Columbia's Life Science Laboratory. Experiment 3 uses improved ultrasound hardware, as well as a new electro-mechanical test-bed apparatus coupled to a human cadaver tendon. It allows for further development and validation of the speckle tracking technique for tracking single tendons on a cadaver hand. Experiment 4 is designed to validate the new sparse quad-array design, using the new electro-mechanical test-bed hardware in order to actuate multiple cadaver tendons simultaneously, and to collect multiple image sequences from each sub-array. Experiment 5 uses the electro-mechanical test-bed hardware with the improved ultrasound hardware, or with the new quad array, from Experiments 4 and 5 respectively. The motivation is to determine the minimum detectable displacement, or onset of displacement, as well as the minimum displacement needed to auto-locate a tendon. Together, Experiments 1 through 5 provide validation for the proposed techniques and deliverables of this thesis, aimed at providing a novel solution towards improving prosthetic control.

6.2. EXPERIMENT 1: PRELIMINARY CADAVER-BASED STUDY TO OPTIMIZE EXPERIMENTAL SET-UP

6.2.1. Introduction

The motivation of this preliminary study is to develop electro-mechanical hardware to couple and actuate a single tendon of a human cadaver, and also to obtain a library of B-Scan ultrasound cine loops of single tendon excursion. Such libraries of B-Scan data are used to further develop the tracking software in order to obtain estimates of interframe and total displacement. The hardware design involves the development of a standard reference system which couples to the middle finger's FDS tendon on a cadaver hand. As well, the standard reference system actuates the tendon by a known displacement, velocity and acceleration by means of a single stepper motor with a built-in controller. Further design requirements involve the development of two holders, one for the transducer and one for the cadaver material. These holders will keep the respective parts static. The image libraries obtained will be used to develop the SAD speckle tracking algorithm. This study has been approved by the Dept. of Cellular & Physiological Sciences, Body Donation Program, Life Sciences Centre at the University of British Columbia, (approval #: W0137).

6.2.2. Set-Up

The hardware set-up is comprised of: (a) an actuation system, (b) a tendon coupler, (c) a cadaver stabilization system, and (d) a transducer assembly, as shown in Fig. 33. Other components include a PC, ultrasound machine, and a standard linear array transducer, as shown in Fig. 33, label (e). Given the highly individualistic nature of hand dimensions, the apparatus is designed to be used with a variety of hand sizes, using the average values from Table 1 (Chapter 2). The actuation system provides the standard reference, against which the estimated displacements given by the speckle tracking technique can be compared. The actuation system is comprised of a stepper motor, which spins a lead screw to produce the linear motion of an x-stage. The motor is programmed to rotate by a known amount and speed, with a known motion profile. As the motor turns the lead screw, the x-stage displaces with this known motion profile, thus providing the standard reference. The tendon coupler is attached to the x-stage and also attached to the tendon, thereby making tendon actuation possible. The ultrasound transducer and the cadaver hand are separately fixed and grounded in a static position. The transducer is placed on the cadaver wrist area with ultrasound gel in-between, overtop of the middle finger's FDS tendon on intact skin. The ultrasound system will record a sequence of B-Scan frames and combine them into a cine-loop. The tendon displacement estimated by the developed speckle tracking technique using the cine-loop, can be compared to that of the standard reference motion profile to provide verification of the proposed technique. A further description into the apparatus components are as follows:

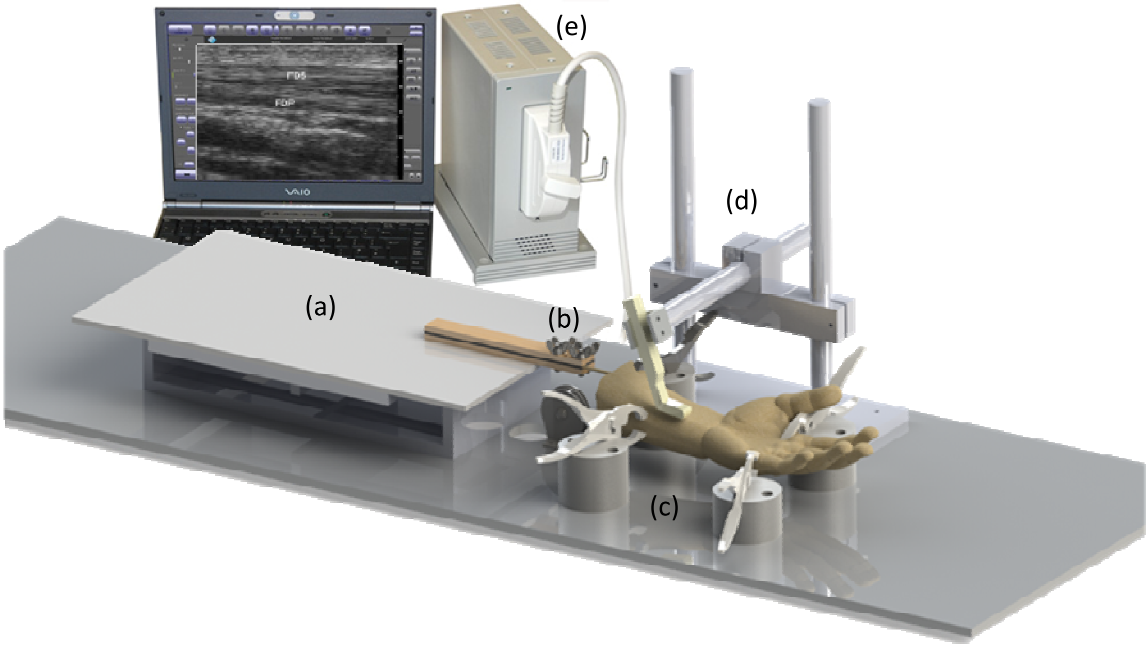

Figure 33: The hardware set-up is comprised of: (a) an actuation system with and x-stage and linear stepper motor (not shown), (b) a tendon coupler, (c) a cadaver stabilization system, and (d) a transducer assembly. Other components include a PC, ultrasound machine, and a standard linear array transducer, as shown in (e).

a) Actuation System

As shown in Fig. 33, label (a), the actuation system is comprised of a linear stepper motor (model CRK 569BKP, Oriental Motor USA Corp.), which drives a 16 mm lead screw (4 start, 4 mm pitch, NSK). As the lead screw turns, an x-stage platform actuates with a programmed motion profile. This system constitutes the standard reference, whereby the programmed motion profile gives the known value of displacement, velocity and acceleration.

b) Tendon Coupler

Tendons, being biological materials, present an inherent difficulty for coupling to mechanical equipment. Hooks, and other piercing hardware, may tear the tendon at the point of attachment, while the tendon is being actuated. A novel tendon coupling system is developed, which is comprised of two plates lined with a rough material, which encompasses the tendon (Fig. 33 label (b), and Fig. 34). For this preliminary study, the outer plates are made from ¼" wood pieces, and the inner rough lining material is coarse-grit, non-slip tape normally used on stairs and skateboards. When the tendon is compressed in-between these lined-plates by bolts and wing nuts, the tendon will not slide out or tear when being actuated with forces at physiological levels. For the flexor tendon, a longer tendon coupler is designed such that it has sufficient clearance when it's bolted to the x-stage.

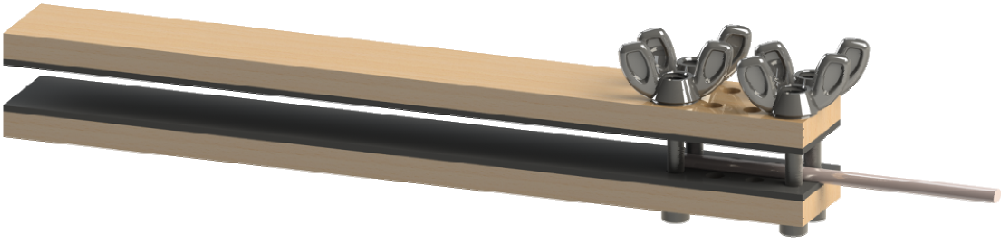

Figure 34: A novel tendon coupling system is comprised of two ¼" wood plates lined with a coarse-grit tape material, which encompasses the tendon. When the tendon is compressed in between these lined-plates by bolts and wing nuts, the tendon will not slide out or tear when being actuated with physiological forces.

After the flexor tendon is actuated in flexion, it must return to its initial position by being actuated in extension. This is achieved with the use of a counter-weight on the extensor tendons (Fig. 35). A smaller tendon coupler is designed for the extensor tendons, which attaches the tendon to a string-pulley-weight system. The 200g weight provides sufficient tension so that the finger (and flexor tendon) can safely return to its natural position.

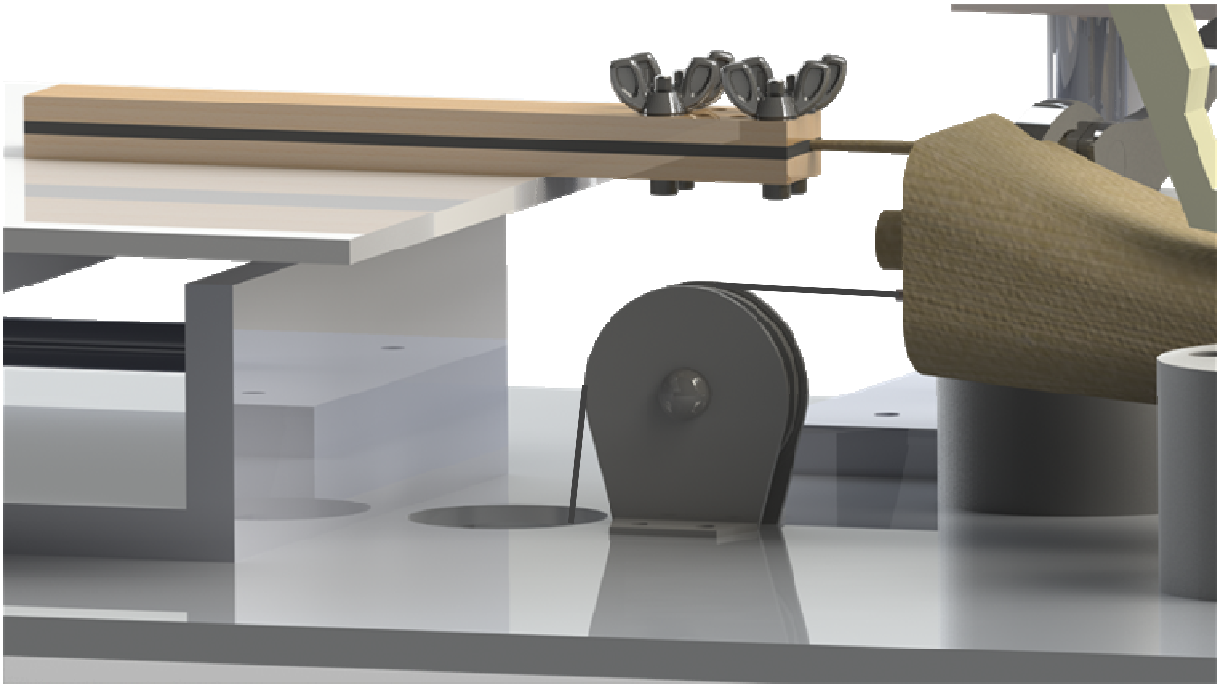

Figure 35: A close up view of the extensor-pulley system, consisting of the pulley and string (shown) and the extensor coupler (not shown) and weight (not shown).

c) *Stabilizing the Cadaver Hand*

The cadaver hand must be rigidly fixed to ground in order to collect useful tendon displacement data. This is to ensure the bone and non-tendon tissue remains stationary with respect to the transducer, which is also rigidly fixed to ground. It is possible to restrain the cadaver hand in various ways: such as using exterior hand straps, or by bolting the bones directly with fixture screws, or by fixing the bones with clamps. In considering these approaches, exterior hand straps may not fix the hand entirely, as they would allow for soft tissue motion if they weren't tight enough. As well, if the straps were too tight, the tendon may not glide in a natural manner. Likewise, bolting the bones requires expertise and specialized equipment so that the fragile bones will not break, when the cadaver hand is subjected to forces. An alternative solution is developed which uses a custom clamping system (Fig. 33, label (c)). This system is comprised of off-the-shelf vice clamps which have been altered so that they can be rigidly fixed to specialized blocks. This way, small incisions can be made into the hand along the metacarpal, radius and ulna bones, and the clamps can easily be inserted within the opening, and then grip the bones at these locations. This achieves a rigid hold on the bones of the hand at four points.

d) Transducer holder

In order to collect images containing just the moving tendon, the transducer must also be fixed to ground. Since hands are highly individualistic, a custom transducer assembly is developed in order to allow for adjusting the transducer's spatial position in height, width, as well as its rotation (Fig. 36). The entire apparatus can be slid to any location on the worktable. The transducer itself is held in place by a custom end-holder, which is connected to a telescoping bar that grasps the transducer with set-screws.

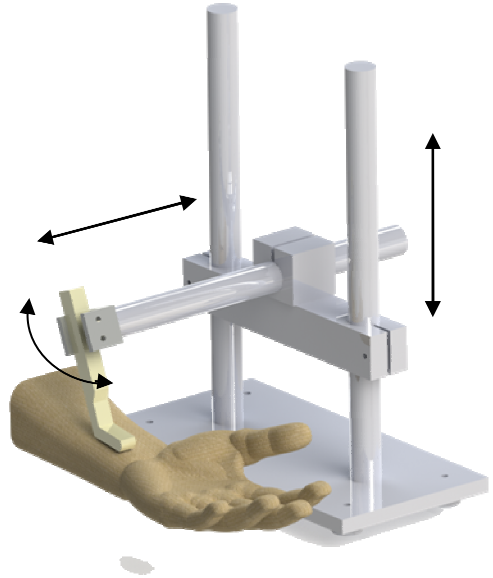

Figure 36: The custom transducer assembly consists of a telescoping and rotational bar which holds the transducer and allows for adjustment. As well, the transducer may be adjusted in height, as indicated by the arrows.

e) The Ultrasound System

The ultrasound system used in Experiment 1, comprised of a commercial 128-element 12 MHz linear array transducer and compact B-Scan ultrasound machine (LogicScan 128, Telemed, Vilnius, Lithuania). The LogicScan scanner is a stand-alone system that transmits and receives sound waves with the linear array transducer, processes the signal, and displays the B-Scan on a

PC via USB. Using a PC, Telemed's onboard software (EchoWave II) can be accessed for displaying purposes. The ultrasound settings are found in Table 3.

TABLE 3: SETTINGS ON THE LOGICSCAN ULTRASOUND SYSTEM FOR EXPERIMENT 1

Property	Value
Frame Rate	40 fps
Depth	20 mm
Dynamic Range	80
Power	55 %
Gain	80
Frequency	12 MHz
Line Density	High
Frame Average	3
Rejection	11
Image Enhancement	4
PC	Asus, Windows 7, i5 Intel Core

f) The Cadaver Material

This experiment requires a fresh, un-embalmed cadaver hand with the wrist and forearm intact. By intact, it is meant that there are no lacerations, injuries, or previous experimentation. Generally, cadaver material is embalmed in formaldehyde to preserve it for multi-use purposes. Unfortunately, the embalming process makes the tissue and joints highly rigid, and hence ruins the natural mobility of the fingers and hand. In such circumstances, the body donation program has some donor material that is allowed to go through rigor mortis process after the donor is deceased, and is then frozen-fresh, and remains frozen until required for experiment. Prior to arrival at the University of British Columbia Life Science laboratory, the hands were thawed. The use of fresh-frozen hand cadaver material is highly time sensitive, since fresh material with decompose to various levels within 12 – 72 hours.

6.2.3. Experiment Protocol

Upon arrival at the University of British Columbia Life Science laboratory, the hardware described in Section 6.2.2 is set-up onto a table. The cadaver hand is prepared by the usual protocol, which involves thawing and removal from the body. The hand is then dissected by Kurt McBurney, an Instructor an Anatomist from the University of Victoria. He dissected the hand in order to expose the middle finger's FDS tendon, as well as the opposing extensor tendon and the bone-clamping locations. The extensor tendon is attached to a tendon coupler, which in turn is connected to the string-pulley-weight system. The flexor tendon is attached to the larger tendon coupler, which is fixed to the x-stage actuation system. The hand metacarpal, radius and ulna bones are then clamped to their respective vice assemblies, which are fixed to ground. The transducer assembly is set up and adjusted for optimal placement.

Before collecting any data, the transducer must be properly positioned so that the images contain the displacing tendon. Optimal positioning of the transducer is done by actuating the tendon and viewing the images for quality. Once the proper position of the transducer is established, the tendon is actuated with a peak velocity of 15 mm/s and with a total displacement of 15 mm. For this motion profile, the x-stage actuates the tendon back and forth seven times, creating a seven-cycle motion profile (Fig. 37). The B-Scan image sequence is saved as an .avi file for later retrieval. At a later date, the data in .avi format is imported into Matlab (MathWorks, USA). The SAD speckle tracking algorithm described by Eqn. {3} in Chapter 5, is then developed using the obtained cine-loop libraries containing the collected B-Scan tendon data. The speckle tracking algorithm developed using the data from this experiment employs the SAD similarity measure with the stationary searching region, along with the parameters shown in Table 4. The template tracking location on the tendon is chosen by reviewing several cine-loops and visually determining an optimal placement. The interframe displacement is estimated using Eqn. {3}, and then added cumulatively to create a displacement versus time curve, in units of mm. This is achieved by converting the estimated displacement in units of pixels, into mm by using a conversion factor. The conversion factor is a function of the lateral and axial resolution as well as the compression of the B-Scan images into an .avi file. Using the same machine settings in Table 3, the conversion factor between pixels and mm is found by placing a known object (a 4-pin connector) in between gel pads (Aquaflex, Cone Instruments), and collecting B-Scan images (Fig. 38).

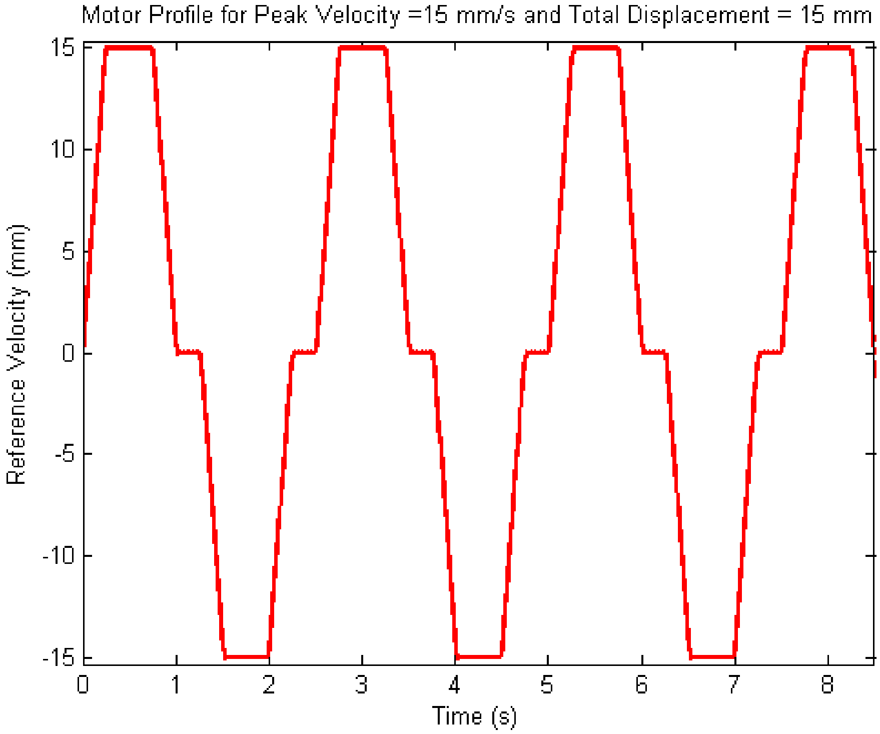

Figure 37: Sample motor profile, for peak velocity = 15 mm/s and total displacement = 15 mm. As illustrated, the positive profile refers to when the tendon excursion is in flexion, followed by a 0.25 second wait time, then the negative profile occurs when the tendon is in extension. This is repeated, creating four flexions and three extensions.

TABLE 4: PARAMETERS USED FOR SPECKLE TRACKING

Property	**Value**
Similarity Measure	SAD
Searching Technique	Stationary search
Template Size	(x by z) =30 by 15 pixels
ROI Size	(x by z)= 70 by 26 pixels
Template Location	(x_1,z_1) =(555,124)
Resolution Conversion Factor	0.03825 mm/pixel (axial and lateral)

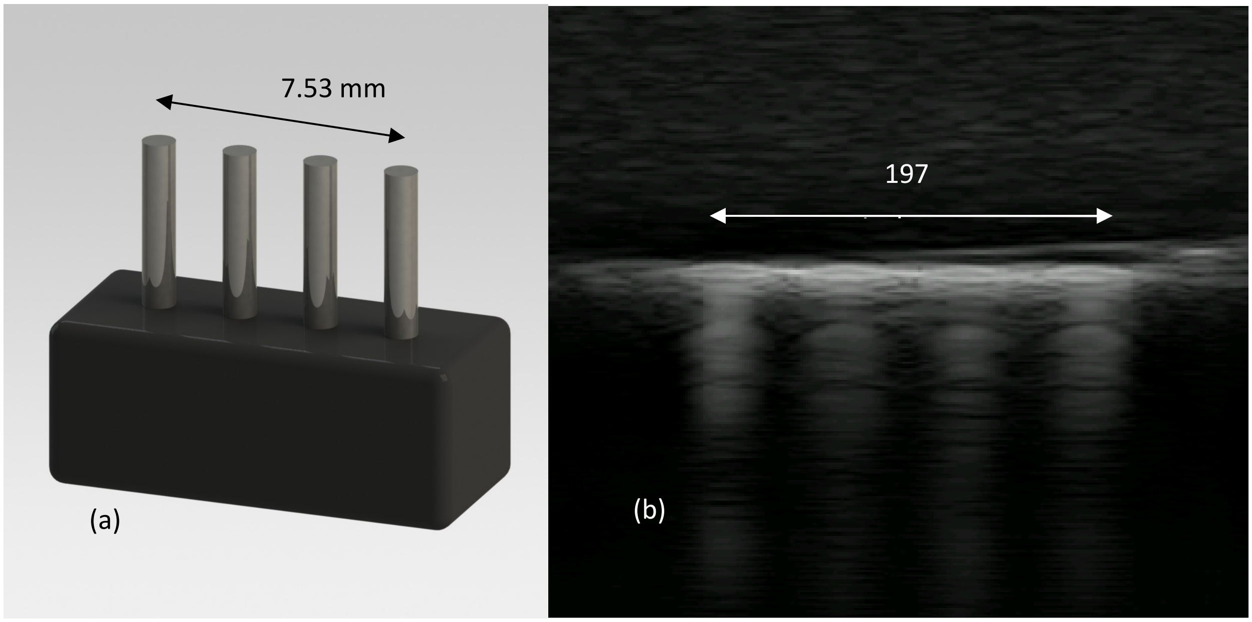

Figure 38: A calibrating 4-pin connector is used to determine the mm/pixel conversion factor. (a) the physical length is 7.53 mm, and (b) the B-Scan image showing the same measurement is 197 pixels, thus giving a conversion factor of 0.03825 mm/pixel.

6.3. EXPERIMENT 2: HUMAN-BASED STUDY TO ESTIMATE SINGLE TENDON EXCURSION

6.3.1. Introduction

The aim of this experiment is to further develop the proposed ultrasound-based method of estimating the instantaneous and total displacement of a single tendon. This experiment uses human volunteer patients, during their regularly scheduled carpal tunnel surgeries. The ultrasound-based tendon motion estimation is directly compared with the actual tendon displacement in the hand, since the volunteer's tendons are surgically exposed in the open palm. By video recording the motion of the exposed flexor tendons, commercial video tracking software can be used in order to provide the standard reference displacement. In this way, the experimental set-up provides a direct displacement comparison in the most realistic anatomic setting, in contrast to other work which uses simulations and phantoms. This study underwent a full ethics review from both the Vancouver Island Health Authority and the University of Victoria Research Ethics Board (Ethics No. C2012-27). Patients who were pre-scheduled for carpal tunnel release surgery at Royal Jubilee Hospital were recruited and individually signed consent forms for this study weeks in advance of the data collection period. The patient volunteers consisted of six patients: four females and two males, all requiring carpal tunnel release in their hands. They are otherwise healthy individuals with relatively normal tendon displacement. Only the data from two of the females and one of the males are used for this study. One female patient did not want to participate. In another instance, the reference from a female data set did not record, and cannot be used. Also, one of the male's flexed with a very fast rate of speed and the resulting B-Scan cine loops are not of high quality.

Using the same LogicScan ultrasound system described in Experiment 1, B-Scan images are collected with the 12-MHz transducer placed proximal to the wrist. Using this image sequence data of the moving tendon, the speckle-based tracking algorithms described in Chapter 5 are investigated, using FT, SAD and SSD as similarity measures. The previously described stationary searching technique is employed in order to minimize temporal drift errors. As well, a subset of data obtained from this experiment is also used to demonstrate the importance of parameter selection, as described in Chapter 5, Sections 5.5.1 – 5.5.4. The parameters investigated are: (a) additional similarity measures (NCC and the two hybrid metrics described in Chapter 5), (b) searching without a stationary ROI, (c) hierarchical search, (d) template location, (e) template and ROI size, and (f) frame rate (temporal resolution). The effect of frame skipping (Section 5.5.5) is discussed in Chapter 7.

6.3.2. Set-Up

(a) Equipment

The LogicScan ultrasound machine previously described in Experiment 1 is used to acquire consecutive B-scan images of the moving middle finger's FDS tendon. The ultrasound machine settings used for data collection, are listed in Table 5. For this experiment, a different laptop is used which cannot acquire images at a high frame rate, even though it has the same specifications as the one used in Experiment 1. In order to minimize computational load, the frame averaging is turned off, thus improving the frame rate to 20 fps. All other settings as used in Experiment 1, are used for this experiment. The consecutive image frames are saved as a cine loop in an uncompressed (.avi) format, to improve the lateral resolution for speckle tracking. This is because the compression affects the mm-to-pixel conversion factor, as described in Experiment 1. The microscope video camera (Karl Zeiss OPMIO 700, Jena, Germany) is installed equipment in the hospital operating room, and acquired video frames at 59 fps, which are saved directly to the .mp4 format with an image size of 1920 × 1080 pixels.

TABLE 5: SETTINGS ON THE LOGICSCAN ULTRASOUND SYSTEM

Property	Value
Frame Rate	20 fps
Depth	20 mm
Dynamic Range	80
Power	55 %
Gain	80
Frequency	12 MHz
Line Density	High
Frame Average	0
Rejection	11
Image Enhancement	4
PC	Asus, Windows 7, i5 Intel Core

(b) Preparation of patients and sites

Before the experiment, the patient is prepared for the carpal tunnel surgery in the hospital operating room (OR). The preparations include disinfection of the surgical site on the patient, intravenous anesthetic and local anesthetic. During preparation, the patient is lying on her or his back, with their arm extended on a platform, with the hand palmer side up, as illustrated in Fig. 39. During these preparations, the data collection process is explained to the patient, which includes the verbal command to flex and extend the middle finger. The verbal commands are practiced with the patient along with the flexion/extension speed, for about 1 to 2 minutes. The FDS tendon is then located within the arm by placing the ultrasound sensor proximal to the patient's wrist. The patient is then asked to flex and extend as he or she had done previously, while the ultrasound screen is monitored to find an optimal placement position for the transducer. This location is marked with ink. This procedure is done just before surgery in order to: (i) explain our process to patients, (ii) train them before they are heavily anesthetized, and (iii) minimize the time needed to explain procedures once the surgical site in the palm is opened. Next, the microscope video camera is positioned over the surgical site by the OR nurse (Fig. 39), and the video recording is started.

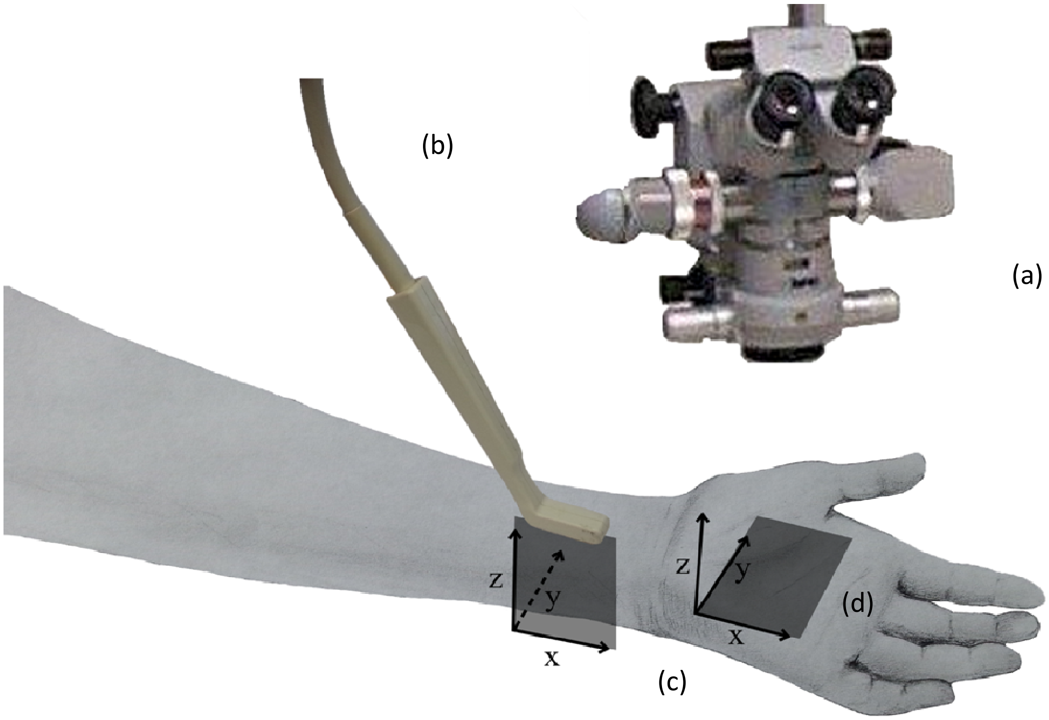

Figure 39: Equipment setup. (a) Microscope video reference. (b) Ultrasound transducer. (c) ***xz*** **field-of-view plane of the ultrasound transducer. (d)** ***xy*** **field-of-view plane of the microscope video reference.**

Next, a surgical screen is implemented by OR nurses to separate the ultrasound sensor site proximal to the wrist from the open surgical site in the palm (Fig. 40, label b). The surgeon, Dr. Slobodan Djurickovic, then begins the carpal tunnel surgery by making an incision in the palm on the hand and exposing the middle finger's FDS tendon with the aid of self-retaining retractors. The surgeon then places three ink dots on the tendon and dots on the surrounding stationary tissue (Fig. 40, label c). Next, the surgeon places a sterile ruler alongside the tendon, which is recorded in the microscope video data. The ruler is later used to obtain the correct dimensional scale of the tendon displacement in the video, as described in the next section.

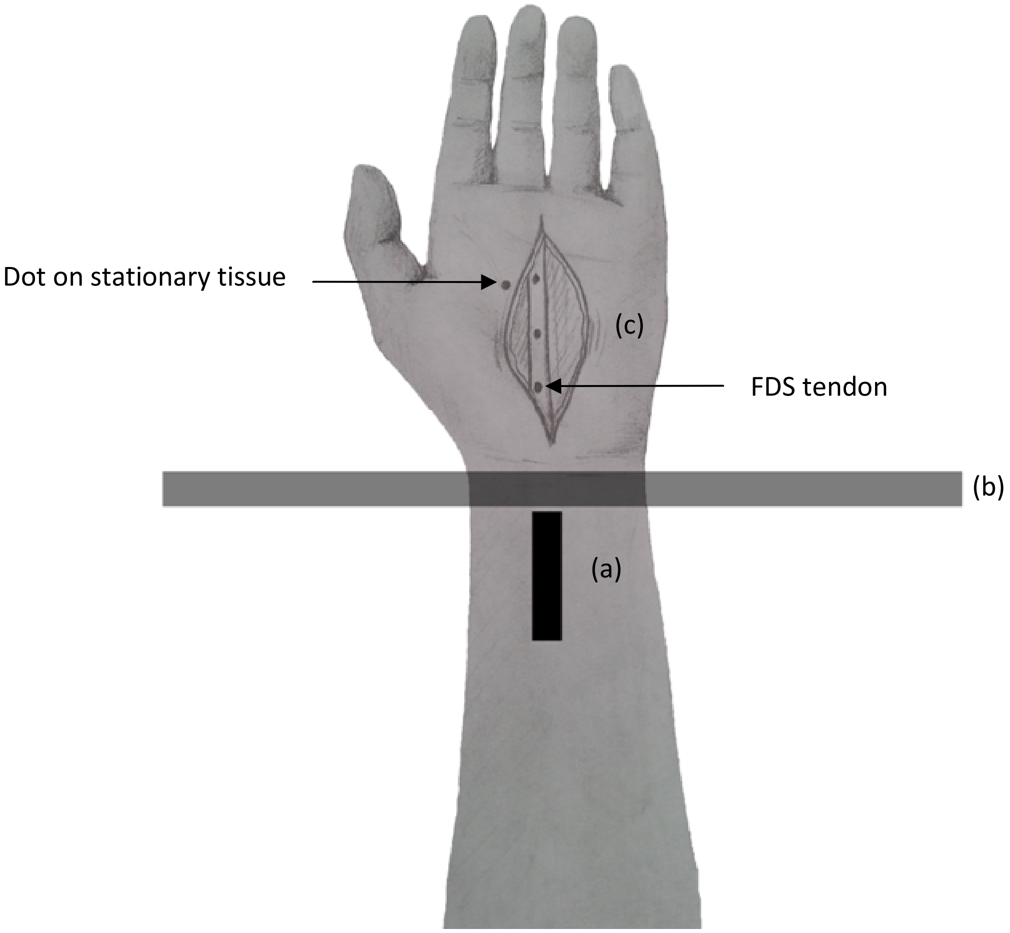

Figure 40: Palmer view of the hand. (a) Ultrasound transducer location. (b) Surgical screen location. (c) Incision area, in which is the exposed flexor digitorum superficialis (fds) tendon with three marker dots. An additional marker dot is placed on adjacent stationary tissue.

6.3.3. Experiment Protocol

(a) Patient instruction

Although patient is heavily sedated, she or he can follow simple commands such as “close” and “open” when instructed to do so, at approximately the speeds practiced earlier. Next, the ultrasound transducer is placed onto the ink-marked location that was determined in the previous section. The patient is then instructed to “open” and “close” (flex and extend) the finger, to assess if the ultrasound transducer is placed in the correct location.

(b) Data collection and processing

On verbal command, the patient is asked to flex and extend the middle finger five times, hence displacing the middle FDS tendon five times in both directions. The flexion/extension data set only contains five excursions (flexion/extension) for each patient, due to the short window of opportunity for data collection. Once the patient finishes the required flexions and extensions, the ultrasound transducer is removed and the microscope video recording is stopped and saved onto USB memory. The ultrasound data is also saved as an uncompressed .avi file. This data collection process is repeated for all patients who volunteered for this study. Off-line at a later date, the ultrasound .avi files are imported into Matlab for analysis. Each patient's ultrasound data set is processed by the SAD (Eqn. {3}, c=1), SSD (Eqn. {3}, c=2) and FT (Eqn. {25}) speckle tracking algorithms. The tendon's flexion and extension on the microscope video files are imported into Kinovea software (Version 0.8.15), which is used to track the ink dots on the exposed tendons. Additionally, a sample set of microscope videos are manually tracked to verify Kinovea tracking. To validate the ultrasound speckle tracking technique, the displacements estimated by speckle tracking are compared with the displacements given by the microscope video. To accomplish this, the millimeter-to-pixel conversion factors for both the ultrasound data and microscope video data are calculated. For the ultrasound data, this is accomplished by placing the 3-pin connector of known dimensions, as shown in Fig. 41, between gel pads and acquiring B-scan images using the same settings which are used in the patient trials. The millimeter/pixel conversion factor for the microscope video is determined by analyzing video frames that contained the ruler that was placed by the surgeon alongside the tendon in the palm. Additionally, there were times when the microscope's video appeared to be shaking. This was due to either actual microscope camera motion, or to patients' slightly rotating their wrists. Either way, this extra unwanted motion is accounted for, by tracking the displacement of a known stationary point on the hand (Fig. 40, label c) and subtracting that motion from the tracked tendon displacement. The parameter settings for speckle tracking as well as the video reference are listed in Table 6.

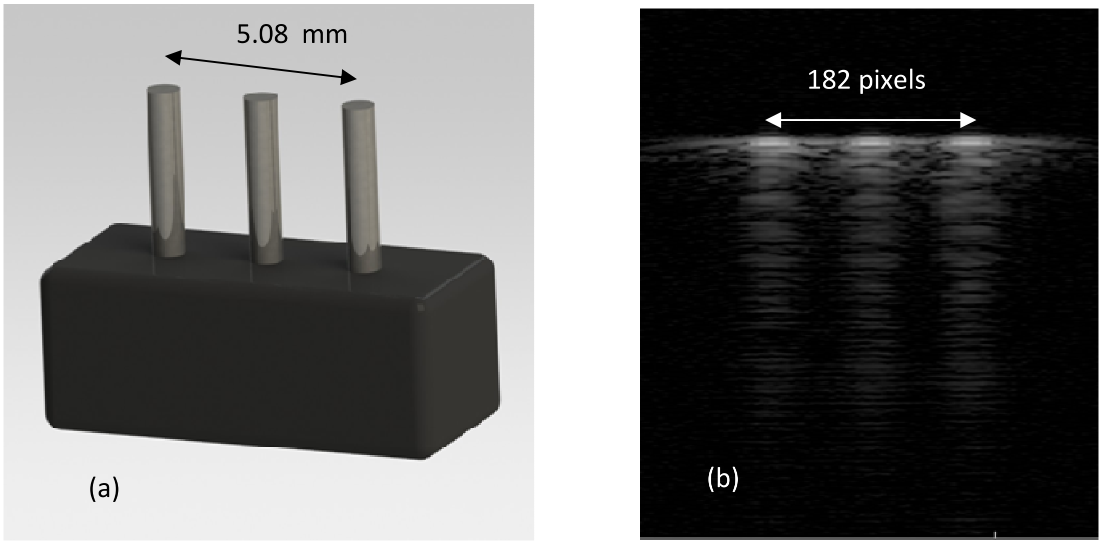

Figure 41: A calibrating 3-pin connector is used to determine the mm/pixel conversion factor. (a) the physical length is 5.08 mm, and (b) the B-Scan image showing the same measurement is 182 pixels, thus giving 0.0279 mm/pixel.

TABLE 6: PARAMETERS USED FOR SPECKLE TRACKING

Property	**Value**
Similarity Measure	SAD, SSD, FT
Searching Technique	Stationary search
Template Size (*x by z*)	20 by 20 pixels
ROI Size (*x by z*)	Patient 1: 75 by 20 pixels Patient 2: 75 by 30 pixels Patient 3: 50 by 20 pixels
Template Location (x_1,z_1)	Patient 1: 787, 281 Patient 2: 675,160 Patient 3: 458, 259
Resolution Conversion Factor (lateral and axial)	
B-Scan	0.0279 mm/pixel
Video Reference	Patient 1: 0.0336 mm/pixel Patient 2: 0.0367 mm/pixel Patient 3: 0.1830 mm/pixel

(c) Determining optimal parameter settings for speckle tracking

As outlined in Chapter 5, the choice of parameters used for speckle tracking can greatly affect the tracking accuracy and computational load, and should be considered in detail. Using a sub-set of data from Experiment 2, a parameter investigation study has been done in this thesis, to study the effect of changing the parameters to optimize the speckle tracking algorithms. The parameters investigated are: (a) additional similarity measures, (b) searching without a stationary ROI, (c) hierarchical search, (d) template location, (e) template and ROI size, and (f) frame rate (temporal resolution).

This optimal parameter study makes use of a sub-set of data from this experiment, along with the FT, NCC and two hybrid similarity measures outlined in Chapter 5. The FT similarity measure is used for comparison, since it performed well for previous data sets. The sub-set of data used in this study are the first patient's 1st, 2nd and 6th flexion, and the second patient's 2nd flexion. Patient 1's flexions are considered ideal, where the ideal flexions consist of motion data in which the patients flexed their finger with slow to moderate speed, in a smooth trajectory. By this definition, patient 2's flexion is considered non-ideal, resulting from high flexion speed, coupled with a low frame rate of the ultrasound machine.

For Part-1 of the parameter study, parameter (a) is investigated. The results of the different similarity measures (FT, NCC and the two hybrid measures) are evaluated for tracking accuracy, computational load, and robustness by comparing the difference in total displacement to the actual displacement. Additionally, the parameters for template size, ROI size, stationary search method, location and resolution conversion from Table 6 are used.

For Part-2 of the parameter study, all four similarity measures from Part-1 are used to demonstrate the effect of changing the algorithm parameters. The parameters include: searching strategy ((b)searching without a stationary ROI, and (c) hierarchical search), (d) template location, (e) template and ROI size, and (f) the frame rate. These parameters are individually applied to an ideal data set from Part-1 (patient 1, flexion 2), in order to demonstrate the direct effect of each change.

For (b), the searching strategy which uses a non-stationary ROI is investigated. The parameters in Table 6 for the template location, template size, ROI size, and resolution, are used.

For (c), hierarchical search strategy is investigated. The hierarchical search makes use of a template and ROI that change size from coarse-to-fine. In the first iteration to determine interframe displacement, a larger (*24 by 24 pixels*) template is used and the match is found in the next frame, as before. In the second iteration, the template size is reduced by half (*12 by 12 pixels*), and the new match to this smaller template is found within an ROI centered on the previous match. In the third iteration, the template is again reduced in size by half (*6 by 6 pixels)* and the new match is found within an ROI centered the previous match. The ROI is also decreased with each iteration; from *54 by 32 pixels* for the first iteration, to *32 by 32 pixels* for the second iteration, and then to *26 by 26 pixels* for the last iteration. The other parameters are the same as in Part-1.

For (d), the effect of changing the template's location is investigated. The template locations investigated are: $(x_1,z_1)=$ *(658,232), (787,281), (415,315), (1007,29*1).

For (e), the effect of changing the template and ROI size is investigated. A smaller template (*10 by 10 pixels*) and a larger template (*30 by 30 pixels*) size are used. The ROI size and other parameters are the same as in Part-1. Also for (e), the ROI sizes of *40 by 35,* and *80 by 35* are investigated, while keeping the template size and location the same as in Part-1.

For (f), the effect of low frame rate on the displacement estimate is investigated by lowering the frame rate to 10 fps, in comparison to the reference. (This is the same as frame skipping by *k=2*). The ROI in this section is increased to *90 by 32 pixels*, because a smaller ROI would not catch the larger interframe displacements. All other parameters are the same as in Part-1.

6.4. EXPERIMENT 3: CADAVER-BASED STUDY TO ESTIMATE SINGLE TENDON EXCURSION

6.4.1. Introduction

Experiment 3 is based on the earlier preliminary experimentation (Experiment 1) in which a linear array collects sequential B-Scan images of a singular moving cadaver tendon. Based on previous knowledge from Experiment 2, the speckle tracking algorithms are further developed to improve interframe and total displacement estimations. As well, the ultrasound hardware is upgraded to a higher resolution research-based system. Also, this experiment used improved hardware that couples to and actuates the tendon, thus providing an improved standard reference.

Experiment 3 is the first part of a four-day data-collection period, in which tendon excursion data is collected from two cadaver hands. This study has been approved by the Dept. of Cellular & Physiological Sciences, Body Donation Program, Life Sciences Centre at the University of British Columbia, (approval #: W0196).

6.4.2. Set-Up

The design of this hardware set-up is inspired by that used in Experiment 1; however, it differs in a number of ways. The Experiment 3 hardware consists of: (a) a multi-tendon actuation system, (b) tendon couplers, and (c) a cadaver stabilization system, as shown in Fig. 42. Other components not shown in Fig. 42 include a computer, the controller and stepper motor drivers, and an Ultrasonix Touch ultrasound machine with a 10 MHz linear array, mounted within the custom transducer holder from Fig. 36. As with previous experiments, the importance of the actuation system is to provide a standard reference of known motion (produced by the precise motion of the motors), against which the estimated displacements given by the speckle tracking technique can be compared. The actuation system is comprised of three linear actuators, which each consist of a stepper motor with an integrated lead-screw that creates precise linear displacement. The motors are connected to motor drivers, which connect them to a controller, which is in turn connected to the computer. A given motor is programmed to displace by a known amount, with a known motion profile. As the motor turns, the linear actuator displaces with a known motion profile, thus providing the standard reference. A tendon coupler is attached to the end of the linear actuator, therefore making tendon actuation possible. The ultrasound transducer and the cadaver hand are separately fixed and grounded to a main board, where the main board is clamped to a general purpose laboratory table. The transducer is placed on the cadaver wrist area with coupling gel, overtop of a finger's FDS tendon on intact skin. The ultrasound system will record tendon displacement through a sequence of B-Scan frames, and where the frames are stored as an array of integer values in proprietary .b8 format. A further description into the apparatus components are as follows:

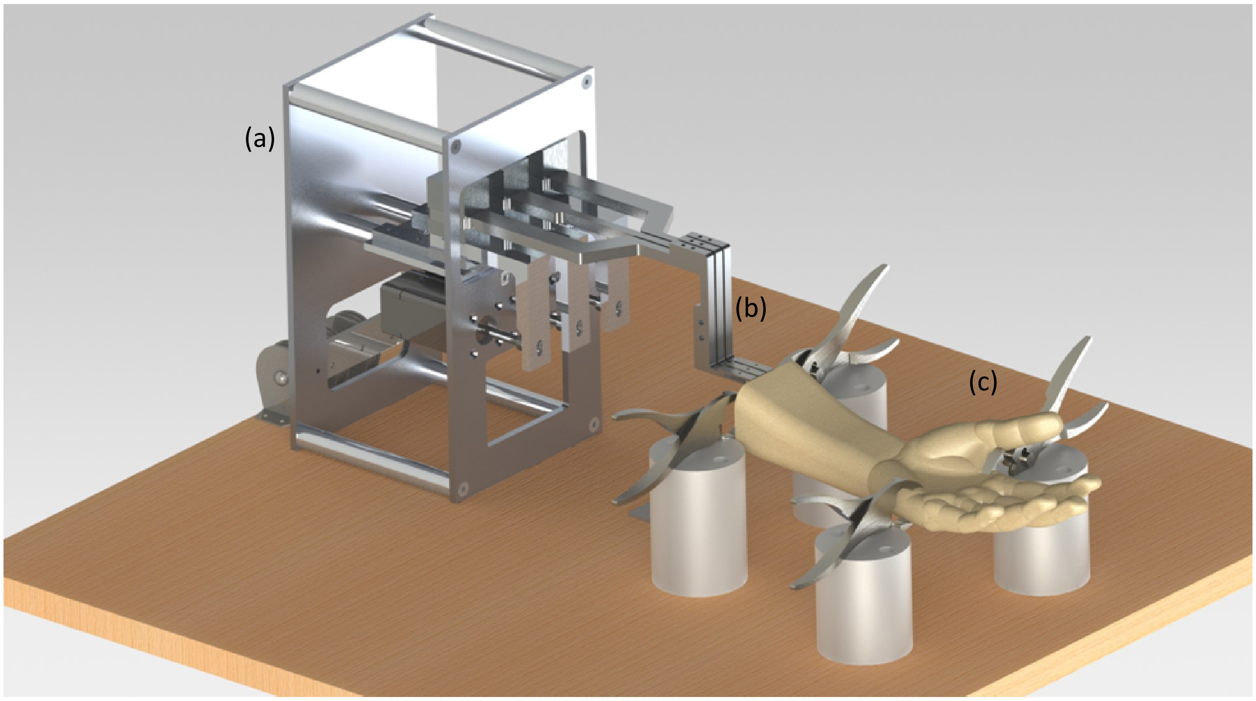

Figure 42: The hardware for Experiment 3 is comprised of: (a) a multi-tendon actuation system, (b) tendon couplers, and (c) a hand stabilization system. Other components not shown here include a computer, a custom electronics box containing the Galil controller and drivers, an Ultrasonix Touch ultrasound machine, and the 14 MHz linear array within the transducer holder.

a) Actuation System

As shown in Fig. 42 label (a), and Fig. 43, the actuation system is comprised of three linear stepper motors (model DRL42BP2-04MG, Oriental Motor USA Corp.), which individually displace three linear guides (RSR9WZMUU+110LM, THK), thus allowing for multiple-tendon actuation. For the first hand used in this experiment, motors A, B and C are attached to the index, middle and ring finger's tendon couplers, respectively. For the second hand used in this experiment, motors A, B and C are attached to the ring, middle and index finger's tendon couplers, respectively. As a given stepper motor turns, the linear guide displaces with a programmed motion profile using a Galil controller (DMC-21x3, Galil, USA) and three motor drivers (model CRD5107P, Oriental Motor USA Corp.), which are interfaced to a computer. This system constitutes the standard reference, whereby the programmed motion profile gives the known value of displacement, velocity and acceleration.

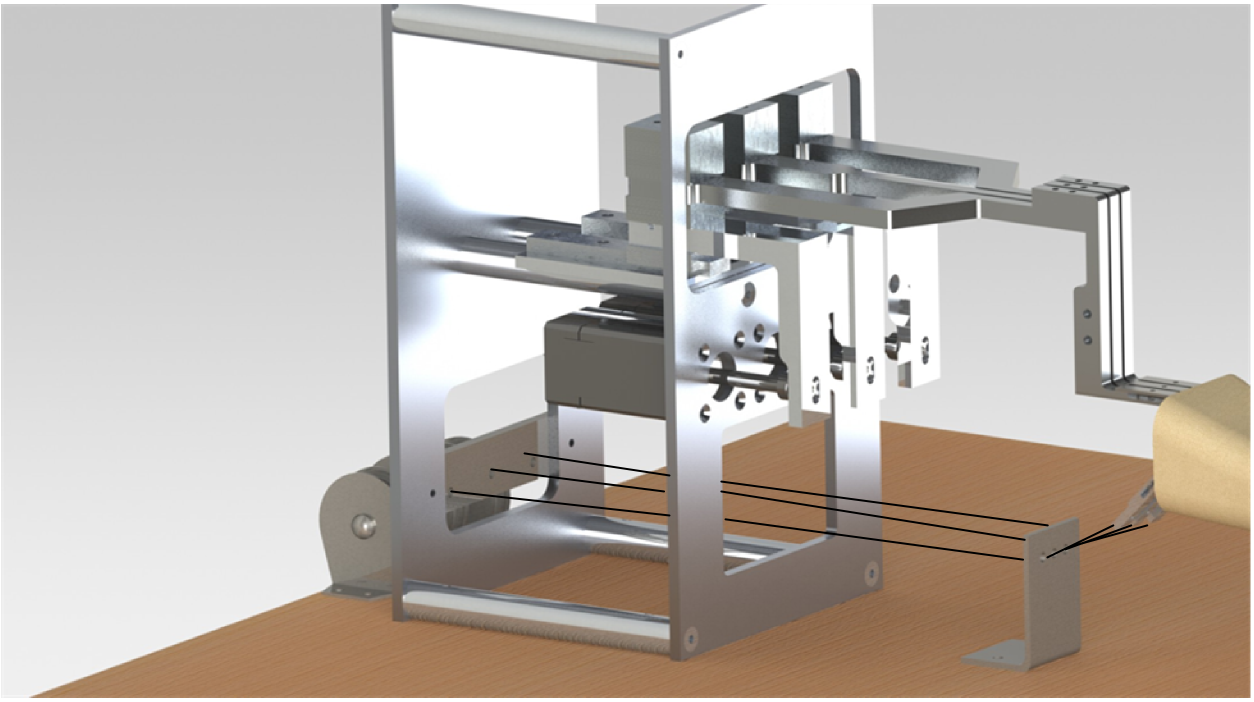

Figure 43: A close up view of the actuation system. Each motor is connected to a tendon coupling system in order to have individual actuation of a tendon. This system allows for individual actuation of the index, middle and ring fingers.

b) Tendon Coupler

The tendon coupling system previously described in Experiment 1 is further developed into a more compact and accurate system. Each coupler is designed as a pinch mechanism, which is comprised of two plates, each lined with a rough course-grit grip tape. The two plates sandwich the tendon (Fig. 42 label (b), and Fig. 44 label (a)), by means of a screw passing through the top plate and threaded into the lower plate. Although it's based on the previous design used in Experiment 1, the new developments include using aluminum and steel as an upgraded material. The flexor tendon coupler is attached to a bracket piece, which is connected to a linear actuator. The bracket piece is adjustable in height, thus allowing the coupler to be aligned with the tendon major axis, in a horizontal orientation. A total of three flexor couplers are used, one for each tendon, which are individually actuated by a separate linear motor.

After the flexor tendon is actuated in flexion, it must be returned to its initial position. This return motion is achieved by means of a counter-weight attached to the corresponding extensor tendon (Fig. 43). A smaller tendon coupler is designed for the extensor tendons, which attaches the extensor tendon to a string-pulley-weight system (Fig. 44 label (b)). It was determined that a 200 g weight provides sufficient tension so that the finger (and flexor tendon) can safely return to its natural position, without excessive force on the extensor tendon. A total of three extensor couplers are used, one for each extensor tendon.

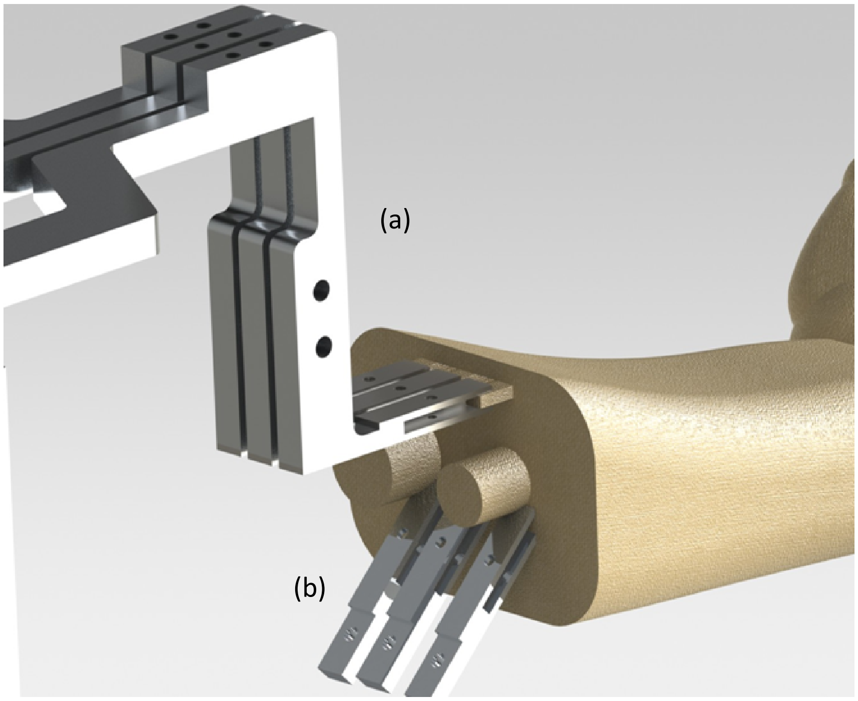

Figure 44: Each tendon coupler is comprised of a 1/16" thick aluminum plate (bottom) and steel plate (top) lined with a coarse-grit tape material. The tendon is sandwiched between these two grip lined plates, by means of a #4-40 bolt. The flexor coupling system is shown by label (a), and the extensor coupling system is shown by label (b).

c) Stabilizing the Cadaver Hand and Transducer

The cadaver hand must be rigidly secured to the main board (ground) via the stabilization clamps, in order to collect useful tendon displacement data. The same vice-clamp assembly used in Experiment 1 is used for this experiment. This system is comprised of off-the-shelf vice clamps, which have been altered to attach them to riser blocks, to keep the hand elevated above the main board, as illustrated in Fig. 42 label (c). The four vice-clamps attach to the metacarpal, radius and ulna bones. Small incisions are made in the hand so that the clamp tips can easily be inserted and grip the bones at these locations. As well, the same transducer holder used in Experiment 1 is also used in this experiment.

d) *The Ultrasound System*

An improved ultrasound system is used for Experiment 3, which is the Sonix Touch system with a research interface, (produced by Ultrasonix Medical Corp., Richmond, BC, Canada). The system employs a 128-element, linear array transducer operating at 10 MHz. This system transmits and receives the soundwaves with user specified parameters, and allows for several modes of data to be saved. For this thesis, the compressed B-Scan images are saved as an array of integer values, and exported to Matlab at a later time. The ultrasound settings are found in Table 7.

TABLE 7: SETTINGS ON THE ULTRASONIX ULTRASOUND SYSTEM

Property	Value
Frame Rate	86 fps
Depth	25mm
Dynamic Range	60
Gain	45
Frequency	10 MHz

e) *The Cadaver Material*

Similar to Experiment 1, the cadaver material was a fresh, un-embalmed cadaver with the forearm intact. This way, the tissue and joints remain pliable for use with the actuation hardware. For Experiments 3-5, two hands are used. They are from the same donor, and are male in gender. It is observed that the second hand is not of the same quality as the first hand. Specifically, the index finger's tendon was accidently severed within the wrist canal. It was however, suspected to be due from a previous trauma as there was a visible incision scar on the skin's surface at that location. As well, the index finger tendon was manually handled with a light force when it broke off, indicating a prior issue.

6.4.3. Protocol

Experiment 3 is part of a four-day data-collection period, in which tendon excursion data is collected from two fresh-thawed cadaver hands. Experiments 4 and 5 which are discussed in Sections 6.5 and 6.6 also make use of the data collected in this four-day period. Upon arrival to the University of British Columbia Life Sciences laboratory, on the first day the hardware described in Section 6.4.2 is set-up onto a general purpose laboratory table. The tendon coupler assembly is test fit to a static silicone hand using a mock set-up. As well, the Galil controller and actuation system are tested by running selected actuation sequences. On the second day of the experiment, both cadaver hands are prepared by the usual protocol, which involves thawing and removal from the body. The hands are then dissected by Kurt McBurney, an Instructor and Anatomist from the University of Victoria. He dissected the hand in order to expose the index, middle and ring fingers' FDS tendons, as well as the opposing extensor tendons, and the bone-clamping locations. Both cadaver hands used in this experiment are male in gender, and are from the same donor. The first hand is used on the second day, while the second hand is placed into refrigeration for the third day.

When using the first hand, the following procedure is used to attach the actuator apparatus to the hand. First the extensor tendons are individually attached to their respective tendon couplers, which in turn are connected to their respective string-pulley-weight systems. Next, the hand is positioned appropriately and clamped with the vice-clamps onto the metacarpal, radius and ulna bones. Next, the riser-blocks are screwed securely to the main board, hence fixing the hand to ground. Then, the flexor tendons are individually attached to their tendon coupler and brackets, which are fixed to their respective linear actuation-motor systems. Finally, the transducer holder assembly, with the transducer held within, is positioned over the wrist and adjusted for the desired tendon to be imaged.

Prior to collecting data, the transducer position is fine-tuned for good image quality of the tendon in motion while it displaces. This is accomplished by first placing the transducer on top of the middle finger's tendon, proximal to the wrist, over coupling gel, on intact skin. Optimal positioning of the transducer is done by actuating the middle finger's tendon by motor B, and viewing the onscreen B-Scan images for quality. Once the proper position of the transducer over the middle finger's tendon is established, the transducer assembly is clamped to ground. Next, the tendon is actuated with peak velocities of 15 mm/s and 10 mm/s, with total displacements of 15 mm and 10 mm, respectively. For a given reference peak velocity and total displacement, the linear actuator displaces the tendon back and forth two times, creating a two-cycle motion profile (Fig. 45). The B-Scan image sequence is saved as an array of integer values for each frame (the proprietary .b8 format) for later retrieval. This process repeated for each reference peak velocity and total displacement combination for the middle finger's tendon. This entire process is repeated for imaging the tendon of the index finger, by moving the transducer over top of the index finger's tendon, and then actuating this tendon using motor A, in order to collect the displacement data. Likewise, this entire process is again repeated on the ring finger's tendon by using motor C. The motion profiles for all tendons can be found in Table 8.

TABLE 8: MOTION PROFILES FOR ACTUATING SINGULAR TENDONS

Tendon	Programmed Peak Velocity (mm/s)	Programmed Total Displacement (mm)
index	15	15
	10	10
middle	15	15
	10	10
ring	15	15
	10	10

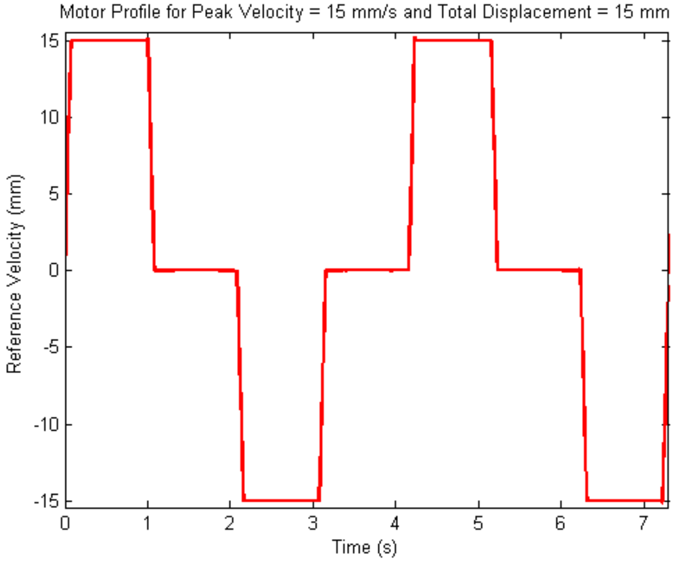

Figure 45: Sample motor profile, for peak velocity = 15 mm/s and total displacement = 15 mm. As illustrated, the positive profile refers to when the tendon excursion is in flexion, followed by a 1.0 second wait time, then the negative profile occurs when the tendon is in extension. This is repeated, creating two flexions and two extensions.

On the third day of data collection, the second hand is removed from refrigeration, and is then attached to the tendon coupler hardware as previously described. Due from the severed index finger's tendon and time constraints, only the middle finger's tendon displacement data is collected, using the motion profiles with peak velocities of 15 mm/s and 10 mm/s and total displacement 15 mm and 10 mm, respectively. At a later date, the data for a given tendon is imported into Matlab, using a custom script that reads .b8 files. In order to validate the proposed multi-tendon detection and displacement estimations, the data is processed as follows:

(a) Auto-location

As outlined in Section 5.4, a suitable value for the location (x_1,z_1) of the template is automated. The auto-location technique used in this thesis, estimates the total displacement at many locations in a sequence of image frames to create a displacement field. Using the parameters in Table 9, a displacement field for a given motion profile is estimated at many points along the tendon, using SAD, FT and NCC as similarity measures. The motion profiles can be found in Table 8. The location giving the largest total tendon excursion in units of mm is considered the optimal template location for subsequent data sets for a given tendon. As before, the total displacement in units of pixels is converted into mm by using a conversion factor. Using the same machine settings listed in Table 7, the conversion factor between pixels and mm is found by placing an object of known geometry (a 6-pin connector and a flatbar) in between gel pads, and collecting and importing the B-Scan data (Fig. 46).

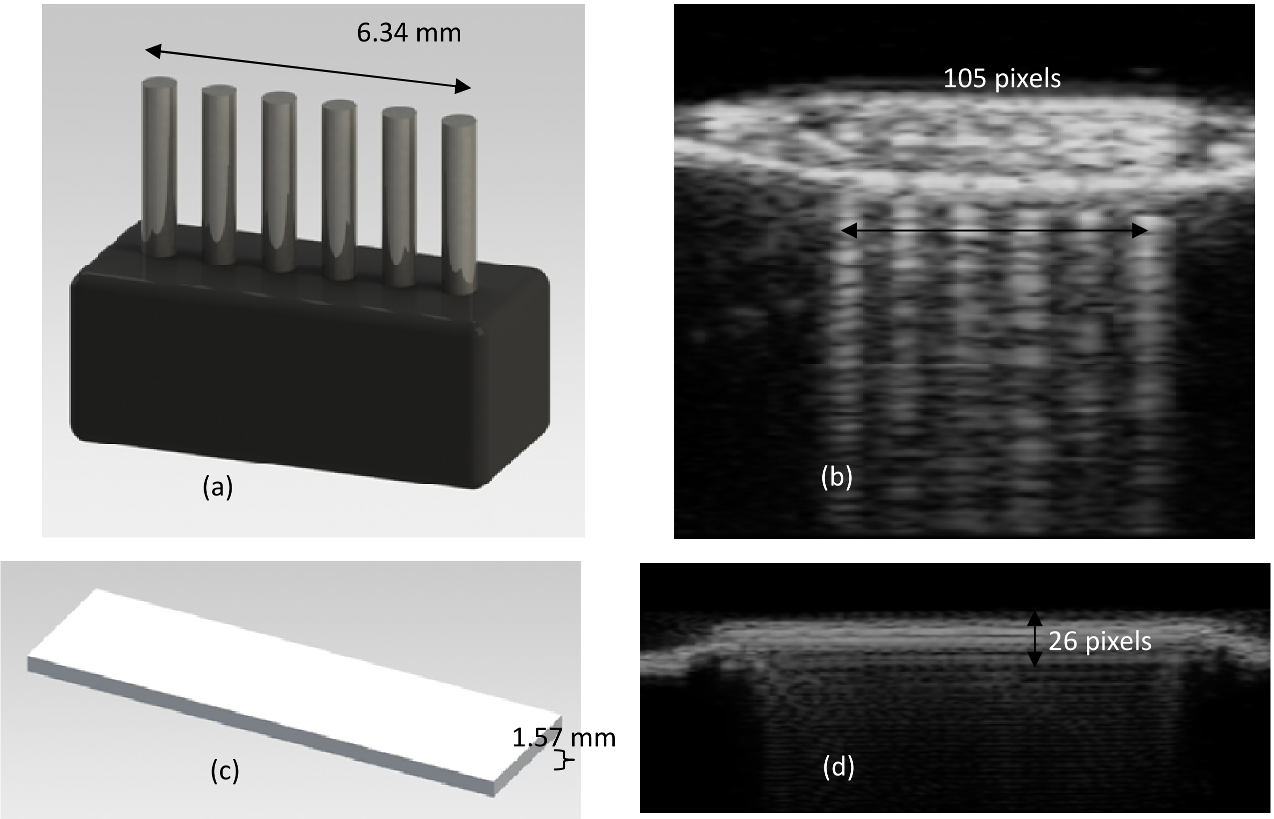

Figure 46: Illustration of objects with known geometries, for calibration of B-Scan imaging. A 6-pin connector, and a flatbar are used to determine the lateral and axial mm/pixel conversion factors, respectively. (a) the physical length of the 6-pin connector is 6.34 mm (center of pin to center of pin), and (b) the B-Scan image showing the same measurement is 105 pixels, thus giving 0.06 mm/pixel in the lateral direction. (c) The physical height of the flatbar is 1.57 mm, and (d) the B-Scan image showing the same measurement is 26 pixels, giving 0.06 mm/pixel in the axial direction.

TABLE 9: PARAMETERS USED FOR SPECKLE TRACKING

Property	**Value**
Similarity Measure	SAD, FT, NCC
Searching Technique	Stationary search
Template Size (*x by z*)	25 by 25 pixels
ROI Size (*x by z*)	45 by 37 pixels
Resolution Conversion Factor	0.06 mm/pixel
Template Locations	x ∈ [101,601] in steps of 10, and z ∈ [180,280] in steps of 2

(b) Interframe and Total Displacement Estimation

Once the optimal location of the template is found, the interframe displacement for a given tendon and reference motion profile is estimated, and then added cumulatively to create a displacement versus time curve, in units of mm. The cumulative displacement versus time curve given by the standard reference is also plotted on this graph for comparison. The estimated total displacement is obtained from this graph, and compared to the reference total displacement. This is repeated for each similarity measure used in this experiment. The auto-location part (a) and interframe and total displacement analysis in part (b) is repeated for each motion profile in Table 8.

(c) Validation of the Frame Skipping Technique

Most speckle tracking algorithms compare the template in frame *t* to the blocks in the next frame in *t+1*. Since every ultrasound imaging system is different, the resolution may not be sufficient to detect small interframe displacements. This is a function of the system's frame rate and lateral resolution, as well as the tendon's lateral displacement and velocity, as previously described. This study investigates if skipping frames can mitigate tracking issues. Frame skipping is defined as the comparison between the template in frame *t*, to the blocks in frame *t+k*, where *k* is an integer. Thus, this necessitates the development of a technique, which can determine the optimal frame skipping number, *k*. This study uses data from the first hand, and motion profiles with peak velocity of *15 and 10 mm/s*, and total displacements of *15 mm and 10 mm* (respectively). To empirically determine the optimal frame skipping constant γ from Eqn. {32}, the data from a given data set from Table 8 is reprocessed using the frame skipping numbers, *k=1,2,3,4,5*. The data is re-analyzed to determine which one has the lowest total displacement relative error, when being compared to the reference. The frame skipping number with the lowest error is chosen as the optimal frame skipping number, and then Eqns. {31} and {32} are used to estimate the average frame skipping constant, γ, which is assumed to be valid for any data set imaged by any ultrasound system. After the constant is determined, Eqn. {33} can be used for all future data sets in order to determine the frame skipping number, *k*.

6.5. EXPERIMENT 4: CADAVER-BASED STUDY TO ESTIMATE MULTI-TENDON EXCURSION

6.5.1. Introduction

The previous experiments (Experiments 1-3) form the basis of the proposed tendon tracking technique using B-Scan ultrasound of this thesis work, and are aimed at estimating singular tendon excursion. Experiment 4 extends the singular tendon tracking technique, into a multiple-tendon detection and tracking system, consisting of both novel transducer hardware and novel software. Experiment 4 is a validation step toward the goal of detecting multiple tendon displacement for prosthetic control applications. In order to detect and track multi-tendons simultaneously, a novel sparse quad-array transducer has been designed and constructed, as described in Chapter 5. To validate the new transducer, the apparatus outlined in Experiment 3 is used. Experiment 4 is part of the previously described four-day data collection period, in which a cadaver hand is used to validate the proposed technique. Experiment 4 has been approved by the Dept. of Cellular & Physiological Sciences, Body Donation Program, Life Sciences Centre at the University of British Columbia, (approval #: W0196).

6.5.2. Set-Up

The same set-up as used in Experiment 3 is also used for Experiment 4. The hardware consists of: (a) a multi-tendon actuation system, (b) tendon couplers, (c) a cadaver stabilization system, and (d) a transducer sparse array assembly, as shown in Fig. 47. Other components not shown include a computer, the controller and drivers, and an Ultrasonix Touch ultrasound machine. As with Experiment 3, the importance of the actuation system is to provide a standard reference of known motion (produced by the precise motion of the motors), against which the estimated displacements given by the speckle tracking technique can be compared. The actuation system is comprised of three linear actuators, which each consist of a stepper motor with an integrated lead-screw that creates precise linear displacement. The motors are connected to motor drivers, which connect them to a controller, which is in turn connected to the computer. A given motor is programmed to displace by a known amount, with a known motion profile. As the motor turns, the linear actuator displaces with a known motion profile, thus providing the standard reference. As before, a tendon coupler is attached to the end of the linear actuator, therefore making tendon actuation possible. The custom quad-array ultrasound transducer and the cadaver hand are separately fixed and grounded in a static position. The quad-array transducer is placed on the cadaver wrist area with coupling gel, which is centered on the middle finger's FDS tendon, overtop intact skin.

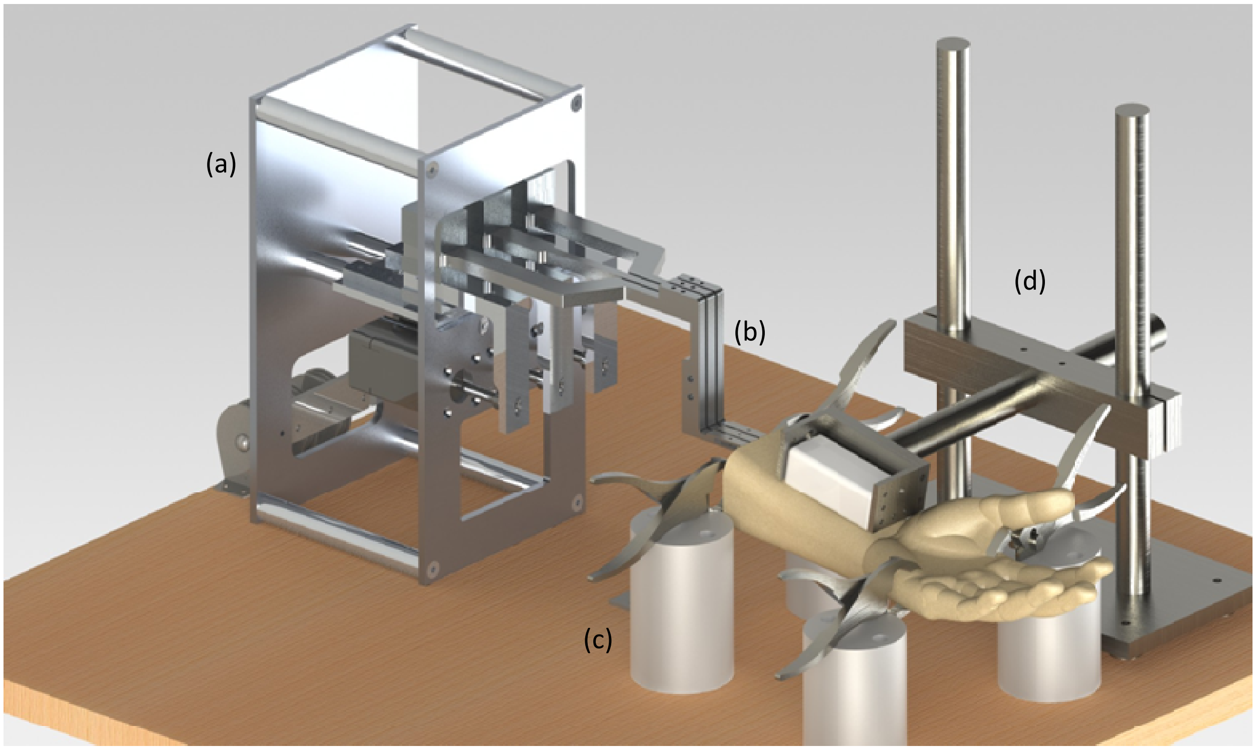

Figure 47: The hardware for Experiment 4 is comprised of: (a) a multi-tendon actuation system, (b) tendon couplers, (c) a cadaver stabilization system, and (d) the quad-array transducer and holder. Other components not shown in here includes a computer, a custom acrylic box containing the Galil controller and drivers, and the Ultrasonix Touch ultrasound machine.

The Ultrasonix Touch Research ultrasound system allows for custom software to be integrated with its internal hardware, by using a proprietary SDK kit, as described in Chapter 5. A custom software package is developed by LJB Developments and is implemented on the Sonix Touch. The custom GUI displays the four B-Scans on-screen from the four sub-arrays. As well, the focal depth, power, gain and line density can be adjusted. Ten seconds of data can be stored in RF format, and transferred into Matlab for further processing.

6.5.3. Experiment Protocol

Experiment 4 is the second part of a four-day data-collection period, in which tendon excursion data is collected from a cadaver hand. As previously described for Experiment 3, the hardware used in Experiment 4 is described in Section 6.5.2 is set-up onto a general purpose laboratory table. The same cadaver hands used in Experiment 3, are used in Experiment 4. The first hand is used on the second day of experimentation, initially for Experiment 3, and then for Experiment 4. On the third day, the second hand was used for Experiment 3, and on the fourth day the first hand is re-used to collect more data for Experiment 4. The second hand was not used for Experiment 4, due to the poor tissue quality observed on the third day with Experiment 3.

Experiment 4 directly follows after Experiment 3, and hence the hand is already set-up into position, vice-clamped, and fixed to ground. Its three flexor tendons and corresponding three extensor tendons are already attached to the tendon couplers and actuation system. The linear array transducer is removed from the setup, and the sparse quad-array transducer assembly is set up and adjusted for optimal placement, by approximately centering the middle finger's flexor tendon with the center of the quad-array. As before, the quad-array transducer must be properly positioned on the wrist, so that the four sub-arrays capture images that contain the displacing tendons. Optimal positioning of the transducer is done by placing the transducer over the middle finger's tendon, and then actuating each individual finger's tendon by its attached motor, and viewing the onscreen four B-Scan images for quality. Even though the transducer has fixed sub-array spacing, it is anticipated that the sub-arrays can capture each tendon in their field of view. Once the proper position of the transducer over the tendons is established, the motion profiles of the actuation sequences for the multi-tendon system shown in Table 10 are performed with peak velocities of 15 mm/s and 10 mm/s and with total displacements of 15 mm and 10 mm, respectively. For a given motion profile in Table 10, the linear actuator displaces the tendon back and forth two times, creating a two-cycle motion profile, as shown in Fig. 45. The data is saved as four separate RF files, one from each sub-array, for later retrieval in Matlab. This is repeated for each motion profile in Table 10. On the fourth day of data collection, this process is repeated using the same hand.

At a later date, the data for a given tendon is imported into Matlab using a custom script initially provided by LJB Development, but edited to run smoother. The custom script imports the RF file, and performs envelope-detection and logarithmic compression in order to render a sequence of B-Scan images. In order to validate the proposed multi-tendon detection and displacement estimations, the data is processed as follows:

(a) Auto-location using Sparse Quad-Array

For the A, B and C motion profiles in Table 10, a displacement field for the tendon's entire excursion for each sub-array is estimated, using SAD, FT and NCC as similarity measures. This is accomplished by using the auto-location algorithm described in Chapter 5, along with the parameters in Table 11. This way, the total displacement at many points in each sub-array can be estimated. The template sizes used for processing data are smaller for this experiment, in comparison to the linear array based experiments, due to the smaller field of view when using the quad-array. Using a given similarity measure, the optimal template location for subsequent tracking data sets can be determined by the location of the maximum total displacement in each sub-array. As before, the total displacement in units of pixels is converted into mm by using a conversion factor. Using the settings as listed in Table 11 for the ultrasound machine, the conversion factor between pixels and mm is found by placing a known object (a 6-pin connector and flatbar) in between gel pads, and collecting and importing the RF data to Matlab to be rendered as a B-Scan (Fig. 48).

The optimal template locations from the individual fingers determined above are used as the locations on the multi-tendon excursion data. In this sense, the individual tendon locations are first used as calibrations, in order to auto-locate the tendons in any subsequent data containing multiple tendon motion. Thus, the above described process for separately auto-locating the index, middle and ring fingers from their tendon displacement fields can be used as a calibration for multi-tendon excursion. For illustrative purposes, displacement fields are created from the data of each sub-array, for a given multi-tendon motion profile in Table 10, using each similarity measure. These displacement fields are not used to auto-locate the index, middle and ring fingers. This is because multiple tendons are moving at the same time, thus it doesn't make sense to auto-locate on all this data simultaneously.

(b) Interframe and total displacement using Sparse Quad-Array

Once the optimal location of the template is found, the interframe displacement for a given reference motion profile is estimated at the locations (using SAD, FT and NCC), and then added cumulatively to create a displacement versus time curve for each measure, in units of mm. The cumulative displacement versus time curve given by the standard reference is also plotted on this graph for comparison. The estimated total displacement is obtained from this graph, and compared to the reference total displacement. The auto-location part (a) and interframe and total displacement analysis in part (b) is repeated for each motion profile in Table 10.

Table 10: Motion Profiles for Actuating Multiple Tendons

Motor Series (Tendon)	**Peak Velocity (Reference) (mm/s)**	**Total Displacement (Reference) (mm)**
A (index)	15	15
	10	10
B (middle)	15	15
	10	10
C (ring)	15	15
	10	10
AB (index+middle)	10	10
AC (index+ring)	10	10
BC (middle + ring)	10	10
ABC (index+middle+ring)	10	10

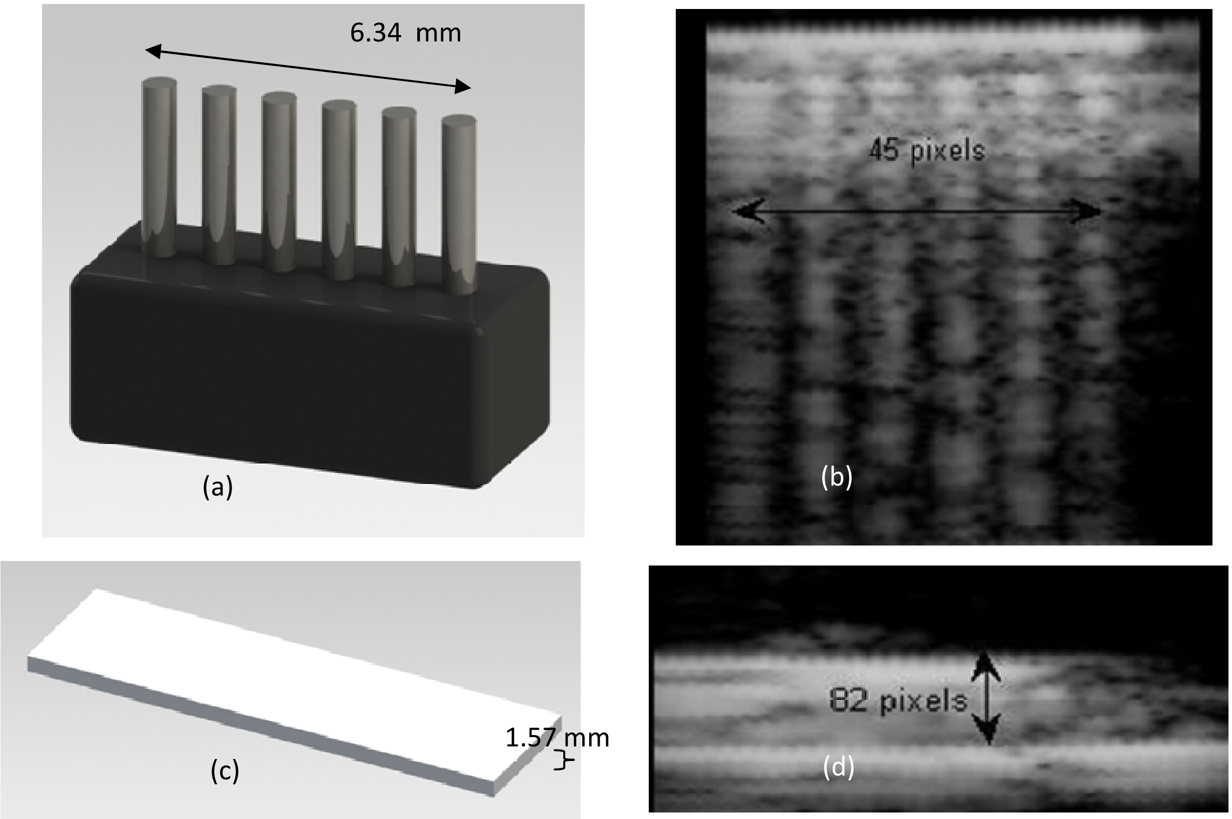

Figure 48: A calibrating 6-pin connector and flatbar is used to determine the lateral and axial mm/pixel conversion factors, respectively, for a sub-array. (a) the physical length of the 6-pin connector is 6.34 mm, and (b) the B-Scan image showing the same measurement is 45 pixels, thus giving 0.1408 mm/pixel in the lateral direction. (c) The physical height of the flatbar is 1.57 mm, and (d) the B-Scan image showing the same measurement is 82 pixels, giving 0.019 mm/pixel in the axial direction.

TABLE 11: PARAMETERS USED FOR SPECKLE TRACKING

Property	**Value**
Similarity Measure	SAD, FT and NCC
Searching Technique	Stationary search
Template Size (*x by z*)	5 by 50 pixels
ROI Size (*x by z*)	25 by 62 pixels
Resolution Conversion Factor	Lateral: 0.1408 mm/pixel Axial: 0.0190 mm/pixel
Template Locations	x $\in$ [21,54] in steps of 1, and z $\in$ [500,800] in steps of 10

6.6. EXPERIMENT 5: CADAVER-BASED STUDY TO ESTIMATE THE ONSET OF TENDON EXCURSION

6.6.1. Introduction

The previous experiments (Experiments 1-4) estimate the interframe and total displacement of a finger from a non-amputee with a tendon performing a large excursion. However, one hypothesis of this thesis is that ultrasound-based tendon tracking can be used to detect and monitor the tendon displacement from an amputee. In such circumstances, it is assumed that the tendon excursion in an amputee will be greatly reduced in magnitude, thus justifying further investigation into the limiting factors of the proposed technique. Experiment 5 forms the basis for two new investigations, which are: (i) determining the smallest amount of displacement needed to auto-locate the tendon, and (ii) determining the smallest detectable tendon displacement, which is termed as the "onset displacement", in this thesis. In order to validate Experiment 5, the hardware set-up, previously described for Experiments 3 and 4, is used on the third and fourth day of data collection, as previously described. On the third day, the onset experiment is performed with the second hand and the linear array, while on the fourth day, the onset experiment is performed with the first hand and the quad-array. This study has been approved by the Dept. of Cellular & Physiological Sciences, Body Donation Program, Life Sciences Centre at the University of British Columbia, (approval #: W0196).

6.6.2. Set-Up and Protocol

The set up for the single tendon (linear array) and multi tendon (quad array) experiment is the same as shown in Fig. 42 and Fig. 47, respectively. The protocol for the single tendon and multi-tendon onset experiment is as follows:

(a) Auto-location and displacement onset of a single tendon using the linear array

The middle finger's tendon with a given motion profile in Table 12 is actuated, while the linear array and Sonix Touch system collect and saves the .b8 data. The previously described auto-location algorithm is used in order to display the displacement fields using SAD, FT and NCC similarity measures. This is repeated with each motion profile in Table 12 in order to determine which motion profile provides the smallest amount of displacement needed to auto-locate the tendon. As well, from these displacement fields, the smallest detectable displacement (i.e. the onset) is also determined. From these fields, the onset of displacement is determined as the smallest displacement giving the ability to detect the tendon above the background noise.

TABLE 12: ONSET MOTION PROFILES

Motor (Tendon)	**Total Displacement (Reference) (mm)**
B (middle)	0.20
	0.28
	0.36
	0.44
	0.60
	0.80
	1.00

(b) Auto-location and displacement onset of multiple tendons using the quad-array

Similar to (a), the middle finger's tendon is actuated with a given motion profile in Table 12, while the quad-array and custom software integrated with the Sonix Touch system, collect and saves the RF data. The previously described auto-location algorithm is used in order to display the displacement fields for each sub-array using SAD, FT and NCC similarity measures. This is repeated with each motion profile in Table 12 in order to determine which motion profile provides the smallest amount of displacement needed to auto-locate the tendon. As well, from these displacement fields, the smallest detectable displacement (i.e. the onset) is also determined. From these fields, the onset of displacement is determined as the smallest displacement giving the ability to detect the tendon above the background noise.

CHAPTER 7:

EXPERIMENTAL RESULTS

7.1. EXPERIMENT 1: PRELIMINARY CADAVER-BASED STUDY

7.1.1. INTRODUCTION

In this preliminary study, a library of B-scan ultrasound data of single tendon excursion were obtained. Such libraries of B-scan data (cine loops) were used to develop the tracking software in order to obtain estimates of interframe and total displacement. As well, this preliminary study was used to assess the hardware design, for an attempt to develop a motorized standard reference system, and hardware which couples to the middle finger's FDS tendon on a cadaver hand.

7.1.2. RESULTS OF EXPERIMENT 1

(a) Hardware

Overall, the tendon coupler system, the cadaver stabilization vice-clamp system, and the transducer holder designs were successful in that they performed the required task. Unfortunately, the motorized actuation system did not perform the displacement motion profile as required, which prevented the establishment of a valid standard reference for this experiment. This failure is attributed to a controller issue, as well as a problematic angle-effect in the way the tendons were coupled to the actuator. Due to the expiring nature when dealing with fresh, un-embalmed cadaver material, there was no immediate remedy to fix these issues. In terms of the controller failure, the x-stage was visually observed to only displace approximately 13.5 mm, although programmed to displace 15 mm. It was later determined that the controller to the motor had failed, thus the x-stage did not displace the programmed 15 mm, and other motion profiles were suspected to be inaccurate as well. As well, upon further inspection, it was determined that there was an unwanted angle introduced between the tendon and the coupler/x-stage assembly, thus the tendon was not displacing horizontally. As shown in Fig. 49, this introduces an angle-effect, whereby the angle is varying throughout its excursion. Referring to Fig. 49, the solid red indicator outlines the location of the tendon at the initial position, and final position, as it is actuated. Although the difference in the initial position to the final position of the coupler/x-stage was visually approximated as 13.5 mm (which was due from the controller failure), there was no objective way to correlate that approximation to the displacement of the moving tendon. Thus, the visually observed coupler/x-stage displacement does not represent true tendon displacement. Consequently, the programmed displacement does not match the actual displacement of the tendon, and therefore the reference cannot be used.

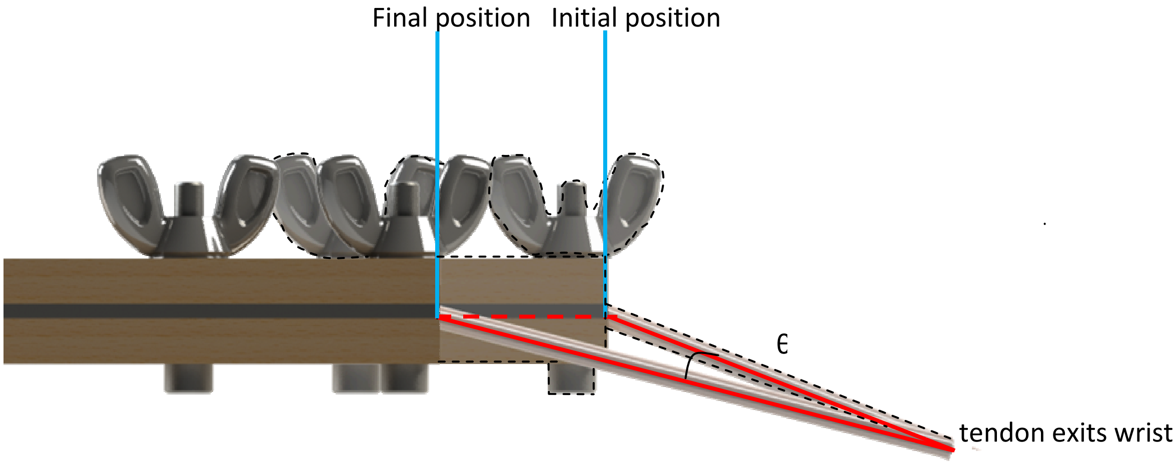

Figure 49: The problem of the angle-effect is illustrated, where the path of the tendon is seen as a solid red line, and the introduced angle is seen. The initial position of the tendon coupler has a dashed black outline. The tendon is forced to stay at the same point as it exits the wrist, thus introducing an angle-effect.

(b) Speckle Tracking

Although the problem with the actuator system described above lead to the failure of the reference system, the collected B-Scan image data and cine-loops served as an image library in order to develop the speckle tracking algorithms. The fact that the displacement was in the range of 13.5 mm allowed for basic investigation of various speckle tracking approaches. The SAD algorithm was first developed using the parameters in Table 4 in Chapter 6, and the resulting displacement versus time curve for a sample motion profile is illustrated in Fig. 50. As seen in Fig. 50, the total displacement for the expected motion profile (peak velocity = 15 mm and total displacement = 15 mm) is estimated as 9.9 mm. Since the reference failed, all of the image libraries are simply used as a tool in order to further develop the algorithms and for designing future experimentation.

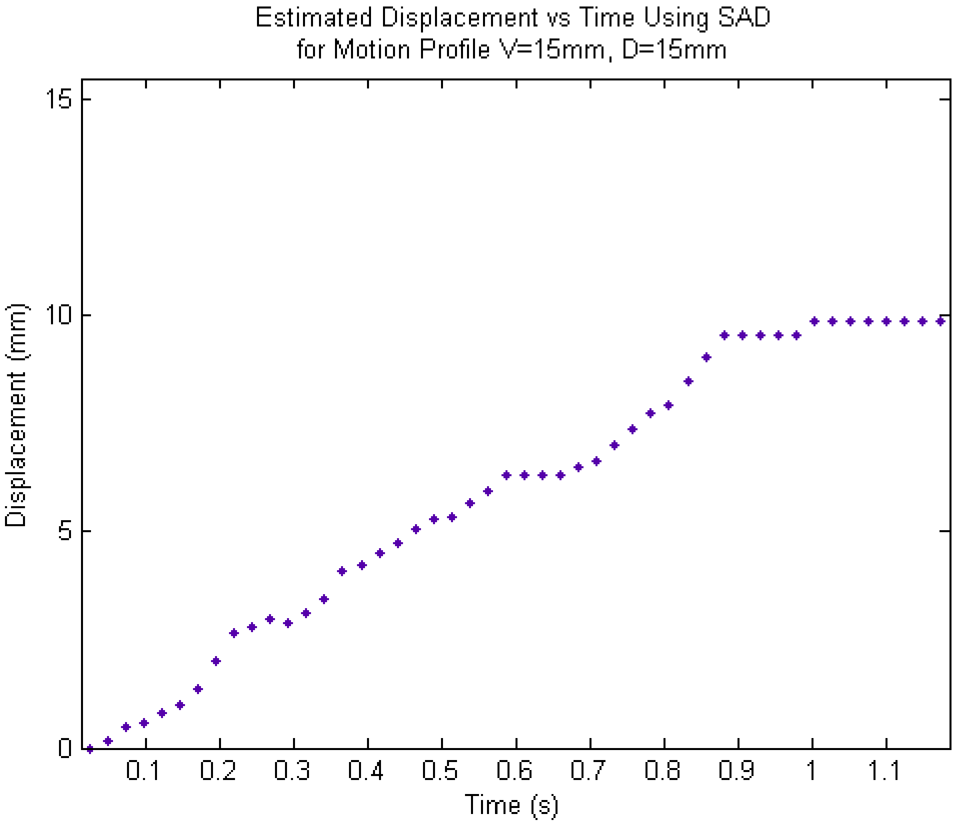

Figure 50: Estimated displacement vs time curve using the SAD speckle tracking technique. From this plot, the estimated total displacement is 9.9 mm. The actual reference displacement is unknown, due from the problem of actuator control failure.

7.2. EXPERIMENT 2: HUMAN-BASED STUDY TO ESTIMATE SINGLE TENDON EXCURSION

7.2.1. INTRODUCTION

The aim of this experiment is to develop the proposed ultrasound-based method to provide non-invasive estimates of the instantaneous and total displacement of a single tendon. This experiment uses human volunteer patients, during their regularly scheduled carpal tunnel surgeries. To validate the method, the ultrasound-based tendon motion estimation is directly compared with the actual tendon displacement, by video recording the surgically exposed tendons in the palm. By video recording the motion of the exposed flexor tendons, a standard reference displacement can be obtained using commercial video tracking software. In this way, the experiment provides a direct displacement comparison using real, live human anatomy, in contrast to other work, which uses simulations and phantoms.

7.2.2. RESULTS OF EXPERIMENT 2

Using the same ultrasound system described in Experiment 1, B-Scan images are collected with a 12-MHz transducer placed proximal to the wrist. Using the collected image sequence data of displacing tendons, the proposed speckle-based tracking algorithms from Chapter 5 are developed, using FT, SAD and SSD as similarity measures, along with the parameters in Table 6 in Chapter 6.

To create the reference displacement vs. time dataset, the microscope video of the exposed tendons was tracked with Kinovea software. To validate the use of the Kinovea software itself, a sample video of tendon motion (patient 1: flexion 2) was also manually tracked, to create a plot of the displacement versus time. Manual tracking was done by counting pixels of motion with Matlab, and knowing the pixel-to-mm scale factor. The results of manual tracking in comparison to Kinovea are shown in Fig. 51, where it appears that Kinovea is a valid program to use for video tracking.

To validate the proposed tracking algorithms, the ultrasound-based tendon displacements are compared with the video reference displacement. This is done for a single flexion or extension, for both total displacement and instantaneous displacement. Since the reference displacement is sampled at different time intervals, a cubic spline to first fit to the reference displacement data points, as illustrated in Fig. 52 for patient 1, flexion 2, as an example. This allows the video reference displacements to be sampled at the same time points as the displacements estimated by the ultrasound-based techniques.

Three metrics are used to quantify the comparison between the proposed algorithms and the reference displacement. These metrics calculate the total displacement relative error, the average instantaneous displacement absolute error for the entire excursion, and the average instantaneous displacement absolute error for sectioned data (Table 13). Using the relative and absolute error in this way is similar to methods employed by similar studies [179]. The average absolute error (mm) for FT, SSD and SAD based techniques in S1, S2 and S3 as shown in Table 14. The metrics are described as follows:

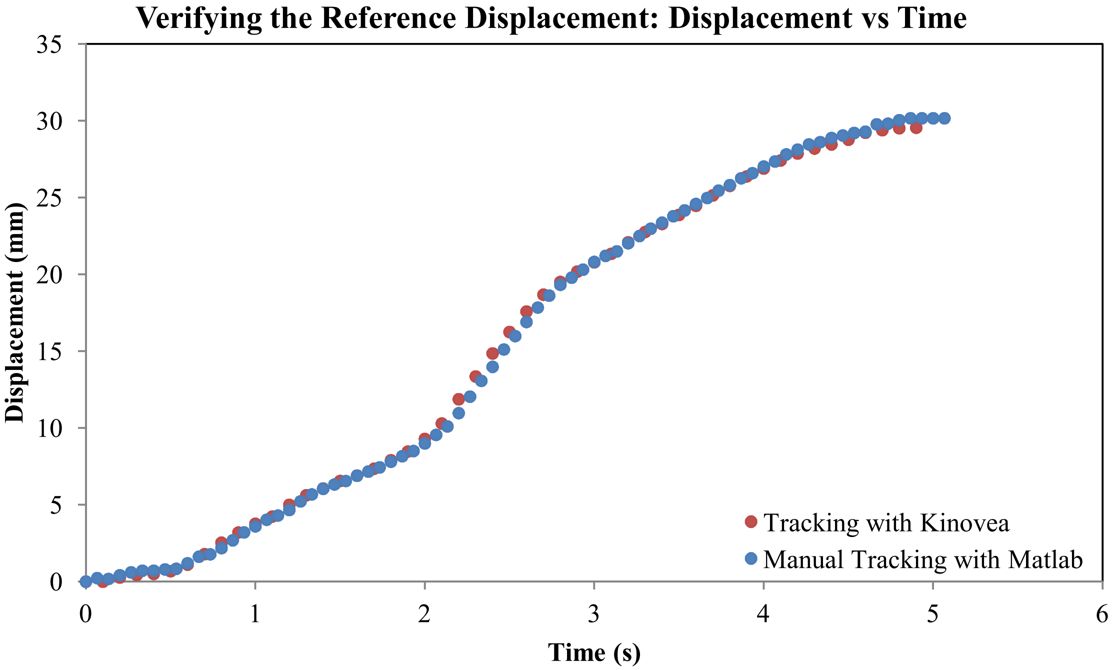

Figure 51: Verifying the Kinovea tracking technique to determine the reference displacement.

a) **Relative Error:** The first metric compares the total estimated displacement from the proposed techniques, with the reference displacement as a relative error, R_D for a single flexion or extension, using the equation:

$$R_D = \frac{D_{MVR} - D_{PT}}{D_{MVR}} * 100\% \qquad \{25\}$$

Where: D_{MVR} is the total displacement given by the video reference, and D_{PT} is the estimated total displacement given by proposed technique (FT, SSD or SAD).

b) **Absolute Error:** The second metric is the absolute error A_{id}, which compares the average instantaneous displacement, *id*, as an absolute error comparison between the proposed techniques and the video reference. With the displacement from the video reference and the estimated displacement from the proposed method, sampled at the same point in time, this metric was calculated for a single flexion or extension using the Eqn.$\{26\}$. This is repeated for each set of sampled data points for the entire excursion (flexion or extension) to obtain the average value.

$$A_{id} = \frac{id_{MVR} - id_{PT}}{id_{MVR}} \qquad \{26\}$$

Where: id_{MVR} is the instantaneous displacement given by the video reference, and id_{PT} is the estimated instantaneous displacement given by proposed technique (FT, SSD or SAD).

c) **Sectioned Error:** For the third metric, a single excursion (flexion or extension) is first separated into three equal sections in time, denoted as S1, S2 and S3. These sections depend on the total excursion time, *T*. Therefore, S1 corresponds to the first section in time *t*, that is, t = [0 to 1/3*T*], S2 corresponds to *t* = [1/3*T* to 2/3*T*] and S3 corresponds to *t* = [2/3*T* to *T*]. Eqn.{26} is then used for each set of sampled data points for a given section, and then each section is averaged to give a value for the instantaneous displacement absolute error. Please refer to Table 13 and Figs. A.1.1-A.1.3 in the Appendix section at the end of this thesis, for the displacement comparison analysis for patients 1 and 2.

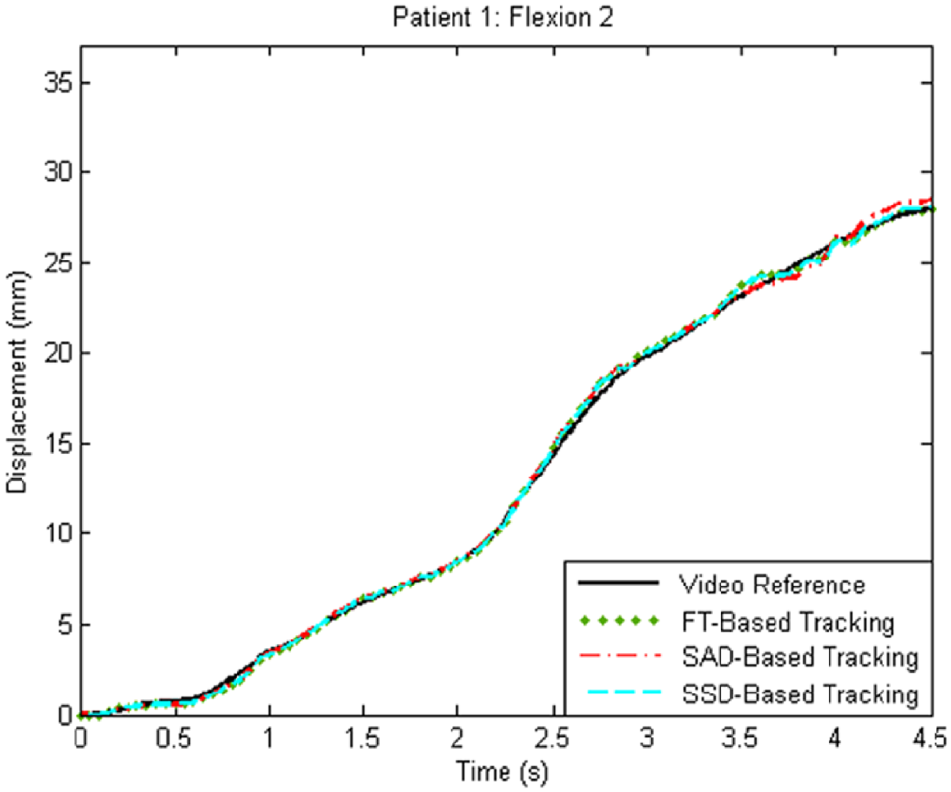

Figure 52: An example of the data analysis procedure, where the video reference is plotted next to the speckle tracking algorithms for tendon flexion from patient 1. The excursions from all patients can be found in the Appendix.

TABLE 13: ANALYSIS OF ESTIMATED DISPLACEMENT USING FISHER-TIPPET (FT), SUM OF ABSOLUTE DIFFERENCE (SAD) AND SUM OF SQUARED DIFFERENCE (SSD) AS A SIMILARITY FUNCTION

Patient	Excursion	No	R_D Total displacement relative error %			A_{id} Avg. instantaneous displacement absolute error (mm)			Instantaneous displacement absolute error in sections (mm)			
			FT	SAD	SSD	FT	SAD	SSD	Sections	FT	SAD	SSD
Patient 1	Flexion	1	1.9	3.96	7.5	0.57	0.73	0.56	S1	0.30	0.43	0.50
									S2	0.82	0.95	0.42
									S3	0.58	0.80	0.76
		2	0.2	1.85	0.80	0.16	0.24	0.16	S1	0.11	0.11	0.11
									S2	0.21	0.19	0.17
									S3	0.17	0.41	0.20
		3	3.0	8.64	24.73	0.32	1.54	2.97	S1	0.12	0.53	0.63
									S2	0.30	1.46	2.64
									S3	0.52	2.62	5.60
		4	0.35	4.34	2.69	0.33	0.94	0.62	S1	0.20	0.20	0.20
									S2	0.31	0.91	0.55
									S3	0.49	1.69	1.10
		5	33.26	0.83	5.45	3.47	0.90	1.46	S1	0.45	1.02	1.41
									S2	3.40	1.27	1.37
									S3	6.31	0.35	1.53
		6	0.68	21.55	14.66	0.27	3.34	2.43	S1	0.17	0.73	0.53
									S2	0.42	4.68	3.41
									S3	0.21	4.65	3.30
	Extension	1	29.21	31.55	32.19	5.97	6.69	6.86	S1	3.04	3.33	3.35
									S2	6.90	7.94	8.18
									S3	7.98	8.81	9.07
		2	0.26	23.74	14.47	0.18	5.37	5.10	S1	0.34	3.08	2.87
									S2	0.05	6.56	6.42
									S3	0.16	6.43	5.96
		3	11.32	0.74	2.23	1.88	0.85	2.02	S1	0.74	1.74	3.11
									S2	2.00	0.65	1.90
									S3	2.86	0.18	1.08
		4	0.81	29.34	14.81	0.69	6.73	3.99	S1	1.13	5.49	4.19
									S2	0.64	7.32	4.05
									S3	0.32	7.37	3.76
		5	4.47	9.04	2.55	0.64	1.53	0.31	S1	0.51	0.43	0.41
									S2	0.53	0.95	0.17
									S3	0.86	0.80	0.39
Patient 2	Flexion	1	2.89	0.46	4.76	1.08	1.88	2.60	S1	0.65	0.11	0.67
									S2	1.59	0.19	3.76
									S3	0.90	0.41	3.17
		2	12.45	8.20	15.98	2.75	1.06	3.87	S1	1.30	0.53	1.80
									S2	2.57	1.46	4.57
									S3	4.36	2.62	5.23
	Extension	1	1.83	7.33	4.07	1.01	1.99	1.79	S1	0.51	0.20	3.10
									S2	1.36	0.91	0.79
									S3	1.14	1.69	1.46
		2	6.90	6.76	8.88	0.82	0.80	1.18	S1	0.47	1.02	0.70
									S2	0.36	1.27	0.55
									S3	1.62	0.35	2.24

TABLE 14: AVERAGE ABSOLUTE ERROR FOR SECTIONS S1, S2 AND S3 FOR PATIENTS 1 AND 2

Section	FT: Average absolute error (mm)	SAD: Average absolute error (mm)	SSD: Average absolute error (mm)
S1	0.67	1.40	1.57
S2	1.51	2.66	2.60
S3	1.90	2.83	2.99

Another way to represent the error is to implement error bars on the displacement vs. time curves. This would require multiple, repeatable flexions. However, each patient flexion collected in this experiment was unique, and corresponded to a distinctive reference motion profile. Even the same patient flexed with a different reference motion profile each time. Thus, it is not possible to use error bars in this experiment.

As previously described in Section 6.3.1, there were 6 patients scheduled to participate in this study. The data-sets from three patients could be used, as previously described. Of those three, all the collected data was reviewed and it was found that six flexions and five extensions for patient 1 and two flexions and two extensions for patient 2 were usable. The video reference did not record patient 1's last extension and, thus, it could not be used. Also, after patient 2 flexed and extended twice, the data collection had to be stopped to allow the surgeon to release more tissue. When data collection resumed, the transducer was not in a good location to image the tendon, and the remaining data could not be used. Patient 3 performed four flexions and four extensions, but this patient's data sets could not be used. For this patient, the placement of the transducer was problematic, and thus, the B-scan image sequence of the tendon's displacement throughout its excursion was of poor quality. This resulted in a loss of tracking, as illustrated in Fig. 53, which is evident after 1.7 s. Loss of tracking at this point occurred on all excursions of patient 3, using the FT-based, SSD-based or SAD-based technique.

Peak tendon velocities (maximum rate of flexion or extension) for patients 1 and 2 are listed in Table 15. In general, patient 2 flexed and extended at a much higher velocity than patient 1. Also, these patients performed at a much faster velocity and exhibited less control in extension than flexion.

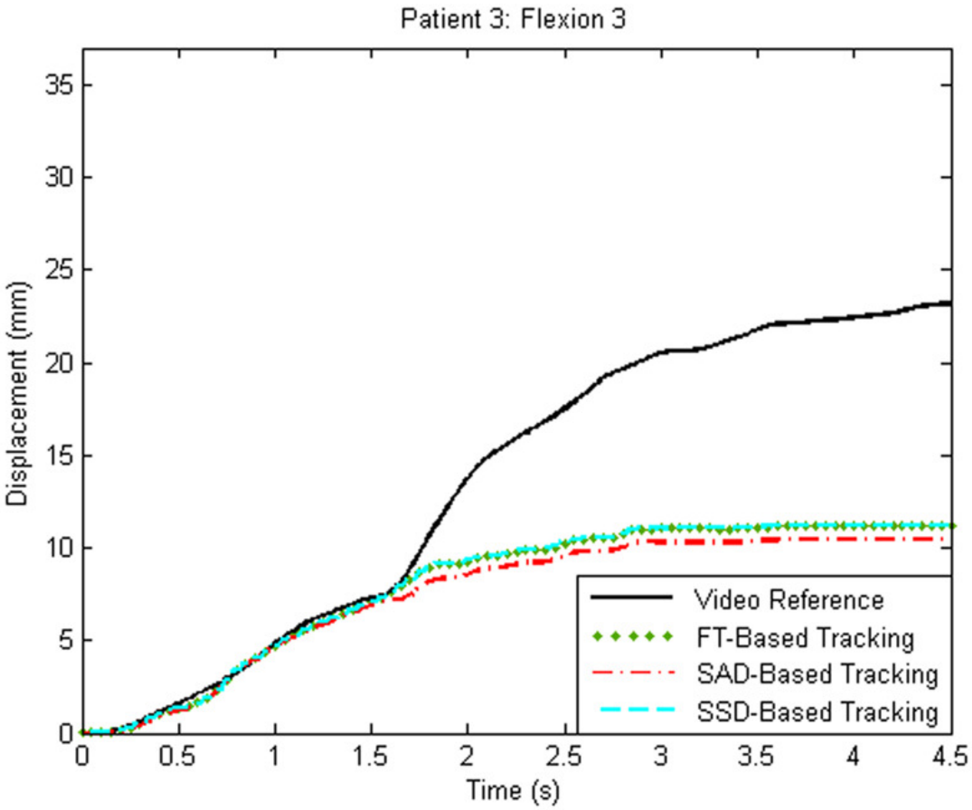

Figure 53: Displacement-versus-time curve for patient 3's third flexion. After 1.7 s, tracking is lost completely and may be attributed to out-of-plane tendon motion (in the *y* direction).

TABLE 15: PEAK VELOCITIES FOR TENDON EXCURSIONS FROM PATIENTS 1 AND 2

Patient No.	Excursion No. F=Flexion E=Extension	Peak Velocity (mm/s)
1	F1	22.5
	F2	14.3
	F3	20.1
	F4	18.3
	F5	23.6
	F6	27.3
	E1	41.4
	E2	35.8
	E3	36.8
	E4	42.8
	E5	22.9
2	F1	39.9
	F2	39.3
	E1	34.8
	E2	44.0

7.3. DETERMINING THE OPTIMAL PARAMETERS FOR SPECKLE TRACKING

7.3.1. INTRODUCTION

This section investigates 2D speckle tracking parameters to better estimate the interframe and total displacement of the flexor wrist tendons. This study uses a sub-set of the data obtained in Experiment 2. The success of speckle tracking is highly dependent on many parameters. The parameters investigated are: (a) additional similarity measures (NCC and the two hybrid metrics described in Chapter 5), (b) searching without a stationary ROI, (c) hierarchical search, (d) template location, (e) template and ROI size, and (f) frame rate (temporal resolution). Frame skipping is another important tracking parameter, and is further discussed in Section 7.4.

In Part-1 of this study, the computational load, accuracy and robustness of the proposed tracking method is compared using four different similarity measures: FT, NCC and the two new hybrid metrics incorporating the SAD measure, as previously described in Chapters 5 and 6. The data used in Part-1 are the excursions from patient 1 (flexions 1, 2 and 6) and patient 2 (flexion 2), obtained from Experiment 2. In Part-2 of this study, the effect of changing the above mentioned tracking parameters are investigated using same similarity measures. The data used in Part-2 is the excursion from patient 1 (flexion 2).

7.3.2. RESULTS OF SPECKLE TRACKING PARAMETER INVESTIGATION

(a) Part 1: Similarity Measure Comparison

The four similarity measures described in Chapters 5 and 6 (FT, NCC and the two hybrid measures) are used with the stationary ROI technique. The total displacement estimate obtained by using each similarity measure, is compared to the actual displacement (reference displacement) determined from the microscope video. This is done with four different patient flexion data, from Experiment 2. One of the patient data flexions is not ideal (patient 2, flexion 2), in order to test the robustness of the four different techniques. The ideal flexions consist of motion data in which the patients flexed their finger with slow to moderate speed, in a smooth trajectory. Thus, patient 1's flexions 1,2 and 6 are selected based on the criteria for an ideal data-set, while patient 2's flexion 2 is selected for the non-ideal data-set.

For the analysis, a reference curve representing the actual tendon displacement is established by fitting a cubic spline to the video reference displacement data, as before. This allows for a comparison of the ultrasound-based displacement estimate at the same time points as the reference displacement. Referring to Figs. 54-55, the cumulative displacements are illustrated for an example of an ideal (patient 1: flexion 2) and non-ideal (patient 2: flexion 2) excursion, respectively. These figures contain the four similarity measures along with the reference for the flexion. The cumulative displacements using all similarity measures followed the reference in the case of the ideal data set in Fig. 54. When referring to the non-ideal data set in Fig. 55, the displacements estimated using the NCC measure seemed to follow the reference better than the other metrics. In order to compare the estimated total displacement with the reference, the metric R_D is calculated using Eqn. $\{25\}$. Referring to Table 16, the total displacement relative error, R_D, is shown for each similarity measure using the four patient flexions.

Also shown in Table 16 is the computational time for each similarity measure and each flexion. For each excursion and similarity measure, it is shown as the time taken in units of milli-seconds per frame comparison. This is so that the computational times from each measure can be compared.

It is important to note that interframe displacement estimation errors can occur. These errors occur because the algorithm chooses an incorrect block as a match, even though that block score is the best score (the extrema coefficient, for example maximum FT or minimum SAD coefficient) within the ROI. These errors can be attributed to the noise distorting the intensity values on the pixels, and so the block with the extrema coefficient may not be the correct match. These interframe displacement errors ultimately lead to an offset error in the total displacement estimate. This problem can be seen in Fig. 27, where due to noise, there are several possible SAD coefficients with similar scores.

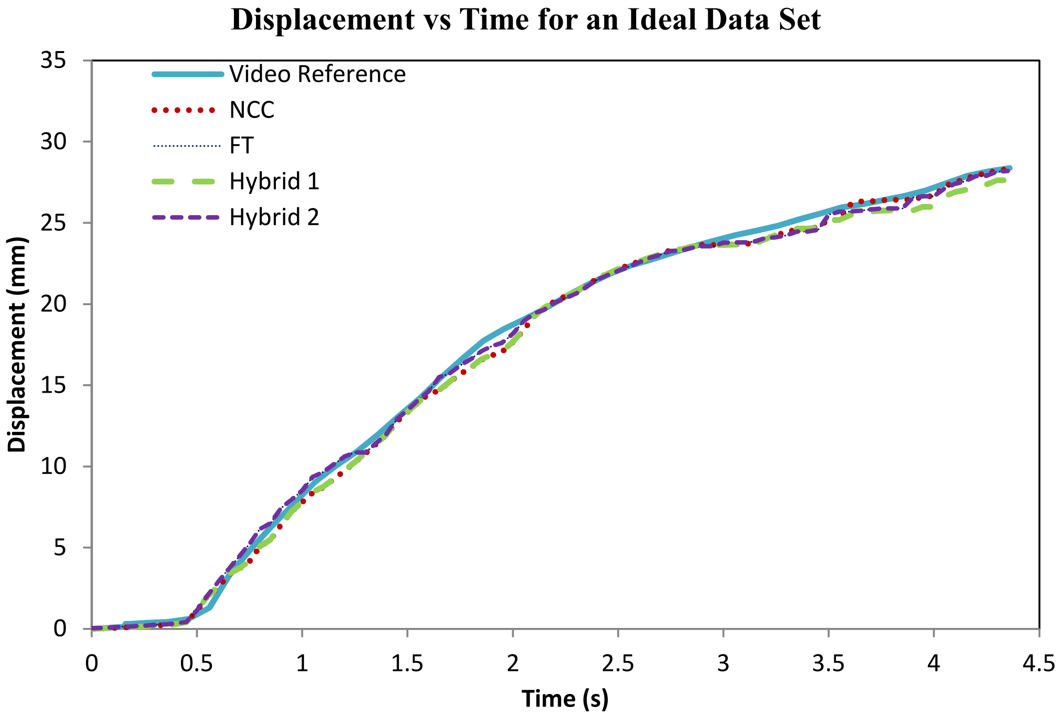

Figure 54: Four different similarity measures (NCC, FT, and two Hybrid metrics) were compared to the reference using an 'ideal' patient data set (patient 1: flexion 2) for Part 1 of the study. All displacement curves are well-matched to the reference. This figure is representative of all flexions in the ideal data set.

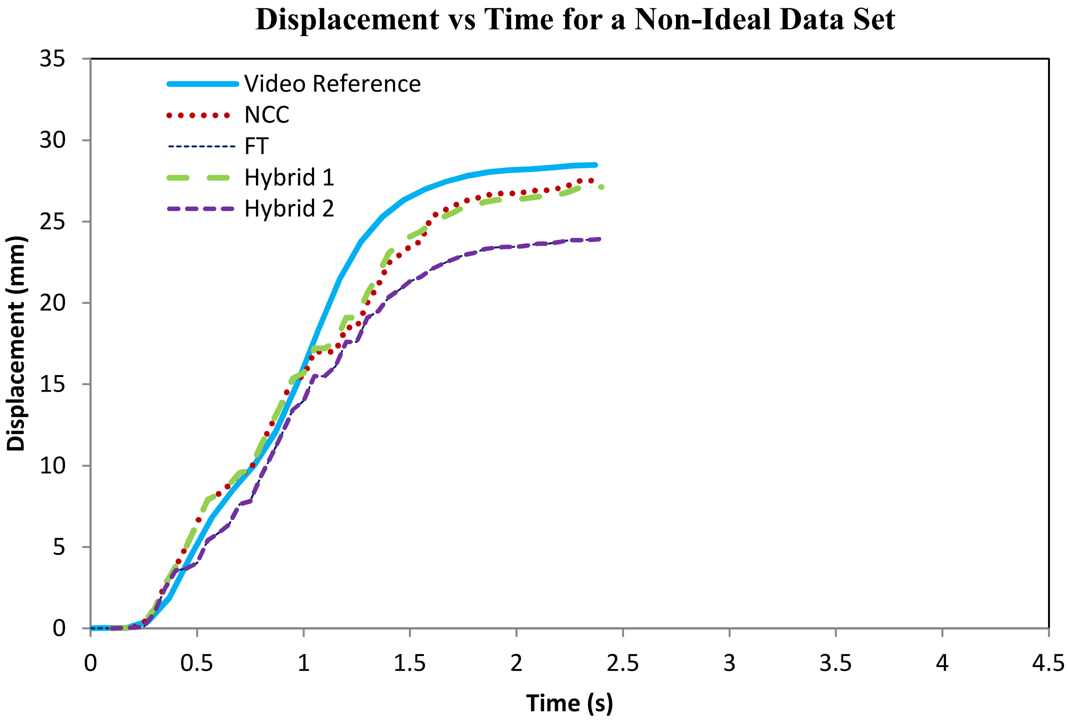

Figure 55: Four different similarity measures (NCC, FT, and two Hybrid metrics) were compared to the reference using a 'non-ideal' patient data set (patient 2: flexion 2) for Part 1 of the study. The FT and second Hybrid technique produced similar results. The NCC curve performed the best for total displacement estimations.

TABLE 16: DISPLACEMENT ANALYSIS FOR PART-1

Similarity Measure	Patient(#)=P(#) Flexion(#)=F(#)	R_D, Total displacement relative error %	Computational Time (ms/frame)	Similarity Measure	Patient(#)=P(#) Flexion(#)=F(#)	R_D, Total displacement relative error %	Computational Time (ms/frame)
FT	P1 F1	0.63	27	Hybrid 1	P1 F1	2.6	46
	P1 F2	2.47	27		P1 F2	3.35	43
	P1 F6	3.18	30		P1 F6	1.82	50
	P2 F2	26.78	30		P2 F2	16.73	70
NCC	P1 F1	0.35	29	Hybrid 2	P1 F1	0.63	46
	P1 F2	1.71	29		P1 F2	2.52	47
	P1 F6	1.82	35		P1 F6	3.18	58
	P2 F2	15.49	35		P2 F2	26.78	77

(b) Part-2: Effect of Parameter Change

The effect of parameter changes, using each of the four similarity measures, is graphically illustrated in Figs. 56-70, only using data from patient 1 (flexion 2). These plots demonstrate the effect of changing the parameters by observing how the estimated displacement curve compares to the reference displacement curve. The parameter changes investigated are: searching with a non-stationary ROI, searching with a hierarchical method, the template location, the template size, the ROI size, and lowering the frame rate.

The displacement curves using different searching strategies are illustrated in Figs. 56-57, for the case of a non-stationary ROI and hierarchical search, respectively. In the case of using a non-stationary ROI, the FT, NCC and second hybrid methods were able to follow the reference displacement curve better than the first hybrid method. All methods were not successful at tracking the entire flexion. This is evident by the fact that when visually observing the plots, not all methods followed the reference for the entire excursion. In the case of using hierarchical searching, the computational time increased due from the increased number of calculations, but all similarity measures were observed to follow the reference.

When considering the effect of changing the location of the template, it is observed on Figs. 58-61, that a location near the center of the image *(658,232)* performed the best using all similarity measures. This is because when observing the estimated curves, the stated location followed the reference curve better than the others. The inconsistencies of displacement estimation at different locations on the tendon, validates the need of an auto-location technique. This will allow for the template selection to be automated, and it is anticipated that such a localization technique will more accurately place the template.

For template size variation, it is observed in Figs. 62-65, that the larger *30 by 30 pixel* template did not work as well as the smaller templates, with all similarity measures. This is because the smaller templates followed the reference more closely. This may be due from the fact that the larger template may include regions of non-uniform motion. Similarly, for ROI size variation, it was observed in Figs. 66-69 that using the larger *80 by 35* and the smaller *40 by 35* ROI's did not perform as well as the *54 by 34* ROI. This may be due from the fact that the large ROI may cause ambiguous matches, as there is an increased chance of having several local extrema when calculating the similarity measure. As well, with the smaller ROI, large tendon displacements between the frames may not be captured, causing mis-match leading to poor tracking.

Referring to Fig. 70, the effect of obtaining data with a low frame rate of *10 fps* was illustrated. In this case, it was observed that the FT and first hybrid method seemed to follow the reference displacement better than the NCC or second hybrid method.

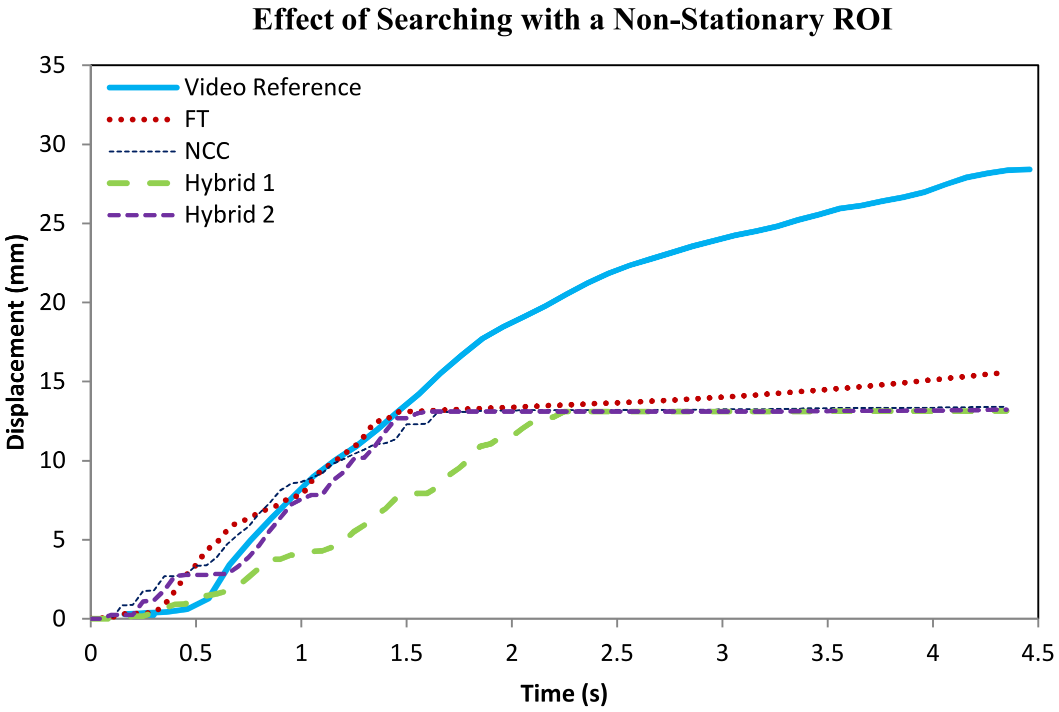

Figure 56: Illustrating the effect of searching with a non-stationary ROI, for Part 2 of the parameter study. All four similarity measures were used.

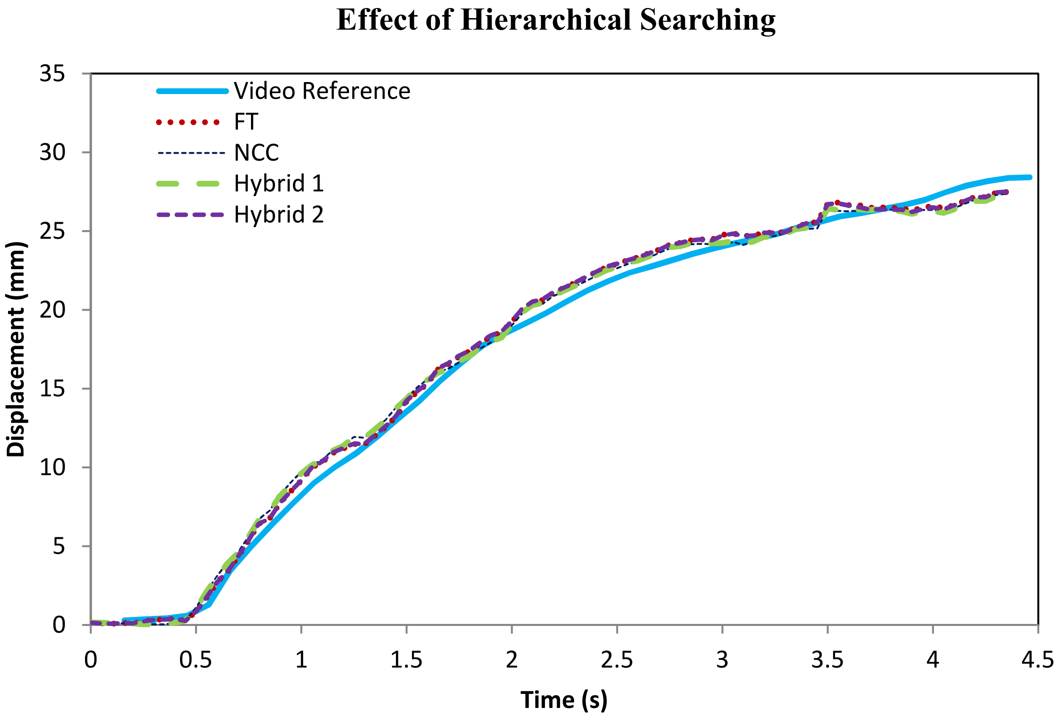

Figure 57: Illustrating the effect of searching with a hierarchical technique for Part 2 of the parameter study. All four similarity measures were used.

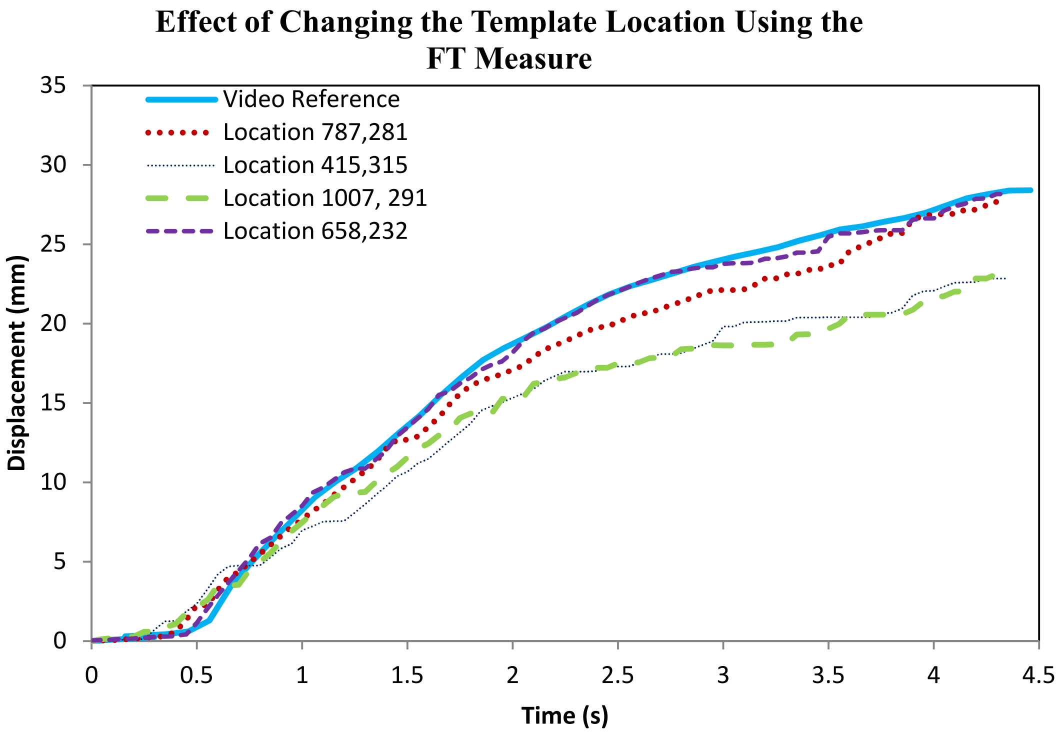

Figure 58: Illustrating the effect of changing the location parameter for Part 2 of the parameter study, when using the FT similarity measure. This demonstrates the need for an auto-localization or multi-template technique.

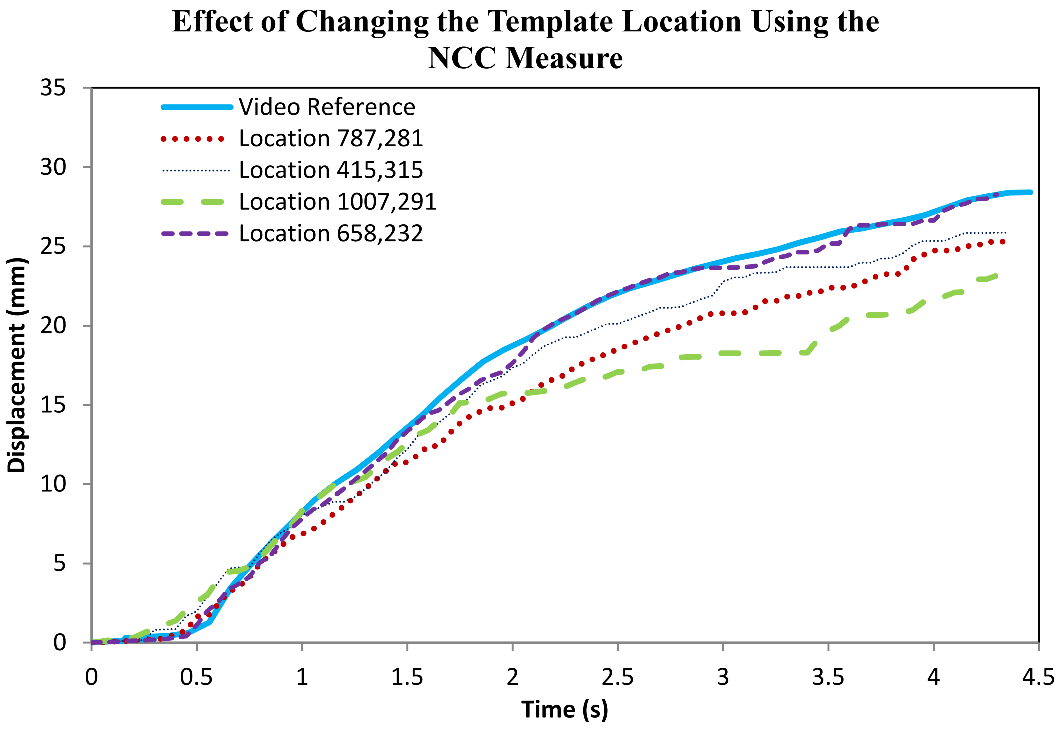

Figure 59: Illustrating the effect of changing the location parameter for Part 2 of the parameter study, when using the NCC similarity measure.

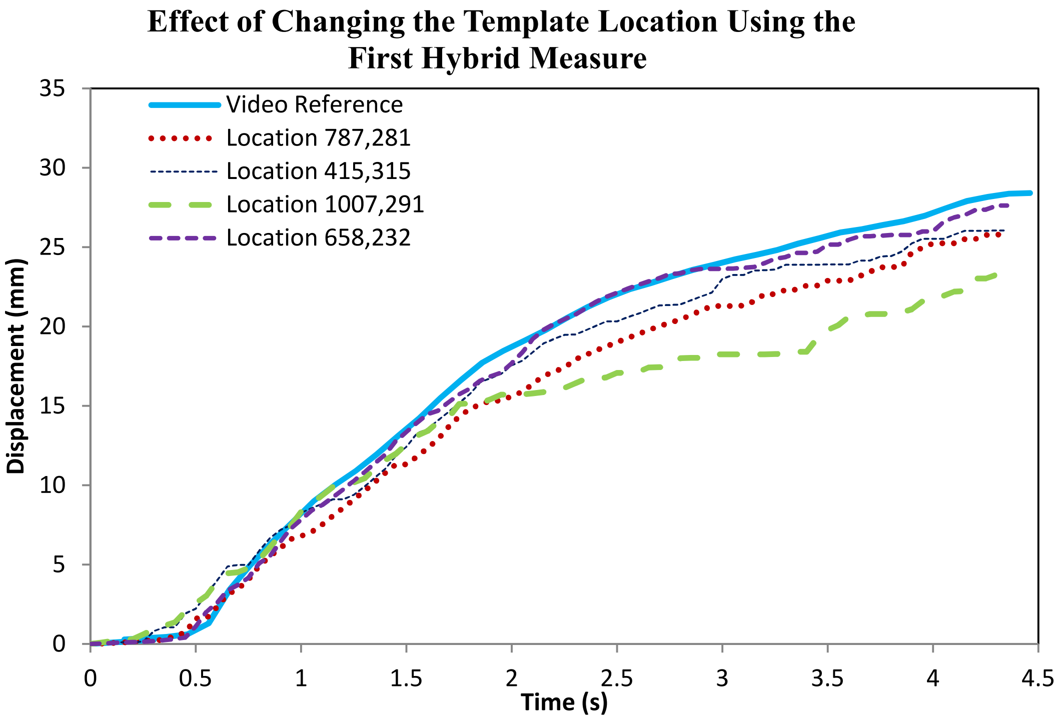

Figure 60: Illustrating the effect of changing the location parameter for Part 2 of the parameter study, when using the first hybrid similarity measure.

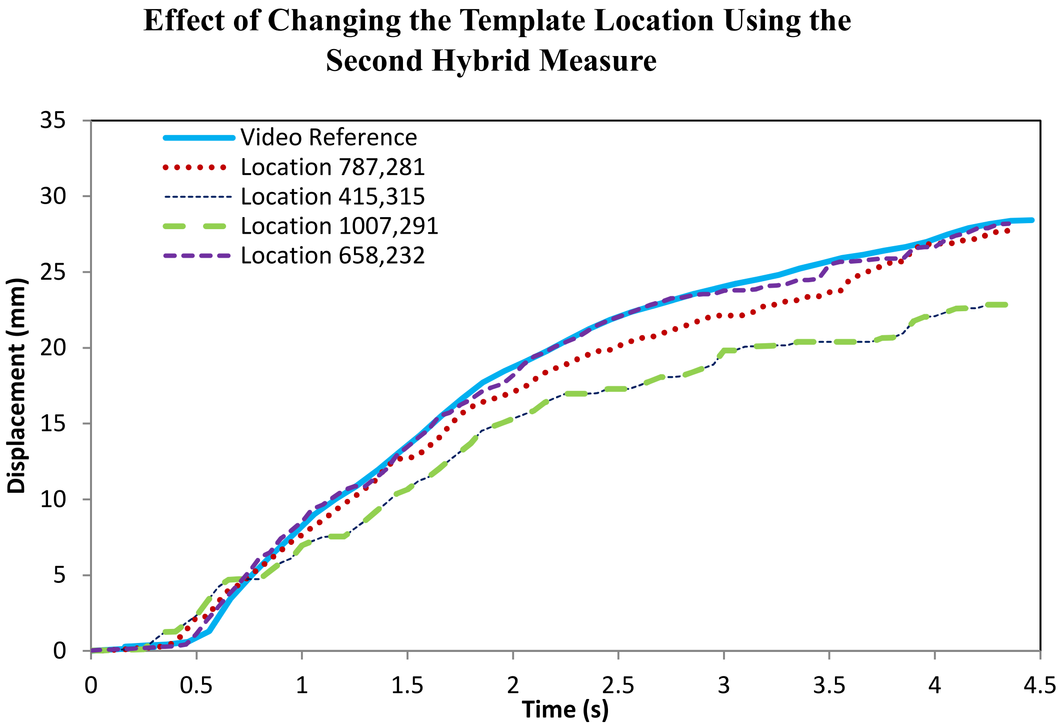

Figure 61: Illustrating the effect of changing the location parameter for Part 2 of the parameter study, when using the second hybrid similarity measure.

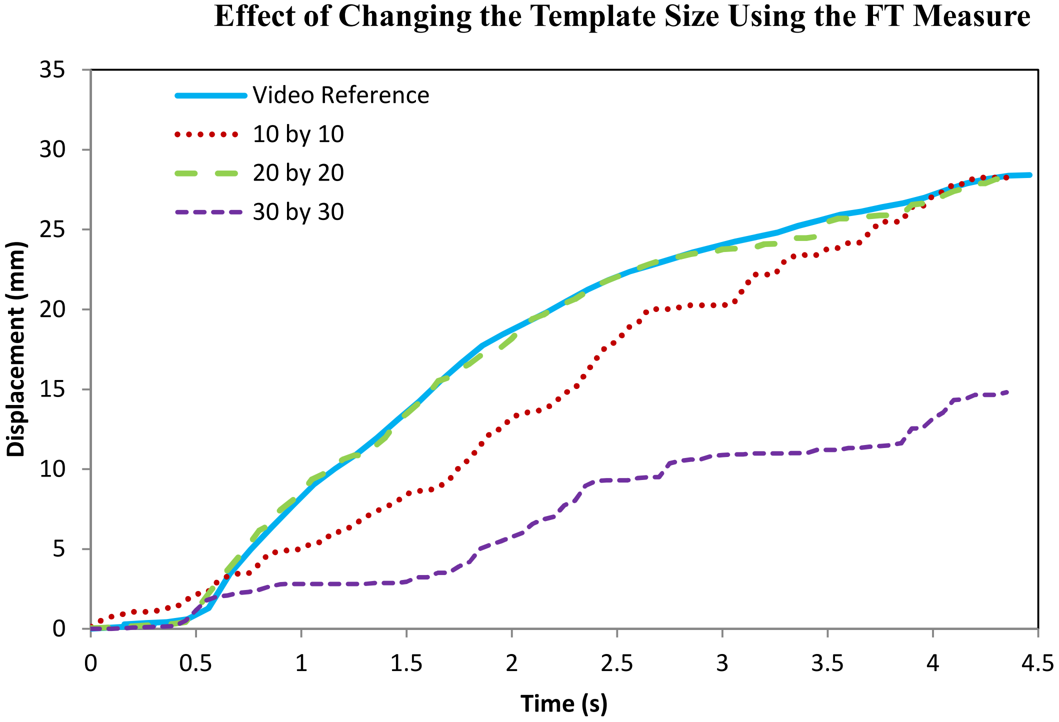

Figure 62: Illustrating the effect of changing the Template size for Part 2 of the parameter study, when using the FT similarity measure. This plot illustrates the effect of changing the template size parameter from 10 by 10 pixels, to 20 by 20 pixels, to 30 by 30 pixels.

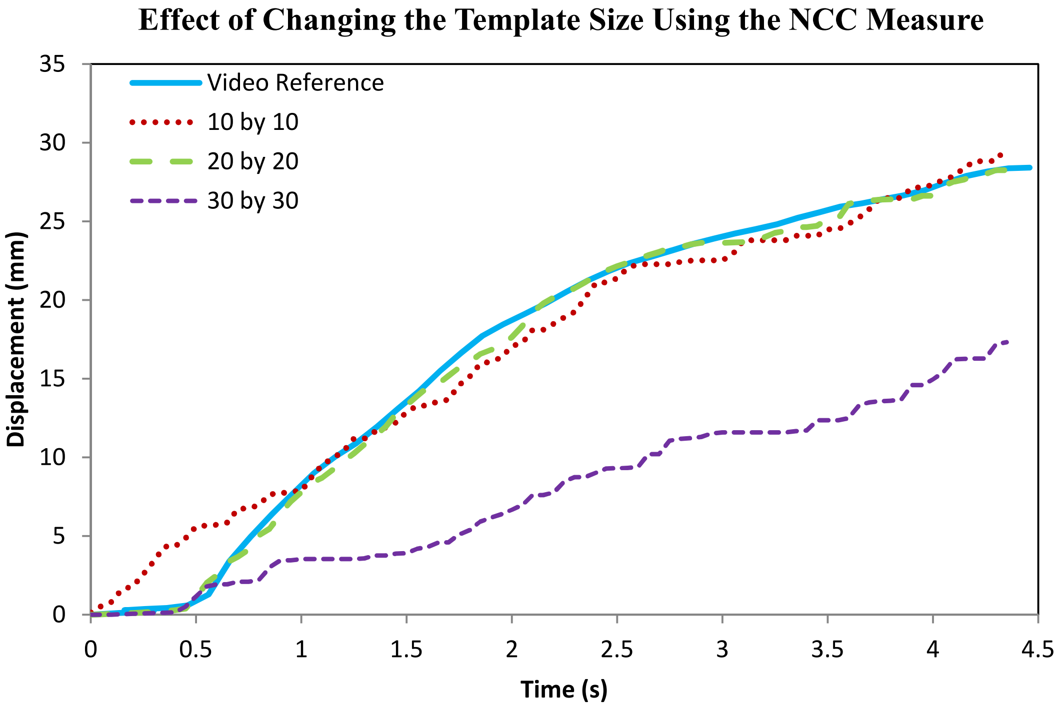

Figure 63: Illustrating the effect of changing the template size for Part 2 of the parameter study, when using the NCC similarity measure. This plot illustrates the effect of changing the Template size parameter from 10 by 10 pixels, to 20 by 20 pixels, to 30 by 30 pixels.

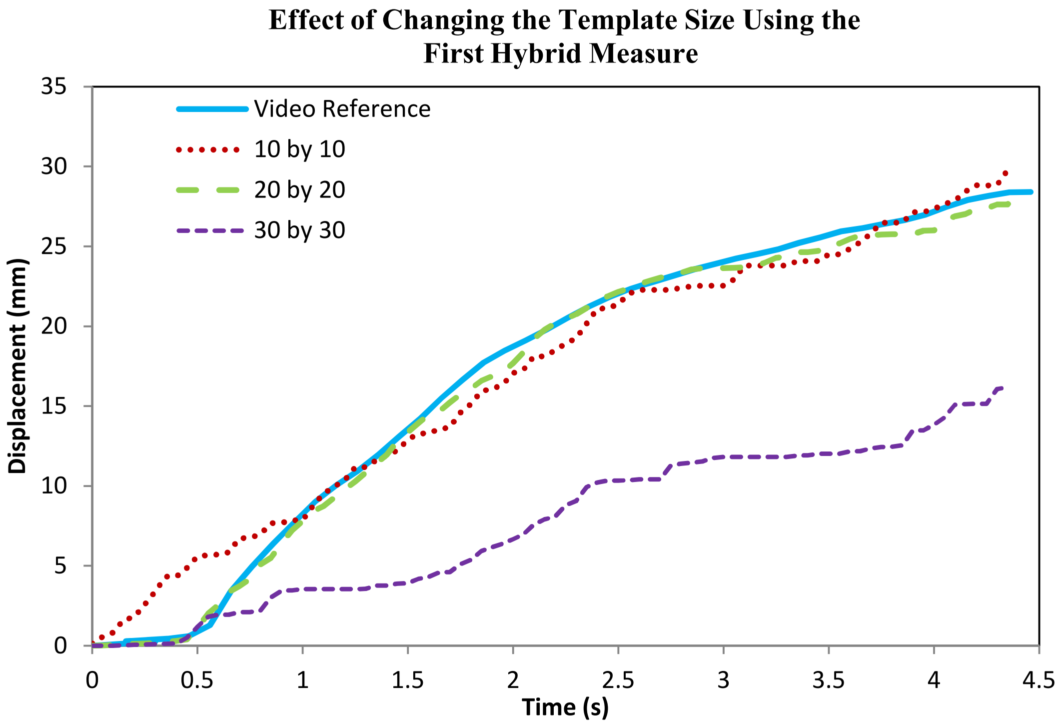

Figure 64: Illustrating the effect of changing the template size for Part 2 of the parameter study, when using the fist hybrid similarity measure. This plot illustrates the effect of changing the Template size parameter from 10 by 10 pixels, to 20 by 20 pixels, to 30 by 30 pixels.

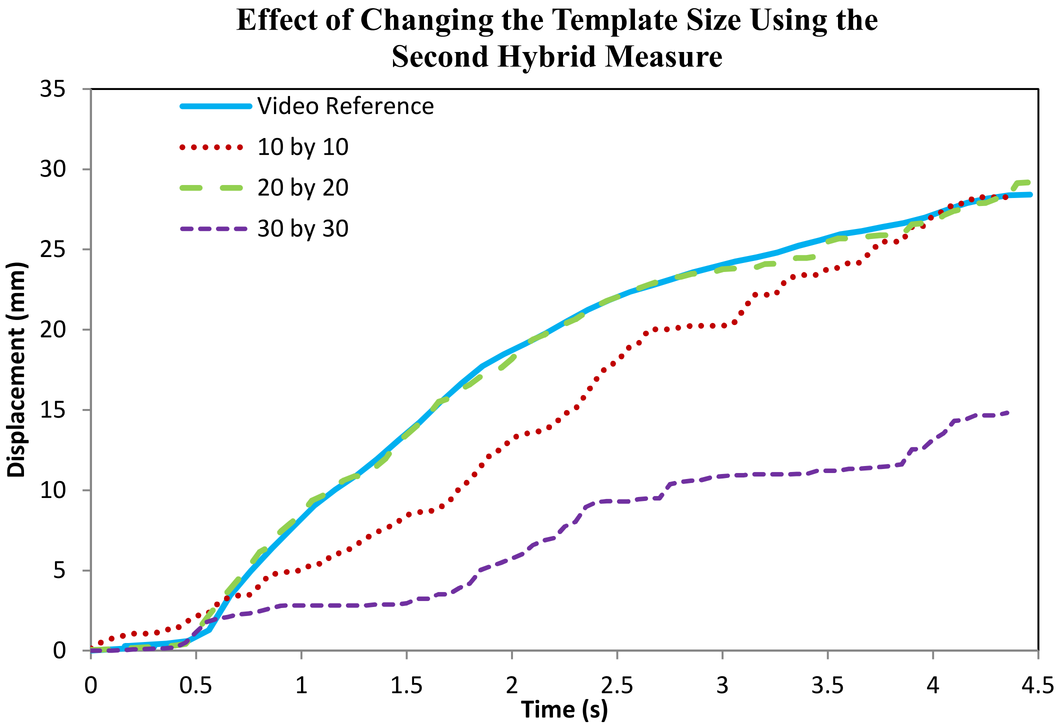

Figure 65: Illustrating the effect of changing the template size for Part 2 of the parameter study, when using the second hybrid similarity measure. This plot illustrates the effect of changing the Template size parameter from 10 by 10 pixels, to 20 by 20 pixels, to 30 by 30 pixels.

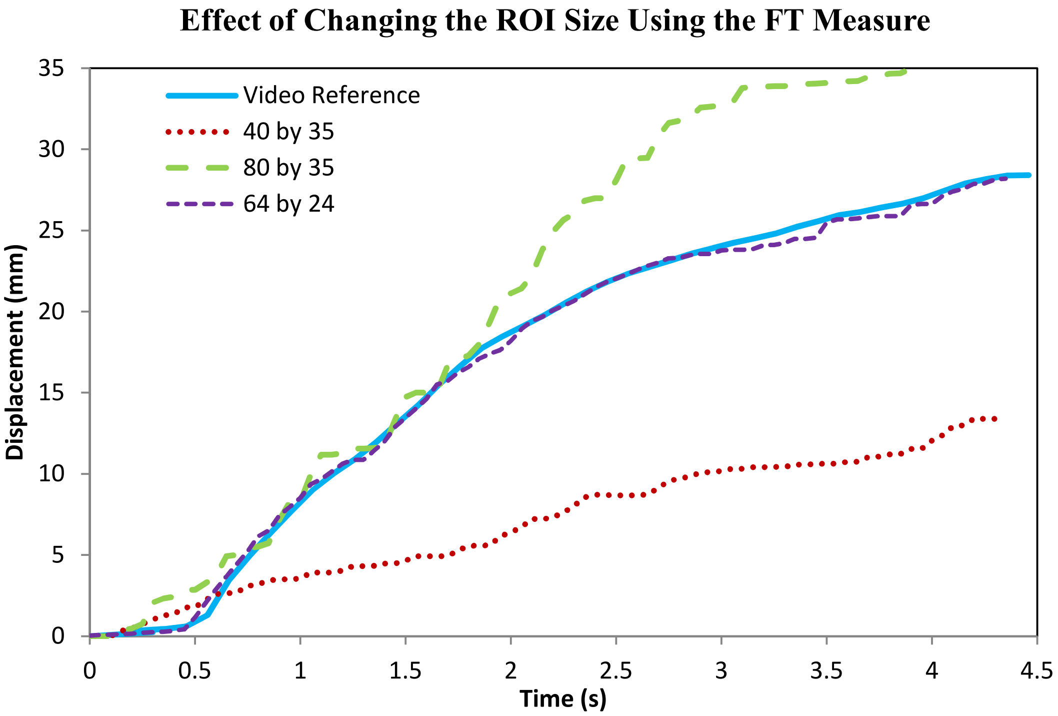

Figure 66:Illustrating the effect of changing the ROI size for Part 2 of the parameter study, when using the FT similarity measure. This plot illustrates the effect of changing the ROI size parameter from 40 by 35 pixels, to 80 by 35 pixels, to 64 by 24 pixels.

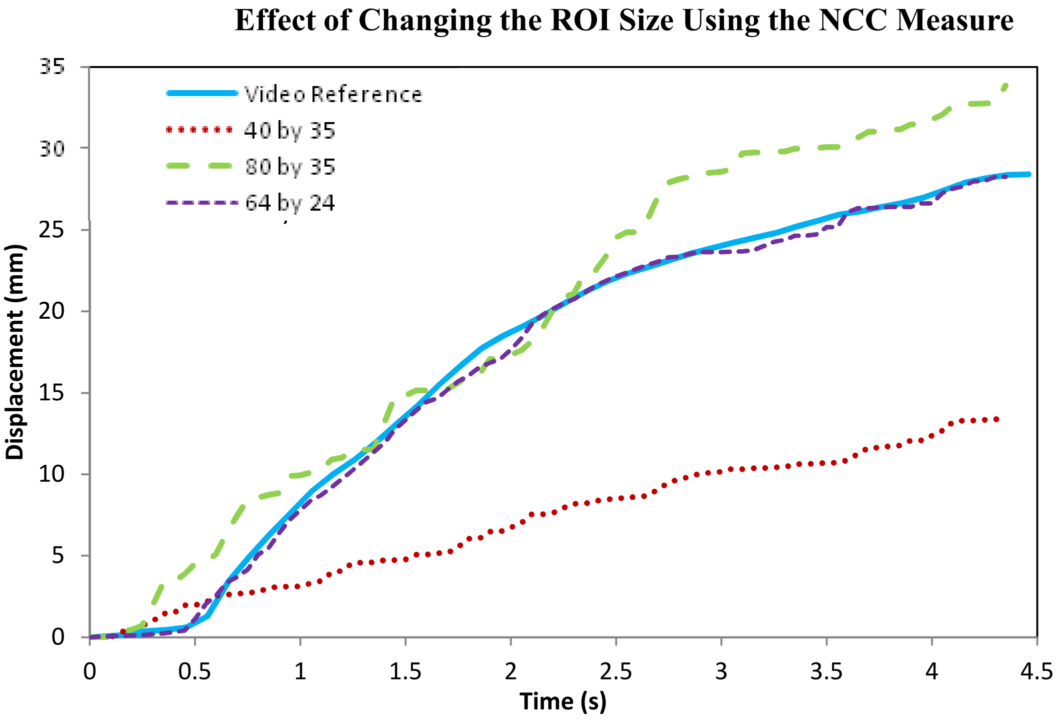

Figure 67: Illustrating the effect of changing the ROI size for Part 2 of the parameter study, when using the NCC similarity measure. This plot illustrates the effect of changing the ROI size parameter from 40 by 35 pixels, to 80 by 35 pixels, to 64 by 24 pixels.

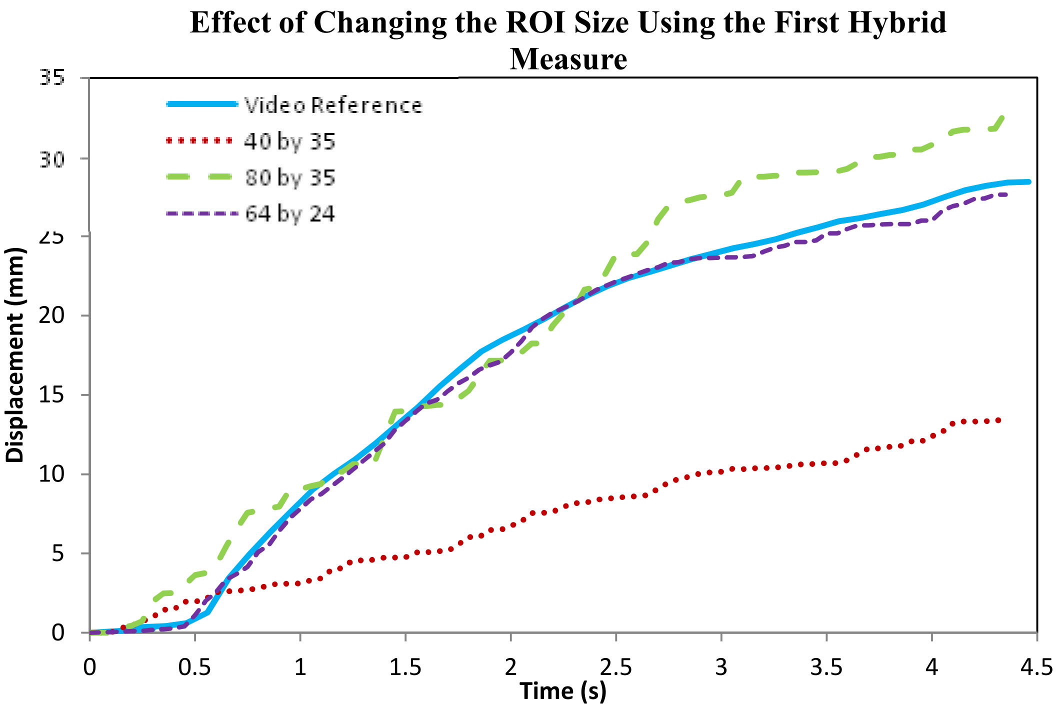

Figure 68: Illustrating the effect of changing the ROI size for Part 2 of the parameter study, when using the First Hybrid similarity measure. This plot illustrates the effect of changing the ROI size parameter from 40 by 35 pixels, to 80 by 35 pixels, to 64 by 24 pixels.

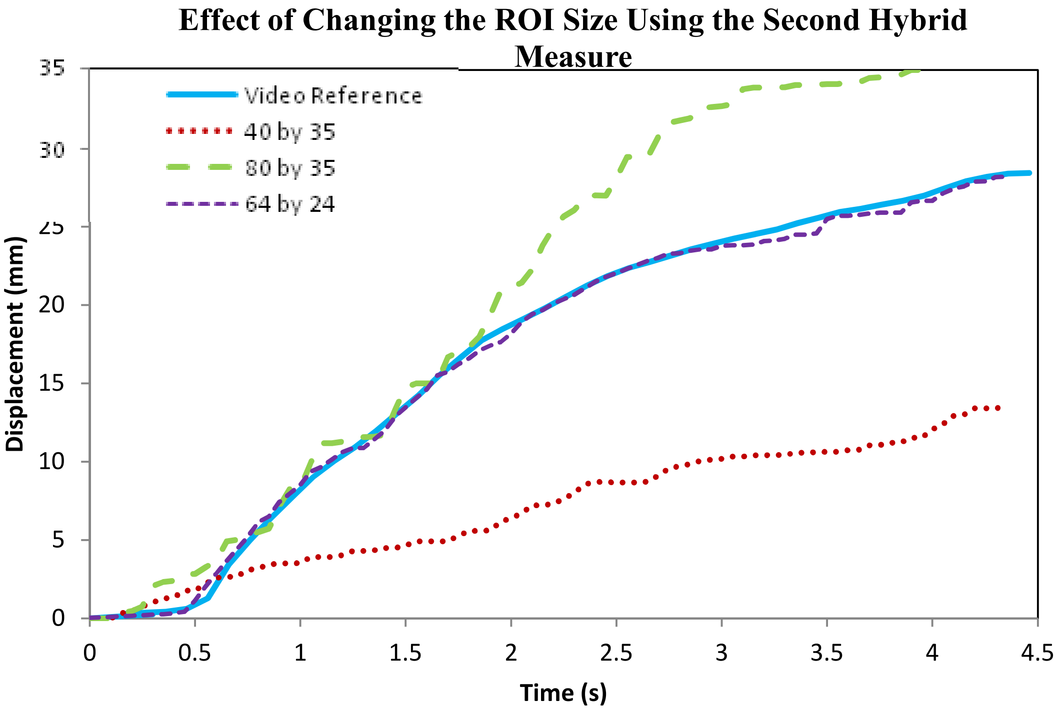

Figure 69: Illustrating the effect of changing the ROI size for Part 2 of the parameter study, when using the Second Hybrid similarity measure. This plot illustrates the effect of changing the ROI size parameter from 40 by 35 pixels, to 80 by 35 pixels, to 64 by 24 pixels.

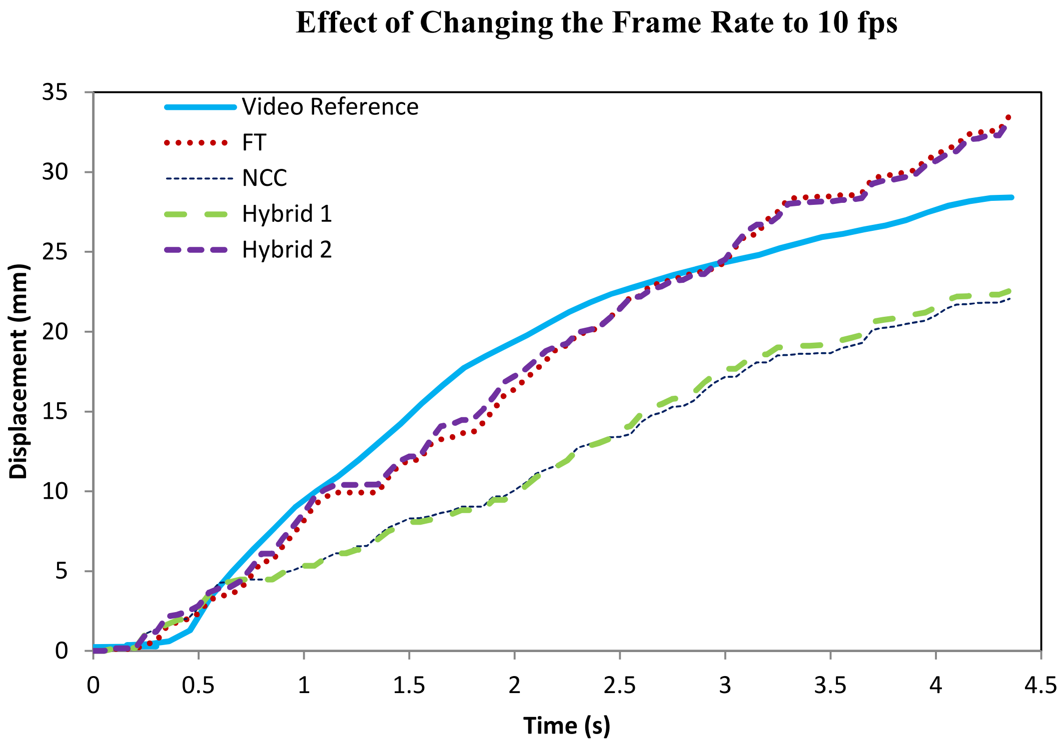

Figure 70: Illustrating the effect of changing the frame rate to 10 frames per second, for Part 2 of the parameter study. All four similarity measures were used.

7.4. EXPERIMENT 3: CADAVER-BASED STUDY TO ESTIMATE SINGLE TENDON EXCURSION

7.4.1. INTRODUCTION

Experiment 3 is inspired by the earlier preliminary experimentation (Experiment 1), whereby a linear array collects sequential B-Scan images of a singular moving cadaver tendon. The motivation for Experiment 3 is to further develop the speckle tracking algorithm accuracy using a research-based ultrasound machine and improved transducer hardware, with real tissue. As well, this experiment used improved hardware that couples to and actuates the tendon, thus providing an improved standard reference. In terms of tendon tracking, based on previous knowledge from Experiment 2, the speckle tracking algorithms are further developed to improve interframe and total displacement estimations. This includes the implementation of an auto-location technique in order to determine the optimal template placement, as well as a new frame skipping technique where the resolution and the tendon speed is taken into consideration. Experiment 3 is the first part of a four-day data-collection period, in which tendon excursion data is collected from two cadaver hands. On the second day, the index, middle and ring finger tendons from hand 1 are used, and on the third day the middle finger tendon from hand 2 is used.

7.4.2. RESULTS FOR EXPERIMENT 3

(a) Tendon Coupling Hardware and Actuator Hardware

Based on previous knowledge from Experiment 1, an improved cadaver tendon coupling and actuation system was developed as a standard reference, as described in Section 6.4.2, and shown by the photograph in Fig. 71. Unlike the coupling and actuation system from Experiment 1, which had the angle-error problem, the new coupling and actuation system ensures that tendon and displaces in the horizontal direction only. This allows for the programmed displacement of the actuators, to be in line with the tendon displacement as imaged by the transducer, and therefore to be a good reference motion. Further, upgraded motors, drivers and controllers are used, thus ensuring proper actuation. This set-up constitutes the standard design for Experiments 3, 4 and 5 with cadavers in the laboratory.

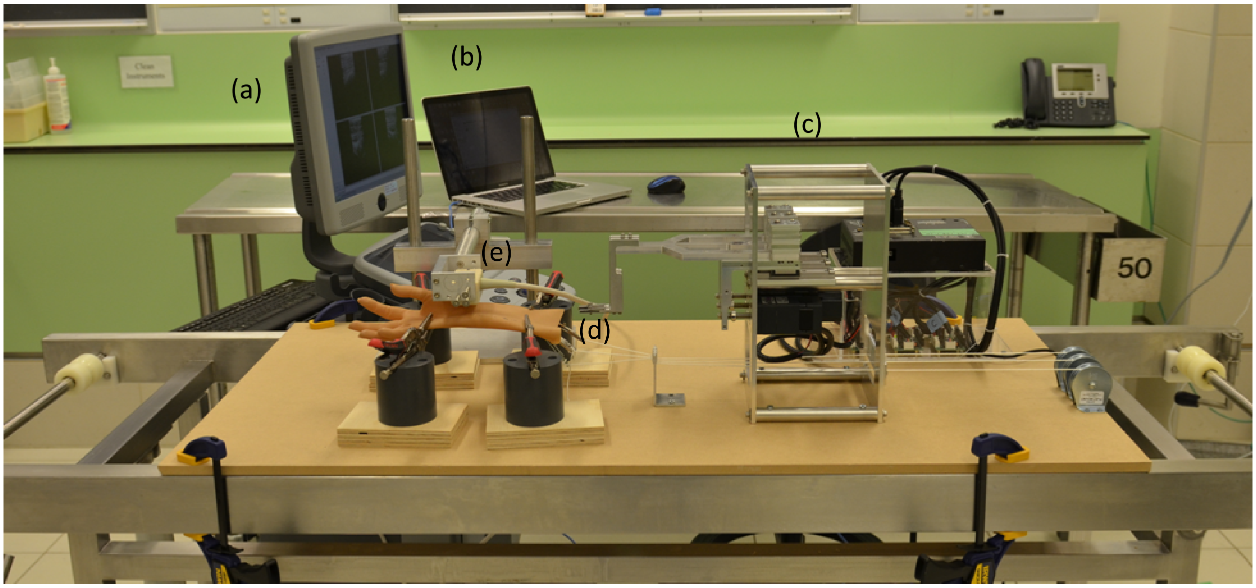

Figure 71: A photograph in the laboratory prior to attaching the cadaver hand. This shows the overall set-up for Experiments 3,4 and 5, using a mock set-up with a silicone glove, with (a) Sonix Touch ultrasound machine, (b) computer for the Galil controller, (c) the actuation system, (d) the hand and vice clamp apparatus, and (e) the transducer holder.

(b) Auto-location

It is important to develop the auto-location algorithm, since the motivation is toward prosthetic control, as was explained in Section 5.4. In addition, an auto-location technique places the task of identifying the template and ROI locations, based on computer algorithms, thereby removing subjective location selection by a human. This standardizes the selection of the optimal template location for any image sequence data set.

Using the parameters in Table 9, from Chapter 6, a displacement field for a given motion profile is estimated at many points along the tendon, using SAD, FT and NCC as similarity measures. The motion profiles for index, middle and the ring fingers individual tendon flexion can be found in Table 8 from Chapter 6. From Table 9 from Chapter 6, the parameters used are: the similarity measures SAD, FT and NCC, the stationary searching technique, *25 x 25 pixels* template size, *45 x 37 pixels* ROI size and the locations: $x \in [101,601]$ in steps of 10, and $z \in [180,280]$ in steps of 2. As well, the frame skipping technique, described in Chapter 5 and validated in 7.4.2 (d) of this Chapter, is used. For the motion profiles with the peak velocity of *15 mm/s* and the total displacement of *15 mm*, the frame skipping number, *k*, is set to *3*; while for motion profiles with the peak velocity of *10 mm/s* and total displacement of *10 mm*, *k* is set to *4*. The location giving the largest total tendon excursion in units of mm is considered the optimal template location for subsequent data sets for a given tendon.

A sample displacement field is shown in Fig. 72, which is computed from the ring finger's tendon, where the motion profile has a peak velocity of *15 mm/s* and a total displacement of *15 mm*. In Fig. 72, a single B-Scan frame is shown, with a red box indicating the location of the displacement field. Under the B-Scan frame, the three displacement fields are shown, computed using the SAD, FT and NCC similarity measures. From each displacement field, the maximum displacement value is found. This value is then used as the optimal template location for the analysis in Section 7.4.2(c)). The optimal template locations for each motion profile found by auto-location are shown in Table 17. This analysis is repeated for the index, middle and ring finger tendons from hand 1, and on the middle finger tendon from hand 2. Figures from remaining data-sets can be found in the Appendix.

(c) Interframe and total displacement

Once the optimal location of the template is found, the interframe displacement for a given tendon and reference motion profile is estimated, and then added cumulatively to create a displacement versus time curve, in units of mm. This is repeated for each similarity measure used in this experiment.

As an example, using an entry in Table 17 for the middle finger's data (motion profile: Day 1, 15mm/s, 15 mm), the speckle tracking algorithms are all used at the location *(131,222)*. As before, the interframe and cumulative displacement is estimated using the stationary ROI technique for each measure (SAD, FT and NCC). The cumulative displacement vs. time using each measure is plotted with the reference, as shown in Fig. 73. The estimated tendon displacement is compared to the reference displacement by first sampling the reference displacement points at the same time points as the displacements estimated by the ultrasound-based technique. The two metrics in Eqn. {25} and Eqn. {26} are used to determine the total displacement relative and instantaneous absolute error, respectively, in order to quantify the comparison between the proposed algorithm and the reference. This is repeated for all entries in Table 17. Alternatively, error bars can be implemented if more flexion data for each motion profile is acquired. This will be incorporated into the future work. The results from the two analysis metrics, as well as the computational time required for processing, for all data-sets can be seen in Table 18. Overall, the SAD algorithm is fastest, but NCC is has the lowest total displacement relative error (Table 19). Figures from remaining data-sets can be found in the Appendix.

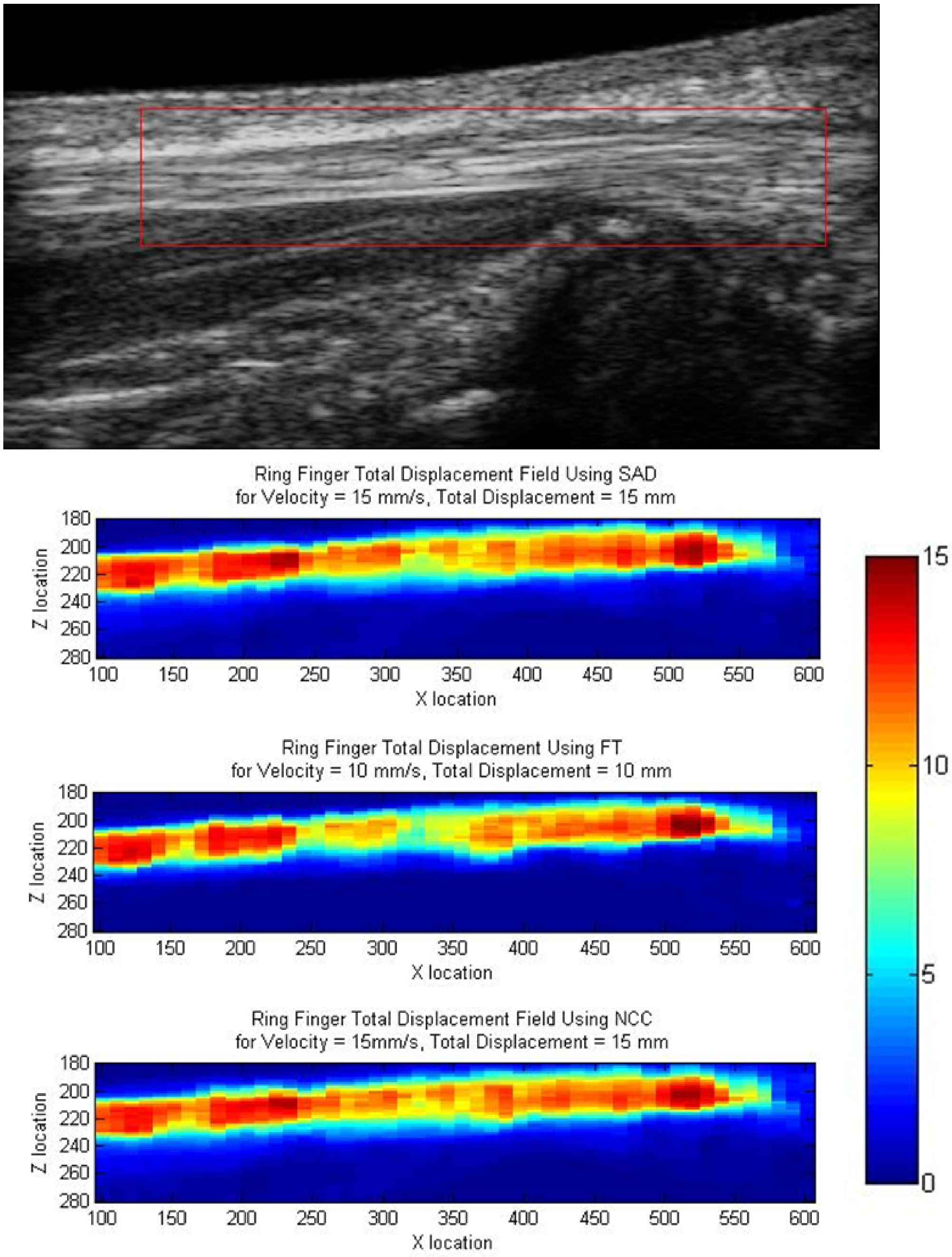

Figure 72: An example of the displacement field analysis using SAD, FT and NCC as similarity measures, for the ring fingers motion profile of peak velocity = 15 mm/s and total displacement = 15 mm.

TABLE 17: AUTO-LOCATION AND DISPLACEMENT FIELD RESULTS FOR SINGULAR TENDON EXCURSION

Hand	Finger's FDS Tendon	Motion Profile Peak Velocity (mm/s) = V Total Displacement (mm) = D	Similarity Measure	Estimated Maximum Displacement (mm)	Location of Maximum Displacement (x_1,z_1)
1	index	V15 D15	SAD	14.16	(201 ,256)
			FT	14.14	(201 ,256)
			NCC	14.53	(201 ,256)
		V10 D10	SAD	9.86	(571, 212)
			FT	9.86	(571, 212)
			NCC	9.83	(571, 212)
1	middle	V15 D15	SAD	14.80	(131, 222)
			FT	14.78	(131, 222)
			NCC	14.92	(131, 222)
		V10 D10	SAD	9.90	(131, 226)
			FT	9.90	(131, 226)
			NCC	10.08	(131, 226)
1	ring	V15 D15	SAD	14.49	(231, 208)
			FT	14.49	(231, 208)
			NCC	14.39	(231, 208)
		V10 D10	SAD	10.27	(511, 206)
			FT	10.27	(511, 206)
			NCC	10.24	(501, 202)
2	middle	V15 D15	SAD	13.66	(341, 208)
			FT	13.64	(341, 208)
			NCC	13.60	(341, 208)
		V10 D10	SAD	9.44	(241, 206)
			FT	9.42	(241, 206)
			NCC	9.57	(244, 207)

TABLE 18: DISPLACEMENT CURVE ANALYSIS FOR SINGLE TENDON EXCURSION

Hand	Finger's FDS Tendon	Motion Profile Peak Velocity (mm/s) = V Total Displacement (mm) = D	Similarity Measure	Total displacement relative error %	Avg. instantaneous displacement absolute error (mm)	Computational Time (ms/frame)
1	index	V15 D15	SAD	5.6	0.04	11
			FT	5.8	0.04	18
			NCC	3.1	0.11	12
		V10 D10	SAD	3.4	0.02	11
			FT	3.4	0.02	19
			NCC	3.6	0.02	12
1	middle	V15 D15	SAD	1.3	0.03	11
			FT	1.5	0.03	19
			NCC	0.5	0.03	12
		V10 D10	SAD	2.9	0.20	11
			FT	2.9	0.20	19
			NCC	1.1	0.20	12
1	ring	V15 D15	SAD	3.4	0.10	11
			FT	3.4	0.10	19
			NCC	4.1	0.25	12
		V10 D10	SAD	0.7	0.07	11
			FT	0.7	0.07	20
			NCC	0.4	0.07	12
2	middle	V15 D15	SAD	8.9	0.08	11
			FT	9.1	0.08	21
			NCC	9.3	0.08	12
		V10 D10	SAD	7.5	0.13	11
			FT	7.6	0.13	19
			NCC	6.1	0.15	12

TABLE 19: AVERAGE RELATIVE ERROR OF TOTAL DISPLACEMENT

SAD: Average relative error (%)	FT: Average relative error (%)	NCC: Average relative error (%)
4.2	4.3	3.5

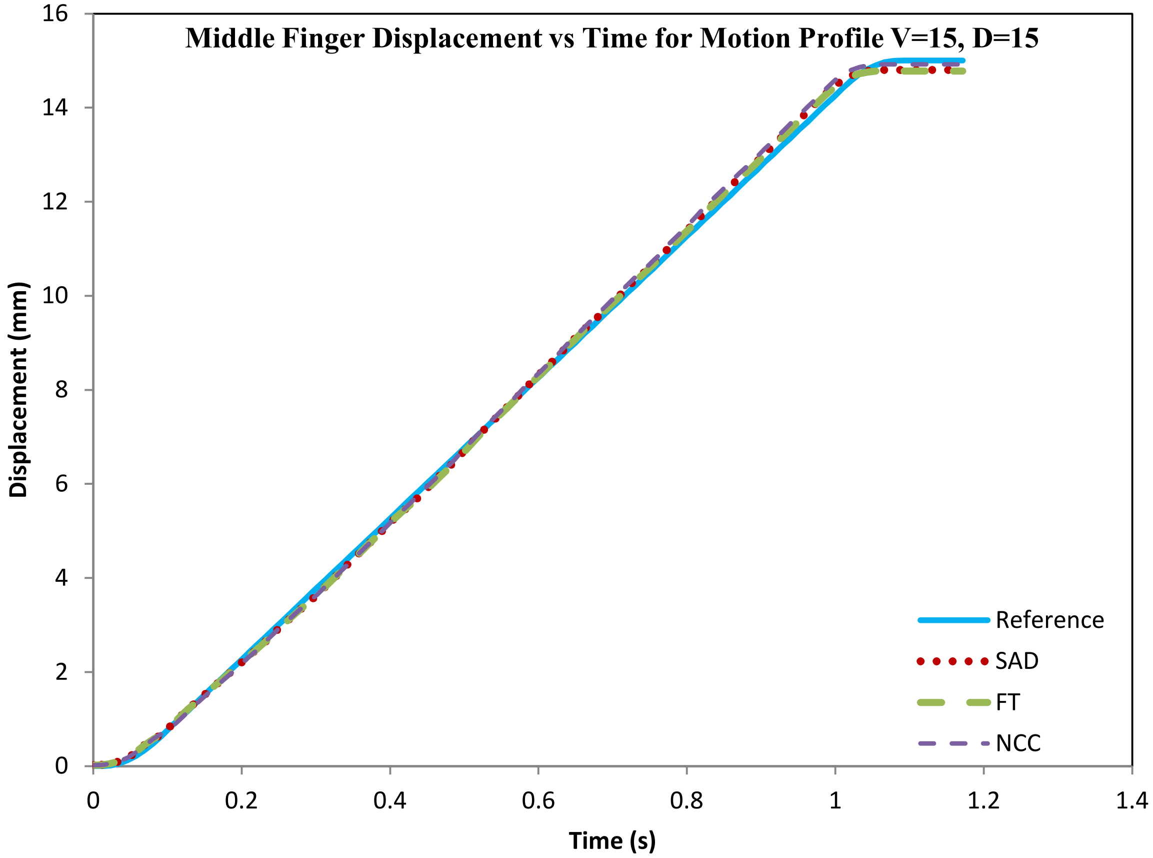

Figure 73: An example of a displacement vs time curve for the proposed speckle tracking techniques SAD, FT and NCC. This data is from the first hands middle finger's tendon displacement, with motion profile V=15, D=15.

(d) Frame Skipping

Most speckle tracking algorithms compare the template in frame *t* to the blocks in the next frame in *t+1,* in order to estimate interframe displacement. Since every ultrasound imaging system is different, the resolution may not be sufficient to detect small interframe displacements. This is a function of the system's frame rate and lateral resolution, as well as the tendon's lateral displacement and velocity, as previously described. This study investigates if skipping frames can mitigate tracking issues. Frame skipping is defined as the comparison of the template in frame *t*, to the blocks in frame *t*+*k*, where *k* is an integer. Thus, this necessitates the development of a technique which can determine the optimal frame skipping number, *k*.

As shown in Fig. 74, using SAD on the ring finger's tendon data (with motion profile V=15,D=15), the highly dependent nature of frame skipping and the success of tracking is illustrated. To empirically determine the optimal frame skipping constant γ from Eqn. {32}, the data from a given data set from Table 8 in Chapter 6 is reprocessed using the frame skipping numbers, $k=1,2,3,4,5$. The data is re-analyzed to determine which one has the lowest total displacement relative error, when being compared to the reference. The analysis for all motion profiles (from the first hand) can be found in Table 20. For a given entry in Table 20, the frame skipping number with the lowest error (highlighted in red) is chosen as the optimal frame skipping number, and then Eqns. {31} and {32} are used to estimate the frame skipping constant, γ, which is assumed to be valid for any data set imaged by any ultrasound system. The average value for γ is estimated as *8.24 pixels*. After the constant is determined, Eqn. {33} can be used for all future data sets in order to determine the frame skipping number, *k*.

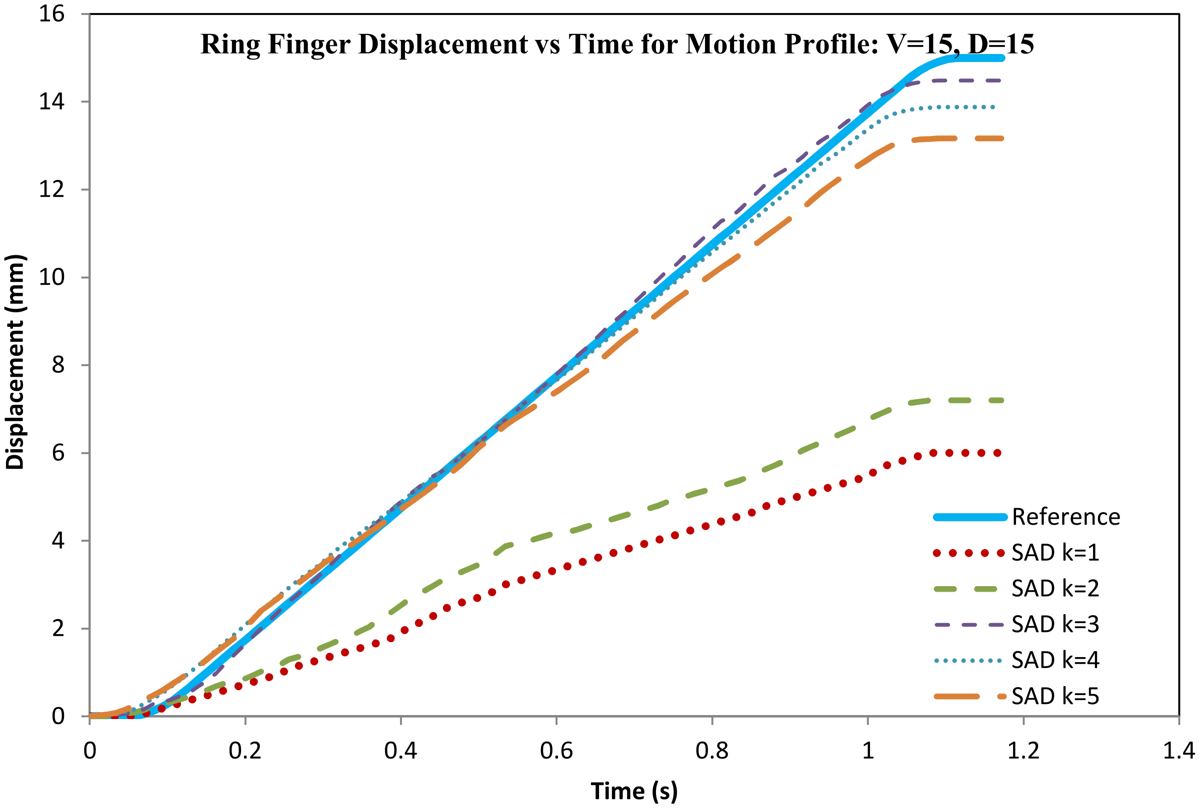

Figure 74: An example of the effect different frame skipping numbers has on tracking success. For the first hand's ring finger tendon displacement with motion profile V=15,D=15, k=3 performed the best.

Table 20: Frame Skipping Comparison Using SAD, FT and NCC by Total Displacement Relative Error (minimum relative error in red)

Hand	Finger's FDS Tendon	Motion Profile Peak Velocity (mm/s) = V Total Displacement (mm) = D	Frame Skipping k	Total displacement relative error % SAD	Total displacement relative error % FT	Total displacement relative error % NCC
1	index	V15 D15	1	66.0	6.7	63.2
			2	19.9	20.1	18.0
			3	5.6	5.8	3.1
			4	6.4	6.54	3.2
			5	9.6	9.62	7.4
		V10 D10	1	51.2	50.6	52.9
			2	49.3	49.3	50.3
			3	16.6	16.8	17.0
			4	3.4	3.4	3.6
			5	6.3	6.3	5.1
1	middle	V15 D15	1	50.8	50.8	53.2
			2	15.0	14.8	16.4
			3	1.3	1.5	0.5
			4	12.3	12.5	11.6
			5	19.0	19.2	18.6
		V10 D10	1	62.3	59.4	61.8
			2	58.5	58.2	61.1
			3	31.5	31.5	36.4
			4	2.9	2.9	1.1
			5	10.2	10.1	8.8
1	ring	V15 D15	1	60.0	60.0	60.0
			2	52.0	52.0	52.0
			3	3.4	3.4	4.1
			4	7.5	7.5	8.3
			5	12.2	12.4	12.9
		V10 D10	1	55.0	55.3	57.6
			2	45.8	45.8	44.0
			3	14.0	14.0	26.6
			4	0.7	0.7	0.4
			5	5.5	5.5	5.2

7.5. EXPERIMENT 4: CADAVER-BASED STUDY TO ESTIMATE MULTI-TENDON EXCURSION

7.5.1. INTRODUCTION

This study uses the sparse quad-array transducer to implement the proposed multiple-tendon detection and tracking system. Experiment 4 is part of the previously described four-day data collection period, in which a cadaver hand is used to validate the proposed technique. The software collects independent image sequences from each of the four sub-arrays. The previously described auto-location technique is employed on each sub-array image sequence, in order to determine the optimal template placement. As well, the optimal template location is used to estimate interframe and total displacement, as before. Since the cadaver hand is actuated using the multi-actuator system, there are a number of possible motion profiles that can be done, with various fingers moving individually, or in combination, at various speeds and displacements. These motion profile combinations (named A, B, C, etc. . .) are listed in Table 10 in Chapter 6. On the second and fourth day of data collection, the index, middle and ring finger tendons from the first hand are used for this experiment. Since the second hand's index tendon was damaged, the second hand was not used for the multi-tendon study.

7.5.2. RESULTS FOR EXPERIMENT 4

(a) Auto-Location

As previously mentioned for Experiment 3, an auto-location technique is developed in order to identify the template locations using computer algorithms, thereby removing subjective location selection by a human. This standardizes the selection of the optimal template location for any image sequence data set.

Using the parameters in Table 11 from Chapter 6, a displacement field for a given motion profile is estimated at many points along the tendon (in each sub-array), using SAD, FT and NCC as similarity measures. The motion profiles for index (A), middle (B) and the ring (C) fingers individual tendon flexion can be found in Table 10 from Chapter 6. From Table 11 from Chapter 6, the parameters used are: the similarity measures SAD, FT and NCC, the stationary searching technique, *5 x 50 pixels* template size, *25 x 62 pixels* ROI size and the template locations: $x \in [21,54]$ in steps of 1, and $z \in [500,800]$ in steps of 10. As well, the frame skipping technique, previously validated in 7.4.2 (d) of this Chapter, is used. For the motion profiles with the peak velocity of *15 mm/s* and the total displacement of *15 mm*, the frame skipping number, *k*, is set to *8*; while for motion profiles with the peak velocity of *10 mm/s* and total displacement of *10 mm*, *k* is set to *12*.

A sample displacement field created for the auto-detection and auto-location technique is illustrated in Fig. 75. In this example, the cadaver hand is actuated using motion profile C (Table 10, Chapter 6), which only moves the ring finger's tendon, while all other fingers remain stationary. This motion profile has a reference peak velocity of *15 mm/s* and reference total displacement of *15 mm* for the ring finger tendon. The short-hand notation for this motion profile is referred to as: Day 2, C-Series, V15, D15. In Fig. 75, the SAD similarity measure is used to compute the four displacement fields, from each of the four sub-arrays. To help the reader visualize the data, displacement fields computed from each sub-array are superimposed onto the four B-Scans acquired from the same sub-arrays. Notice that the displacement field is only computed in the ROI, and is located in the actual ROI location, within the larger B-Scan image. Recall, the displacement field is calculated from the entire B-Scan image sequence, whereas the B-Scan shown here is only from the first motion frame of the sequence. From each field in arrays 1 to 4, the maximum displacement value is found, and the corresponding location of that maximum value is stored, as shown in Table 21. This computational process is then repeated for the FT and NCC similarity measures, on this same motion profile C. Now, the auto-location algorithm must determine which of the four-sub arrays is imaging the moving tendon. This is done by instructing the algorithm to find the array containing the maximum displacement value in Table 21, of any array. The array containing this maximum value will be considered as the array that contains the displacing tendon. For this example, the ring finger's tendon is considered to be in array 1, since the largest displacement value within this table resides there. This is also visible in Fig. 75. The auto-location algorithm then determines the best tracking location for the ROI and template. Using array 1 only, the *x,z* location listed in Table 21 for this array, is used as the template location. Since the three different SAD, FT and NCC algorithms are being investigated, all three are used here in this study.

The auto-location data analysis process described in the previous paragraph, is repeated for the tendon motion profiles for A (index), B (middle) and C (ring) (Table 10, Chapter 6). All displacement fields and their corresponding tables can be found in the Appendix (A.3). As a note, for the proposed prosthetic application, the auto-location can only function when a single finger (A, B, or C) is moving. It will not work for combination profiles. Combination profiles are handled as described next, after auto-location is complete. Once auto-location is complete, the algorithm will record two pieces of information: (i) which finger tendon is being imaged by which array, and (ii) within each array, the optimal location for the template and ROI.

Total Displacement Field Using SAD, Motion Profile: Day 2, C-Series V15, D15

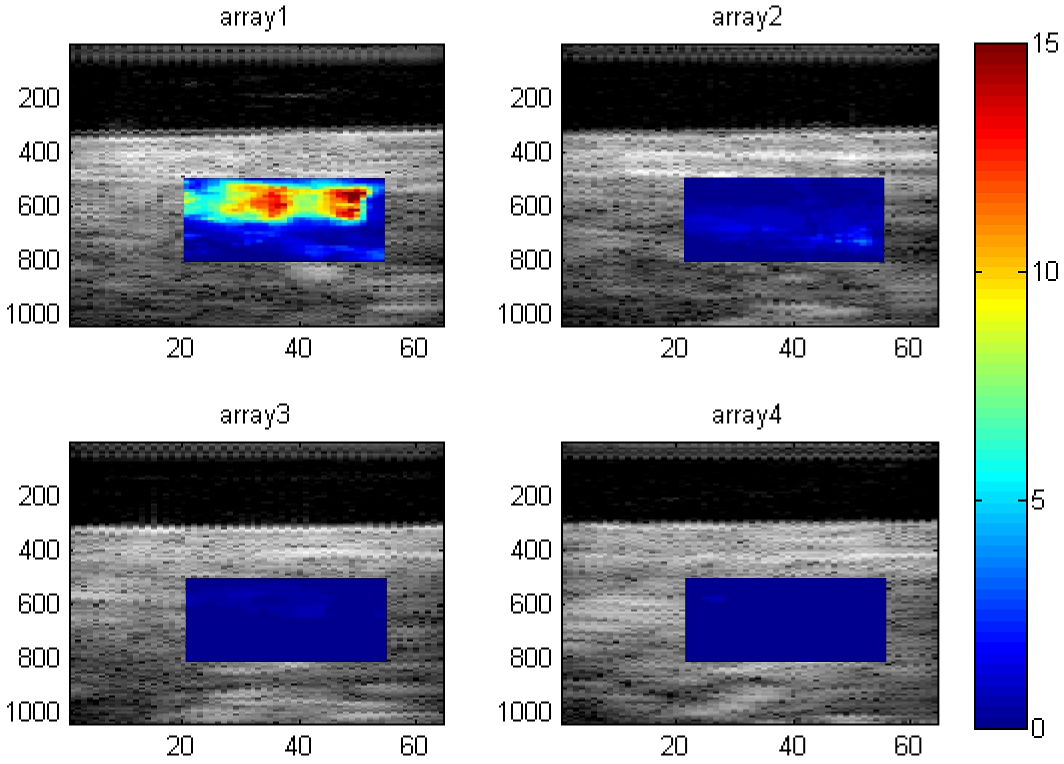

Figure 75: An example of the displacement field analysis using SAD as a similarity measure, for the ring fingers motion profile: Day 2, C-Series, V15, D15.

TABLE 21: DISPLACEMENT FIELD ANALYSIS FOR THE RING FINGER TO DETERMINE OPTIMAL TEMPLATE LOCATION

Ring Finger Tendon
Motion Profile: Day 2, C-series, V15, D15
V=Reference Maximum Velocity (mm/s), D=Reference Total Displacement (mm)

Similarity Measure	Array 1 Maximum Displacement (mm)	Location (x,z)	Similarity Measure	Array 2 Maximum Displacement (mm)	Location (x,z)
SAD	14.60	(49, 560)	SAD	3.74	(50, 720)
FT	14.91	(49, 560)	FT	3.20	(49, 690)
NCC	13.01	(49, 550)	NCC	4.21	(47, 690)
Similarity Measure	Array 3 Maximum Displacement (mm)	Location (x,z)	Similarity Measure	Array 4 Maximum Displacement (mm)	Location (x,z)
SAD	0.67	(41, 620)	SAD	0.88	(26, 570)
FT	0.67	(41, 620)	FT	0.88	(26, 570)
NCC	0.70	(41, 620)	NCC	0.53	(25, 580)

The multi-tendon motion profiles found in Table 10 from Chapter 6 are: AB (index + middle), AC (index + ring), BC (middle + ring) and ABC (index + middle + ring). These profiles, along with the individual A, B and C profiles represent typical motions of human fingers. An example displacement field for the motion profile AB (index + middle) using SAD is illustrated in Fig. 76. From Fig. 76, motion is observed in all arrays, with the highest displacement appearing to occur in arrays 2-4. As mentioned in the previous paragraph, these displacement fields are not used to auto-locate the index and middle finger. They are used to track the displacement of the index and middle finger. This is because multiple tendons are moving at the same time, thus it is not possible auto-locate since that requires a single, known moving finger. Instead, the locations of the individual index and middle finger, determined earlier by auto-location, are used as the ROI locations for tracking the multi-tendon excursion. Therefore, this is a three-stage process for (i) auto-locating the sub-arrays corresponding to the index, middle and ring fingers from their tendon displacement fields, (ii) auto-locating the tracking locations for the index, middle and ring fingers from their displacement fields, and (iii) ongoing tracking of the displacement of the index, middle and ring fingers making use of info from auto-location. In this sense, auto-location can be described as a calibration process for multi-tendon excursion, whereas stage (iii) can be described as an operational process for tracking multi-tendon excursion. In the example given by Fig. 76, using SAD for the AB-series motion profile, the index tendon is found to be located at

(32, 650) in array 4, and the middle finger tendon is found to be located at *(24, 560)* in array 2. These locations are obtained independently, from the A and B motion profile analysis in Tables A.3 found in the Appendix. Likewise, the locations using FT and NCC in arrays 2 and 4 can be also be taken from Table A.3 in the Appendix. This is repeated on all multi-tendon data from days 2 and 4.

Total Displacement Field Using SAD, Motion Profile: Day 2, AB-Series V10,

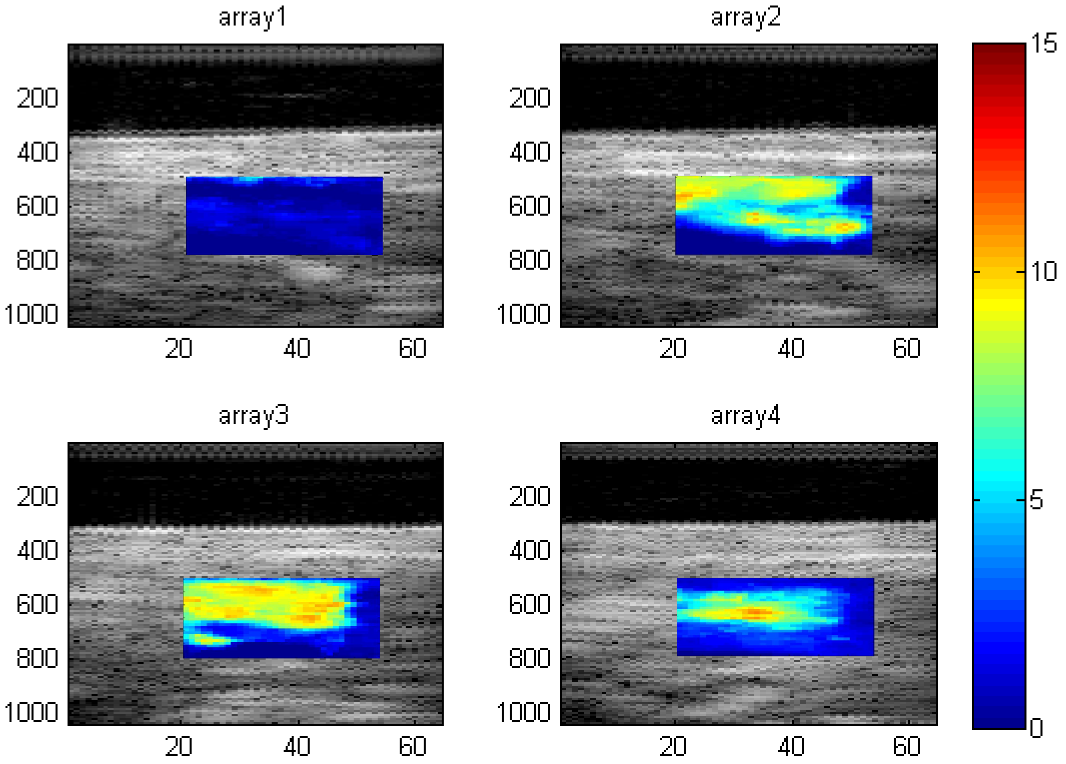

Figure 76: An example of a displacement field from a multi-tendon motion profile. Here, the SAD measure is used with the AB-Series (Day 2, V10, D10) motion profile.

(b) Interframe and Total Displacement

As described in the previous section, once the optimal template location of a given tendon (index, middle or ring finger tendon) is found by auto-location, the interframe and total displacement can be estimated. Interframe and total displacement tracking would be an on-going tracking process, when used for prosthesis control. This is achieved for a given motion profile from Table 10 in Chapter 6, by finding the optimal location for the template with auto-location, and then using SAD, FT or NCC to estimate interframe displacement. The displacement is then added cumulatively to create an estimated displacement vs. time curve, in units of mm. The standard reference cumulative displacement vs. time curve is also plotted on this graph for comparison. The estimated total displacement is obtained from this graph, and compared to the reference total displacement. This is repeated at the determined optimal location for each similarity measure used in this experiment. Using the previous example for the motion profile C ring finger's tendon excursion, the maximum total displacement was found in array 1. The location for a given similarity measure is used to create their respective displacement vs. time curves, as shown in Fig. 77. The total displacement using each measure from in array 1 is taken from this plot. The estimated tendon displacement is compared to the reference displacement by first sampling the reference displacement points at the same time points as the displacements estimated by the ultrasound-based technique. The two metrics in Eqn. $\{1\}$ and Eqn. $\{2\}$ are used to determine the relative total displacement error, R_D, and instantaneous displacement absolute error, A_{id}, respectively, in order to quantify the comparison between the proposed algorithm and the reference. For the given example of the ring finger's motion profile, using the SAD technique with the template location at *(49, 560)*, the relative error $R_D$is 2.6% and the absolute error $A_{id}$is 0.94 mm, as shown in Table 22. Also in this table, are the results using the FT and NCC measures on the same data set. This process is repeated for the index (A-series), middle (B-series) and ring (C-series) finger's tendon excursion from data collected on days 2 and 4, and the analysis can be found in Tables 22 and 23, respectively.

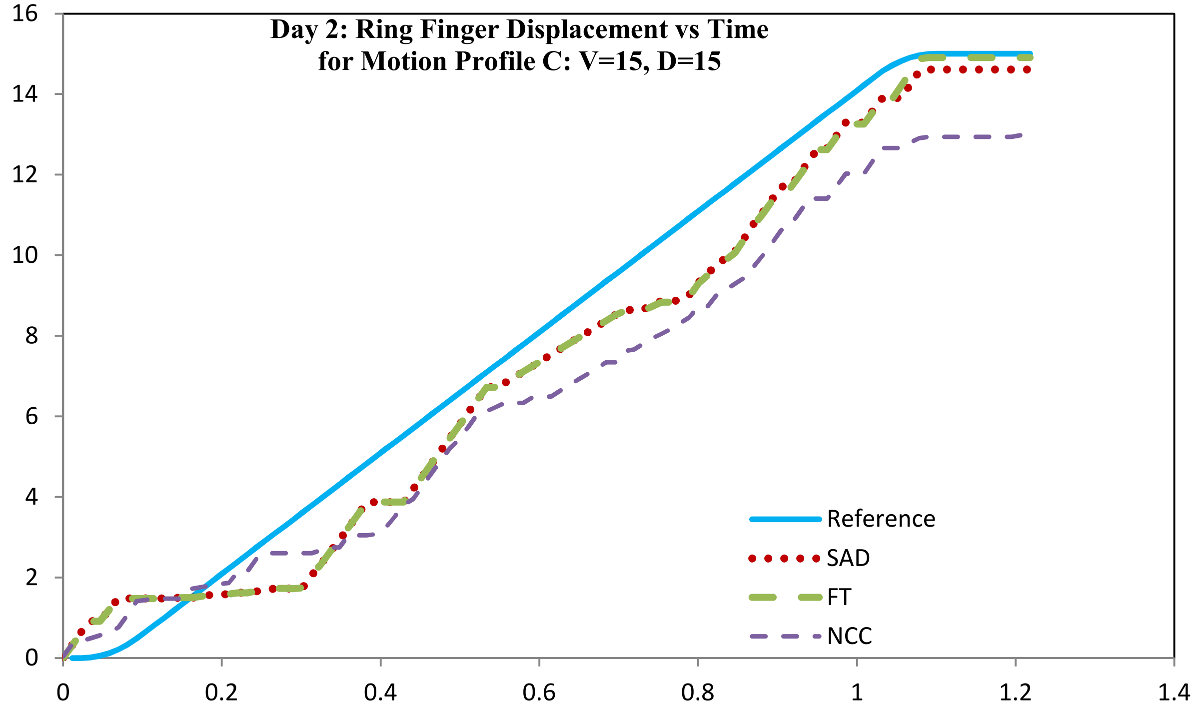

Figure 77: An example of a displacement vs time curve using SAD, FT and NCC for the ring fingers motion profile: Day 2, C-Series, V15, D15.

Similarly for the multi-tendon motion profiles, the template location determined by the individual tendon calibration is used with each similarity measure in order to obtain a cumulative displacement vs. time plot and total displacement estimation. For the example given above for the AB (index + middle) motion profile, the displacement vs. time curves for the middle finger are illustrated in Fig. 78. As well, the relative total displacement error and cumulative displacement absolute error is calculated, in order to quantify the comparison between the proposed algorithm and the reference. For the given example for the middle finger tendon excursion with the AB-series motion profile, the relative error is 4.7% using SAD, and the absolute error using SAD is 0.10 mm, as shown in Table 24. This process is repeated for the data collected on day 2 and 4 for the multi-tendon motion profiles. The results from the analysis metrics for multi-tendon data-sets from both days can be seen in Tables 24-25.

The figures from data-sets can be found in the Appendix. The average total displacement relative error using the SAD, FT and NCC techniques for all data-sets is shown in Table 26. As shown, the NCC technique was more accurate overall in terms of total displacement estimation.

TABLE 22: DISPLACEMENT CURVE ANALYSIS FOR MULTI-TENDON EXCURSION FROM DAY 2

Day	Finger's FDS Tendon	Motion Profile Peak Velocity (mm/s) = V Total Displacement (mm) = D	Similarity Measure	Total displacement relative error %	Avg. instantaneous displacement absolute error (mm)
2	index	A: V15 D15	SAD	5.4	0.16
			FT	20.7	0.83
			NCC	10.2	0.86
		A: V10 D10	SAD	8.7	0.05
			FT	13.9	0.02
			NCC	0.8	0.01
2	middle	B: V15 D15	SAD	4.8	0.09
			FT	4.7	0.06
			NCC	3.1	0.01
		B: V10 D10	SAD	6.3	0.05
			FT	9.5	0.14
			NCC	8.2	0.30
2	ring	C: V15 D15	SAD	2.6	0.94
			FT	0.1	0.25
			NCC	13.7	0.06
		C: V10 D10	SAD	8.1	0.01
			FT	14.2	0.16
			NCC	3.4	0.06

TABLE 23: DISPLACEMENT CURVE ANALYSIS FOR MULTI-TENDON EXCURSION FROM DAY 4

Day	Finger's FDS Tendon	Motion Profile Peak Velocity (mm/s) = V Total Displacement (mm) = D	Similarity Measure	Total displacement relative error %	Avg. instantaneous displacement absolute error (mm)
4	index	A: V15 D15	SAD	14.8	0.02
			FT	15.9	0.03
			NCC	10.5	0.30
		A: V10 D10	SAD	11.2	0.47
			FT	10.5	0.48
			NCC	8.1	0.01
4	middle	B: V15 D15	SAD	1.2	0.03
			FT	9.7	0.11
			NCC	32.3	0.32
		B: V10 D10	SAD	7.8	0.08
			FT	9.9	0.10
			NCC	26.7	0.09
4	ring	C: V15 D15	SAD	29.6	0.48
			FT	34.6	0.55
			NCC	8.8	0.27
		C: V10 D10	SAD	46.0	0.46
			FT	36.0	0.28
			NCC	30.0	0.24

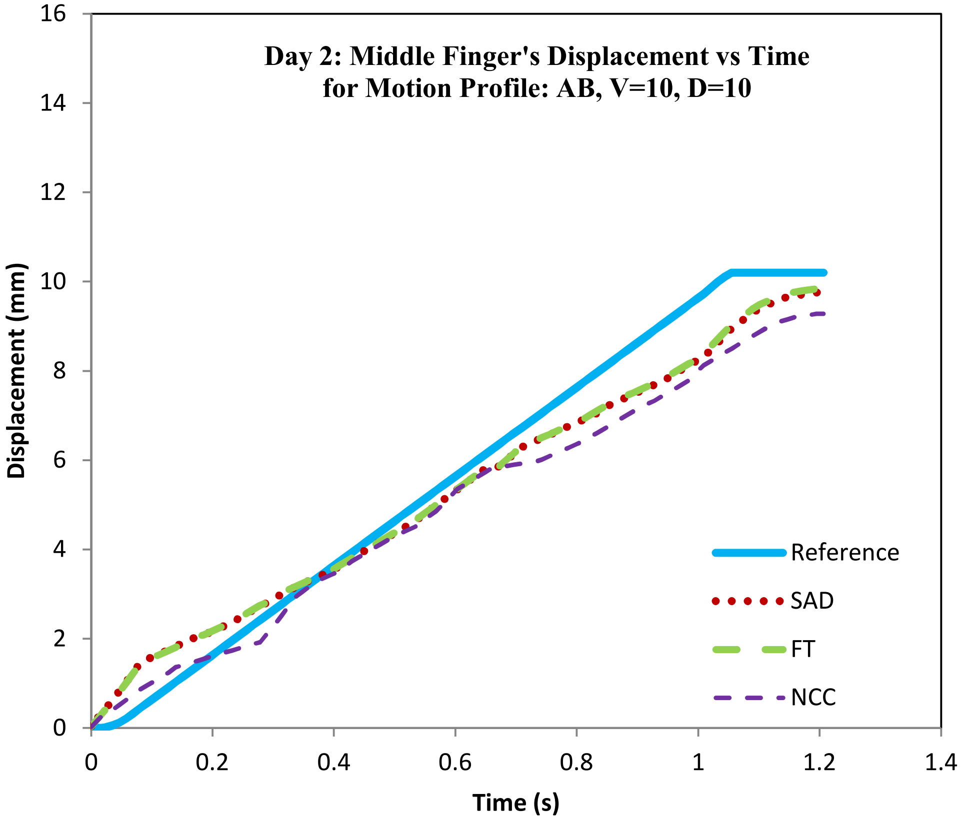

Figure 78: An example of a displacement vs time curve using SAD, FT and NCC for the middle finger, with motion profile: Day 2, AB-Series, V10, D10.

TABLE 24: DISPLACEMENT CURVE ANALYSIS FOR MULTI-TENDON EXCURSION FROM DAY 2

Day	Finger's FDS Tendon	Motion Profile Peak Velocity (mm/s) = V Total Displacement (mm) = D	Similarity Measure	Total displacement relative error %	Avg. instantaneous displacement absolute error (mm)
2	Index	AB: V10 D10	SAD	1.3	0.08
			FT	7.0	0.08
			NCC	13.0	0.06
2	Middle	AB: V10 D10	SAD	4.7	0.10
			FT	4.0	0.09
			NCC	9.5	0.05
2	Index	AC: V10 D10	SAD	16.2	0.08
			FT	14.4	0.07
			NCC	12.8	0.09
2	Ring	AC: V10 D10	SAD	16.3	0.08
			FT	14.5	0.16
			NCC	3.3	0.07
2	Middle	BC: V10 D10	SAD	7.5	0.42
			FT	11.9	0.08
			NCC	1.1	0.12
2	Ring	BC: V10 D10	SAD	34.4	0.13
			FT	47.7	0.33
			NCC	7.8	0.01
2	Index	ABC: V10 D10	SAD	14.1	0.33
			FT	23.3	0.23
			NCC	3.2	0.14
2	Middle	ABC: V10 D10	SAD	17.9	0.10
			FT	4.7	0.07
			NCC	15.3	0.10
2	Ring	ABC: V10 D10	SAD	36.5	0.39
			FT	44.9	0.60
			NCC	15.5	0.19

TABLE 25: DISPLACEMENT CURVE ANALYSIS FOR MULTI-TENDON EXCURSION FROM DAY 4

Day	Finger's FDS Tendon	Motion Profile Peak Velocity (mm/s) = V Total Displacement (mm) = D	Similarity Measure	Total displacement relative error %	Avg. instantaneous displacement absolute error (mm)
4	Index	AB: V10 D10	SAD	1.3	0.08
			FT	7.0	0.08
			NCC	13.0	0.06
4	Middle	AB: V10 D10	SAD	4.7	0.10
			FT	4.0	0.09
			NCC	9.5	0.05
4	Index	AC: V10 D10	SAD	16.2	0.08
			FT	14.4	0.07
			NCC	12.8	0.09
4	Ring	AC: V10 D10	SAD	16.3	0.08
			FT	14.5	0.16
			NCC	3.3	0.07
4	Middle	BC: V10 D10	SAD	7.5	0.42
			FT	11.9	0.08
			NCC	1.1	0.12
4	Ring	BC: V10 D10	SAD	34.4	0.13
			FT	47.7	0.33
			NCC	7.8	0.01
4	Index	ABC: V10 D10	SAD	14.1	0.33
			FT	23.3	0.23
			NCC	3.2	0.14
4	Middle	ABC: V10 D10	SAD	17.9	0.10
			FT	4.7	0.07
			NCC	15.3	0.10
4	Ring	ABC: V10 D10	SAD	36.5	0.39
			FT	44.9	0.60
			NCC	15.5	0.19

TABLE 26: AVERAGE RELATIVE ERROR OF TOTAL DISPLACEMENT FROM MULTI-TENDON DATA

SAD: Average relative error (%)	FT: Average relative error (%)	NCC: Average relative error (%)
14.8	17.5	10.6

7.6. EXPERIMENT 5: CADAVER-BASED STUDY TO ESTIMATE THE ONSET OF TENDON EXCURSION

7.6.1. INTRODUCTION

The previous experiments (Experiments 1-4) estimate the interframe and total displacement of a tendon from a non-amputee performing a large excursion. However, the hypothesis of this thesis is that the previously described techniques can be used to detect and monitor the tendon displacement from an amputee. In this case, the tendon system may be partially intact, damaged, or have low function. Therefore, it is envisioned that the tendon excursion will not displace with the same magnitude as a healthy person, thus justifying further investigation into the limiting factors of the proposed technique. This study forms the basis to such investigations by determining the smallest amount of displacement needed to auto-locate the tendon, as well as determining the smallest detectable tendon displacement, known as the onset displacement. The data for this experiment is obtained on the third day with the second hand, using the linear array. On the fourth day, the onset experiment is performed with the first hand and the quad-array.

7.6.2. RESULTS OF EXPERIMENT 5

(a) Auto-location and displacement onset of a single tendon using the linear array

The experiment was accomplished by actuating the middle finger's tendon with a given motion profile in Table 12 from Chapter 6, while the linear array and the Sonix Touch system collected and saved the .b8 data. The motion profiles in Table 12 from Chapter 6 are that of small displacements, ranging from 0.2 mm to 1.0 mm.

First, the previously described auto-location algorithm is used in order to display the displacement fields using SAD, FT and NCC similarity measures. Since the interframe displacements are so small, the displacement between frame *t* and frame *t+10* is compared, and a total displacement value is obtained. The entire excursion is contained between these frames, and so the interframe displacement technique is not used in this study. This is repeated with each motion profile in Table 12 from Chapter 6 in order to determine which motion profile provides the smallest amount of displacement needed to auto-locate the tendon. It is important to note that the tracking algorithms can only determine integer pixel displacements, and is limited by the image resolution (Table 27). Thus, the minimum displacement which can be detected is 0.06 mm, or a single pixel of displacement using the linear array. For this experiment, the smallest onset of displacement is the 0.2 mm motion profile. As an example using SAD, the displacement field shows a highlighted area of the tendon for the motion profile of 0.20 mm (Fig. 79). As the motion profiles increase in displacement, the tendon becomes more visible. From Fig. 79 using SAD, it is determined that the motion profile of 0.44 mm can be used to auto-locate the tendon. As well, from these displacement fields, the smallest detectable displacement (i.e. the onset) is also determined. From these fields using SAD, the onset of displacement is determined as the smallest displacement giving the ability to detect the tendon above the background noise. For the example using SAD, the motion profile with 0.2 mm of displacement shows adequate displacement in order to quantify if the tendon is moving or not. The other measures (FT and NCC), performed similarly.

TABLE 27: CORRESPONDING DISPLACEMENT IN PIXELS AND MILLIMETERS FOR THE LINEAR ARRAY

Displacement in Pixels	Displacement in mm
1	0.06
2	0.12
3	0.18
4	0.24
5	0.30
6	0.36
7	0.42
8	0.48
9	0.54
10	0.60
11	0.66
12	0.72
13	0.78
14	0.84
15	0.90
16	0.96
17	1.02

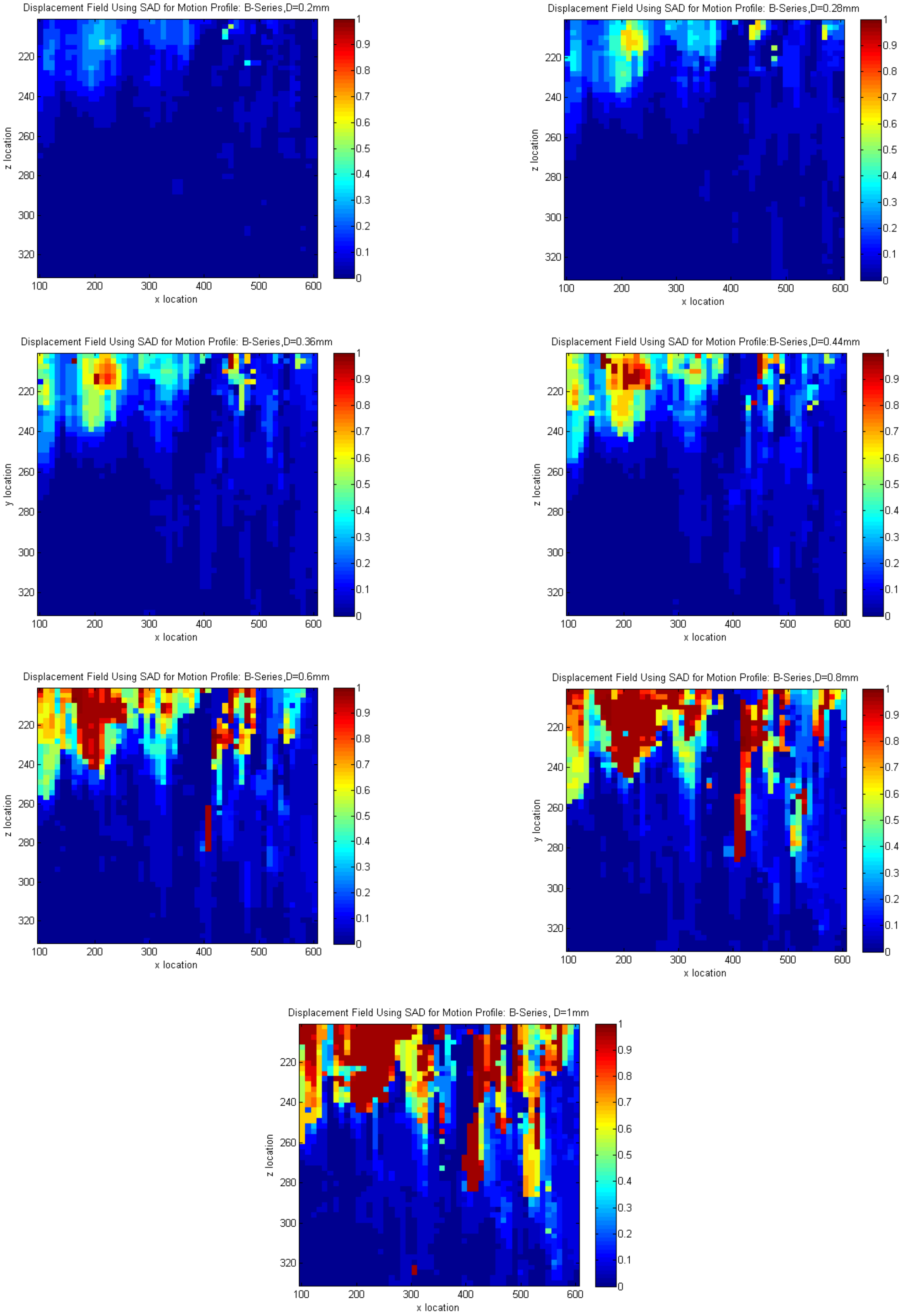

Figure 79: Onset displacement fields using SAD with the B-Series motion profiles: 0.2mm, 0.28mm, 0.36mm, 0.44mm, 0.60mm, 0.80mm, and 1mm

(b) Auto-location and displacement onset of multiple tendons using the quad-array

Similar to Section 7.6.2(a), the middle finger's tendon is actuated with a given motion profile as listed in Table 12 from Chapter 6, while the sparse quad-array and custom software, integrated with the Sonix Touch system, collect and saves the RF data. The previously described process from (a) is used in order to display the displacement fields for each sub-array using SAD, FT and NCC similarity measures. This is repeated with each motion profile in Table 12 from Chapter 6 in order to determine which motion profile provides the smallest amount of displacement needed to auto-locate the tendon. It is important to note that the tracking algorithms can only determine integer pixel displacements, and is limited by the image resolution. Thus, the minimum displacement which can be detected using the quad-array is 0.1408 mm (in the x-direction) and 0.019 mm (in the z-direction), which is a single pixel on the image using the quad-array. From Fig. 80 using SAD, it is determined that the motion profile of 1 mm can be used to auto-locate the tendon. As well, from these displacement fields, the smallest detectable displacement (i.e. the onset) is also determined. From these fields, the onset of displacement is determined as the smallest displacement giving the ability to detect the tendon above the background noise. It is determined that 0.36 mm is the smallest detectable displacement, as shown in Fig. 81 using SAD.

Total Displacement Field Using SAD for Motion Profile: Day 4, B-Series, D=1mm

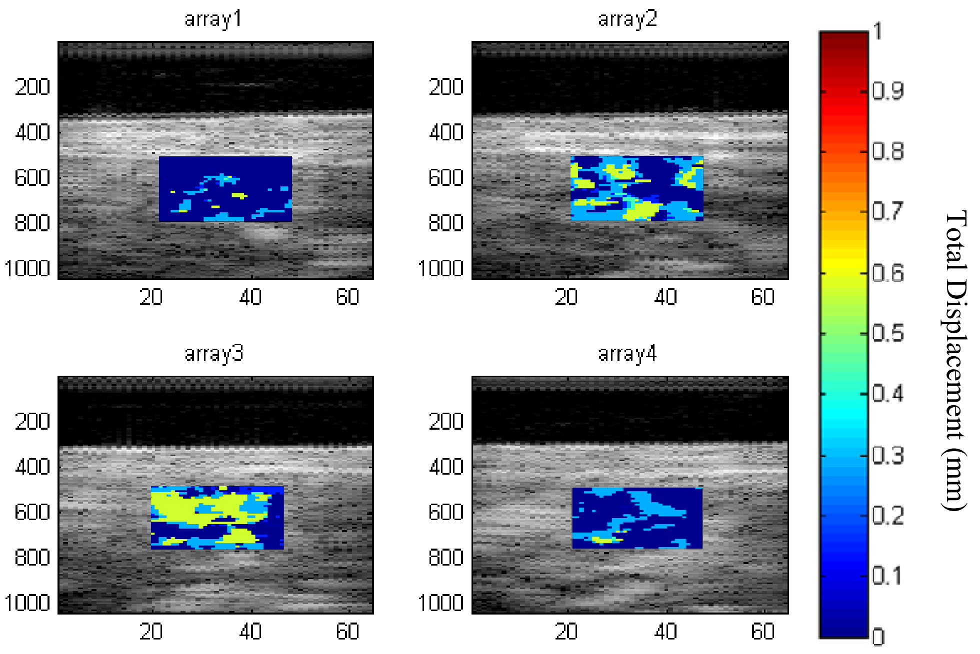

Figure 80: Onset displacement fields using SAD with the B-Series motion profiles D= 1 mm. This is the minimum displacement to create a displacement field.

Total Displacement Field Using SAD for Motion Profile: Day 4, B-Series,

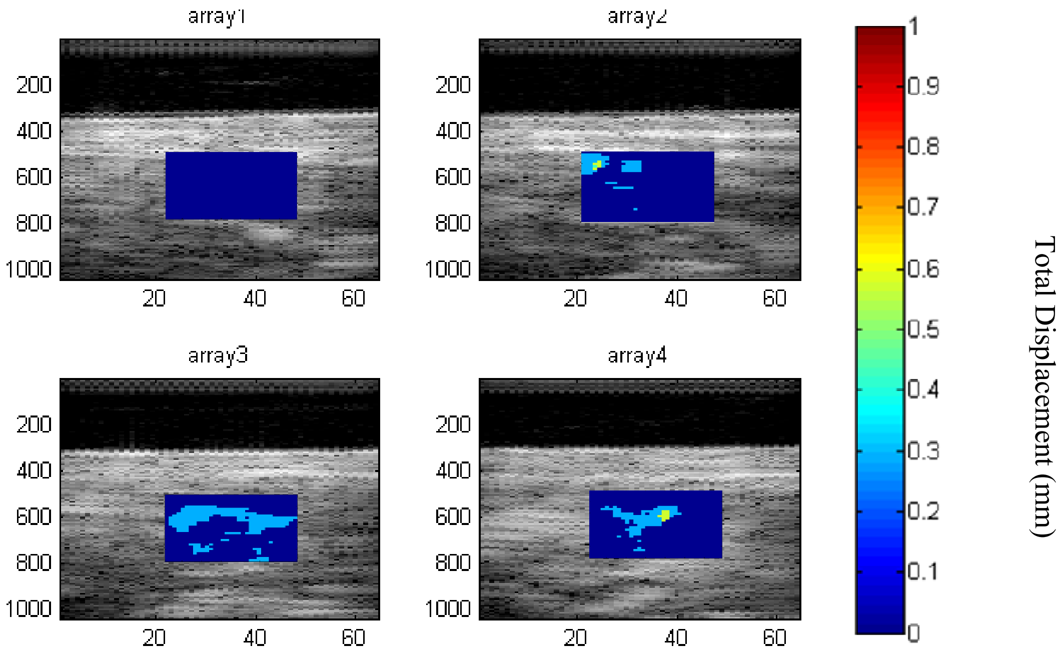

Figure 81: Onset displacement fields using SAD with the B-Series motion profile D= 0.36mm. This is the minimum detectable displacement.

CHAPTER 8:

DISCUSSION

8.1. INTRODUCTION

This thesis proposes the development of ultrasound-based software and hardware in order to determine its feasibility for use in hand prosthetic applications. In terms of the software, several speckle tracking algorithms were developed in order to detect and track the tendon's displacement using a sequence of B-Scan ultrasound images. In order to prove this new concept, five experiments were performed that used either human subjects or cadaver material. These studies were custom designed in that they provided a standard reference, in which actual values can be compared to the estimated values. Specialized hardware was also designed and built for the cadaver-based studies. As well, an off-the-shelf linear array and a custom designed quad-array transducer were used to obtain a sequence of images of single and multiple tendon displacement. The following sections discuss the usability of the speckle tracking algorithms, the success of the hardware apparatus for the cadaver-based studies, the results from the five experiments, and the feasibility of the proposed techniques for hand prosthesis applications.

8.2. DISCUSSION ON SPECKLE TRACKING ALGORITHMS

8.2.1. SIMILARITY MEASURES

In terms of the tracking algorithms themselves, there exist many permutations of similarity measures, speckle tracking parameters, and searching techniques. For instance SAD is easy to implement in hardware as it has no square operations, but it can be more susceptible to noise [184]. Log-compressed Rayleigh statistics (Fisher-Tippett) is a common similarity measure used in areas of dense speckle [151,175,182,183]. NCC is often used to overcome uneven illumination and other issues, because this measure removes local means [177-179,187]. Because Rayleigh distributions are thought to be valid if the SNR is below 1.91, a hybrid method introducing a threshold was developed here. If the SNR was above this threshold in the ROI, SAD was used, otherwise FT was used.

As with any similarity measure, there is a chance of interframe mismatch due to the presence of many local extrema. This is because the intensity pixel values within the template and block are plagued by noise. Therefore, because of noise, there is a subset of potential matches. A second hybrid method was also developed to first estimate the non-stationary noise present in the image. The minimum extrema was then calculated (minimum SAD), and then a tolerance was applied as calculated by the noise estimation, creating a subset of potential matches. NCC was used as a secondary measure to find the match within the subset.

8.2.2. ESTIMATING INTERFRAME, CUMULATIVE AND TOTAL DISPLACEMENT

The process to estimate frame-to-frame or interframe displacement, between comparison frames *t* and *t+k* was used with the stationary ROI technique. The stationary ROI is useful for two reasons: (i) if the B-Scan had a small field-of-view as with the quad-array, it can still track an object which passes through it, or (ii) if there was a tracking mis-match at some place in its displacement the remaining displacement estimations would not suffer by compounding the error (temporal drift). This was in contrast to many traditional speckle tracking algorithms in the literature, which track a specific location on the tendon itself, as the tendon displaces across consecutive image frames. In traditional tracking, if the specific location on the tendon moves out of the field of view, tracking is lost and hence only displacements smaller than the field of view could be tracked.

In order to estimate the total displacement, the interframe displacements were added cumulatively to obtain the total displacement from the entire excursion. Therefore, the total displacement estimations could be subject to interframe displacement errors, and hence a cumulative error. This cumulative error would grow with the number of template to block mismatches, and would result in an offset with respect to the standard reference displacement curve. In this sense, the stationary ROI technique was robust against a single mismatch, up to a few mismatches. If the stationary ROI technique was not used, then a significantly mis-matched block in one frame comparison would become the following template in the next comparison, thus tracking may be lost completely.

8.2.3. OPTIMIZING PARAMETERS

The choice of similarity measures and tracking parameters will affect the accuracy and computational efficiency of the displacement estimations. The values of relevant parameters are often simply reported in literature, but few details into the possible effects of choosing such values are provided. As well, studies are mainly done with uncompressed B-scan or RF data, and not with compressed B-scan data. For example, one study used the NCC similarity measure with

RF data and investigated the parameters noise, bandwidth, stationary echoes, template size, down-sampling, interpolation and demodulation [176]. Another study investigated the relative performance of NCC and SAD on simulated RF data [200]. These factors provided motivation for this study in which relevant parameters were further investigated using compressed B-Scan data of human tendon motion. Using a sub-set of data from Experiment 2, the effects of changing the parameters were investigated in order to optimize the speckle tracking algorithms. The parameters investigated were: additional similarity measures, searching without a stationary ROI, hierarchical search, template location, template and ROI size, and frame rate (temporal resolution). In Part-1 of this study, the total displacement was estimated using speckle tracking with four similarity measures, which were FT, NCC and two hybrid measures. These were used with a sub-set of data containing the first patient's 1st, 2nd and 6th flexion, and the second patient's 2nd flexion. In Part-2 of this study, the effect of changing the parameters was investigated using the first patient's 2nd flexion.

Additionally, in Part-3 of the parameter investigation study, the effect of the developed frame skipping technique was investigated using data from Experiment 3. Having an effect similar to lowering the frame rate, frame skipping was defined as the comparison of the template in frame t, to the blocks in frame $t+k$, where k is an integer. In this thesis, a new technique was developed which can determine the optimal frame skipping number, k. To provide validation for the new frame skipping technique, data from Experiment 3 was used.

A further discussion regarding the optimization of relevant tracking parameters is as follows:

a) Discussion on Part-1:Total Displacement Estimation using Various Similarity Measures

In Part-1 of this study, four similarity measures were individually used to estimate total displacement, using B-Scan image sequences collected from four FDS tendon flexions from Experiment 2. These tendon displacement estimates were compared to the displacement reference, as obtained from the microscope video reference. The total displacement relative error, R_D (%), for the four different tracking techniques was calculated for four flexions. NCC had the lowest relative displacement error for the first flexion. Since the flexion data used was of high quality, all the similarity functions performed well. High quality flexion data means that the patient flexed at moderate speed with good control, which provided smooth motion and small displacement steps between frames, so that the ultrasound machine's low frame rate does not become a major issue. Lower quality flexion data means that the patient flexed with fast tendon motion, or a sporadic flexion motion captured with a low frame rate, resulting in large steps between some image frames. With the lower quality case, the NCC measure seemed to be more robust, producing the lowest relative total displacement error. Given the performance of the similarity measures and the proposed applications in this thesis, the stationary-ROI exhaustive search method using the SAD measure is recommended for future work.

The interframe displacement was cumulatively added in order to obtain a complete displacement versus time curve. Due from the cumulative nature of the tracking technique, there was an offset between the displacement curve and the video reference. In contrast to the cumulative displacement using B-Scan ultrasound, a displacement calculated from the microscope video reference data was determined by the vector displacement between the first video frame, and each subsequent video frame.

b) Discussion on Part-2:Effect of Changing the Values of Tracking Parameters

In Part-2 of this study, the effect of changing the parameters was investigated using data from Experiment 2. Given this dataset, it was observed that the best results were achieved when using a template size of *20 by 20 pixels*, at location *(x,z)* = (*658,232)* on the B-Scan, with images sampled at *20 fps*, with a stationary ROI search technique, and using a ROI of *54 by 24 pixels*. In the following paragraphs, each of these tracking parameters (i.e. searching without a stationary ROI, hierarchical search, template location, template and ROI size, and frame rate), will be discussed in relation to this dataset.

Non-Stationary ROI: In this work, a stationary ROI technique was used for Parts-1, -2, and -3, with the exception of this non-stationary ROI trial. The stationary ROI method was first introduced by [179], and was used with the NCC measure with multiple templates. Generally, most others use a non-stationary ROI technique, but often report a temporal drift in their displacement curves [178]. This occurs because the match to the previous interframe displacement is updated to be the new template for the next interframe displacement estimation. But, a single interframe mis-match can result in rapid tracking failure; because if the previous match was incorrect, the mistake is carried through. To test this result, the conventional non-stationary ROI method was applied to a dataset in Experiment 2. From the displacement vs. time plot, it was observed that the tracking does not perform well, as seen in Fig. 56. The FT, NCC and second hybrid methods were able to follow the reference displacement curve better than the first hybrid method. All methods were not successful at tracking the entire flexion. The best way to amend this issue for non-stationary ROI techniques, is to use hardware with high frame rate capabilities. This way, speckle decorrelation and mismatches occur less frequently. Based on these effects, it is determined that the stationary ROI technique is best suited for the proposed applications in this thesis, since tracking is more easily lost with the non-stationary ROI technique.

Hierarchical Searching: An additional hierarchical searching technique has been proposed in this work, as described in Section 5.5.2. This technique used a coarse-to fine searching scheme that makes use of the benefits of both large and small templates and ROIs. It was observed that if the displacement estimation by the first iteration with the larger template was incorrect, the remaining iterations increased the errors. This was also reported by [178] and they used other methods to reduce errors. Even though the computational time increased, the tracking was overall successful and comparable for all similarity measures (Fig. 57). Based on this result, even though the hierarchical searching technique is comparable to others in terms of accuracy, it is computationally more intensive, due from the increased number of calculations.

Template Location: Evaluating interframe displacement at different locations along the tendon in the B-Scan image sequence may give different results. For example, if a template is located partially over the tendon during its excursion through the template, a poor estimate will result. It is therefore highly important to investigate different template locations along the tendon, which gives rise to a need to develop a method to do so. Selecting the template location is usually a task for a trained technician, who locates the area of the tissue in order to implement tracking. However, the technician may also choose poorly, and as a result, the chosen location may or may not produce ideal tracking results. As well, poor results attributed to location may arise from uneven illumination, or out of plane motion for part of the tendon excursion. This was evident with the data. Two of the chosen locations encountered several interframe displacement errors, thus producing an offset in total displacement. The ideal template location was found to be at the center of the image *(658,232)* using all similarity measures. To overcome the effect of uneven illumination, others employed a method which subtracted local means first, before block matching [175].

To overcome the effect of an ill-placed template, the auto-location technique has been developed in this thesis, as described in Section 5.4. The auto-location technique removes the need for a technician and removes subjectivity in selecting the template location. As well, it is able to account for problems with uneven illumination and out-of-plane excursion, since it computes the result over the entire excursion image sequence. It is a calibration step, as described in Section 7.5.2, that would occur infrequently, to select the optimal template location.

Template and ROI Size: The size of the template and ROI has a direct effect on the tracking success. If the template is too large, it is less susceptible to noise, but it may also contain non-uniform motion. Also, if the template is too small, there may be an aperture problem, and tracking may not be successful. For template size variation for this dataset, it is observed that the larger *30 by 30 pixel* template did not work as well as the smaller templates, with all similarity measures. Similarly, the size of the ROI is an important parameter to consider. A small ROI is computationally quick, but it may not capture large displacements. A larger ROI size also has issues, since the bigger it is, the more likely it will have several possible local extrema. This makes it difficult for the algorithm to select the correct (best) block location. This effect was observed, where there can be several locations of possible matches (within noise), thus causing an interframe displacement error. This was evident in all cases using the larger *80 by 35 pixel* ROI. One way to improve the issue of interframe displacement errors from a large ROI, is to incorporate an adaptive strategy. When the interframe displacement is found to be low (by monitoring the previous few interframe displacements), the ROI size can be decreased by the algorithm. This should resolve the issue of having many similar valued extrema, leading to better selection of the matching block.

Frame Rate: A high frame rate capability is reported to be one of the most important factors when sourcing ultrasound hardware for motion-detection studies [201]. Current technology, which offers ultrasound machines with portability and miniaturization, often sacrifice the frame rate. If the frame rate is too low (or the moving tissue velocity is too high), speckle decorrelation occurs, and tracking will ultimately fail. This can be attributed to the speckle pattern changing too much between consecutive frames, thus losing tracking. The data used in this study was from patients who were under anesthetics, and hence their tendon excursion velocity could not be controlled. Even with coaching, the velocity was sporadic or inconsistent between each excursion and each patient. This study uses *20 fps*, which is considered low in comparison to current available hardware. To demonstrate the effect of lowering the frame rate further, the data set was adjusted by removing every other frame, which effectively reduced the capture rate to *10 fps*. None of the similarity measures were successful at tracking interframe or total displacement, which demonstrates the importance of higher frame rates. Even so, it was observed that the FT and first hybrid method seemed to follow the reference displacement better than the NCC or second hybrid method.

c) Part-3: Development of a Frame Skipping Technique

A new frame-skipping technique has been developed in this thesis work to allow for an automated selection of which frames to compare. It makes use of the expected motion profile of the tendon, as well as the constraints given by the ultrasound hardware, such as the frame rate and the resolution. Thus, in this thesis, the relationship between these factors was derived, and the frame skipping constant, γ, was empirically determined.

Since most speckle tracking algorithms compare the template in frame t to the blocks in the next frame in $t+1$, and every ultrasound imaging system is different, the resolution may not be sufficient to detect small interframe displacements. This is a function of the system's frame rate and lateral resolution, as well as the tendon's displacement and velocity. This study investigated if skipping frames can mitigate the resultant tracking issues from small tendon displacements, coupled with a high frame rate ultrasound machine. First, it was shown that the success of tracking is highly dependent on frame skipping. Secondly, the optimal frame skipping constant, γ, was determined using data from Experiment 3, and the frame skipping numbers, $k=1,2,3,4,5$. The data was reanalyzed to determine which one has the lowest total displacement relative error, when being compared to the reference. The average frame skipping constant, γ, was estimated as *8.24 pixels* and is assumed to be valid for any data set imaged by any ultrasound system. After the constant was determined, the developed equation (Eqn. {33}) can be used for all future data sets in order to determine the frame skipping number, k.

Another important parameter, although not investigated here, is out-of-plane tendon motion. Tendons move in all three dimensions within the arm and wrist as excursion takes place. Linear array transducers on the other hand, only image in 2D (in the x-z plane). If the tendon moves in the y-direction (out of the field of view of the transducer), tracking can be lost completely. If the transducer placement is close to the edge of a tendon, and that tendon exhibits sufficient motion in the *y*-direction, it can disappear from the image. As well, for the data from Experiment 2, the resultant B-Scans were imaging the *x-z* plane, while the reference is imaging the *x-y* plane. Thus, major displacement in the *z* or *y* direction will cause discrepancy between the ultrasound-based estimations and the video displacement reference. Additionally, for the cadaver-based studies, the reference was providing a displacement in the *x*-direction. Here, the linear array can only capture the *x-z* plane. Thus, the vector addition of the estimated displacement in the *x-z* plane should equate to the reference displacement. Even though the tendon was displacing mostly in the *x* direction under the transducer (in the wrist canal), there were smaller components in the *y-z* plane. This provides a source of error since the *y* plane was not monitored.

8.2.4. SUMMARY OF SPECKLE TRACKING ALGORITHMS

The speckle tracking algorithms were developed and investigated using experimental data from humans and cadavers. In summary, the similarity measures SAD, SSD, FT, NCC and two hybrid measures, were developed and investigated using various data from Experiments 2-5. They all have a relatively similar performance, with NCC performing slightly better overall. In terms of searching strategy, the strategy using the stationary ROI technique performed better than the non-stationary ROI technique. As well, the hierarchical search performed well, but was computationally more intensive. The template size, ROI size, template location and frame rate were also investigated and their effects on tracking success were discussed. As well, a new frame skipping technique was developed and verified using data from Experiment 3. The speckle tracking algorithms are further discussed in Section 8.9.2, in the context of the feasibility of its use for the proposed application in this thesis.

8.3. DISCUSSION ON HARDWARE APPARATUS FOR CADAVER-BASED EXPERIMENTATION

For the cadaver-based studies in Experiments 1,3,4 and 5, specialized hardware was designed in order to: provide a standard reference of tendon excursion, displace the tendon(s) using a programmable motorized actuation system, couple the tendon(s) to the actuation system, hold the transducer in a static position, and fix the cadaver hand in a solid orientation.

8.3.1. Motorized Actuation System

For the preliminary cadaver-based study described in Experiment 1, the preliminary actuation system was tested by evaluating the initial set-up. The preliminary actuation system used a single stepper motor actuating an x-stage, which was in turn coupled to the flexor tendon. The x-stage with the connected coupler displaced the flexor tendon by a known amount, thus constituting a standard reference system. The opposing extensor tendon was also attached to a shorter coupler that was in turn connected to a string-pulley-weight system. This provided a constant force on the extensor tendon, which allowed the finger (and the flexor tendon) to safely return to its natural position when the x-stage moved toward the fingers.

Unfortunately, the preliminary actuation system did not perform the displacement excursion as expected, which ultimately led to the failure of a valid standard reference for this experiment. The problems with the preliminary actuation system are described in detail in Section 7.1.2. Consequently, the programmed displacement did not match the actual displacement of the tendon, and therefore the reference from Experiment 1 could not be used. There are several improvements to the preliminary actuation system that could mitigate such undesirable effects. Firstly, the angle between the longitudinal axis of the tendon, and that of coupler and x-stage, should be close to zero. As well, there should be an ability to adjust the coupler up and down, to achieve this desired zero angle. Another option involves an implantable-based reference, whereby a metal marker is implanted onto the part of the tendon which is in the field of view of the ultrasound transducer. This way, the marker can be tracked visually using the sequence of collected ultrasound images. Unfortunately, this reference isn't entirely external; it is coupled to the ultrasound imaging system. As well, inserting such a reference will disturb the natural tissue surrounding the tendon, which may have an impact on the image quality of the ultrasound image. Another alternative similar to Experiment 2 is to record the exposed tendon with a video camera, and then track a visible feature using Kinovea tracking software. Unfortunately, the video camera would only record displacements in the *x-y* plane and not the *x-z* plane. Thus, any motion in the *y*- or *z*-direction may cause tracking errors.

Based on all the knowledge gained from Experiment 1, a new actuation system for Experiments 3-5 was designed, using upgraded linear-actuator motors, linear guides, a dedicated motor controller, and a new mechanical layout. This new actuation system was able to actuate the tendons horizontally, and to provide an accurate standard reference. This means that the tendon at the coupler junction displaced in the *x* direction, thus alleviating the undesirable angle-effect. Together, the new actuation system mitigated the issues observed in Experiment 1.

Further, the new actuation system used in Experiments 3-5, had the ability to independently displace three flexor tendons, by the use of three linear-actuator motors. The new multi-tendon actuation system, as detailed in Section 6.4.2, performed well as a reference, and constitutes the standard design for Experiments 3-5 with cadavers in the laboratory.

8.3.2. Tendon Coupler

Tendons, being biological materials, present an inherent difficulty for coupling to mechanical equipment. Hooks, and other piercing hardware, may tear the tendon at the point of attachment, while the tendon is being actuated. The custom coupler design used in Experiment 1, compressed the tendon between two wooden plates lined with a rough non-slip material. This coupler design performed well, and was successful at grasping with tendon for the entirety of the experiment, with no observed slip. Based on this knowledge, the tendon coupling system for Experiments 3-5 made use of the same clamping technique. For these experiments, the tendon coupling system was further developed into a more compact system, where three couplers could be placed side-by-side for the multi-tendon actuation system. The new developments included using aluminum and stainless steel as the structural material, as well as a screw and nut fastener which compressed the plates onto the tendon. The inner surfaces were lined with the same coarse-grit non-slip tape used with Experiment 1. Each of the three flexor tendon couplers was attached to a corresponding bracket piece, which was attached to a corresponding linear actuator. The bracket piece was adjustable in height, thus allowing the coupler to be aligned with the longitudinal axis of the flexor tendon, and hence to be actuated horizontally. Overall, this coupler design performed very well, and was successful at grasping the tendon for the entirety of the experiment, with no observed slip.

8.3.3. Stabilizing the Cadaver Hand

The cadaver hand was fixed to ground in order to minimize any undesired tissue motion under the transducer. To accomplish this, custom apparatus was developed, which clamped the hand in four areas. Off-the-shelf vice grips were modified (vice-clamps) so that they could be fixed in specialized blocks. This technique is described in detail in Section 6.2.2(c), and was employed for Experiments 1, 3, 4 and 5, where it was very successful at stabilizing the hand. No observable motion of the wrist or clamped bones was evident, while the multi-tendon actuator system was in operation. Other techniques drill directly into the bones for stabilization. Due to the unpredictable nature of cadaver bone material, it was not considered as a viable option for the experiments of this work.

8.3.4. The Ultrasound System (Experiments 1 and 2)

The ultrasound system was comprised of a LogicScan 128 ultrasound machine, a 12 MHz linear array transducer, a general purpose laptop PC. As well, a dedicated transducer holder was designed, as described in Section 6.2.2(d), which provided transducer adjustment and stabilization for the cadaver-based studies. Overall, the LogicScan system performed well, but there were obvious limitations with this hardware. Firstly, since it was a table-top system, its processing speed was limited by the laptop PC which was used, thus limiting the frame rate of the B-Scans. For example, in Experiment 1 the frame rate was suitable *(40 fps),* but in Experiment 2, the frame rate was considered to be too low *(20 fps).* As well, this system will not allow for any RF data access, and the B-Scan compression/encoding method into an *.avi* file is not controlled by the user. Hence, different PC's will use different compressions, which will affect the resulting B-Scan resolution and tracking.

8.3.5. The Ultrasound System (Experiments 3, 4 and 5)

For Experiments 3, 4 and 5, a new research-grade ultrasound system was used. This consisted of the Sonix Touch ultrasound system, made by Ultrasonix Medical Corp. Two different transducers were used, which were the 10 MHz linear array for Experiment 3, and the sparse quad-array transducer for Experiments 4 and 5. The quad-array independently imaged four *x-z* planes in order to capture the displacements from multiple tendons simultaneously. The software to use the custom quad-array was developed by a third party using an SDK provided by Ultrasonix. The software was integrated on the research interface on the Sonix Touch and the four independent B-Scans were displayed onscreen. Using the above described ultrasound system for a given experiment, the collected data files were imported into Matlab for further processing using the proposed speckle tracking algorithms. Overall, the Ultrasonix system performed better than the LogicScan system. The Ultrasonix system has a high frame rate and a research interface, which allows for better tracking performance and the use of the quad-array.

8.4. EXPERIMENT 1: PRELIMINARY CADAVER-BASED STUDY TO OPTIMIZE EXPERIMENTAL OVERVIEW AND METHODOLOGY

The preliminary study allowed for the development and testing of electro-mechanical hardware to couple and actuate a single flexor tendon of a cadaver, and also to obtain a library of B-Scan ultrasound cine loops of single tendon excursion. Such libraries of B-Scan data were used to further develop the tracking software in order to obtain estimates of interframe and total displacement. The tendon coupler, cadaver clamp system and the transducer holder used in this experiment were successful, as previously described. Unfortunately, the actuation system did not perform the displacement excursion as expected, which ultimately led to the failure of a valid standard reference for this experiment. This failure is attributed to a controller issue as well as the introduction of an angle-effect. Due to the expiring nature when dealing with cadaver material, there was no immediate remedy to fix these issues. Although the above described factors lead to the ultimate failure of the reference system, the collected B-Scans cine-loops served as an image library. These image libraries were used very effectively as a tool to further develop the speckle tracking algorithms, and for designing the subsequent experiments (2, 3, 4, and 5).

8.5. EXPERIMENT 2: HUMAN-BASED STUDY TO ESTIMATE SINGLE TENDON EXCURSION

The aim of this experiment was to further develop the proposed speckle tracking method for estimating the instantaneous and total displacement of a single tendon. This experiment used human volunteer patients, during their regularly scheduled carpal tunnel surgeries. To validate the method, the ultrasound-based estimation was directly compared with the actual tendon displacement in the hand, by using video to record the surgically exposed tendons in the palm. The video of the exposed flexor tendons was then used to create a standard reference displacement, using commercial video tracking software. In this way, the experiment provided the most realistic anatomic setting, in contrast to work by others that uses simulations and phantoms.

Total displacement and instantaneous displacement were estimated using the proposed FT-based, SSD-based, and SAD-based speckle tracking techniques, on B-scan image sequences collected from FDS tendon motion in human patients during surgery. These ultrasound-based tendon displacement estimates are compared with the actual displacement as obtained from the video reference displacement. For FT-based tracking, the total displacement relative error, R_D, was < 5% in 10 cases, and > 5% in 5 cases. For SAD-based tracking, R_D was < 5% in 6 cases and > 5% in 9 cases. For SSD-based tracking, R_D was < 5% in 6 cases, and > 5% in 9 cases. Overall, the average value of R_D was 7.3% using the FT-based method, which is less than the average value of R_D for the SAD-based method (10.6%), and average R_D for the SSD-based method (10.4%). The average instantaneous absolute error (mm), A_{id}, using FT-based tracking was < 1 mm in 9 cases and > 1 mm in 6 cases. The maximum absolute error was 5.97 mm in the case of patient 1, extension 1, which also had a high peak velocity. Likewise, A_{id} (mm) using SAD-based tracking was < 1 mm in 6 cases, and > 1 mm in 9 cases. Also with the SAD technique, the maximum absolute error was 6.69 mm in the case of patient 1, extension 1, which also corresponds to the highest absolute error when using FT- and SSD-Based tracking. For SSD, A_{id} (mm) was < 1 mm in 4 cases and > 1 mm in 11 cases. The maximum absolute error using SSD was 6.86 mm for patient 1, extension 1.

Recall that the displacements estimated by either FT, SSD or SAD are inter-frame estimates. This means that the displacement between two consecutive frames is estimated and then added as a cumulative displacement, to obtain a complete displacement-versus-time curve. Therefore, the total displacement with FT, SSD and SAD estimations can be subject to a cumulative error. This cumulative error will grow with the number of template-to-block mismatches, and will result in an offset to the reference curve in the displacement. For example, the displacement curve in Fig. A.1.2 (b) in the Appendix obtained using SAD has a single mismatch of an inter-frame displacement occurring at 0.6 s, and then immediately regains tracking from that point onward because of the use of the stationary ROI technique. Notice the offset between the SAD curve and the reference displacement curve, due from the cumulative nature of the tracking technique. If the stationary ROI technique was not used, a mismatched block in frame $t + 1$ would become the next template in frame $t + 2$; thus, tracking may be lost completely. In contrast, the reference displacement curve calculated from the microscope video was determined by the vector displacement between the first video frame and each subsequent video frame.

Among the three techniques, the FT-based technique performed better overall in comparison to the SAD and SSD technique. This result coincides with the study by [182], which stated that ultrasound images are poorly characterized by Gaussian statistics. In a few cases, however, SSD-based or SAD-based instantaneous displacement was more accurate than that estimated by the FT technique. This may be due to the fact that the underlying statistics may not always be represented by a Rayleigh distribution in the region of interest [151]. Further investigation is needed to quantify when Rayleigh/FT, SSD or SAD is best suited for the B-scan properties within the ROI, or if a hybrid algorithm combining the two methods is possible. Also, the block matching technique employed assumes that the elements within the template and block are independent, which may not always be a valid assumption [151].

In some cases, the ultrasound-based tracking algorithms lost tracking when the tendon velocity was high. This can be attributed to the excessive change in speckle pattern (*i.e.,* speckle decorrelation) between consecutive frames caused by noise, causing tracking to be lost between frames. Speckle decorrelation is a widely known issue, and methods to quantify its effect on tracking have been investigated. The patients used in this study were under anesthetics, which made patient performance, and hence their tendon excursion velocity, difficult to control. Even with coaching, velocity was inconsistent between excursions and between patients. In general, patient 2 flexed and extended at a much higher rate than patient 1. In cases of high velocity, tracking loss occurred. For example, the peak velocity for patient 1's first extension was > 40 mm/s occurring at the 1 s mark in the extension. This corresponds to a loss of tracking at this section in time, as illustrated in Fig. A.1.2 (a) in the Appendix. Even though tracking recovered (because of the stationary ROI technique) later, the subsequent total displacement suffered from an offset. This was due to the cumulative addition of estimates, as previously described. The ultrasound machine used for Experiment 2 had a low frame rate of *20 fps*; therefore, it appears that FT, SSD and SAD-based tracking performed better when the velocity was < 30 mm/s. To improve tracking performance at higher tendon velocities, an ultrasound machine with a faster frame rate could be used. In this way, the displacement between successive B-scan frames will be smaller, and may be handled by the current tracking techniques.

During tendon excursion, it is possible for the tendon to displace out of the field-of-view of the ultrasound probe, and thus, tracking can be lost. As previously described, the placement of the transducer provides a B-scan image in the *x–z* plane. If the transducer placement was close to the edge of a tendon, and that tendon exhibits sufficient *y*-direction (out of plane) motion, it can disappear from the image. This likely occurred for patient 3, as illustrated in Fig. 53, where FT-based, SSD-based and SAD-based tracking appears to stall, while the video reference shows full excursion. This is because the microscope video reference was monitoring tendon excursion in the palm in the *x-y* plane, whereas the ultrasound probe is monitoring tendon excursion in the *x-z* plane proximal to the wrist, as previously stated. Thus, major displacement in the lateral *z* or *y* direction will cause discrepancy between the ultrasound-based estimations and the video reference. The time with each patient was constricted to 5 min, and could not pre-process the data to immediately determine tracking success, rectify any transducer placement issues or identify if the tendon was moving too fast or out of frame.

8.6. EXPERIMENT 3: CADAVER-BASED STUDY TO ESTIMATE SINGLE TENDON EXCURSION

Experiment 3 is based on the earlier preliminary experimentation (Experiment 1) in which a linear array collected sequential B-Scan images of a singular moving cadaver tendon. The motivation for Experiment 3 was twofold. Firstly, to further develop the speckle tracking algorithms for interframe and total displacement estimations. Secondly to further develop the hardware that couples to and actuates the tendon, thus providing an improved standard reference.

(a) Discussion on Data Collection Protocol

For this experiment, and the research-grade Sonix Touch ultrasound system with a linear array transducer was used. It was successful at imaging the displacing tendon with a high frame rate and good image quality. As previously described, the upgraded multi-tendon actuation system also performed well as an actuation system and as a reference.

In all data-sets, the linear array was manually placed on the given tendon overtop intact skin. Prior to recording the data, the motion from a given tendon was observed onscreen, and the quality of the B-Scan sequences were visually assessed. As shown by the index finger's field for the example in Fig. A.2.1 in the Appendix, the transducer placement was adequate, but not perfect. It is difficult to know the exact anatomy and tendon location under the transducer, for optimal placement. One possible solution is the implantation of a reflective (non-magnetic) device, such as a small bolt into an adjacent bone, near the tendon. If available, the hand could undergo MRI (Magnetic Resonant Imaging) prior to data collection. The tendons and the implanted device would be clearly visible in the MRI image, and relative measurements to each tendon location could be made. When the hand is ready for data collection, the transducer could then be placed at these optimal locations, by first imaging the implanted bolt and then moving the transducer by the known amount to be over top of the desired tendon.

(b) Discussion on Auto-location with Single Linear Array

An auto-location technique is needed in order to standardize the selection of the optimal template location for any image sequence data-set. Further, a major motivation for the proposed tendon tracking technique is for prosthetic control, thus necessitating the development of automated template location selection. Using the developed algorithms for SAD, FT and NCC with the frame skipping technique, displacement fields were created for the prescribed motion profiles of a single flexion from each data set. A displacement field represents the total displacement from the tendon's entire excursion, at many points along the tendon. From each displacement field using a given similarity measure, the maximum displacement value is found. This value is then used as the optimal template location for the analysis.

On a given displacement field, the tendon was clearly observed, using any measure or motion profile. In the center portion of the index finger's displacement field, the total displacement was estimated at less than the edge portions. A continuous field was expected, with the entirety of the tendon's displacement being uniform, since a tendon is a solid and inelastic object. At the center location on the B-Scan image, the tendon appears darker, thus tracking may be lost at this location. As well, the tendon may have a component of out-of-plane motion at this location. Even so, the total displacement at the edge portions represents the total displacement of its motion profile. For the Day 2 experiment for the index finger, with the V15,D15 motion profile the total displacement was estimated as: 14.16 mm using SAD, 14.14 mm using FT and 14.54 mm using NCC. For the V10,D10 motion profile on Day 2, the total displacement was estimated as: 9.86 mm using SAD, 9.86 mm using FT and 9.83 mm using NCC. The optimal location of the template is at the same location using any similarity measure for a given motion profile. This infers that the SAD, FT and NCC measure perform equally in this respect. However, the optimal template location for the V15,D15 and V10,D10 motion profiles are different. This can be attributed to many factors: such as noise, tracking errors, and reduced image quality during portions of the image sequences.

The displacement fields for the middle finger tendon were more uniform. For the V15,D15 motion profile on Day 2, the maximum total displacement was estimated as: 14.80 mm using

SAD, 14.78 mm using FT and 14.92 mm using NCC. As well, it is observed that the optimal location of the template determined by the auto-location algorithm, was at the same location using any similarity measure for a given motion profile. However, the location determined using data from the V15,D15 and V10,D10 motion profiles, are different. The second hand was used on Day 3, and was not of the same quality. Thus only the middle finger's data-set was repeated. Even so, for the V15,D15 motion profile on Day 3, the maximum total displacement was estimated as: 13.66 mm using SAD, 13.64 mm using FT and 13.60 mm using NCC. For the V10,D10 motion profile on Day 3, the maximum total displacement was estimated as: 9.44 mm using SAD, 9.42 mm using FT and 9.57 mm using NCC. For both the V15,D15 and V10,D10 motion profiles, the maximum total displacement within the field estimated by any measure, was determined to occur at the same location in the image.

Likewise, the displacement fields for the ring finger were also uniform. For the V15,D15 motion profile on Day 2, the maximum total displacement was estimated as: 14.49 mm using SAD, 14.49 mm using FT and 14.39 mm using NCC. For the V10,D10 motion profile on Day 2, the maximum total displacement was estimated as: 10.27 mm using SAD, 10.27 mm using FT and 10.24 mm using NCC. For both the V15,D15 and V10,D10 motion profiles, the maximum total displacement estimated by the NCC measure is at a different location than the location estimated by the SAD and FT measure.

Overall, the SAD, FT and NCC techniques performed well. This may be attributed to the algorithms themselves, coupled with using great data to verify the algorithms. The SAD auto-location technique is the fastest (11 ms/frame), followed by the NCC algorithm (12 ms/frame), followed by the FT algorithm (19 ms/frame).

(c) Discussion on Interframe and total displacement

For a given tendon displacement data set and similarity measure, the interframe and total displacement was compared to the reference displacement. From the indicated optimal template location for a motion profile using a particular similarity measure, the interframe and cumulative displacement was estimated. The two metrics were used to determine the total displacement relative and instantaneous absolute error, respectively, in order to quantify the comparison between the proposed algorithm and the reference.

The estimated displacement vs. time curves using the SAD, FT or NCC measures were all observed to follow the reference displacement curve well. In terms of instantaneous displacement absolute error, the SAD and FT measure performed equally. The instantaneous absolute error, A_{id}, was in the range of 0.02 mm to 0.20 mm. Although acceptable, the absolute error from the NCC measure did not perform as well as the SAD and FT overall. The instantaneous absolute error, A_{id}, using NCC was in the range of 0.02 mm to 0.25 mm. In terms of the total displacement, the average of the relative error, R_D , using SAD was 4.2%, using FT was 4.3%, and using NCC was 3.5%; which indicated that overall, NCC was more accurate at estimating total displacement.

8.7. EXPERIMENT 4: CADAVER-BASED STUDY TO ESTIMATE MULTI-TENDON EXCURSION

This study used the novel quad-array transducer to comprise a multiple-tendon detection and tracking system. Experiment 4 was part of the previously described four-day data collection period, in which a cadaver hand was used to validate the proposed technique. The software collected independent image sequences from all four sub-arrays, and the previously described auto-location technique (Section 5.4) was employed on each sub-array in order to determine the optimal template placement. As well, the optimal template location was used to estimate interframe and total displacement, as before. On the second and fourth day of data collection, the index, middle and ring finger tendons from the first hand are used. The second hand was not of good quality, and was not used for this study.

(a) Discussion on Data Collection

For this experiment, Ultrasonix Sonix Touch machine was used with the quad-array, and was successful at imaging the multiple displacing tendons with a high frame rate and adequate image quality. As previously described, the upgraded multi-tendon actuation system also performed well as an actuation system and as a reference.

For a given data collection day, the quad-array was manually centered overtop of the middle finger's tendon. As before, it is difficult to know the exact anatomy and tendon's location under the transducer, in order to determine optimal placement. The previously suggested solution of implanting a bolt and imaging with an MRI machine prior to data collection, is also a valid option to improve quad-array placement. This suggestion however, is only useful in the context when experimenting with cadavers.

Prior to recording the data, the motion from all three tendons were observed onscreen and the quality of the B-Scan sequences were assessed visually in order to confirm adequate transducer placement. Using the first hand on Day 2, it was observed that when actuating the index finger tendon, motion appeared in sub-arrays 2, 3 and 4. When actuating the middle finger tendon, there appeared to be motion mostly in sub-arrays 2 and 3, and when actuating the ring finger tendon, there only appeared to be motion in sub-array 1. On using the first hand on Day 4, it was observed that when actuating the index finger tendon, motion appeared in sub-arrays 3 and 4. When actuating the middle finger tendon, there appeared to be motion mostly in sub-arrays 2 and 3, and when actuating the ring finger tendon, there only appeared to be motion in sub-array 1. The observed motion of an individual tendon occurring in two or more arrays suggests a redundancy-effect, where the displacement in each array can be compared as a duplication measurement.

It was also observed that the first hand became stiffer in the joints from Day 2 to Day 4. This is not a rigor mortis effect, but likely drying of the hand tissue, or other type of tissue degeneration. As a result, when the hand was fresh on Day 2, when an individual tendon was actuated the adjacent finger joints did not rotate. This insured that the displacement B-Scan image contained only the actuated tendon. However, upon individual tendon actuation of the same hand on Day 4, the adjacent finger joints did rotate slightly. This isn’t unexpected, as this hand was used for 8 hours on Day 2, and for 4 hours on Day 4. As well, the second hand was not used in this study, due from the poor tissue quality observed in Experiment 3.

(b) Auto-Location with Quad-Array

The previously discussed auto-location technique used for Experiment 3, was also used in this experiment in order to standardize the selection of the optimal template location for any data-sets. Using the developed algorithms for SAD, FT and NCC with the frame skipping technique, displacement fields were created for the prescribed motion profiles of individual flexion, in each sub-array. The individual motion profiles are A (index), (B) middle and (C) ring finger tendon actuation. The resulting data is processed into a displacement field, where the tendon is clearly observed, using any measure or motion profile, in the sub-array(s) that are imaging that particular tendon. Recall that for the auto-location technique, only a single tendon may be moving. From each displacement field in sub-arrays 1 to 4, using a given similarity measure and motion profile, the maximum displacement value is found. The corresponding location of that maximum was then stored, for each similarity measure. For a given motion profile, the sub-array containing the maximum displacement value using any measure, is considered the array which contains the displacing tendon. Thus, *only* using this sub-array, the three locations listed were used as template locations for the SAD, FT and NCC algorithms. This process is repeated for the tendon motion profiles for A (index), B (middle) and C (ring) fingers, in order to auto-locate the index, middle and ring fingers, respectively.

As shown by Table 28, for the data collected on Day 2 and Day 4 with a given motion profile, the maximum displacement is shown for the tendon, in its corresponding array(s). As observed earlier, there was motion in adjacent arrays when an individual tendon was actuated. This was observed with several displacement fields, especially for B-Series data on Day 2, and A-Series data on Day 4, as shown in Table 28. In these cases, the maximum displacements in adjacent arrays were very similar. This could be an example of redundant tracking of the same tendon. Redundant tracking, if further developed, has the potential to significantly increase tracking accuracy. It is important to recall that on Day 4, the hand was stiffer which caused unwanted tendon motion from adjacent fingers. Although small in magnitude, this unwanted motion would add to the displacement fields, potentially causing errors.

Additionally, the locations of the maximum displacement for the sub-array using SAD, FT and NCC are different. This is unlike earlier experimentation using the linear array (Experiment 3), in which all similarity measures performed almost equally in this regard, by choosing the same location of the maximum displacement. This isn't unexpected, as the quad-array is a completely different transducer, with a different image resolution being a consequence of the different apertures and firing sequences. Hence, the speckle tracking algorithms may not perform equally, thus indicating different locations for the maximum displacement within the sub-array.

Using the previously described process, the displacement field was found in each sub-array for a given multi-tendon motion profile, using each similarity measure. The multi-tendon motion profiles were: AB (index + middle), AC (index + ring), BC (middle + ring) and ABC (index + middle + ring). These displacement fields were not used to auto-locate the index, middle and ring fingers. This is because multiple tendons were moving at the same time, thus the auto-location algorithm cannot work. Instead, the locations of maximum tendon displacement, identified by the displacement field of auto-location for the individual fingers, were used as the locations for tracking the multi-tendon excursion data. In this sense, the auto-location process serves as a calibration step to locate the tendons, and the best location on them for the tracking algorithm. Therefore, any subsequent data containing multiple, simultaneous tendon motion can be analyzed, using the previously determined template locations. The maximum displacement at the determined locations can be found in Table 28.

(c) Interframe and Total Displacement with Quad-Array

Once the optimal template location for a given tendon (index, middle or ring finger tendon) was found by auto-location, the interframe and total displacement was estimated. This was achieved by placing the template at the optimal location, and using SAD, FT and NCC to estimate interframe displacement. These interframe displacements were then added cumulatively to create a displacement vs. time curve, in units of mm. The standard reference displacement vs. time curve was also plotted for comparison. The two curves were used to determine the total displacement relative error, R_D, and instantaneous displacement absolute error, A_{id}, respectively, in order to quantify the comparison between the proposed algorithm and the reference. The estimated total displacement was obtained from this graph, and compared to the reference total displacement. This was repeated at the determined optimal location for each similarity measure used in this experiment. This process was then repeated for the index (A-series), middle (B-series) and ring (C-series) data sets, as well as the multi-tendon data sets collected on days 2 and 4. For the multi-tendon data, the displacement vs. time curve was created for each tendon performing an excursion. For example, in reference to the AB-Series, the index and the middle finger each had an individual displacement vs. time curve, at the prescribed location determined earlier by the individual index and middle finger tendon displacement analysis.

The estimated displacement vs. time curves using the SAD, FT or NCC measures, were all observed to follow the reference displacement curves in a fair, to adequate manner in comparison to the curves using the linear array in Experiment 3. In terms of instantaneous displacement absolute error, A_{id}, the measures performed similarly. Using SAD, A_{id} was in the range of 0.01 mm to 0.94 mm. Using FT, A_{id} was in the range of 0.02 mm to 0.83 mm. Using NCC, A_{id} was in the range of 0.01 mm to 0.86 mm. These error ranges are more broad than the ones in Experiment 3, indicating a lesser tracking performance with the quad-array. In terms of the total displacement, the average of the relative error, R_D, using SAD was 14.8%, using FT was 17.5%, and using NCC was 10.6%; which indicated that overall, NCC was more accurate at estimating total displacement. This was mainly due from the differences with aperture, resolution and field of view, and is discussed further in Section 8.9.

As previously described in Experiments 2 and 3, the displacements estimated by either the SAD, FT or NCC-based technique were interframe estimates. Therefore, the total estimations were subject to a cumulative error. This cumulative error grew with the number of template-to-block mismatches, and would result in an offset to the reference curve in the displacement. This was observed in Fig A.3.1 in the Appendix for the index finger's V15, D15 motion profile.

TABLE 28: DISPLACEMENT CURVE ANALYSIS FOR MULTI-TENDON EXCURSION

Day	Finger	Motion Profile V(mm/s), D(mm)	Array Number	Max Displacement Using SAD (mm)	Max Displacement Using FT (mm)	Max Displacement Using NCC (mm)
2	index	A: V15 D15	4	14.15	11.86	13.58
		A: V10 D10	4	9.36	8.85	10.34
2	middle	B: V15 D15	3	14.24	15.68	15.67
		B: V10 D10	2	11.09	9.53	9.50
2	ring	C: V15 D15	1	14.61	14.91	13.01
		C: V10 D10	1	9.33	8.76	10.73
4	index	A: V15 D15	3	17.26	17.37	13.97
		A: V10 D10	4	11.42	11.38	11.07
4	middle	B: V15 D15	2	15.18	13.54	19.99
		B: V10 D10	2	11.16	11.37	13.34
4	ring	C: V15 D15	1	19.44	20.19	16.40
		C: V10 D10	1	14.77	13.87	13.27
2	index	AB: V10 D10	4	10.35	9.51	8.87
	middle		2	9.75	9.83	9.26
2	middle	AC: V10 D10	4	8.56	8.76	8.91
	ring		1	8.49	8.70	9.83
2	middle	BC: V10 D10	2	10.94	8.98	10.06
	ring		1	6.66	5.33	9.39
2	Index	ABC: V10 D10	4	8.78	7.86	9.91
	middle		2	8.35	9.74	8.65
	ring		1	6.48	5.62	8.64
4	index	AB: V10 D10	4	8.60	8.99	7.25
	middle		2	9.26	8.30	12.05
4	index	AC: V10 D10	4	11.93	11.29	8.34
	middle		1	9.60	11.46	12.12
4	middle	BC: V10 D10	2	7.49	7.52	11.87
	ring		1	8.95	8.00	8.48
4	Index	ABC: V10 D10	4	7.42	8.03	7.11
	middle		2	9.12	7.45	11.63
	ring		1	11.59	7.45	10.14

8.8. EXPERIMENT 5: CADAVER-BASED STUDY TO ESTIMATE THE ONSET OF TENDON EXCURSION

The previous experiments (Experiments 1-4) estimated the interframe and total displacement of a tendon from a non-amputee performing a large excursion. However, a major motivation of this thesis is to detect and monitor the tendon displacement from an amputee. In this case, the tendon system may be partially intact, damaged, or have low function. This study formed the basis to such investigations by determining the smallest amount of displacement needed to auto-locate the tendon, as well as determining the smallest detectable tendon displacement, known as the onset displacement. The data for this experiment was obtained on the third day with the second hand, using the linear array. On the fourth day, the onset experiment was performed with the first hand and the quad-array.

(a) Auto-location and displacement onset of a tendon using the linear array

Given the processing approach to identify onset, as described in Section 7.6.2, and the corresponding results, a number of observations are now made. Using all measures, it was determined that the motion profile of 0.44 mm (Table 12, Chapter 6) can be used to auto-locate the tendon. At this amount of displacement, the tendon becomes more visible and uniform. As well, from these displacement fields, the smallest detectable displacement (i.e. the onset) was determined to be 0.2 mm.

It is important to note that for such small displacements of the tendon, the tracking algorithms are highly dependent on the image resolution. The algorithms can only determine tendon displacements with integer values, where those integers correspond to the pixel resolution of the image. Further, the image resolution is a function of the transducer hardware, among other factors. In this work, the image resolution produced by the linear array transducer is 0.06 mm in the x and z directions. Thus, the minimum displacement which can be detected is 0.06 mm, or a single pixel of displacement. For this experiment, the smallest motion profile used is a displacement of 0.2 mm. Other researchers have employed a sub-pixel interpolation algorithm in attempts to remedy this issue of integer pixel displacement estimations [177].

(b) Auto-location and displacement onset of a tendon using the quad-array

The results of onset detection with the quad-array are discussed here. Given the setup described in Section 7.6.2(b), the middle finger's tendon was actuated with a given motion profile of small displacement, while the quad-array and custom software on the Sonix Touch system collected and saved the RF data.

As described in Section 6.6.2(b), each motion profile in Table 12 in Chapter 6 was performed, while the quad-array imaged the middle tendon in the wrist. The motivation is determine which the smallest possible tendon motion that can be definitively detected by the algorithm (auto-location and displacement), since it is likely that an injured user would have limited tendon motion. The displacement fields for this study were computed using the SAD, FT and NCC similarity measures, for each sub-array. Upon reviewing the results, it was found that all similarity measures needed at least 1 mm of tendon motion, to auto-locate the tendon. As well, the smallest detectable displacement (i.e. the onset) was determined from these displacement fields. Recall, the onset of displacement is defined as the smallest tendon displacement needed, for the algorithm to detect that tendon motion, above the background noise. For the quad-array transducer, it is determined that 0.36 mm was the smallest detectable displacement, using any measure. As before, it is important to note that the tracking algorithms can only determine displacement values with a resolution that is equal to the ultrasound image resolution produced by the transducer. Thus, the minimum possible displacement that can be detected with the quad-array was 0.1408 mm (in the x-direction) and 0.019 mm (in the z-direction), which is a single image pixel of the quad array.

8.9. FEASIBILITY OF APPROACH USING PROPOSED TECHNIQUES FOR HAND PROSTHESIS APPLICATIONS

8.9.1. Discussion on Potential Users and Prerequisites

In reference to the potential users who can benefit from the proposed technology in this thesis, their injuries may consist of a single finger amputation, multiple finger amputations or an amputation of the entire hand at the wrist level. The biomechanics of an amputee's tendon displacement are widely unknown, due to the diversity of individual anatomy and cases. Regardless, it is envisioned that such users can contract their muscles to some degree, to provide a small tendon displacement. After consulting on a number of occasions with a hand surgeon, Dr.

Slobodan Djurickovic, this is a reasonable conjecture [64]. Dr. Djurickovic is a Medical Doctor, a member of FRCSC, and a Clinical Instructor in the Division of Plastic Surgery, Dept. of Surgery, at the University of British Columbia, in Vancouver, Canada. As described in Chapter 2, the muscle will suffer atrophic effects if left without resistance and rehabilitation. Thus, the prerequisites require the user to have their remnant FDS tendons to be sutured to nearby structures. This may not require additional surgery, and can be performed at the time of the scheduled amputation or post-injury medical intervention. Afterwards, the user must undergo rehabilitation to exercise the muscles to retain strength. This is not an additional protocol, and is within the usual standard following an amputation. Given these prerequisites, it is hypothesized that the user can flex their muscles to perform small tendon displacements. In such case, the proposed techniques in this thesis have demonstrated feasibility to comprise a system which can detect the small onset of tendon displacement. This in turn, may be used as the bio-signal for prosthetic control.

8.9.2. Discussion on the Proposed Speckle Tracking Algorithms

The speckle tracking algorithms using the similarity measures SAD, FT and NCC, along with the stationary ROI, and frame skipping technique are all useful algorithms for the proposed application. Overall the NCC-based algorithm performed better at total displacement estimations, while all the measures performed approximately the same for interframe displacement. The SAD algorithm is faster overall, due from the smaller amount of calculations involved. Thus, it is concluded that the proposed SAD algorithm can be implemented for both the auto-location and interframe displacement estimations. This allows for performance approximately as well as NCC, but with faster processing.

In order to detect the onset of tendon displacement, it is concluded that the SAD-based displacement field can be used as an initial calibration, in order to determine the tendon's location. Once the location is determined, the interframe SAD algorithm can continuously run, in order to determine if the user is displacing their tendon. This is a term described as detecting the "onset" of tendon displacement. Once this estimated displacement is above a pre-defined threshold considered as onset motion, this information can be used as bio-signal for prosthetic control.

8.9.3. Discussion on the Proposed Quad-array

This thesis proposes a tracking system for monitoring multiple tendons simultaneously, to allow for multi-DOF prosthesis control. To facilitate the ability for multi-tendon tracking, a new hardware solution that can monitor several tendons simultaneously, has been designed in the form of a custom sparse quad-array transducer. This quad-array design has been developed to be compatible with the Ultrasonix Touch Research open architecture ultrasound machine. This is so that the 128-channel beamformer within the Ultrasonix Touch Research can still be used, along with the system's proprietary software development kit (SDK). The custom sparse quad-array transducer presented in this thesis is a completely new concept. The quad-array transducer design is a 10 MHz multi-array transducer. It has four 32-element linear sub-arrays, where all four are in parallel, spaced 3 mm apart. In this configuration, it was demonstrated that the quad-array can auto-locate and track multi-tendons simultaneously. As well, in some cases, two separate arrays may be imaging the same tendon, thus providing possible redundancy with further investigation. Even with the reported total displacement relative error, R_D, being upwards of 10%, multi-tendon auto-location and tendon displacement is still possible. As well, regarding the onset experimentation, the proposed technique of auto-location and onset of small tendon excursions is feasible, thus demonstrating the usability of this new transducer.

In the current design, the 3mm spacing between the sub-arrays may not be suitable for everyone's hands, because hands are individual. This value was chosen when designing the transducer, based on measuring the tendon spacing using four embalmed cadaver hands, at the University of Victoria gross anatomy laboratory. Male hands generally have bigger tendons which are spaced further apart, in comparison to female hands. Thus, for Experiments 3-5, it was requested that the cadaver hand be male in gender. Perhaps an improvement to this design would be to have more sub-arrays in parallel, which are more closely spaced, in order to be suitable for both genders.

In the current design, each sub-array contains 32 elements. This limits the field of view of each sub-array, as well as restricting its ability to create a suitable aperture at the end elements. This will reduce the tracking potential at these locations. One possible solution is to have more elements in each sub-array. However, a drawback of adding more elements to each sub-array is the limitations of the beamformer. The beamformer only has 128 channels, thus restricting the elements in each sub-array. Possibly, an upgraded 256-channel beamformer can be implemented, allowing for more elements in a sub-array, or more sub-arrays in parallel.

CHAPTER 9:

CONCLUSION, FUTURE WORK AND THESIS CONTRIBUTIONS

9.1. CONCLUSION

The human hand is a dexterous bio-mechanism, that even with today's technology, cannot be completely replicated as a fully functional prosthetic device. Current prosthetic devices have functional limitations, which can be attributed to a lack of technology to obtain multiple, independent bio-signals from the body. If such multiple and independent bio-signals could be collected, they can be used as an input for advanced prosthesis control. Such limitations with current prosthesis inspired the ideas proposed in this thesis. In this thesis, the following nine objectives (described in Section 1.2) were successfully achieved:

A. The development of 2D B-Scan ultrasound software algorithms to:

  (1) Automatically locate the tendon position within a sequence of image frames,

  (2) Track the displacement of a single tendon within a sequence of image frames,

  (3) Track the displacement of multiple tendons simultaneously, on a sequence of image frames, and

  (4) Detect and track the onset of tendon motion and quantify the onset of small tendon displacements, within a sequence of image frames.

B. The design of custom hardware, which included:

  (7) Design of a custom quad-array ultrasound transducer, capable of monitoring multiple tendons simultaneously, and

  (8) Design of custom multi-tendon actuator system, along with other test-bed hardware to verify the objectives in (1-4).

C. Design and Development of experiments to test the validity of the proposed speckle tracking techniques, including:

(10) A Cadaver-based study: a preliminary experiment to optimize the software algorithms, settings and hardware configuration,

(11) A Human study: an experiment using volunteers undergoing carpal surgery to establish an anatomically ideal standard reference to validate the specking tracking techniques for a single tendon (Objective 2) and to further develop those techniques, and

(12) A Cadaver study: an experiment using two cadaver hands to validate the techniques for detecting and tracking single and multiple tendon displacements (Objectives 1-4).

9.2. FUTURE WORK

In order to extend the developments in this thesis for the application of controlling a hand prosthesis, several improvements can be made in future work. In terms of improving the tendon tracking software, the selection of tracking parameters should be fully automated. The use of an auto-location technique for identifying the optimal location of the template was verified in this thesis, but it can be improved upon. For instance, there are many other localization techniques used with B-Scan ultrasound, including optical flow [200], employing algorithms using the Lucas-Kanade approach [201], and others [202], which all can be used to determine where the tendon is moving in a sequence of B-Scan images. As well, a complementary algorithm to the auto-location technique will be developed to ensure that the transducer and tendons are in optimal view. Another improvement that could be done is to automatically set the template and ROI size, which was not automated in this thesis. The automation of the template and ROI size can be a function of the ultrasound hardware, such as its lateral and axial resolution. Another possible improvement to the algorithm, which is of particular importance for the onset detection, is to further develop the displacement estimation by sub-pixel extrapolation techniques. This will allow the displacement to be estimated at more than an integer pixel value. One possible approach to sub-pixel extrapolation is a bi-linear interpolation technique, introduced by [200]. Here, they created 0.25 granularity by expanding the template and ROI by 4 in length and height. Then, the newly generated pixel intensity at a given *(x,z)* point is a weighted average of its four neighboring points. This altered the data, but was reported to retain image quality. Another possible point of future investigations include further work with the redundancy-effects produced with the quad-array. Gathering redundant data allows for multiple estimations of the same tendon displacement, which may improve accuracy. As well, it is important to stream-line the data flow and processing by using RF-data directly for real time implementation.

In terms of the hardware, the quad-array design can be further improved in order to increase its versatility with hands of different sizes. Firstly, more than four sub-arrays can be used, where they are more closely spaced (i.e. less than 3 mm). Additionally, more elements can be used to improve the image field of view. Both these improvements may come at a cost of more elements needed, which requires the use of a beamformer with 256 channels.

It is important to note that the overall hardware must be miniaturized to be practical for controlling prosthetic devices. Thus, the quad-array design changes are restricted by this constraint. Current miniaturized ultrasound machine technology, such as the V-Scan (GE), P10 (Siemens), or the systems from Mobisante[203], may be investigated in future work. The Mobisante system was first developed at Washington University in St. Louis, Missouri. All of the circuitry of the Mobisante system is contained in the transducer probe console itself, which is in stark contrast to other commercial systems. The 2-sided circuit board is 0.9 inches by 3.4 inches, which includes the ultrasonic pulser, a transmit and receive switch, a pre-amplifier, a logarithmic amplifier for dynamic range compression, an analogue to digital converter, and other electronics. These miniaturized devices can provide the basic technology in order to further the work proposed in this thesis. As well, new powerful portable computing devices like the Parallela platform should be investigated [204]. Parallella is a high performance computing platform the size of a credit card, with low power consumption. Given these other current technologies, it is hypothesized that the ideas proposed in this thesis may be miniaturized for portable purposes.

Other considerations for prosthetic applications involve further investigations into tissue heating from the continuous scanning of ultrasound. The thermal effects produced by ultrasound are often used for rehabilitative purposes and can be considered therapeutic. In these cases, it is used for short time intervals to reduce mild inflammation, decrease pain, or decrease blood flow, to name a few. Further investigations with a tissue-heating phantom must be implemented in order to determine if the proposed system is safe to be used continuously.

Another important improvement is the development of a different ultrasonic coupling gel. These coupling gels are used in between the transducer and the skin, to allow the soundwave to pass from the transducer into the tissue, and vice versa, with no unwanted attenuation or reflections. These gels evaporate in a relatively short time, which can lessen their usability with a prosthetic device. Current examinations of alternative coupling materials are underway, which includes different medical-grade adhesives with suitable acoustic properties, which can be removed when desired.

9.3. THESIS CONTRIBUTIONS

This work provides a new way to detect and track the displacement of moving flexor tendons within the human arm, using a non-invasive ultrasound-based technique. In addition, it provides a way to detect a person's intention (user intention) to move their hands and fingers. This has application to hand prosthetic control, which has significant contributions to the medicine and rehabilitation community. Using tendon displacement as a bio-signal for prosthetic control is a completely new concept. The novelty of the proposed sensor system itself is comprised of several major developments. These were briefly introduced in Chapter 1, with the details provided by the following:

The first major contribution is the creation of new signal processing routines to estimate tendon tissue motion from a sequence of ultrasound images. Since it is ultrasound-based, it allows for non-invasive monitoring of bio-signals. These new algorithms use the speckle tracking technique in order to estimate the displacement of a tendon throughout a sequence of ultrasound images. They employ a new combination of tracking parameters. This includes using the measures SAD, SSD, FT and NCC, along with the stationary ROI technique. The FT similarity measure was derived in full, which is not found in the literature. As well a new frame skipping method is developed and integrated into the algorithms. Additionally, two new hybrid similarity measures are developed, which accounted for noise in the images, as well as the underlying signal-to-noise ratio. Another contribution includes the analysis of parameter variation, and hence optimization of those for use in speckle tracking. Most literature simply state the values of the tracking parameters, without any indication or explanation of their effects, if they were different. This thesis addresses the effect of speckle tracking success when choosing the values for relevant parameters. Another contribution is the development of the auto-location technique, to automatically determine the tendons location in a sequence of B-Scan images, and to determine the optimal template location for displacement tracking.

The second major contribution is the hardware design of a new custom quad-array ultrasonic transducer, capable of imaging up to four tendons simultaneously. Developing such a quad-array sensor is instrumental to the success of controlling a multi-DOF prosthetic. The quad-array successfully imaged the tendon displacement from multiple tendons simultaneously. The developed speckle tracking techniques were able to detect the tendon's location in one of the sub-arrays, and then estimate the interframe, cumulative and total displacement.

A third major contribution involves the design of a multi-tendon actuator system, along with other specialized test-bed hardware, in order to actuate and couple to the tendons on a cadaver hand. This was a difficult task, given the many factors to consider when designing experiments involving biological tissue, and the limited experimental time before biological tissue deteriorates. The custom tendon couplers were developed, which grasped the tendons without slipping or tearing. As well, a transducer holder was developed, with interchangeable end-holders, which can grasp a linear array, or the quad-array. Together this system performed very well and will become the standard design within our group.

The fourth major contribution is the experiments themselves. Several experiments are performed and the results analyzed, to verify the concepts in this thesis. These experiments provide a comprehensive study into estimating tendon incremental displacement, total displacement, tendon velocity, as well as the onset of small displacements. These experiments are unique in that they use human material (cadavers and human volunteers) instead of gel-based medical calibration phantoms. Experiments that employ biological tissue allow for a gold standard reference for comparison to the estimated values. Hence, one of the novelties of this thesis is that tracking techniques are verified by directly observing real tendon motion in live human subjects with exposed tendons, or by observing real tendon motion in cadaver hands which are actuated by motors. This way, the tendon tracking techniques are verified in the most realistic way.

Together, the aforementioned developments can be used toward prosthesis control, to provide a user with up to four independent signals to control an advanced prosthetic system. (US Patent # 14058022, filing date: Oct. 18th, 2013). This can significantly improve the state of the art by allowing for a prosthetic device to have increased functionality. This could help those suffering with hand impairment such as multiple finger amputations, by restoring some function. In addition, the tendon tracking algorithm that has been developed has applicability to clinicians dealing with other hand injuries. Clinicians can use the proposed ultrasonic technique to assess tendon motion in order to determine tendon velocity and displacement. This technique may be useful for applications involving the treatment, diagnosis or assessment of post/pre-operative repair of tendon injuries (Provisional Patent # 61/841,156, filing date: June 27th, 2013).

REFERENCES

[1] V Schöffl, A Heid, T Küpper, "Tendon injuries of the hand," vol. 3, p. 62, 2012.

[2] PJ Evans, NI Mogekwu, "Carpal Tunnel Surgery," in *Perioperative Management of Patients with Rheumatic Disease*. New York: Springer, 2013, pp. 319-321.

[3] Bureau of Labor Statistics, U.S. Department of Labor. Internet: http://www.bls.gov/, 2011.

[4] K Ziegler-Graham, EJ MacKenzie, PL Ephraim, TG Travison, R Brookmeyer, "Estimating the prevalence of limb loss in the United States:2005 to 2050," *Archives of Physical Medicine and Rehabilitation*, vol. 89, no. 3, pp. 422-429, 2008.

[5] M Zecca, S Micera, M Carrozza, P Dario, "Control of multifunctional prosthetic hands by processing the electromyographic signal," *Critical Reviews in Biomedical Engineering*, vol. 30, no. 4-6, 2002.

[6] P. Downey and M. Siegel, "Bone biology and the clinical implications for osteoporosis," *Physical therapy*, vol. 86, no. 1, pp. 77-91, 2006.

[7] "Bone Structure and Function, An Introduction to Nutrition". Internet: http://2012books.lardbucket. org/books/an-introduction-to-nutrition/s13-01-bone-structure-and-function.html, 2013

[8] A. Freivalds, *Biomechanics of the Upper Limbs*.: CRC Press, Ch 2,3,5, 2004.

[9] A. Agnihotri, B. Purwar, N. Jeebun and S. Agnihotri , "Determination Of Sex By Hand Dimensions," *The Internet Journal of Forensic Science*, vol. 1, no. 2, 2006.

[10] P. Brand and A. Hollister, *Clinical Mechanics of the Hand*, 3rd ed.: Mosby Inc, 1999.

[11] G. ElKoura and K. Singh, "Handrix: animating the human hand," *In Proceedings of the 2003 ACM SIGGRAPH/Eurographics symposium on Computer animation, Eurographics Association*, pp. 110-119, 2003.

[12] F. Rossiter, *The Practical Guide To Health*. Mountain View, California, USA: Pacific Press Publishing Association, Fig 12, pg 29, 1910.

[13] "Sliding Filament Theory". Internet: http://www.ucl.ac.uk/~sjjgsca/muscleSlidingFilament.html, 2013

[14] "Muscle Structure and Order". Internet: http://nscanotes.wordpress.com/microscopic-muscle-structure-and-order/

[15] J. Kastelic, A. Galeski, E. Baer , "The multicomposite structure of tendon," *Connect Tissue Res*, vol. 6, pp. 11-21, 1978.

[16] S. Ward,G. Loren, S. Lundberg, and R.Lieber, "High stiffness of human digital flexor tendons is suited for precise finger positional control," *Journal of neurophysiology*, vol. 96, no. 5, pp. 2815-2818, 2005.

[17] JR. Doyle and MJ. Botte, *Surgical anatomy of the hand and upper extremity*, 75th ed.: Lippincott Williams & Wilkins, 2003.

[18] H Gray, *Gray's Anatomy*.: Philadelphia Lea and Febige, 1918.

[19] "Tendon Laceration". Internet: http://www.iowahand.com/tendons.html, 2013.

[20] "Structure of the Nervous System". Interent: http://www.biomedresearches.com/root/pages /researches/epilepsy/structure_of_nervous_system.html, 2013.

[21] "Structure of the Nerve".
Internet: http://neuroanatomyblog.tumblr.com/post/33654136457/com-plete-struc-ture-of-a-nerve-endoneurium-wraps, 2013.

[22] "Neuron". Internet: http://upload.wikimedia.org/wikipedia/commons/thumb/b/bc/Neuron_ Hand-tuned.svg/400px-Neuron_Hand-tuned.svg.png, 2013.

[23] "The Anatomy of Movement". Internet: http://brainconnection.positscience.com/the-anatomy-of-movement/, 2013.

[24] "The Brain". Internet: http://thebrain.mcgill.ca/flash/d/d_06/d_06_cr/d_06_cr_mou/ d_06_cr_mou.html, 2013.

[25] "Structure of the Nervous System". Internet: http://www.biomedresearches.com/root/pages/ researches/epilepsy/structure_of_nervous_system.html, 2013.

[26] "The Brain". Internet: http://www.me.umn.edu/~wkdurfee/projects/itasca/lectureNotes.pdf,2013.

[27] S. Mcphee , "“Functional hand evaluations: a review," *The American Journal of Occupational Therapy*, vol. 41, no. 3, pp. 158-163.

[28] A. Sapienza, HK. Yoon, R.Karia, and S.Lee, "Flexor tendon excursion and load during passive and active simulated motion: a cadaver study," *Journal of Hand Surgery (European Volume)* , 2012.

[29] M. Wehbé, J.Hunter, "Flexor tendon gliding in the hand. Part I. In vivo excursions," *The Journal of Hand Surgery*, vol. 10, no. 4, pp. 570-574 , 1985.

[30] M. Hume, H. Gellman, H. McKellop, R. Brumfield Jr, "Functional range of motion of the joints of the hand," *The Journal of Hand Surgery*, vol. 15, no. 2, pp. 240-243, 1990.

[31] W. Thomas, W. Miltner, R. Huonker, R. Friedel, I. Schmidt, E. Taub , "Rapid functional plasticity of the somatosensory cortex after finger amputation," *Experimental Brain Research* , vol. 134, no. 2, pp. 199-203, 2000.

[32] M. Merzenich, RJ. Nelson, MP. Stryker, MS. Cynader, A. Schoppmann, JM. Zook , "Somatosensory cortical map changes following digit amputation in adult monkeys," *J Comp Neurol* , vol. 224 , pp. 591–605, 1984.

[33] MB. Calford and R. Tweedale , "Immediate and chronic changes in responses of somatosensory cortex in adult flying-fox after digit amputation," *Nature*, vol. 332, pp. 446–448, 1988.

[34] JG. Ojemann and DL. Silbergeld, "Cortical stimulation mapping of phantom limb rolandic cortex: Case report," *J Neurosurg* , vol. 82, pp. 641–644, 1995.

[35] A. Pascual-Leone, M. Peris, JM. Tormos, AP. Pascual, MD. Catala, "Reorganization of human cortical motor output maps following traumatic forearm amputation," *Neuroreport* , vol. 7, pp. 2068–2070, 1996.

[36] H. Flor, T. Elbert, S. Knecht, C. Wienbruch, C. Pantev, N. Birbaumer, W. Larbig, E. Taub , "Phantom-limb pain as a perceptual correlate of cortical reorganization following arm amputation," *Nature* , vol. 375, pp. 482–484, 1995.

[37] T. Weiss, WHR. Miltner, J. Dillmann, W. Meissner, R. Huonker, H. Nowak , "Reorganization of the somatosensory cortex after amputation of the index finger," *Neuroreport* , vol. 9, pp. 213–216, 1998.

[38] S. Florence,TA. Hackett, and F. Strata, "Thalamic and cortical contributions to neural plasticity after limb amputation," *Journal of neurophysiology*, vol. 83, no. 5, pp. 3154-3159, 2000.

[39] H.Flor, "Phantom-limb pain: characteristics, causes, and treatment," *The Lancet Neurology*, vol. 1, no. 3, pp. 182–189, July 2002.

[40] TS. Jensen, B. Krebs, J. Nielsen, P. Rasmussen, "Phantom limb, phantom pain and stump pain in amputees during the first 6 months following limb amputation," *Pain*, vol. 17, pp. 243-256, 1983.

[41] PL. Carlen, PD. Wall, H. Nadvorna, T. Steinbach, "Phantom limbs and related phenomena in recent traumatic amputations," *Neurology*, vol. 28, pp. 211-217, 1978.

[42] C. Kooijman, P. Dijkstra, J. Geertzen, A. Elzinga, C. Schans, "Phantom pain and phantom sensations

in upper limb amputees: an epidemiological study," *Pain*, vol. 87, no. 1, pp. 33-41, 2000.

[43] T. Kuiken, G. Dumanian, R. Lipschutz, L. Miller, and K. Stubblefield, "Targeted muscle reinnervation for improved myoelectric prosthesis control," in *in Proc. 2nd Int IEEE EMBS Conf. Neural Eng*, 2005, pp. 396–399.

[44] T. Kuiken, L. Miller, R. Lipschutz, B. Lock, K. Stubbefield, P. Marasco, P. Zhou, and G. Dumanian, "Targeted reinnervation for enhanced prosthetic arm function in a woman with a proximal amputation: A case study," *Lancet*, vol. 369, pp. 371–380, 2007.

[45] P. Zhou, M. Lowery, K. Englehart, H. Huang, G. Li, L. Hargrove, J. Dewald, and T. Kuiken, "Decoding new neural machine interface for control of artificial limbs," *J. Neurophysiol*, vol. 98, pp. 2974–2982, 2007.

[46] G. Di Pino, E. Guglielmelli, P.M. Rossini, "Neuroplasticity in amputees: Main implications on bidirectional interfacing of cybernetic hand prostheses," *Progress in Neurobiology*, vol. 88, no. 2, pp. 114-126, June 2009.

[47] S. Edwards. "Wrist and Forearm Amputations". Internet: http://emedicine.medscape.com/article /1245535-overview#a0101, 2013.

[48] JH. Malone, "Immediate postsurgical management of upper extremity amputation: conventional, electric and myoelectric prosthesis," *Orthot Prosthet*, vol. 35, no. 2, pp. 1-9, 1981.

[49] E. Burgess, J.Zettl, "Amputations Below the Knee," *Digital Resource Foundation for the Orthotics and Prosthetics Community* , vol. 13, no. 1, pp. 1-12, 1969.

[50] P.F. Pasquina, P.R. Bryant, M.E. Huan, T.L. Roberts, V.S. Nelson, "Flood Advances in amputee care," *Arch Phys Med Rehabil*, vol. 87, no. 3.1, pp. S34–S43, 2006.

[51] E. Isakov, H. Burger, M. Gregoric, and C. Marinccek, "Stump length as related to atrophy and strength of the thigh muscles in trans-tibial amputees," *Prosthetics and orthotics international 20*, vol. 20, pp. 96-100, 1996.

[52] E Isakov, H Burger, M Gregoric, C Marincek, "Isokinetic and isometric strength of the thigh muscles in below-knee amputees," *Clinical Biomechanics*, vol. 11, no. 4, pp. 233-235, 1996.

[53] M Baratz, A Watson, J Imbriglia, *Orthopaedic surgery: The Essentials*.: Thieme, 1999.

[54] T. McIsaac, and A.Fuglevand, "Motor-unit synchrony within and across compartments of the human flexor digitorum superficialis," *Journal of neurophysiology*, vol. 97, no. 1, pp. 550-556, 2007.

[55] TJ. Butler, SL.Kilbreath, RB. Gorman, SC. Gandevia , "Selective recruitment of single motor units in

human flexor digitorum superficialis muscle during flexion of individual fingers," *J Physiol*, vol. 567, pp. 301–309, 2005.

[56] SL. Kilbreath, SC. Gandevia, "Limited independent flexion of the thumb and fingers in human subjects," *J Physiol*, vol. 479, pp. 487–497, 1994.

[57] JL Cronenwett , MD McDaniel, RM Zwolak , "Limb Salvage Despite Extensive Tissue Loss: Free Tissue Transfer Combined With Distal Revascularization," *Arch Surg.*, vol. 124, no. 5, pp. 609-615, 1989.

[58] T.Schoeller, G. Wechselberger, H.Hussl, G.Huemer, "Functional transposition of the latissimus dorsi muscle for biceps reconstruction after upper arm replantation," *Journal of Plastic, Reconstructive & Aesthetic Surgery*, vol. 60, no. 7, pp. 755-759, 2007.

[59] K.Kawamura , H.Yajima , Y.Tomita , Y.Kobata , K.Shigematsu , Y.Takakura, "Restoration of elbow function with pedicled latissimus dorsi myocutaneous flap transfer," *Journal of Shoulder and Elbow Surgery*, vol. 16, no. 1, pp. 84–90, 2007.

[60] AM. Reyzelman, S. Hadi, DG. Armstrong, "Limb salvage with Chopart's amputation and tendon balancing," *J Am Podiatr Med Assoc.*, vol. 89, no. 2, pp. 100-103, Feb 1999.

[61] S.Watve,G.Dodd, R.MacDonald, E.Stoppard, "Upper limb prosthetic rehabilitation," *Orthopaedics and Trauma*, vol. 25, no. 2, pp. 135-142, 2011.

[62] M. Kuttuva, G.Burdea, J.Flint, and W.Craelius, "Manipulation practice for upper-limb amputees using virtual reality," *Presence: Teleoperators and Virtual Environments* , vol. 14, no. 2, pp. 175-182, 2005.

[63] B. Kegel, E.Burgess, T.Starr, and W.Daly, "Effects of isometric muscle training on residual limb volume, strength, and gait of below-knee amputees," *Physical Therapy*, vol. 61, no. 10, pp. 1419-1426, 1981.

[64] S Djurickovic, Cosmedic, Hand and Microsurgery, Victoria BC, personal coorespondance.

[65] T. Schreuders, "The quadriga phenomenon: a review and clinical relevance," *Journal of Hand Surgery (European Volume)*, vol. 37, no. 6, pp. 513-522, 2012.

[66] "Transfemoral Amputation".Interent: http://www.ampsurg.org/html/ak2/AK2outline.html,2013.

[67] J. Hong, H. Choi. "Dynamic analysis of transfemoral amputee's musculoskeletal system using muscle activation control parameters measured by FES experiments". Internet:http://www.univ-valenciennes.fr/congres/3D2006/Abstracts/169-Hong.pdf, 2013.

[68] B. Persson, "Lower limb amputation Part 1: Amputation methods-a 10 year literature review," *Prosthetics and orthotics international* , vol. 25, no. 1, pp. 7-13, 2001.

[69] B Schnebel, D Flesher and C Garcia-Moral, "Isolated traumatic avulsion of the flexor digitorum sublimis: a case report," *The American Journal of Sports Medicine*, vol. 17, pp. 692-694, 1989.

[70] CY Chen, TS Li, YT Liu, and HC Chen, "Miniplate Hooking Method for Repair of Type III Flexor Digitorum Profundus Avulsion Injury With a Small Bone Fragment: Case Report," *Journal of Hand Surgery*, vol. 34, no. A, pp. 1449–1453, 2009.

[71] M Silva, S Hollstein, A Fayazi, P Adler, R Gelberman and M Boyer, "The Effects of Multiple-Strand Suture Techniques on the Tensile Properties of Repair of the Flexor Digitorum Profundus Tendon to Bone," *J Bone Joint Surg Am.*, vol. 80, pp. 1507-1514, 1998.

[72] V. Putti, "Historical Prostheses," *The Journal of Hand Surgery: British & European Volume*, vol. 30, no. 3, pp. 310-325, 2005.

[73] A. Pare, Wellcome Library, London. Wellcome Library Catalogue. Internet:. http://catalogue. wellcomelibrary.org/record=b1455316, 2013.

[74] N. Robinson."myArmoury.com". Internet: http://www.myarmoury.com/talk/viewtopic.php?t=7161, 2010

[75] C. Martin, D. Edeer. "WorkSafe BC". Internet: http://www.worksafebc.com/health_care_providers /Assets/PDF/UpperLimbProstheses2011.pdf, 2011.

[76] Touch Bionics. "living skin". Internet: http://www.touchbionics.com/products/passive-functional-prostheses/livingskin/, 2013.

[77] A. Nichols Jr." Captain Christopher Newport: Admiral of Virginia". Internet: http:// www.captainchristophernewport.com/, 2012.

[78] Hosmer. Internet: http://hosmer.com/products/wrists/, 2013.

[79] G. Smit, R. Bongers, C. Van der Sluis, D. Plettenburg, "Efficiency of voluntary opening hand and hook prosthetic devices: 24 years of development?," *Journal of Rehabilitation Research and Development*, vol. 49, no. 4, pp. 523-534, 2012.

[80] Touch Bionics. Internet: http://www.touchbionics.com/products/active-prostheses/i-limb-ultra/, 2013.

[81] Ottobock. Internet: http://professionals.ottobock.ca/cps/rde/xchg/ob_com_en/hs.xsl/6901.html, 2013

[82] N Dechev, WL Cleghorn, S Naumann, "Multiple finger, passive adaptive grasp prosthetic hand," *Mechanism and machine theory*, vol. 36, no. 10, pp. 1157-1173, 2001.

[83] A. Biddiss, T. Chau , "Upper limb prosthesis use and abandonment: A survey of the last 25 years," *Prosthetics and orthotics international*, vol. 31, no. 3, pp. 236-257, 2007.

[84] D. Atkins, D. Heard, W. Donovan , "Epidemiologic overview of individuals with upper-limb loss and their reported research priorities," *J Prosthet Orthot*, vol. 9, pp. 2-11, 1996.

[85] J. Shaperman, M. LeBlanc, Y. Setoguchi, DR. McNeal , "Is body powered operation of upper limb prostheses feasible for young limb deficient children? ," *Prosthet Orthot Int.*, vol. 19, no. 3, pp. 165-175, 1995.

[86] GH. Kejlaa, "Consumer concerns and the functional value of prostheses to upper limb amputees," *Prosthet Orthot Int.*, vol. 17, no. 3, pp. 157-163, 1993.

[87] MA. LeBlanc, "Innovation and improvement of body-powered arm prostheses: A first step. ," *Clin Prosthet Orthot.*, vol. 9, no. 1, pp. 13-16, 1985.

[88] S. Micera, J. Carpaneto, S. Raspopovic, "Control of hand prostheses using peripheral information," *Biomedical Engineering, IEEE Reviews in*, vol. 3, pp. 48-68, 2010.

[89] William Selpho, "Construction of Artificial Hands," Wearable mechanism 18,021, August 18, 1857.

[90] P. Ventimiglia. "Design of a Human Hand Prosthesis". Internet: http://www.wpi.edu/Pubs/E-project/Available/E-project-042612-145912/unrestricted/MQP_PaulV_Complete_Final_3.pdf,2013.

[91] JP. Donoghue, "Connecting cortex to machines: recent advances in brain interfaces," *Nature Neuroscience*, vol. 5, pp. 1085-1088, 2002.

[92] M. Velliste, S. Perel, M. Spalding, A. Whitford, A. Schwart, "Cortical control of a prosthetic arm for self-feeding," *Nature*, vol. 453, pp. 1098-1101, June 2008.

[93] L. Hochberg, M. Serruya, G.Friehs, J.Mukand, M. Saleh, A. Caplan, A. Branner, D. Chen, R. Penn,JP. Donoghue, "Neuronal ensemble control of prosthetic devices by a human with tetraplegia," *Nature*, vol. 442, pp. 164-171, 2006.

[94] Brain Gate. Internet: http://www.braingate.com/, 2013.

[95] E. Maynard, C. Nordhausen, R. Normann, "The Utah Intracortical Electrode Array: A recording structure for potential brain-computer interfaces," *Electroencephalography and Clinical Neurophysiology*, vol. 102, no. 3, pp. 228–239, 1997.

[96] A. Schwartz, "Cortical neural prosthetics," *Ann. Rev. Neurosci*, vol. 27, pp. 487–507, 2004.

[97] M. A. Lebedev and M. A. Nicolelis, "“Brain-machine interfaces: Past,present and future," *Trends Neurosci*, vol. 29, pp. 536–546, 2006.

[98] S. Micera, X. Navarro, L. Citi, O. Tonet, P. Rossini, K. Hoffmann, M. Vivó, K. Yoshida, and P. Dario, "On the Use of Longitudinal Intrafascicular Peripheral Interfaces for the Control of Cybernetic Hand Prostheses in Amputees," *NEURAL SYSTEMS AND REHABILITATION ENGINEERING, IEEE TRANSACTIONS ON*, vol. 16, no. 5, pp. 453-471, 2008.

[99] University of Reading. Internet: http://www.reading.ac.uk/news-and-events/releases/ PR16530.aspx, 2013.

[100] A. Schwartz, X. Cui, D. Weber, D. Moran, "Brain-Controlled Interfaces: Movement Restoration with Neural Prosthetics," *Neuron*, vol. 52, no. 1, pp. 205-220, 2006.

[101] C. Guger, W. Harkam, C. Hertnaes, G. Pfurtscheller, "Prosthetic control by an EEG-based brain-computer interface (BCI).," in *In Proc. aaate 5th european conference for the advancement of assistive technology*, Düsseldorf, Germany, 1999, pp. 3-6.

[102] R.Lauer, H. Peckham, K.Kilgore, "EEG-based control of a hand grasp neuroprosthesis," *NeuroReport* , vol. 10, pp. 1767-1771, 1999.

[103] D. Cohen D and BN. Cuffin , "Demonstration of useful differences between the magnetoencephalogram and electroencephalogram," *Electroencephalogr Clin Neurophysiol.*, vol. 56, pp. 38-51, 1983.

[104] S. Waldert, H. Preissl, E. Demandt, C. Braun, N. Birbaumer, A. Aertsen, and C. Mehring, "Hand movement direction decoded from MEG and EEG," *J Neuroscience*, vol. 28, no. 4, pp. 1000-1008, 2008.

[105] V. Aggarwal, A. Chatterjee, Y. Cho, R. Rasmussen, S. Acharya, and N. V. Thakor, "Noninvasive cortical control of a prosthetic hand with local machine control and haptic feedback," in *Meeting Biomed. Eng. Soc. (BMES 2006)*, Chicago, IL, 2006.

[106] C. Mercier, K. T. Reilly, C. D. Vargas, A. Aballea, and A. Sirigu, "Mapping phantom movement representations in the motor cortex of amputees," *Brain*, vol. 129, no. 8, pp. 2202-2210, 2006.

[107] K. T. Reilly, C. Mercier, M. H. Schieber, and A. Sirigu, "Persistent hand motor commands in the amputees’ brain," *Brain*, vol. 129, no. 8, pp. 2211–2223, 2006.

[108] G. D. Pino, E. Guglielmelli, and P. M. Rossin, "Neuroplasticity in amputees: Main implications on

bidirectional interfacing of cybernetic hand prostheses," *Prog Neurobiol*, vol. 88, no. 2, pp. 114–126, 2009.

[109] D. J. Edell, "A peripheral nerve information transducer for amputees: Long-term multichannel recordings from rabbit peripheral nerves," *IEEE Trans. Biomed. Eng.*, vol. 33, no. 2, pp. 203–214, Feb 1986.

[110] R. R. Riso, "Strategies for providing upper extremity amputees with tactile and hand position feedback—Moving closer to the bionic arm," *Technol. Health Care*, vol. 7, no. 6, pp. 401–409, 1999.

[111] T. Stieglitz, M. Schuetter, and K. P. Koch, "Implantable biomedical microsystems for neural prostheses," *IEEE Eng. Med. Biol. Mag*, vol. 24, no. 5, pp. 58–65, May 2005.

[112] K. H. Polasek, H. A. Hoyen, M. W. Keith, R. F. Kirsch, and D. J. Tyler, "Stimulation stability and selectivity of chronically implanted multicontact nerve cuff electrodes in the human upper extremity ," *IEEE Trans. Neural Syst. Rehabil. Eng.*, vol. 17, no. 5, pp. 428-437, 2009.

[113] J. Hoffer, K. Strange, P. Christensen, Y. Chen, and K. Yoshida, "Multichannel recordings from peripheral nerves: properties of Multi-Contact Cuff (MCC) and Lontigutidnal Intra-Fascicular Electrode (LIFE) arrays implanted in cat forelimb nerves," *Proc. Int. Conf. Int. Functional Electrical Stimulat. Society*, vol. 2, pp. 4310-4313, 1997.

[114] M. Tarler and J. Mortimer, "Selective and independent activation of four motor fascicles using a four contact nerve cuff electrode," *IEEE Trans. Neural Syst. Rehabil. Eng.*, vol. 12, no. 2, pp. 251–257, June 2004.

[115] D. Tyler and D. Durand, "A slowly penetrating interfascicular nerve electrode for selective activation of peripheral nerves," *IEEE Trans.Rehab. Eng.*, vol. 5, no. 1, pp. 51–61, March 1997.

[116] D. Leventhal and D. Durand, "Subfascicle stimulation selectivity with the flat interface nerve electrode," *Ann Biomed. Eng.*, vol. 31, pp. 643-652, 2003.

[117] K. Yoshida and R. B. Stein, "Characterization of signals and noise rejection with bipolar longitudinal intrafascicular electrodes," *IEEE Trans. Biomed. Eng.*, vol. 46, no. 2, pp. 226–234, Feb 1999.

[118] S. M. Lawrence, G. S. Dhillon, W. Jensen, K. Yoshida, and K. W. Horch, "Acute peripheral nerve recording characteristics of polymer-based longitudinal intrafascicular electrodes," *IEEE Trans.NeuralSyst Rehabil. Eng.*, vol. 12, no. 3, pp. 345–348, Sept 2004.

[119] G. Dhillon and K. Horch, "Direct neural sensory feedback and control of a prosthetic arm," *IEEE*

Trans. Neural Syst. Rehabil. Eng., vol. 13, no. 4, pp. 468–472, Dec 2005.

[120] P.Rossinia, S. Micerac, A. Benvenuto, J.Carpaneto, G. Cavallo, L. Citi, C.Cipriani, L.Denaro, V. Denaro, G. Di Pino, F.Ferreri, E. Guglielmelli, K.Hoffmann, S. Raspopovic, J.Rigosa, L.Rossini, M. Tombini, P. Dario, "Double nerve intraneural interface implant on a human amputee for robotic hand control," *Clinical Neurophysiology, Volume 121, Issue 5, May 2010, Pages*, vol. 121, no. 5, pp. 777-783, May 2010.

[121] G. S. Dhillon, S. M. Lawrence, D. T. Hutchinson, and K. W. Horch, "Residual function in peripheral nerve stumps of amputees: Implications for neural control of artificial limbs," *J. Hand Surg. Amer.*, vol. 29, no. 4, pp. 605–615.

[122] J. Keesey, "How Electric Fish Became Sources of Acetylcholine Receptor," *Journal of the History of the Neurosciences*, vol. 14, no. 2, pp. 149-164, 2005.

[123] C. Fleischer, A. Wege, K. Kondak, G. Hommel , "Application of EMG signals for controlling exoskeleton robots," *Biomed Tech (Berl)*, vol. 51, no. 5-6, pp. 314-319, 2006.

[124] G.Drost, D.Stegeman, B.van Engelen, M. Zwarts, "Clinical applications of high-density surface EMG: A systematic review ," *Journal of electromyography and kinesiology : official journal of the International Society of Electrophysiological Kinesiolog*, vol. 16, no. 6, pp. 586-602, 2006.

[125] R. Weir, P.Troyk, G. DeMichele, and T. Kuiken, "Implantable Myoelectric Sensors (IMES) forUpper-E:xtremity Prosthesis Control-Preliminary Work," in *In Engineering in Medicine and Biology Society. Proceedings of the 25th Annual International Conference of the IEEE*, 2003, pp. 1562-1565.

[126] D. Young, B. Farnsworth, R. Triolo, "Wireless implantable EMG sensor for powered prosthesis control," in *Solid-State and Integrated-Circuit Technology, 2008. ICSICT 2008. 9th International Conference on*, 2008, pp. pp.2541-2544.

[127] K. Masuda, T. Masuda, T. Sadoyama, M. Inaki and S. Katsuta , "Changes in surface EMG parameters during static and dynamic fatiguing contractions," *J Electromyogr Kinesiol.* , vol. 9, no. 1, pp. 39-46, 1999.

[128] R. Barea, L. Boquete, M. Mazo, and E.Lopez , "System for Assisted Mobility Using Eye Movements Based on Electrooculography," *IEEE Transaction on Neural Systems and Rehabilitation Engineering*, vol. 10, no. 4, pp. 209-218, 2002.

[129] J. Gu, M. Meng, A. Cook and G. Faulkner, "Simulation study of artificial ocular movement with intelligent control," *Control Engineering*, vol. 13, no. 4, pp. 509-518, 2005.

[130] M. Williams and R. Kirsch, "The Feasibility of EOG as a Command Interface for a high Tetraplegia Neural Prosthesis," in *The 10th Annual Conference of the International Functional Electrical Stimulation Society*, 2005.

[131] JW. Coburn, TJ. Housh, JT Cramer, JP Weir, JM Miller, TW Beck, MH.Malek, and GO.Johnson, "Mechanomyographic and electromyographic responses of the vastus medialis muscle during isometric and concentric muscle actions," *J Strength Cond Res.*, vol. 19, no. 2, pp. 412-420, 2005.

[132] P. Madeleine, L. Jørgensen, K. Søgaard, L. Arendt-Nielsen, G. Sjøgaard , "Development of muscle fatigue as assessed by electromyography and mechanomyography during continuous and intermittent low-force contractions: Effects of the feedback mode," *Eur J Appl Physiol.*, vol. 87, no. 1, pp. 28-37, 2002.

[133] JP. Weir, KM. Ayers, JF.Lacefield and KL Walsh , "Mechanomyographic and electromyographic responses during fatigue in humans: Influence of muscle length," *Eur J Appl physiology*, vol. 81, no. 4, pp. 352-359, 2000.

[134] J Silva, W Heim, and T Chau , "A self-contained, mechanomyography driven externally powered prosthesis," *Arch Phys Med Rehabil.*, vol. 86, no. 10, pp. 2066-2070, 2005.

[135] C.Orizio, "Muscle sound: Bases for the introduction of a mechanomyographic signal in muscle studies," *Crit Rev Biomed Eng.*, vol. 21, no. 3, pp. 201–243, 1993.

[136] A. Jaskólska,W. Brzenczek, K Kisiel-Sajewicz, A. Kawczyski, J. Marusiak and A. Jaskólski , "The effect of skinfold on frequency of human muscle mechanomyogram," *J Electromyogr Kinesiol.*, vol. 14, no. 2, pp. 217–225, 2004.

[137] R. Abboudi , C. Glass, A. Newby, J. Flint and W. Craelius , "A biomimetic controller for a multifinger prosthesis," *Rehabilitation Engineering, IEEE Transactions* , vol. 7, no. 2, pp. 121-129, 1999.

[138] D. Curcie,J. Flint,and W. Craelius , "Biomimetic finger control by filtering of distributed forelimb pressures," *Neural Systems and Rehabilitation Engineering IEEE Transactions*, vol. 9, no. 1, pp. 69 – 75, 2001.

[139] LP. Kenney, I. Lisitsa, P. Bowker, G. H. Heath, and D. Howard., "Dimensional change in muscle as a control signal for powered upper limb prostheses: a pilot study," *Medical Engineering & Physics*, vol. 21, no. 8, pp. 589 – 597.

[140] J. Canderle, JPJ. Kenney, A. Bowen, D. Howard, H. Chatterton , "A dual task approach to the evaluation of the myokinemetric signal as an alternative to EMG," *Engineering in Medicine and*

Biology Society, vol. 2, no. 6, pp. 4548 – 4551, 2004.

[141] XP. Zheng, MM. Chan, J. Shi, X. Chen, QH. Huang , "Sonomyography: monitoring morphological changes of forearm muscles in actions with the feasibility for the control of powered prosthesis," *Med Eng Phys.* , vol. 28, no. 4, pp. 405-415, 2006.

[142] JY. Guo, YP. Zheng, QH. Huang, and X.Chen , "Dynamic monitoring of forearm muscles using one-dimensional sonomyography system," *J Rehabil Res Dev.*, vol. 45, no. 1, pp. 187-196, 2008.

[143] KJ. Stegman, N. Dechev, EJ. Park, and R.Podhorodeski, "Measurement of tendon excursion using an audio-based Fourier technique with pulsed-wave Doppler ultrasound," in *American Society of Mechanical Engineers (ASME), Proc. of the ASME Int. Mech. Eng. Congress*, Vancouver, BC Canada, 2010, pp. 2:777-783.

[144] KJ. Stegman, RP. Podhorodeski, EJ. Park, "A feasibility study for measuring accurate tendon displacements using an audio-based Fourier analysis of pulsed-wave Doppler ultrasound signals. ," in *Conference proceedings : Annual International Conference of the IEEE Engineering in Medicine and Biology*, Minneapolis, Minnesota, 2009, pp. 1363-1366.

[145] KJ. Stegman, EJ. Park, and N. Dechev, "Doppler ultrasound-based measurement of tendon velocity and displacement for application toward detecting user-intended motion.," *Proceedings of the Institution of Mechanical Engineers, Part H: Journal of Engineering in Medicine* , vol. 226, pp. 536-547, 2012.

[146] KJ. Stegman, "Towards Detection of User-Intended Tendon Motion with Pulsed-Wave Doppler Ultrasound for Assistive Hand Exoskeleton Applications," *M.A.Sc.thesis, University of Victoria,* 2009.

[147] F. Kremkau, *Diagnostic Ultrasound: Principles and Instruments*.: W.B.Saunders Company, 2nd ed, 1995.

[148] P. Hoskins, K. Martin, A. Thrush, *Diagnostic Ultrasound: Physics and Equipment*. : Cambridge University Press, Jun 17, 2010.

[149] JT. Bushberg, J. Seibert, EM. Leidholdt Jr, JM. Boone , *The Essential Physics of Medical Imaging*, 3rd ed.: Lippincott Williams & Wilkins, 2011.

[150] Ultrasonix Medical Corportation. "Transmit control: Wikisonix". Internet: http://www.ultrasonix.com /wikisonix/index.php/Transmit_Control, 2013.

[151] RF. Wagner, SW. Smith, JM. Sandrik, and H. Lopez, "Statistics of speckle in ultrasound B-scans," *IEEE Trans. Soniss Ultrasonics*, vol. 30, no. 3, pp. 156-163, 1983.

[152] TC. Aysal and KE. Barner, "Rayleigh-maximum-likelihood filtering for speckle reduction of ultrasound images," *Medical Imaging, IEEE Transactions on*, vol. 26, pp. 712-727, 2007.

[153] Bionnovel. Internet: http://www.bioinnovel.com/pdf/15.pdf, 2013.

[154] P. Burns. "Introduction To The Physical Principles Of Ultrasound and Doppler". Internet: http://medbio.utoronto.ca/students/courses/mbp1007/MBP1007_Burns_US.pdf, 2013.

[155] K. An, Y. Ueba, E. Chao, W. Cooney, R. Linscheid , "Tendon excursion and moment arm of index finger muscles," *Journal of Biomechanics*, vol. 16, pp. 419-425, 1983.

[156] TJ. Armstrong, DB. Chaffin , "An investigation of the relationship between displacements of the finger and wrist joints and the extrinsic finger flexor tendons," *Journal of Biomechanics*, vol. 11, no. 119-128, 1978.

[157] HJ. Buchner, MJ. Hines, H. Hemami, "A dynamic model for finger interphalangeal coordination," *Journal of biomechanics* , vol. 21, pp. 459-468, 1988.

[158] J. Lee, K. Rim, "Maximum finger force prediction using a planar simulation of the middle finger," *Proceedings of the Institution of Mechanical Engineers, Part H: Journal of Engineering in Medicine*, vol. 204, pp. 169-178, 1990.

[159] N. Brook, J. Mizrahi, M. Shoham, J. Dayan, "A biomechanical model of index finger dynamics," *Medical engineering & physics* , vol. 17, pp. 54-63, 1995.

[160] Landsmeer, "Study in the anatomy of articulation 1: the equilibrium of the 'intercalated' bone," *Acta Morphologica Neerlando-Scandinavica* , vol. 3, pp. 287-303, 1961.

[161] JW. Garrett , "Anthropometry of the hands of male air force flight personnel," *DTIC Document*, 1970.

[162] BS. Cigali, HM. Buyruk, CJ. Snijders, JS. Laméris, WP. Holland, R. Mesut, HJ. Stam , "Measurement of tendon excursion velocity with colour Doppler imaging: a preliminary study on flexor pollicis longus muscle," *European Journal of Radiology* , vol. 23, pp. 217-221, 1996.

[163] H. Buyruk, W. Holland, C. Snijders, J. Laméris, E. Hoorn, R. Stoeckart, H. Stam, "Tendon excursion measurements with colour doppler imaging: A calibration study on an embalmed human specimen," *The Journal of Hand Surgery: British & European* , vol. 23, pp. 350-353, 1998.

[164] W. Holland, H. Buyruk, E. Hoorn, H. Stam , "Tendon displacement assessment by pulsed Doppler

tissue imaging: validation with a reciprocating string test target," *Ultrasound in medicine & biology* , vol. 25, no. 1229-1239, 1999.

[165] JN. Soeters, ME. Roebroeck, WP. Holland, SE. Hovius, HJ. Stam , "Reliability of tendon excursion measurements in patients using a color Doppler imaging system," *The Journal of Hand Surgery* , vol. 29, pp. 581-586, 2004.

[166] N. Soeters, E. Roebroeck, P. Holland, E. Hovius, J. Stam, "Non-invasive measurement of tendon excursion with a colour Doppler imaging system: a reliability study in healthy subjects," *Scandinavian journal of plastic and reconstructive surgery and hand surgery*, vol. 38, pp. 356-360, 2004.

[167] KJ. Stegman KJ, RP. Podhorodeski, EJ. Park , "A feasibility study for measuring accurate tendon displacements using an audio-based Fourier analysis of pulsed-wave Doppler ultrasound signals," *Conference proceedings : Annual International Conference of the IEEE Engineering in Medicine and Biology*, pp. 1363-1366, 2009.

[168] KJ. Stegman, N. Dechev, EJ. Park, RP. Podhorodeski, "Measurement of Tendon Excursion Using an Audio-based Fourier Technique with Pulsed-Wave Doppler Ultrasound," *Conference Proceedings: American Society of Mechanical Engineers (ASME)*, vol. 2, pp. 777-783, 2010.

[169] KJ. Stegman, EJ. Park, N. Dechev, "Doppler ultrasound-based measurement of tendon velocity and displacement for application toward detecting user-intended motion.," *Proceedings of the Institution of Mechanical Engineers, Part H: Journal of Engineering in Medicie*, vol. 226, pp. 536-547, 2012.

[170] GE. Trahey, JW. Allison, OT. von Ramm, "Angle independent ultrasonic detection of blood flow," *Biomedical Engineering, IEEE Transactions on* , pp. 965-967, 1987.

[171] PM. Embree, W. O'Brien Jr, "Volumetric blood flow via time-domain correlation: experimental verification," *Ultrasonics, Ferroelectrics and Frequency Control, IEEE Transactions on* , vol. 37, no. 176-189, 1990.

[172] BH. Friemel, LN. Bohs, GE. Trahey , "Relative performance of two-dimensional speckle-tracking techniques: normalized correlation, non-normalized correlation and sum-absolute-difference," *Ultrasonics Symposium,1995. Proceedings* , vol. 2, pp. 1481-1484.

[173] J. Meunier, "Tissue motion assessment from 3D echographic speckle tracking," *Physics in Medicine and Biology*, vol. 43, p. 1241, 1998.

[174] F. Yeung, SF. Levinson, KJ. Parker, "Multilevel and motion model-based ultrasonic speckle tracking algorithms.," *Ultrasound in medicine and biology* , vol. 24, no. 427-442, 1998.

[175] D. Boukerroui, J. Noble, M. Brady, "Velocity estimation in ultrasound images: A block matching approach," *Information Processing in Medical Images: Lecture Notes in Computer Science*, vol. 2732, pp. 586-598, 2003.

[176] GF. Pinton, JJ. Dahl, GE. Trahey , "Rapid tracking of small displacements with ultrasound.," *Ultrasonics, Ferroelectrics and Frequency Control, IEEE Transactions on*, vol. 53, pp. 1103-1117, 2006.

[177] J. Revell, M. Mirmehdi, D. McNally , "Combined ultrasound speckle pattern similarity measures," *Medical Image Understanding and Analysis* , pp. 149-153, 2004.

[178] J. Revell, M. Mirmehdi, D. McNally , "Computer vision elastography: speckle adaptive motion estimation for elastography using ultrasound sequences," *Medical Imaging, IEEE Transactions on*, vol. 24, pp. 755-766, 2005.

[179] J. Korstanje, RW. Selles, HJ. Stam, S. Hovius, JG. Bosch, "Development and validation of ultrasound speckle tracking to quantify tendon displacement," *Journal of biomechanics*, vol. 43, p. 1373, 2010.

[180] JW. Goodman, "Statistical properties of laser speckle patterns," in *Laser speckle and related phenomena*., 1975, pp. 9-75.

[181] TC. Aysal TC, KE. Barner, "Rayleigh-maximum-likelihood filtering for speckle reduction of ultrasound images.," *Medical Imaging, IEEE Transactions on*, vol. 26, pp. 712-727, 2007.

[182] M. G. Strintzis and I. Kokkinidis, "Maximum likelihood motion estimation in ultrasound image sequences," *Signal Processing Letters, IEEE*, vol. 4, pp. 156-157, 1997.

[183] B. Cohen and I. H. Dinstein, "New maximum likelihood motion estimation schemes for noisy ultrasound images," *Pattern Recognition*, vol. 35, pp. 455-463, 2002.

[184] L. Bohs, B. Geiman, M. Anderson, S. Gebhart, and G. Trahey, "Speckle tracking for multi-dimensional flow estimation," *Ultrasonics*, vol. 38, pp. 369-375, 2000.

[185] PC Li and WN Lee, "An efficient speckle tracking algorithm for ultrasonic imaging," *Ultrasonic imaging*, vol. 24, no. 4, pp. 215-228, 2002.

[186] SY. Wu, SL. Wang, and PC Li, "Performance evaluation on high frame-rate speckle tracking," *In Ultrasonics Symposium (IUS), 2009 IEEE International*, pp. 2375-2378, 2009.

[187] J. Jiang, and TJ. Hall., "A generalized speckle tracking algorithm for ultrasonic strain imaging using

dynamic programming," *Ultrasound in medicine & biology*, vol. 35, no. 11, pp. 1863-1879, 2009.

[188] A. Papoulis and S. U. Pillai, *Probability, random variables and stochastic processes with errata sheet*, 187,236 pp.130, Ed. New York, NY: McGraw-Hill Education, 2002.

[189] I. Gradshteyn and I. Ryzhik, *Table of Integrals, Series, and Products*, pp. 346, Ed. Orlando, Florida: Academic Press, 2007.

[190] Ultrasonix Medical Corp. "Elastography". Internet: http://www.ultrasonix.com /products/elastography, 2013.

[191] General Electric. "Elastography". Internet: http://www.gehealthcare.com/usen/ultrasound /genimg/products/logiq_e9/docs/ElastoSellSheetv8.pdf, 2013.

[192] S. Langeland, J. D'hooge, H. Torp, B. Bijnens, and P. Suetens, "Comparison of time-domain displacement estimators for two-dimensional RF tracking," *Ultrasound in medicine & biology* , vol. 29, no. 8, pp. 1177-1186, 2003.

[193] A. Barjatya, "Block matching algorithms for motion estimation," *IEEE Transactions Evolution Computation* , vol. 8, no. 3, pp. 225-239, 2004.

[194] F. Yeung, SF. Levinson, D. Fu, and KJ. Parker, "Feature-adaptive motion tracking of ultrasound image sequences using a deformable mesh," *Medical Imaging, IEEE Transactions on* , vol. 17, no. 6, pp. 945-956, 1998.

[195] Y. Zhu, P.Chaturvedi, and MF. Insana, "Strain imaging with a deformable mesh," *Ultrasonic imaging*, vol. 21, no. 2, pp. 127-146, 1999.

[196] GR. Lockwood, JR. Talman, and SS. Brunke, "Real-time 3-D ultrasound imaging using sparse synthetic aperture beamforming," *Ultrasonics, Ferroelectrics and Frequency Control, IEEE Transactions on* , vol. 45, no. 4, pp. 980-988, 1998.

[197] A. Austeng, and S.Holm, "Sparse 2-D arrays for 3-D phased array imaging-design methods," *Ultrasonics, Ferroelectrics and Frequency Control, IEEE Transactions on* , vol. 49, no. 8, pp. 1073-1086, 2002.

[198] JW. Choe, O. Oralkan, and PT. Khuri-Yakub, "Design optimization for a 2-d sparse transducer array for 3-d ultrasound imaging," *Ultrasonics Symposium (IUS), 2010 IEEE*, pp. 1928-1931, 2010.

[199] Ultrasonix. "Ultrasonix Touch". Internet: http://www.ultrasonix.com/ ultrasound-systems/sonixtouch, 2013.

[200] JD Revell, "Computer vision elastography," University of Bristol., PhD diss. 2005.

[201] ID Loram, CN Maganaris, M Lakie. , "The passive, human calf muscles in relation to standing: the short range stiffness lies in the contractile component," *J Physiol* , vol. 584, pp. 677–692, 2007.

[202] J. Darby, John, E. Hodson-Tole, N Costen, and ID. Loram, "Automated regional analysis of B-mode ultrasound images of skeletal muscle movement," *Journal of Applied Physiology*, vol. 112, no. 2, pp. 313-327, 2012.

[203] Mobisante. Internet: http://news.wustl.edu/news/Pages/13928.aspx, 2013.

[204] Parallella. Internet: http://www.parallella.org/board/, 2013.

LIST OF PUBLICATIONS

Ph.D. Work

Stegman KJ, Djurickovic S, and Dechev N. In Vivo estimation of FDS tendon displacement with speckle tracking using Laplacian, Gaussian and Rayleigh techniques. Ultrasound in Medicine and Biology. Accepted September 2013.

Stegman KJ and Dechev N. Ultrasound-Based Sensor for Prosthesis Control. US Patent: # 14058022, filing date: Oct. 18th, 2013.

Stegman KJ, Djurickovic S, and Dechev N. Tissue Displacement Estimation by Ultrasound Speckle Tracking. Provisional Patent # 61/841,156, filing date: June 27th, 2013

Master's Work

Stegman KJ, Park EJ, Dechev N. Doppler ultrasound-based measurement of tendon velocity and displacement for application toward detecting user-intended motion. Proceedings of the Institution of Mechanical Engineers, Part H: Journal of Engineering in Medicine 2012;226:536-47.

Stegman KJ, Dechev N, Park EJ, Podhorodeski RP. Measurement of Tendon Excursion Using an Audio-based Fourier Technique with Pulsed-Wave Doppler Ultrasound. Conference Proceedings: American Society of Mechanical Engineers (ASME), Proc. of the ASME Int. Mech. Eng. Congress 2010; 2:777-783.

Stegman KJ, Podhorodeski RP, Park EJ. A feasibility study for measuring accurate tendon displacements using an audio-based Fourier analysis of pulsed-wave Doppler ultrasound signals. Conference proceedings :Annual International Conference of the IEEE Engineering in Medicine and Biology Society IEEE Engineering in Medicine and Biology Society Conference 2009;2009:1363-6.

Stegman, KJ. Towards detection of user-intended tendon motion with pulsed wave Doppler ultrasound for assistive hand exoskeleton applications. M.A.Sc thesis, Department of Mechanical Engineering, University of Victoria, 2009.

APPENDIX

A.1: Figures for Experiment 2

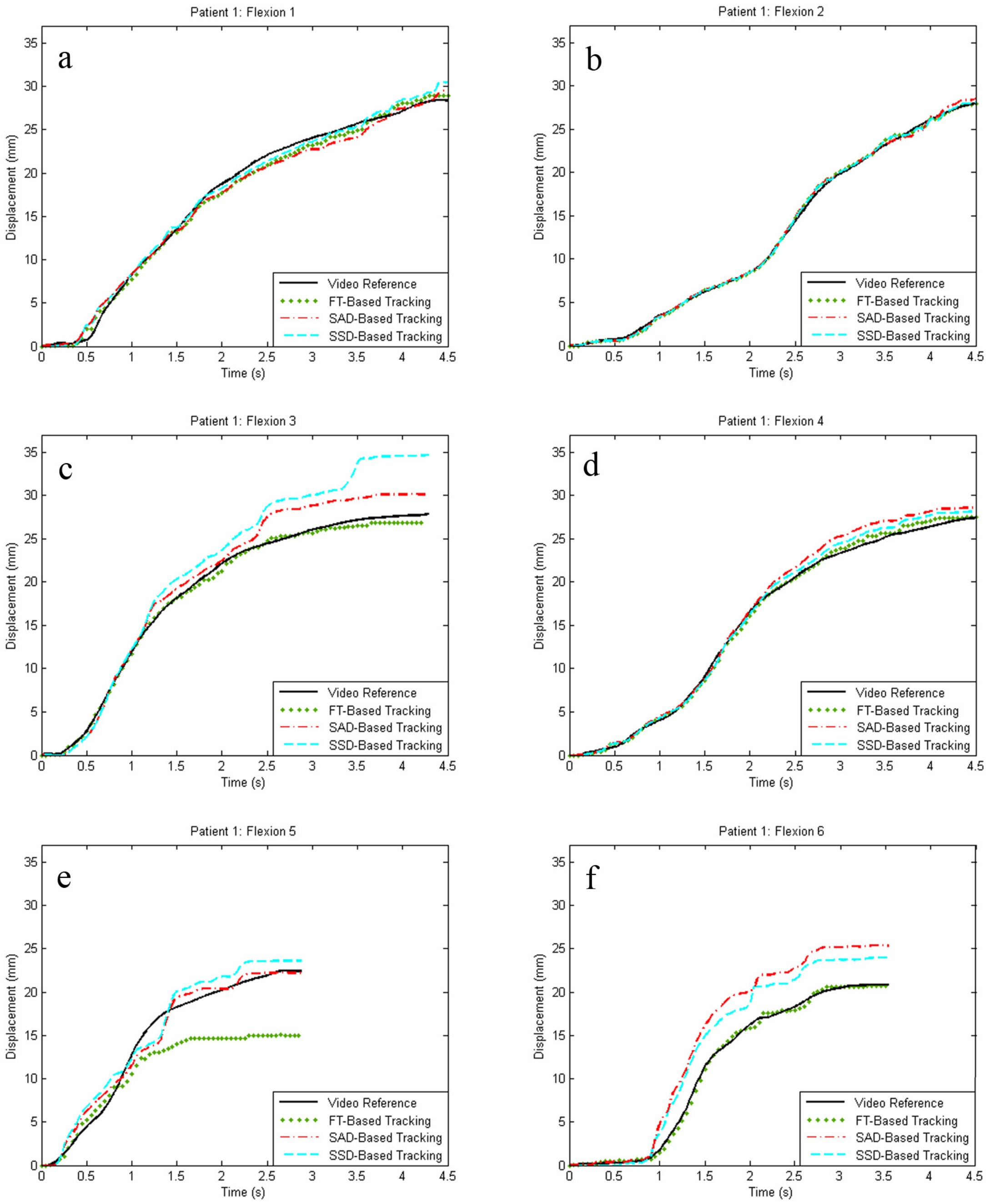
Patient 1: Flexion 1

Patient 1: Flexion 2

Patient 1: Flexion 3

Patient 1: Flexion 4

Patient 1: Flexion 5

Patient 1: Flexion 6

Figure A.1.1: Displacement vs time curve for Patient 1's flexions in Experiment 2.

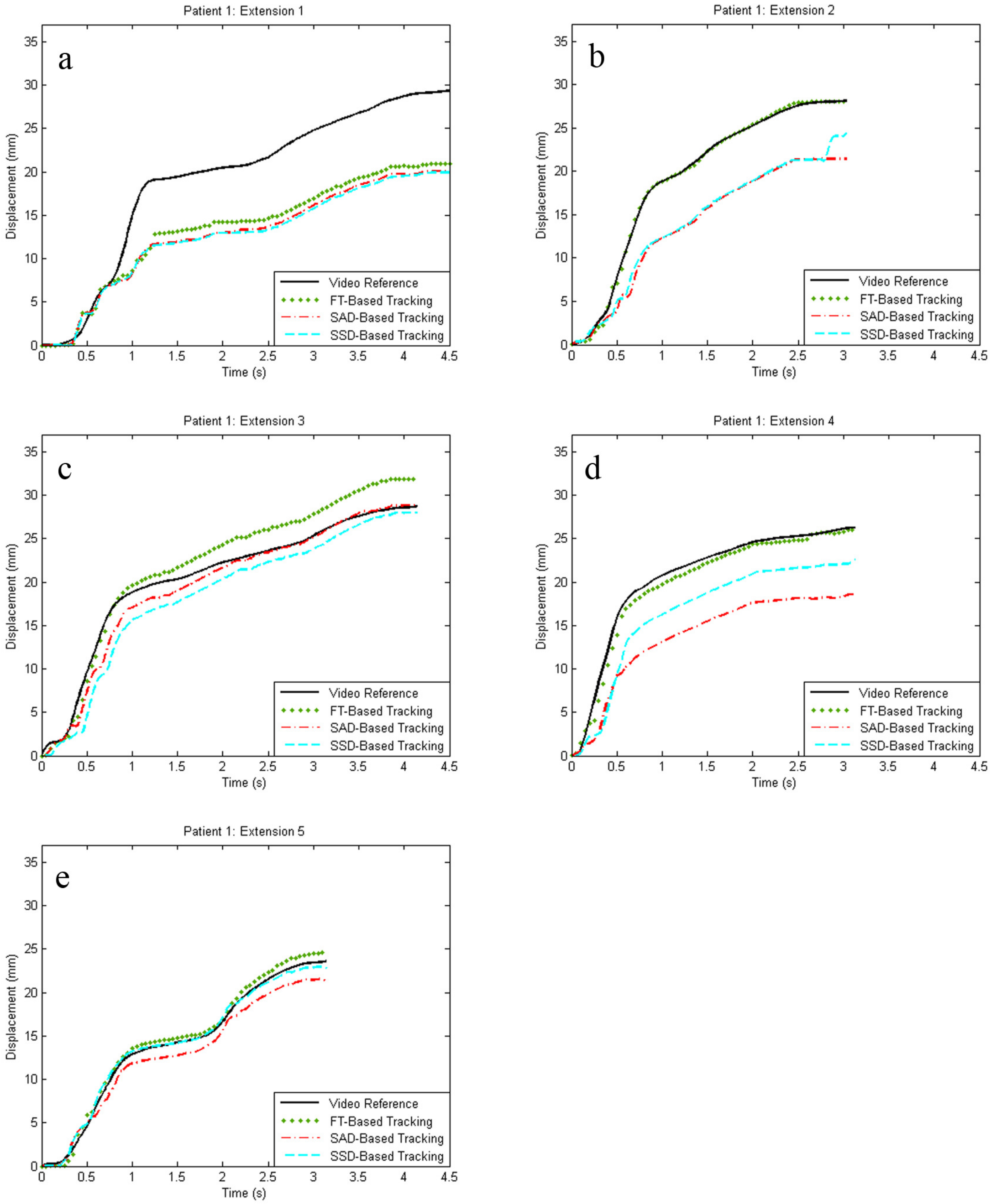
Patient 1: Extension 1

Patient 1: Extension 2

Patient 1: Extension 3

Patient 1: Extension 4

Patient 1: Extension 5

Figure A.1.2: Displacement vs time curve for Patient 1's extensions in Experiment 2.

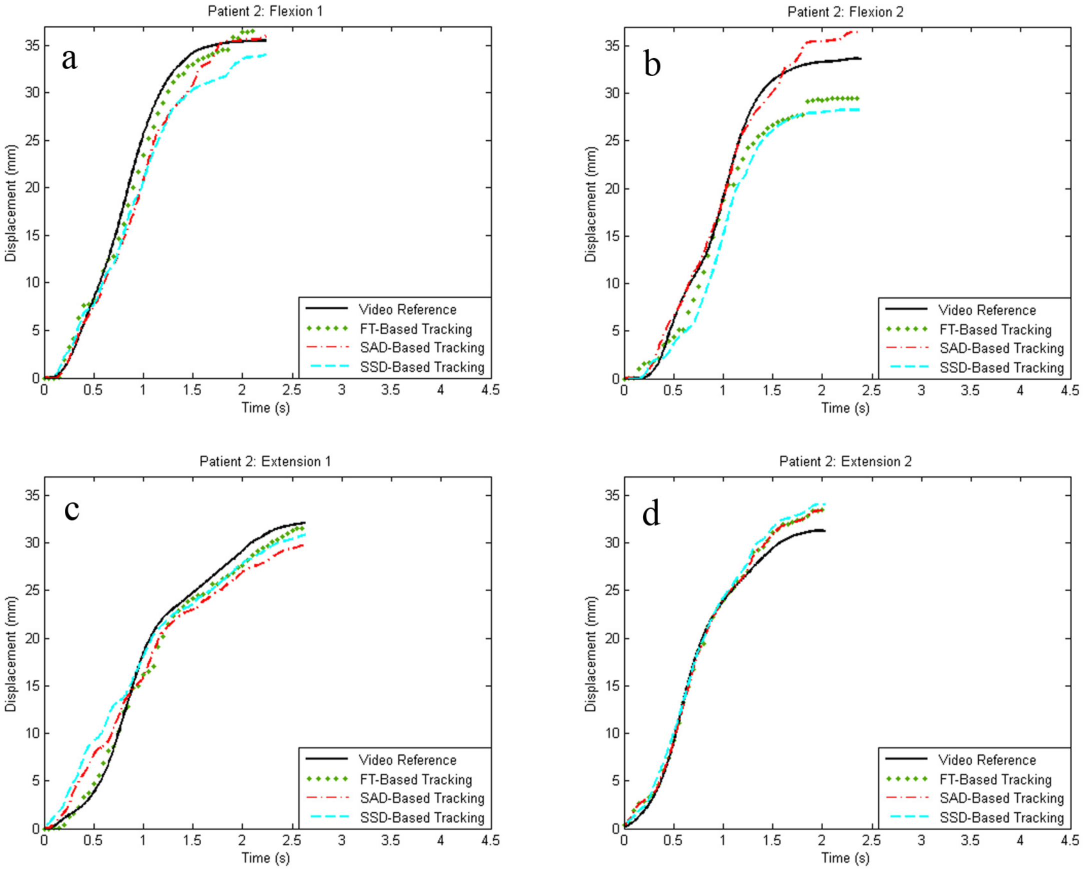

Figure A.1.3: Displacement vs time curve for Patient 2's flexions and extensions in Experiment 2.

A.2: Figures for Experiment 3

Total Displacement Field Results: Index Finger: A Series

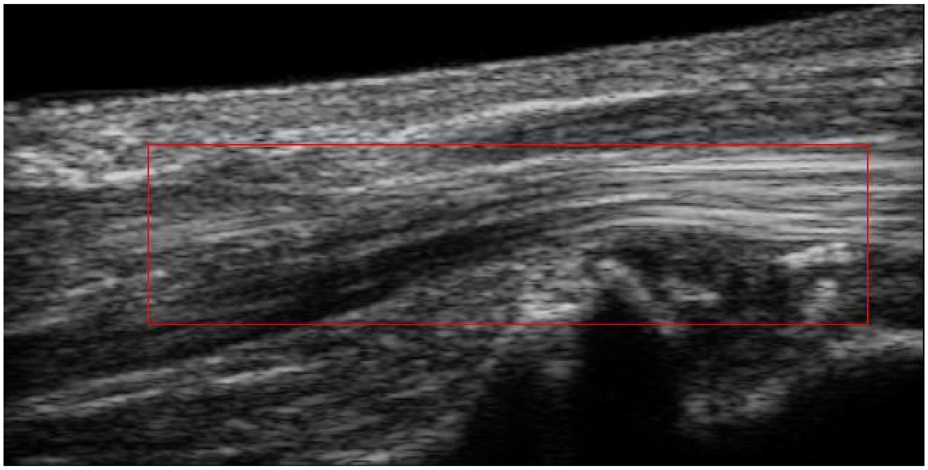

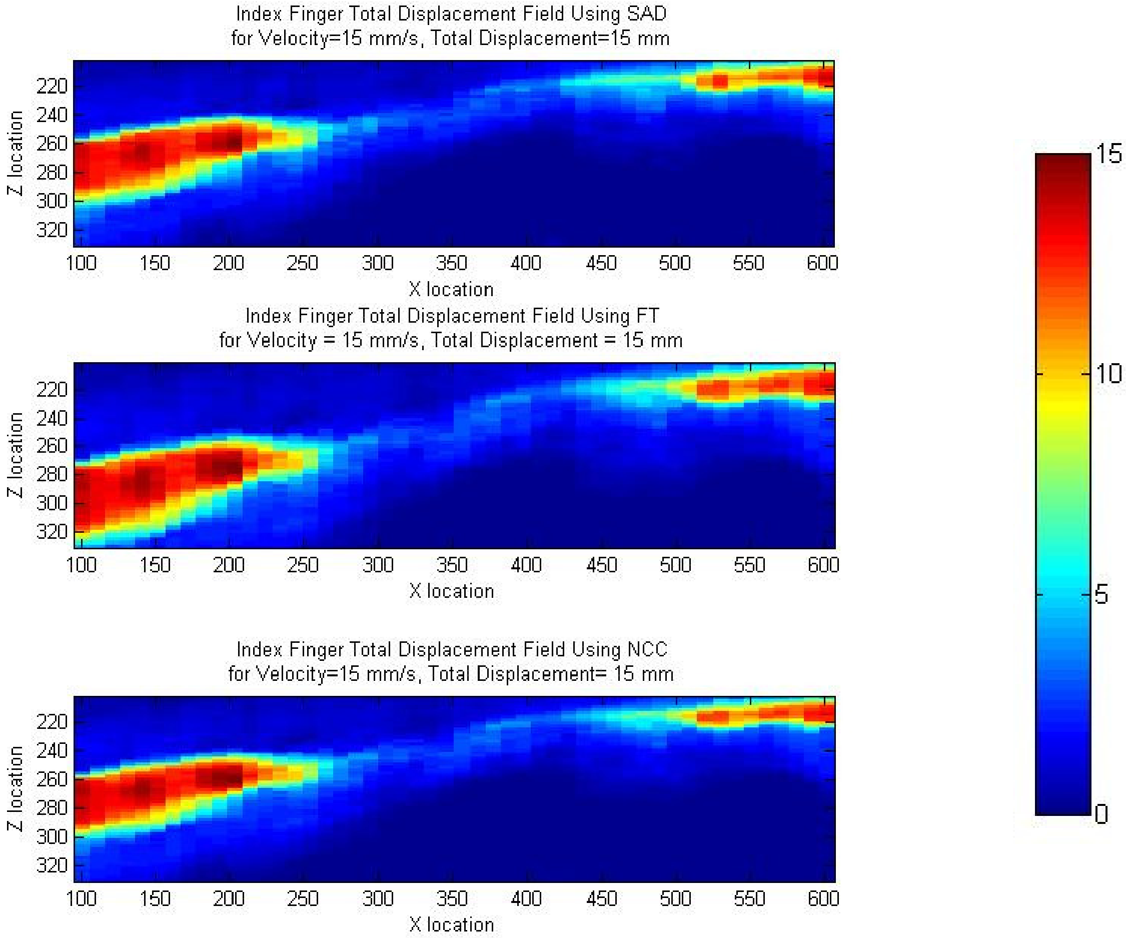

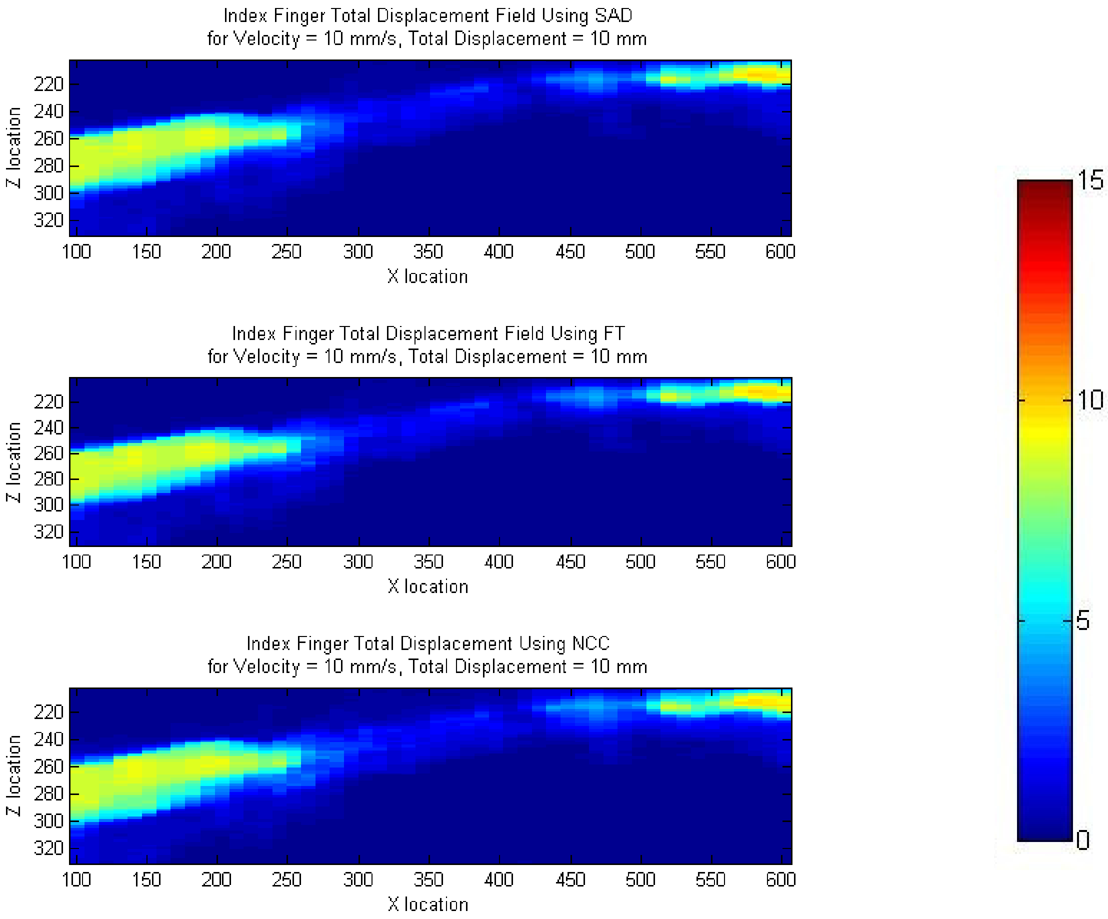
Index Finger Total Displacement Field Using SAD
for Velocity = 10 mm/s, Total Displacement = 10 mm

Index Finger Total Displacement Field Using FT
for Velocity = 10 mm/s, Total Displacement = 10 mm

Index Finger Total Displacement Using NCC
for Velocity = 10 mm/s, Total Displacement = 10 mm

Figure A.2.1: Displacement Field for the index finger (Day 2)

Total Displacement Field Results: Middle Finger: B Series

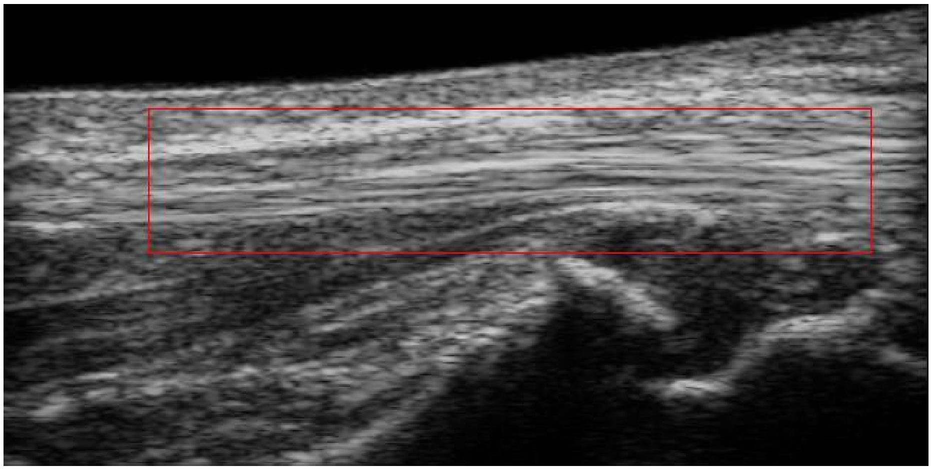

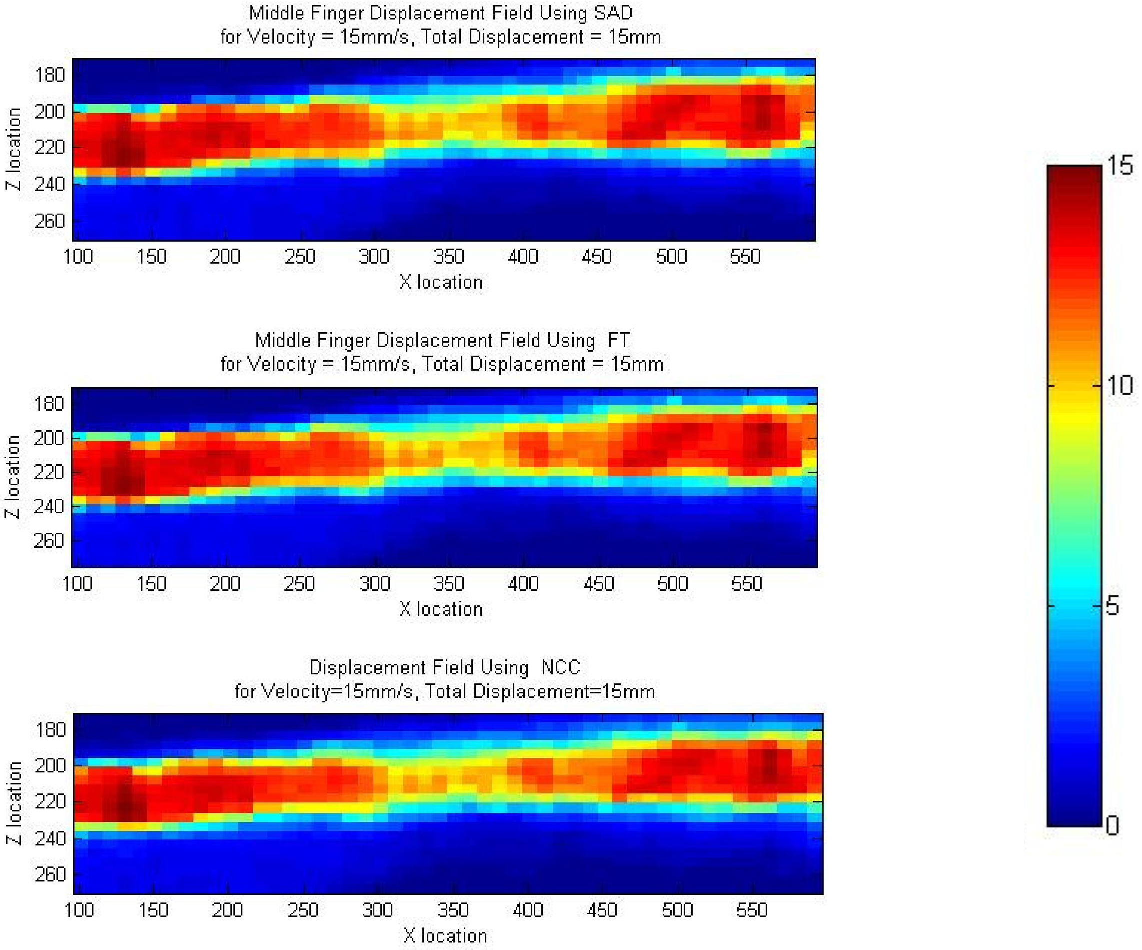

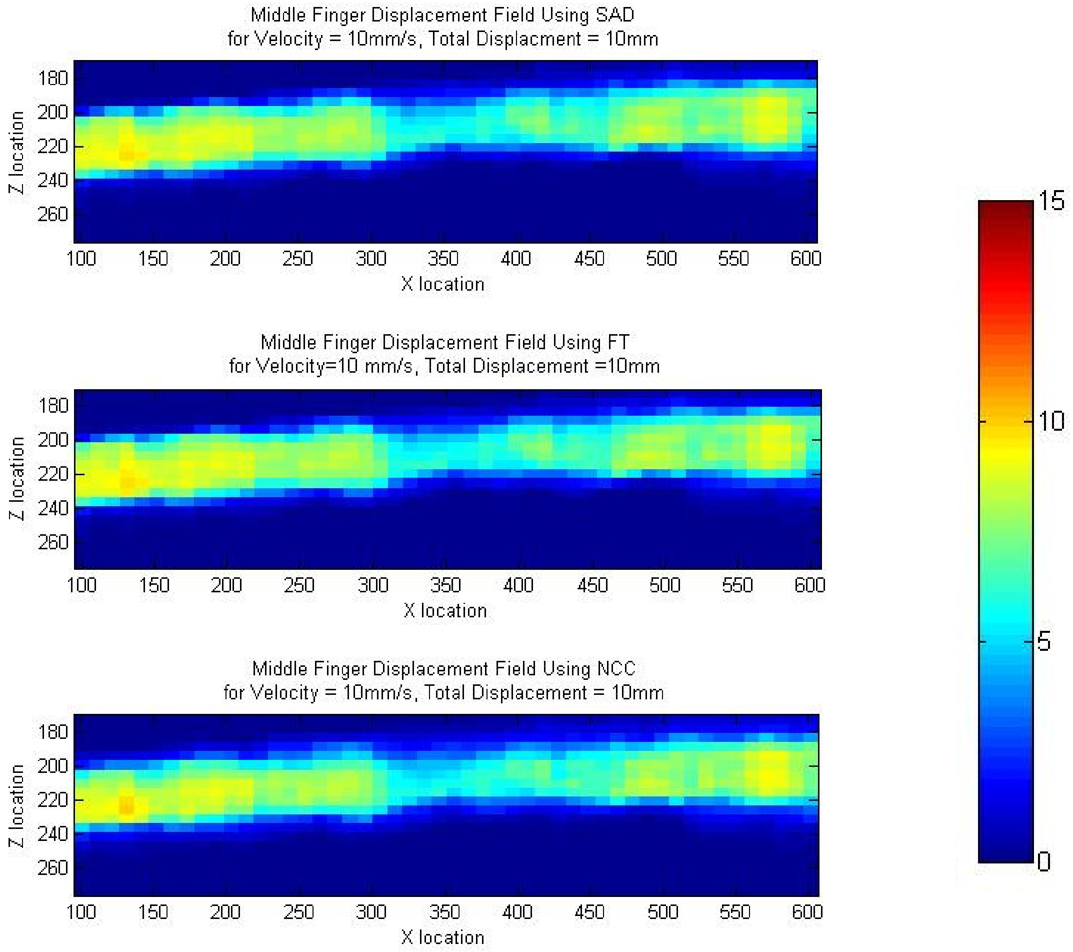
Middle Finger Displacement Field Using SAD
for Velocity = 10mm/s, Total Displacment = 10mm

Middle Finger Displacement Field Using FT
for Velocity=10 mm/s, Total Displacement =10mm

Middle Finger Displacement Field Using NCC
for Velocity = 10mm/s, Total Displacement = 10mm

Figure A.2.2: Displacement Field for the middle finger (Day 2)

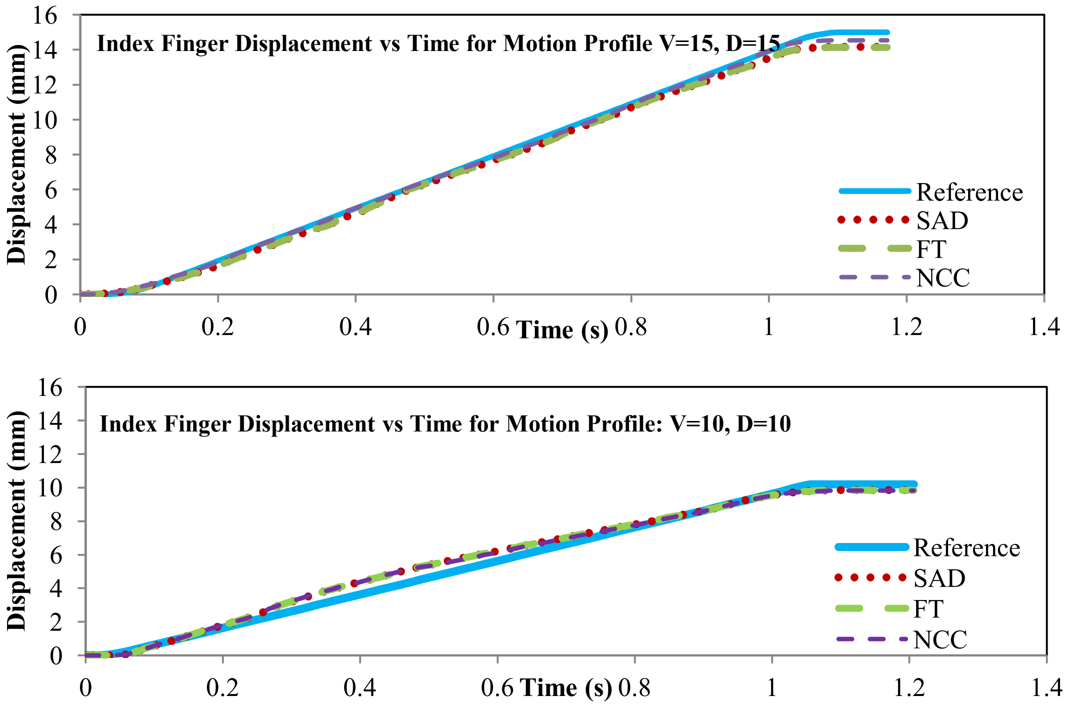

Figure A.2.4: Displacement vs time curves for the index finger (Day 2)

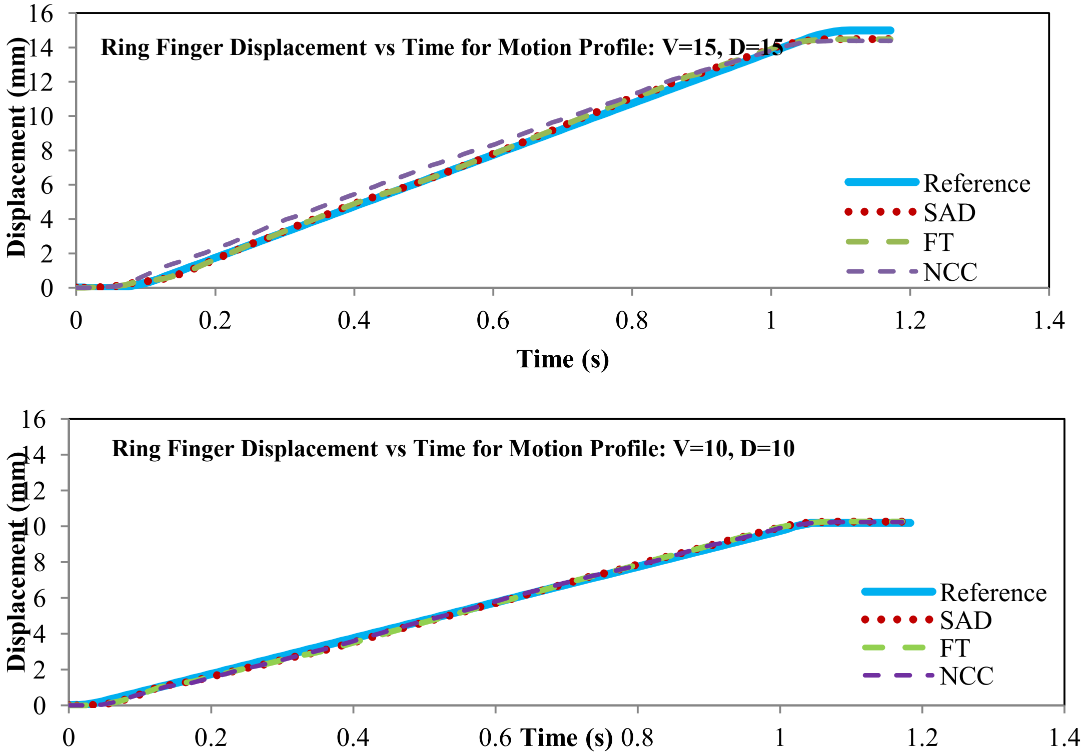

Figure A.2.6: Displacement vs time curves for the ring finger (Day 2)

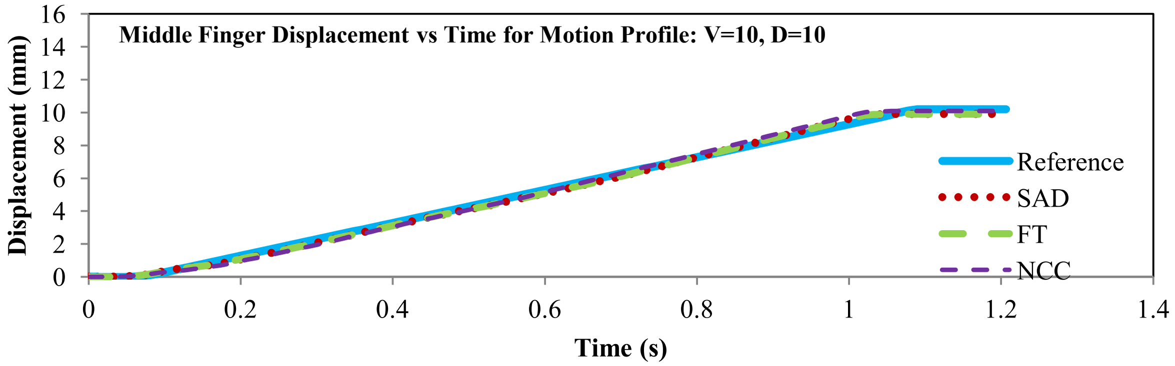

Figure A.2.7: Displacement vs time curves for the middle finger (Day 2)

A.3: Figures and Tables for Experiment 4

Index Finger Tendon: Hand 1, Day 2
A-Series
Maximum Velocity = 15 mm/s, Total Displacement = 15 mm

Similarity Measure	Array 1 Maximum Displacement (mm)	Location (x,z)	Similarity Measure	Array 2 Maximum Displacement (mm)	Location (x,z)
SAD	2.95	27,500	SAD	11.36	31,620
FT	2.95	27,500	FT	8.34	31,620
NCC	3.49	29,500	NCC	12.37	35,630
Similarity Measure	Array 3 Maximum Displacement (mm)	Location (x,z)	Similarity Measure	Array 4 Maximum Displacement (mm)	Location (x,z)
SAD	11.62	25,630	SAD	14.15	39,590
FT	11.67	25,630	FT	11.86	26,640
NCC	13.23	31,650	NCC	13.58	29,660

Middle Finger Tendon: Hand 1, Day 2
B-Series
Maximum Velocity = 15 mm/s, Total Displacement = 15 mm

Similarity Measure	Array 1 Maximum Displacement (mm)	Location (x,z)	Similarity Measure	Array 2 Maximum Displacement (mm)	Location (x,z)
SAD	7.94	24,660	SAD	13.83	26,590
FT	7.94	24,660	FT	14.04	26,550
NCC	9.60	39,490	NCC	13.51	42,550
Similarity Measure	Array 3 Maximum Displacement (mm)	Location (x,z)	Similarity Measure	Array 4 Maximum Displacement (mm)	Location (x,z)
SAD	14.24	23,550	SAD	4.89	41,600
FT	15.68	24,550	FT	4.85	41,600
NCC	15.67	23,550	NCC	6.27	23,590

Ring Finger Tendon: Hand1, Day 2
C-Series
Maximum Velocity = 15 mm/s, Total Displacement = 15 mm

Similarity Measure	Array 1 Maximum Displacement (mm)	Location (x,z)	Similarity Measure	Array 2 Maximum Displacement (mm)	Location (x,z)
SAD	14.60	49,560	SAD	3.74	50,720
FT	14.91	49,560	FT	3.20	49,690
NCC	13.01	49,550	NCC	4.21	47,690
Similarity Measure	Array 3 Maximum Displacement (mm)	Location (x,z)	Similarity Measure	Array 4 Maximum Displacement (mm)	Location (x,z)
SAD	0.67	41,620	SAD	0.88	26,570
FT	0.67	41,620	FT	0.88	26,570
NCC	0.70	41,620	NCC	0.53	25,580

Index Finger Tendon: Hand 1, Day 2
A-Series
Maximum Velocity = 10 mm/s, Total Displacement = 10 mm

Similarity Measure	Array 1 Maximum Displacement (mm)	Location (x,z)	Similarity Measure	Array 2 Maximum Displacement (mm)	Location (x,z)
SAD	1.95	27,500	SAD	7.36	32,600
FT	2.02	27,500	FT	5.35	28,640
NCC	3.29	36,510	NCC	9.08	50,660
Similarity Measure	Array 3 Maximum Displacement (mm)	Location (x,z)	Similarity Measure	Array 4 Maximum Displacement (mm)	Location (x,z)
SAD	7.51	36,650	SAD	9.36	32,650
FT	6.49	35,640	FT	8.85	31,630
NCC	8.45	31,650	NCC	10.34	35,660

Middle Finger Tendon: Hand1 Day 2
B-Series
Maximum Velocity = 10 mm/s, Total Displacement = 10 mm

Similarity Measure	Array 1 Maximum Displacement (mm)	Location (x,z)	Similarity Measure	Array 2 Maximum Displacement (mm)	Location (x,z)
SAD	2.98	32,480	SAD	11.09	24.560
FT	3.05	32,490	FT	9.53	21,550
NCC	3.02	42,490	NCC	9.50	22,580
Similarity Measure	Array 3 Maximum Displacement (mm)	Location (x,z)	Similarity Measure	Array 4 Maximum Displacement (mm)	Location (x,z)
SAD	9.74	43,600	SAD	2.25	29,600
FT	9.53	34,570	FT	1.85	33,620
NCC	9.86	34,570	NCC	2.14	33,620

Ring Finger Tendon: Hand 1, Day 2
C-Series
Maximum Velocity = 10 mm/s, Total Displacement = 10 mm

Similarity Measure	Array 1 Maximum Displacement (mm)	Location (x,z)	Similarity Measure	Array 2 Maximum Displacement (mm)	Location (x,z)
SAD	9.33	35,600	SAD	0.21	42,600
FT	8.76	33,600	FT	0.21	42,600
NCC	10.74	47,550	NCC	1.13	54,740
Similarity Measure	Array 3 Maximum Displacement (mm)	Location (x,z)	Similarity Measure	Array 4 Maximum Displacement (mm)	Location (x,z)
SAD	0.00	46,510	SAD	0.00	43,550
FT	0.00	46.510	FT	0.00	43,550
NCC	0.02	45,610	NCC	0.00	43,550

Index Finger Tendon: Hand 1, Day 4
A-Series
Maximum Velocity = 15 mm/s, Total Displacement = 15 mm

Similarity Measure	Array 1 Maximum Displacement (mm)	Location (x,z)	Similarity Measure	Array 2 Maximum Displacement (mm)	Location (x,z)
SAD	1.13	(22, 730)	SAD	6.93	(28, 780)
FT	1.41	(21, 730)	FT	6.67	(28, 720)
NCC	1.41	(23, 710)	NCC	8.01	(21, 550)
Similarity Measure	Array 3 Maximum Displacement (mm)	Location (x,z)	Similarity Measure	Array 4 Maximum Displacement (mm)	Location (x,z)
SAD	17.26	(22, 710)	SAD	16.88	(46, 680)
FT	17.37	(21, 710)	FT	14.60	(27, 730)
NCC	13.97	(26, 740)	NCC	15.31	(23, 660)

Middle Finger Tendon: Hand 1, Day 4
B-Series
Maximum Velocity = 15 mm/s, Total Displacement = 15 mm

Similarity Measure	Array 1 Maximum Displacement (mm)	Location (x,z)	Similarity Measure	Array 2 Maximum Displacement (mm)	Location (x,z)
SAD	15.05	(41, 730)	SAD	15.18	(21, 560)
FT	13.32	(41, 730)	FT	13.54	(21, 600)
NCC	15.93	(21, 730)	NCC	19.99	(21, 720)
Similarity Measure	Array 3 Maximum Displacement (mm)	Location (x,z)	Similarity Measure	Array 4 Maximum Displacement (mm)	Location (x,z)
SAD	15.52	(45, 650)	SAD	9.43	(34, 750)
FT	14.71	(28, 660)	FT	9.75	(31, 740)
NCC	14.82	(28, 660)	NCC	11.62	(31, 740)

Ring Finger Tendon: Hand 1, Day 4
C-Series
Maximum Velocity = 15 mm/s, Total Displacement = 15 mm

Similarity Measure	Array 1 Maximum Displacement (mm)	Location (x,z)	Similarity Measure	Array 2 Maximum Displacement (mm)	Location (x,z)
SAD	19.44	(46, 634)	SAD	6.77	(29, 750)
FT	20.19	(46, 630)	FT	6.56	(27, 770)
NCC	16.40	(47, 690)	NCC	6.85	(29, 750)
Similarity Measure	Array 3 Maximum Displacement (mm)	Location (x,z)	Similarity Measure	Array 4 Maximum Displacement (mm)	Location (x,z)
SAD	2.57	(27, 710)	SAD	0.81	(31, 740)
FT	1.41	(28, 710)	FT	0.81	(29, 720)
NCC	1.97	(52, 760)	NCC	1.02	(28, 710)

Index Finger Tendon: Hand 1, Day 4
A-Series
Maximum Velocity = 10 mm/s, Total Displacement = 10 mm

Similarity Measure	Array 1 Maximum Displacement (mm)	Location (x,z)	Similarity Measure	Array 2 Maximum Displacement (mm)	Location (x,z)
SAD	0.26	(47, 690)	SAD	5.84	(23, 700)
FT	0.24	(47, 700)	FT	5.75	(21, 700)
NCC	0.35	(43, 580)	NCC	7.53	(21, 700)
Similarity Measure	Array 3 Maximum Displacement (mm)	Location (x,z)	Similarity Measure	Array 4 Maximum Displacement (mm)	Location (x,z)
SAD	9.28	(31, 750)	SAD	11.42	(35, 690)
FT	8.72	(37, 700)	FT	11.38	(36, 690)
NCC	10.42	(21, 780)	NCC	11.07	(21, 769)

Middle Finger Tendon: Hand 1, Day 4
B-Series
Maximum Velocity = 10 mm/s, Total Displacement = 10 mm

Similarity Measure	Array 1 Maximum Displacement (mm)	Location (x,z)	Similarity Measure	Array 2 Maximum Displacement (mm)	Location (x,z)
SAD	9.13	(23, 690)	SAD	11.16	(23, 740)
FT	9.10	(22, 690)	FT	11.37	(21, 730)
NCC	10.52	(21, 770)	NCC	13.34	(22, 750)
Similarity Measure	Array 3 Maximum Displacement (mm)	Location (x,z)	Similarity Measure	Array 4 Maximum Displacement (mm)	Location (x,z)
SAD	9.90	(22, 680)	SAD	10.08	(29, 760)
FT	9.88	(22, 670)	FT	10.60	(29, 760)
NCC	9.75	(39, 690)	NCC	10.08	(29, 770)

Ring Finger Tendon: Hand 1, Day 4
C-Series
Maximum Velocity = 10 mm/s, Total Displacement = 10 mm

Similarity Measure	Array 1 Maximum Displacement (mm)	Location (x,z)	Similarity Measure	Array 2 Maximum Displacement (mm)	Location (x,z)
SAD	14.77	(43, 620)	SAD	5.96	(40, 720)
FT	13.87	(44, 630)	FT	4.63	(39, 750)
NCC	13.27	(44, 630)	NCC	4.99	(36, 730)

Similarity Measure	Array 3 Maximum Displacement (mm)	Location (x,z)	Similarity Measure	Array 4 Maximum Displacement (mm)	Location (x,z)
SAD	0.56	(43, 720)	SAD	0.21	(44, 620)
FT	0.56	(43, 720)	FT	0.19	(44, 620)
NCC	1.15	(51, 700)	NCC	0.16	(46, 620)

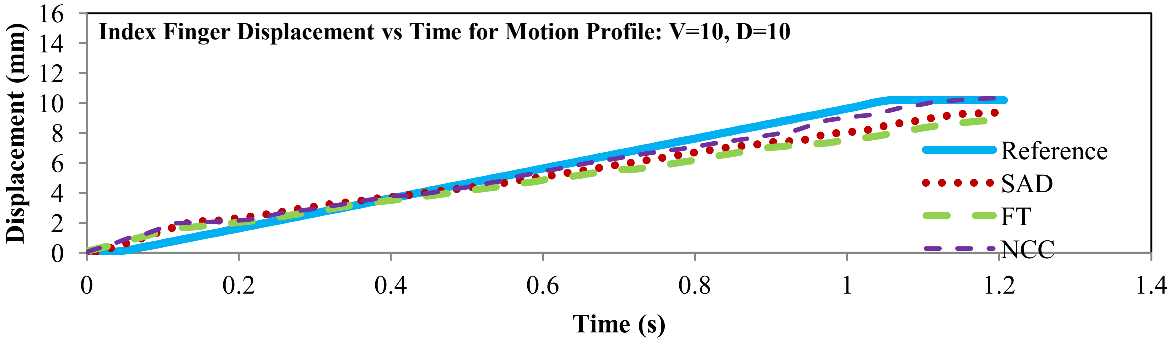

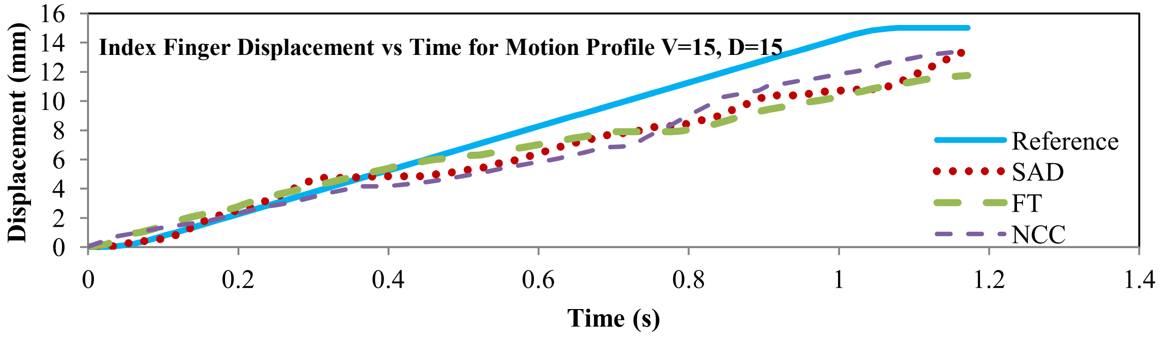

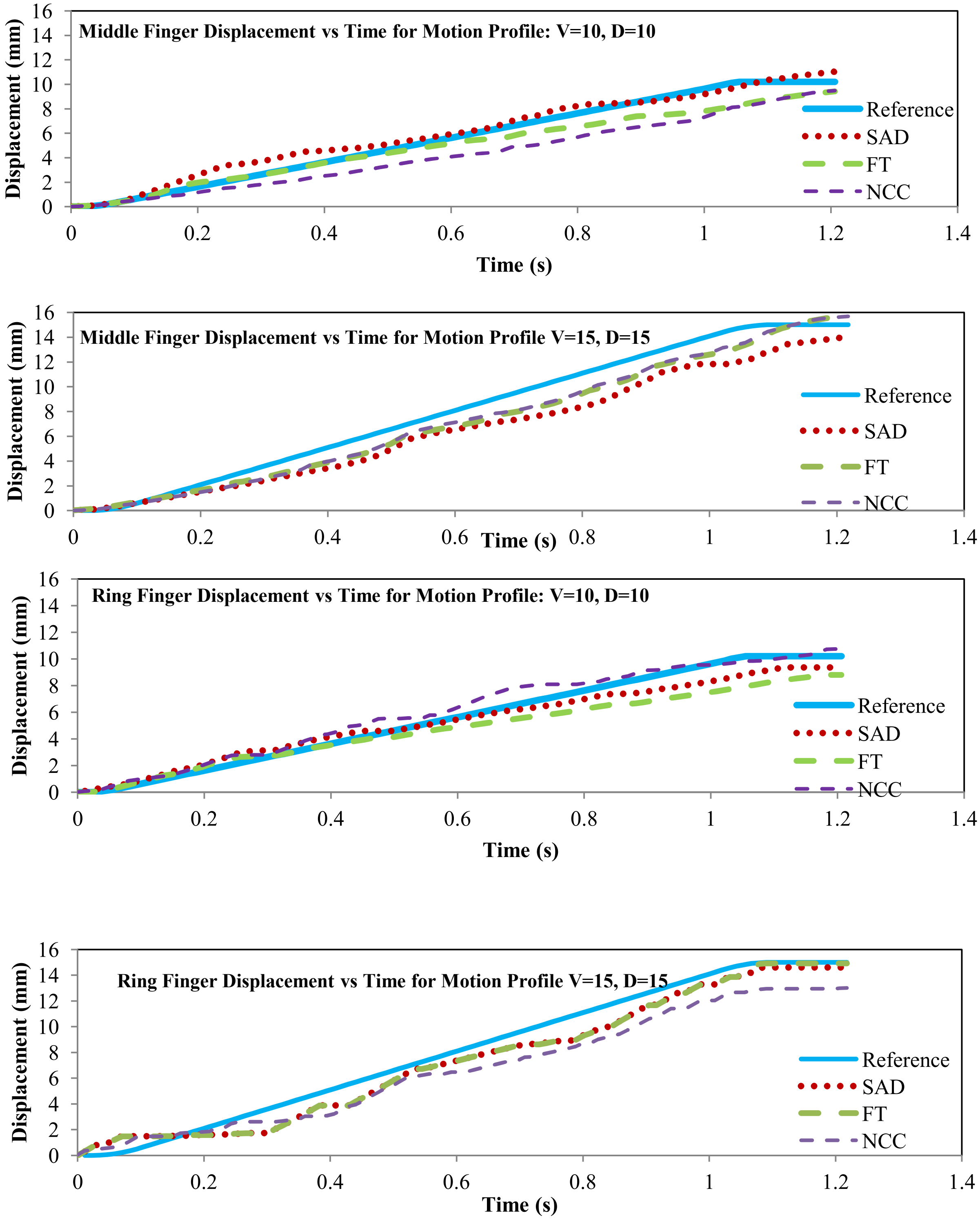
Middle Finger Displacement vs Time for Motion Profile: V=10, D=10

Middle Finger Displacement vs Time for Motion Profile V=15, D=15

Ring Finger Displacement vs Time for Motion Profile: V=10, D=10

Ring Finger Displacement vs Time for Motion Profile V=15, D=15

Figure A.3.1: Displacement vs time curves for the Day 2 (A,B,C) data using the quad array

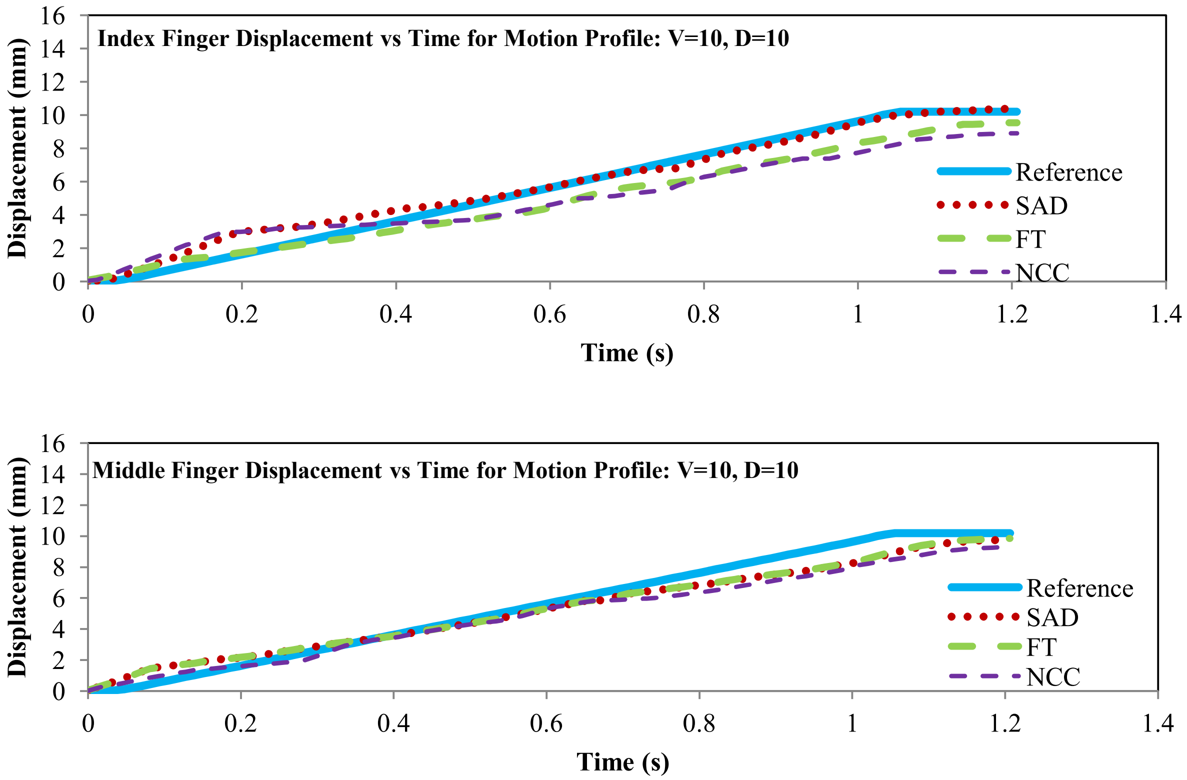

Figure A.3.2: Displacement vs time curves for the Day 2 (AB-Series) data using the quad array

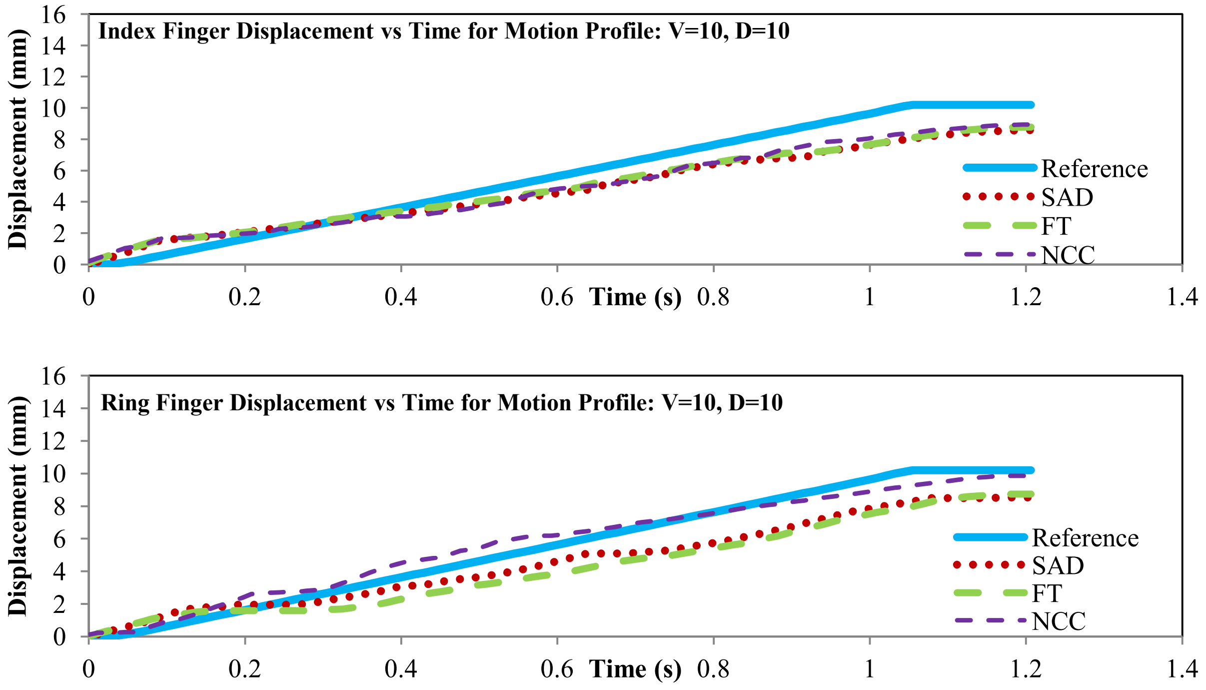

Figure A.3.3: Displacement vs time curves for the Day 2 (AC-Series) data using the quad array

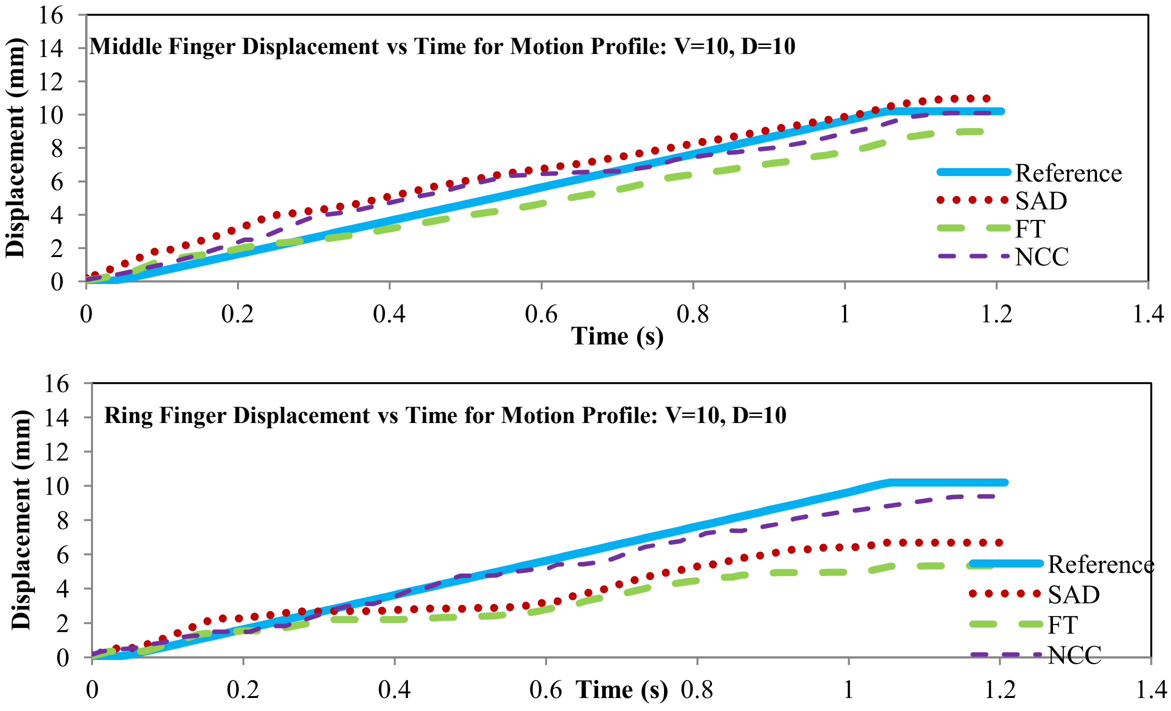

Middle Finger Displacement vs Time for Motion Profile: V=10, D=10

Ring Finger Displacement vs Time for Motion Profile: V=10, D=10

Figure A.3.4: Displacement vs time curves for the Day 2 (BC-Series) data using the quad array

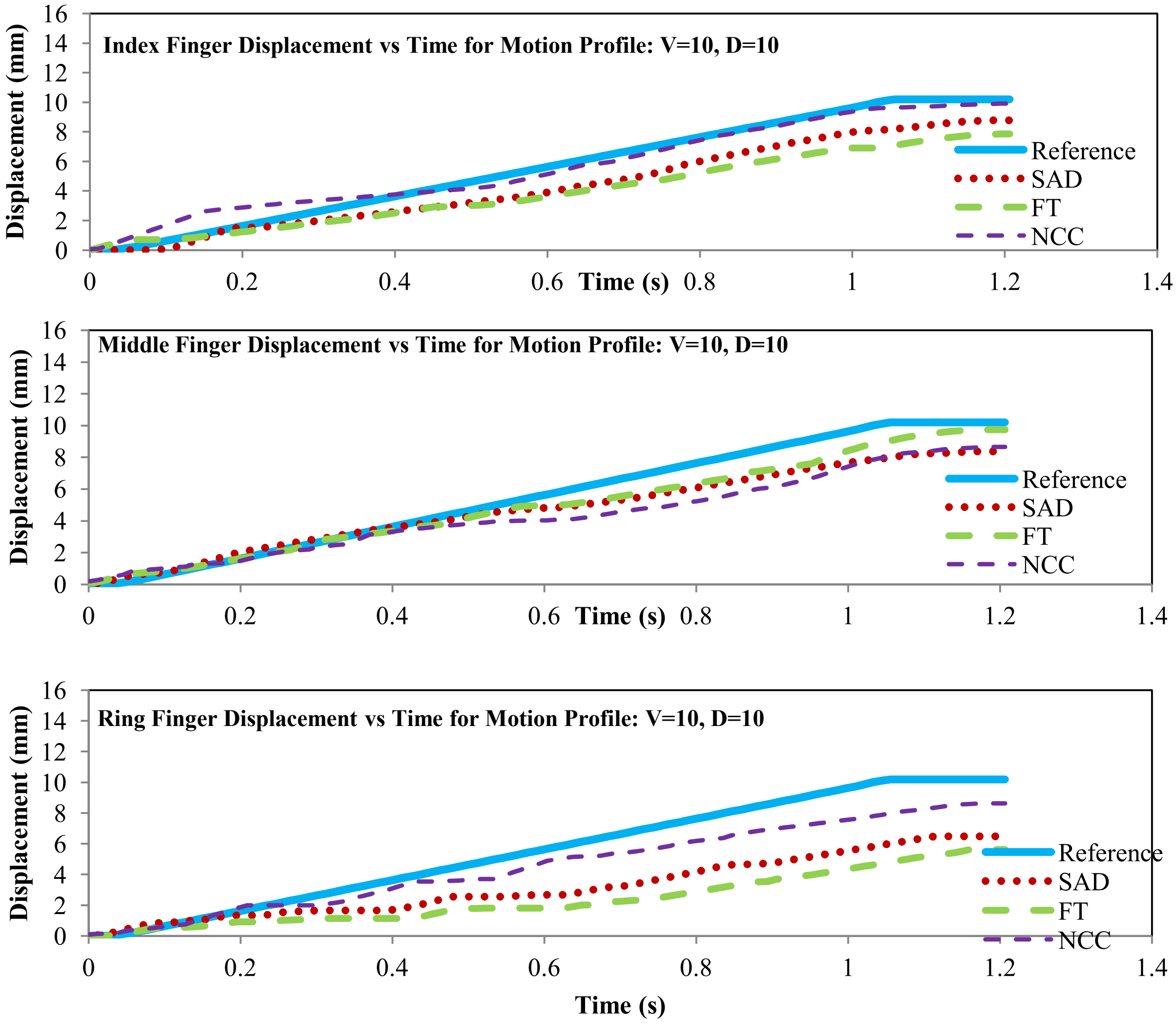

Figure A.3.5: Displacement vs time curves for the Day 2 (ABC-Series) data using the quad array